

COOLANT MIXING IN LMFBR ROD BUNDLES AND  
OUTLET PLENUM MIXING TRANSIENTS

Progress Report

Principal Investigators

Neil E. Todreas - Tasks I and II  
Michael W. Golay - Task III  
Lothar Wolf - Task IV

Massachusetts Institute of Technology  
Department of Nuclear Engineering  
Cambridge, Massachusetts 02139

September 1, 1976 - November 30, 1976

NOTICE  
This report was prepared as an account of work sponsored by the United States Government. Neither the United States nor the United States Energy Research and Development Administration, nor any of their employees, nor any of their contractors, subcontractors, or their employees, makes any warranty, express or implied, or assumes any legal liability or responsibility for the accuracy, completeness or usefulness of any information, apparatus, product or process disclosed, or represents that its use would not infringe privately owned rights.

MASTER

Prepared for the U.S. Energy Research and Development  
Administration under Contract No. AT(11-1)-2245

ef  
DISTRIBUTION OF THIS DOCUMENT IS UNLIMITED

## DISCLAIMER

**This report was prepared as an account of work sponsored by an agency of the United States Government. Neither the United States Government nor any agency Thereof, nor any of their employees, makes any warranty, express or implied, or assumes any legal liability or responsibility for the accuracy, completeness, or usefulness of any information, apparatus, product, or process disclosed, or represents that its use would not infringe privately owned rights. Reference herein to any specific commercial product, process, or service by trade name, trademark, manufacturer, or otherwise does not necessarily constitute or imply its endorsement, recommendation, or favoring by the United States Government or any agency thereof. The views and opinions of authors expressed herein do not necessarily state or reflect those of the United States Government or any agency thereof.**

## **DISCLAIMER**

**Portions of this document may be illegible in electronic image products. Images are produced from the best available original document.**

"This report was prepared as an account of Government-sponsored work. Neither the United States, or the Energy Research and Development Administration nor any person acting on behalf of the Commission

- A. Makes any warranty or representation, expressed or implied, with respect to the accuracy, completeness or usefulness of the information contained in this report, or that the use of any information, apparatus method, or process disclosed in this report may not infringe privately owned rights; or
- B. Assumes any liabilities with respect to the use of, or for damages resulting from the use of, any information, apparatus, method, or process disclosed in this report.

As used in the above, 'person acting on behalf of the Commission' includes any employee or contractor of the Administration or employee of such contractor, to the extent that such employee or contractor prepares, disseminates, or provides access to, any information pursuant to his employment or contract with the Administration or his employment with such contractor."



Reports Issued Under This ContractA. Quarterly Progress Reports

COO-2245-1    Period June 1, 1972 - November 30, 1972  
COO-2245-2    Period December 1, 1972 - February 28, 1973  
COO-2245-3    Period March 1, 1973 - May 31, 1973  
COO-2245-6    Period June 1, 1973 - August 31, 1973  
COO-2245-7    Period September 1, 1973 - November 30, 1973  
COO-2245-8    Period December 1, 1973 - February 28, 1974  
COO-2245-10   Period March 1, 1974 - May 31, 1974  
COO-2245-13   Period June 1, 1974 - August 31, 1974  
COO-2245-14   Period September 1, 1974 - November 31, 1974  
COO-2245-15   Period December 1, 1974 - February 28, 1975  
COO-2245-23   Period March 1, 1975 - May 31, 1975  
COO-2245-25   Period June 1, 1975 - August 31, 1975  
COO-2245-26   Period September 1, 1975 - November 30, 1975  
COO-2245-28   Period December 1, 1975 - February 29, 1976  
COO-2245-30   Period March 1, 1976 - May 31, 1976  
COO-2245-31   Period June 1, 1976 - August 31, 1976

Reports Issued Under This Contract

B. Topical Reports

E. Khan and N. Todreas, "A Review of Recent Analytical and Experimental Studies Applicable to LMFBR Fuel and Blanket Assembly Design," COO-2245-4TR, MIT, Sept. 1973.

E. Khan, W. Rohsenow, A. Sonin and N. Todreas, "A Simplified Approach for Predicting Temperature Distribution in Wire Wrapped Assemblies," COO-2245-5TR, MIT, September 1973.

T. Eaton and N. Todreas, "Instrumentation Methods for Interchannel Coolant Mixing Studies in Wire-Wrap Spaced Nuclear Fuel Assemblies," COO-2245-9TR, MIT, June 1974.

Y. B. Chen, K. Ip, N. E. Todreas, "Velocity Measurements in Edge Subchannels of Wire Wrapped LMFBR Fuel Assemblies," COO-2245-11TR, MIT, September 1974.

E. Khan, N. Todreas, W. Rohsenow, A. A. Sonin, "Analysis of Mixing Data Relevant to Wire-Wrapped Fuel Assembly Thermal-Hydraulic Design," COO-2245-12TR, MIT, Sept. 1974.

E. Khan, W. Rohsenow, A. Sonin, N. Todreas, "A Porous Body Model for Predicting Temperature Distributions in Wire Wrapped Fuel and Blanket Assemblies of a LMFBR," COO-2245-16TR, MIT, March 1975.

E. Khan, W. M. Rohsenow, A. Sonin, N. Todreas, "Input Parameters to the ENERGY Code (To be used with the ENERGY Code Manual ) COO-2245-17TR, MIT, May 1975.

E. Khan, W. Rohsenow, A. Sonin, N. Todreas, "Manual for ENERGY Codes I, II, III," COO-2245-18TR, MIT, May 1975.

E. Khan, W. Rohsenow, A. Sonin, N. Todreas, "Manual for ENERGY Codes I, II, III Computer Programs," COO-2245-18TR Revision 1, MIT, July 1976.

P. Carajilescov and N. Todreas, "Experimental and Analytical Study of Axial Turbulent Flows in an Interior Subchannel of a Bare Rod Bundle," COO-2245-19TR,

B. Chen and N. Todreas, "Prediction of Coolant Temperature Field in a Breeder Reactor Including Interassembly Heat Transfer," COO-2245-20TR, MIT, May 1975.

F. Carre and N. Todreas, "Development of Input Data to Energy Code for Analysis of Reactor Fuel Bundles," COO-2245-21TR, MIT, May 1975.

Reports Issued Under This Contract

B. Topical Reports, Continued

H. Ninokata and N. E. Todreas, "Turbulent Momentum Exchange Coefficients for Reactor Fuel Bundle Analysis," COO-2245-22TR, MIT, June 1975.

R. Anoba and N. Todreas, "Coolant Mixing in LMFBR Rod Bundles and Outlet Plenum Mixing Transients," COO-2245-24TR, MIT, August 1975.

B. Bosy, "Fabrication Details for Wire Wrapped Fuel Assembly Components," COO-2245-27TR, MIT, November 1975.

Ralph G. Bennett and Michael W. Golay, "Interferometric Investigation of Turbulently Fluctuating Temperature in an LMFBR Outlet Plenum Geometry," COO-2245-29TR, MIT, June 1976.

N.E. Todreas, "Analysis Methods for LMFBR Wire Wrapped Bundles," COO-2245-32TR, MIT, November 1976

K.L. Basehore and N.E. Todreas, "Development of Stability Criteria and an Interassembly Conduction Model for the Thermal-Hydraulics Code SUPERENERGY," COO-2245-33TR, MIT December 1976.

Reports Issued under this ContractC. Papers and Summaries

Yi Bin Chen, Ka-Lam Ip, Neil E. Todreas, "Velocity Measurements in Edge Channels of Wire-Wrapped LMFBR Fuel Assemblies," American Nuclear Society Transactions Vol. 19, 1974, pp. 323-324.

P. Carajilescov, N. Todreas, "Experimental and Analytical Study of Axial Turbulent Flows in an Interior Subchannel of a Bare Rod Bundle," J. of Heat Transfer, Vol. 98, No. 2, May 1976, pp. 262-268 (Included as Appendix to Quarterly Progress Report, COO-2245-15).

E. Khan, W. Rohsenow, A. Sonin, N. Todreas, "A Porous Body Model for Predicting Temperature Distribution in Wire-Wrapped Fuel Rod Assemblies," Nuclear Engineering and Design, 35 (1975) 1-12.

E. Khan, W. Rohsenow, A. Sonin, N. Todreas, "A Porous Body Model for Predicting Temperature Distribution in Wire-Wrapped Rod Assemblies Operating in Combined Forced and Free Convection," Nuclear Engineering and Design, 35 (1975) 199-211.

Ralph G. Bennett and Michael W. Golay, "Development of an Optical Method for Measurement of Temperature Fluctuation in Turbulent Flows," American Nuclear Society Transactions, Vol. 22, 1975, p. 581.

B. Chen and N. Todreas, "Prediction of the Coolant Temperature Field in a Breeder Reactor Including Interassembly Heat Transfer," Nuclear Engineering and Design 35, (1975) 423-440 (Included as Appendix to Quarterly Progress Report, COO-2245-23).

R. Bennett and M.W. Golay, "Interferometric Investigation of Turbulently Fluctuating Temperature in an LMFBR Outlet Plenum Geometry," Accepted for the ASME Winter Annual Meeting, Dec., 1976, (Included as Appendix in Quarterly Progress Report, COO-2245-30).

B.B. Mikic, E.U. Khan, N.E. Todreas, "An Approximate Method for Predicting Temperature Distribution in Wire Wrapped Fuel Assemblies of a Liquid Metal Fast Breeder Reactor," Mech. Res. Comm., Vol. 3, 353-360 (1976).

Commencing with report COO-2245-30, a new task, TASK IV, which has been added to the contract, was reported. This TASK IV and TASK IID differ in that TASK IV is initially concentrated on thermal analyses using slug and laminar velocity profiles while TASK IID is concentrated on hydrodynamic analyses of turbulent velocity fields.

COOLANT MIXING IN LMFBR ROD BUNDLES AND  
OUTLET PLENUM MIXING TRANSIENTS

Contract AT(11-1)-2245

Quarterly Progress Report

September 1, 1976 - November 30, 1976

The work of this contract has been divided into the following Tasks:

**TASK I: BUNDLE GEOMETRY (WRAPPED AND BARE RODS)**

TASK IA: Assessment of Available Data

TASK IB: Experimental Bundle Water Mixing Investigation

TASK IC: Experimental Bundle Peripheral Velocity Measurements (Laser Anemometer)

TASK ID: Analytic Model Development - Bundles

**TASK II: SUBCHANNEL GEOMETRY (BARE RODS)**

TASK IIA: Assessment of Available Data

TASK IIB: Experimental Subchannel Water Mixing Investigation

TASK IIC: Experimental Subchannel Local Parameter Measurements (Laser Anemometer)

TASK IID: Analytic Model Development - Subchannels

**TASK III: LMFBR OUTLET PLENUM FLOW MIXING**

TASK IIIA: Analytical and Experimental Investigation of Velocity and Temperature Fields

**TASK IV: THEORETICAL DETERMINATION OF LOCAL TEMPERATURE FIELDS IN LMFBR FUEL ROD BUNDLES**

TASK I: BUNDLE GEOMETRY (WRAPPED AND BARE RODS)

TASK IA: Assessment of Available Data and Codes (Kerry Basehore)

No work was performed this quarter.

TASK IB.2 Experimental Bundle Water Mixing Investigation

Repeat of Laminar and Transition Flow - 61 Pin Fuel Mixing Experiments (Stuart Glazer)

During the past quarter, 3 salt injection rods were built. Initial difficulties in fabrication forced temporary delay of the mixing tests. It was therefore decided to initiate flow split tests while waiting for the completion of the injection rods. Initial flow split data was taken at an approximate Reynolds number of 10,000, the maximum capacity of the outlet plenum. As the eventual goal of the test series is to take flow split and mixing data well into the turbulent regime, it was decided to disassemble the bundle, and add a second water discharge line at the outlet plenum. It is estimated that this will widen the range of Reynolds numbers at which data can be taken to at least 20,000.

While the bundle was disassembled, several of the pins which were recently wrapped and found to be faulty were repaired. Flow split data over a wide range of Reynolds numbers will be taken during the next quarter. Mixing will also be initiated, pending completion of the flow split data.

The hardware modifications to the Interdata Computer, required for use as key component in the Automated Data Acquisition System, were completed. Additional software, comprising the real time operating system, was written, and the entire system is being readied for laboratory checkout early in the current quarter. Completion of the additional software package to be used for analysis of data taken with the computer based system will be completed during the next quarter.

TASK IB.3 217 Pin Mixing Experiments (Stuart Glazer)

Modification of the 217 pin bundle obtained from HEDL was nearly completed during the past quarter. Space and mounting considerations required the shortening of the bundle and all pins to approximately five feet. Additional mounting hardware, necessary to permit bundle assembly with use of the inlet and outlet plenum of the 61 pin fuel bundle, was designed and fabricated. The bundle is expected to be ready for testing early in the next quarter.

TASK IB.4 61 Pin Blanket Bundle Experiment (Chong Chiu)

During this quarter, flow split and mixing experiments were run.

Flow Split - Results are shown in Figs. 1, 2 and 3 for the three subchannel types compared to theoretical flow splits. A strong dip and hump appear in the transition regime for the interior and edge channels. This trend is not apparent from the corner channel data primarily due to the larger error involved with only six corner positions to average. Additional measurements are planned to confirm the transition regime results and explore the laminar regime. Significant differences are also apparent between theoretical and measured results over the Reynolds number region tested which persist even at Reynolds number of  $16 \times 10^3$  where the measurements appear to become constant with Reynolds number.

Mixing - Salt conductivity data was obtained with the injector rod 16 and 22.5 inches from the measurement plane. These data were gathered over the following test conditions.

$$668 \leq Re \leq 10,650$$

for the following geometric conditions

BUNDLE GEOMETRIC PARAMETERS:  
 P/D=1.067  
 NUMBER OF RODS=61  
 ROD DIAMETER=0.501 INCH  
 WIRE DIAMETER=0.0314 INCH  
 FLAT TOLERANCE=0.022

The data was reduced using the experimental flow split presented above. Values of  $\epsilon^*$  and  $C_1$  which fit the data were obtained by a last mean square method utilizing SUPERENERGY. These resulting values are shown on Figs. 4 and 5 which indicate that for this geometry the flow appears to be slipping over the wire wrap more than for geometries of increased  $h/D$ .

TASK IC: Experimental Bundle Peripheral Velocity  
Measurement (Laser Anemometer)

No work was performed this quarter since the equipment is being used for TASK III experiments.



TASK ID: Analytic Model Development - Bundles

TASK ID.1: Steady State SUPERENERGY (Kerry Basehore)

1. SUPERENERGY empirical constants

There has been some confusion on the definition and usage of empirical constants in SUPERENERGY [1]. These difficulties stem from two sources. First, the length parameter used in nondimensionalizing the enhanced eddy diffusivity constant in SUPERENERGY is not consistent with the ENERGY definition [2, 3,4]. SUPERENERGY uses the rod diameter while ENERGY uses the interior subchannel equivalent diameter. In order to correct this inconsistency, the SUPERENERGY code has been revised by simply changing the factor CONVER on line 3 of page 2-3 in the manual. Revision 1 of the Manual [1], now being issued, contains this change along with an updated sample program. Thus, Khan's correlation [2,3] for  $\epsilon^*$  and C can now be used to provide the constants for SUPERENERGY. The constants from this correlation must, however, be adjusted by lateral and axial porosities as specified in the appendices of references 2 and 3 since SUPERENERGY is based on a subchannel arrangement and not on the porous body model used in producing the correlations. This adjustment is frequently missed and is the source of the second difficulty with the empirical constants.

With the aid of some simplifying assumptions, it is possible to put the conversion factors in a usable form. When Khan's correlation is used, the empirical constants for SUPERENERGY are a combination of these conversion factors and the correlation values. The derivation of the two conversion factors follows:

- 1a. Derivation of the Eddy diffusivity conversion factor to transform  $\epsilon^*$  to  $\epsilon_1^*$

$\epsilon^*$  = nondimensional enhanced eddy diffusivity given by Khan's correlation and used in the ENERGY porous body model.

$\epsilon_1^*$  = nondimensionalized enhanced eddy diffusivity used in the ENERGY subchannel model and SUPERENERGY Revision 1.

$$\epsilon^* = \frac{\epsilon_H}{U \cdot D_e} \quad \epsilon_1^* = \frac{\epsilon_H}{V \cdot D_e} \quad (1)$$

where

$\epsilon_H$  = enhanced effective eddy diffusivity for heat transfer  
 $V$  = average bundle velocity (subchannel model)

$U$  = superficial average bundle velocity (porous body model)

$D_e$  = equivalent interior channel hydraulic diameter

then from [1]

$$\epsilon_1^* = \frac{\lambda_a}{\lambda_{L1}} \epsilon^* \quad (2)$$

and

$\lambda_a$  = bundle average axial porosity

$\lambda_{L1}$  = lateral porosity in the bundle interior region.

$$\lambda_a = \frac{\text{void area}}{\text{total area}} = \frac{\frac{\sqrt{3}}{2} D_F^2 - \frac{N\Pi}{4} (D_R^2 + D_W^2)}{\frac{\sqrt{3}}{2} D_F^2} \quad (3)$$

$$\lambda_{L1} = \frac{\text{lateral cross flow area}}{\text{pitch length}} = \frac{P - D_R}{P} = 1 - \frac{D_R}{P} \quad (4)$$

where

$$D_F = \text{duct flat to flat distance} = \left[ \sqrt{3} P N_{\text{RING}} + D_R + 2D_W \right]$$

$P$  = fuel rod triangular pitch

$D_R$  = fuel rod diameter

$D_W$  = wire wrap diameter

$N$  = number of fuel rods in the bundle

$N_{\text{RING}}$  = number of hexagonal rings of fuel rods in the bundle

assume that the fuel rod pitch  $P$  can be approximated by

$$P \cong D_R + D_W$$

then [3] becomes

$$\lambda_a = 1 - \frac{N\Pi}{2\sqrt{3}} \frac{\left[ D_R^2 + (P - D_R)^2 \right]}{\left[ P(\sqrt{3} N_{\text{RING}} + 1) + (P - D_R) \right]^2} \quad (5)$$

$$\lambda_a = 1 - \frac{N\Pi}{2\sqrt{3}} \frac{\left[ \left(\frac{D_R}{P}\right)^2 + \left(1 - \frac{D_R}{P}\right)^2 \right]}{\left[ \sqrt{3} N_{RING} + 2 - \frac{D_R}{P} \right]^2} \quad (5)$$

replacing (4) and (5) into (2) yields

$$\epsilon_1^* = B_1 \epsilon^* \quad (6)$$

where

$$B_1 = \left[ 1 - \frac{N\Pi}{2\sqrt{3}} \frac{\left[ \left(\frac{D_R}{P}\right)^2 + \left(1 - \frac{D_R}{P}\right)^2 \right]}{\left[ \sqrt{3} N_{RING} + 2 - \frac{D_R}{P} \right]^2} \right] \left[ \frac{1}{\left[ 1 - \frac{D_R}{P} \right]} \right] \quad (7)$$

The conversion factor in Eq. (7) is presented graphically in Fig. 6 as a function of  $P/D_R$  and the number of fuel rods,  $N$ .

lb. Derivation of the swirl velocity conversion factor to transform  $C$  to  $C_1$

$C$  = ratio of the superficial swirl velocity to the superficial bundle average axial velocity used in the ENERGY porous body model and given by Khan's correlation.

$C_1$  = ratio of the swirl velocity to bundle average axial velocity in the ENERGY subchannel model and SUPER-ENERGY

$$C = \frac{U_s}{U} \quad C_1 = \frac{V_s}{V} \quad (8)$$

where

$U_s$  = superficial swirl velocity in the bundle peripheral region

$V_s$  = actual swirl velocity in the bundle peripheral region.

then from Eq. (8)

$$C_1 = \frac{\lambda_a}{\lambda_s} C \quad (9)$$

and 6: for bundle ...

$\lambda_{a} =$  bundle average axial porosity as derived above  
 $\lambda_{s} =$  lateral porosity in the peripheral region of length ...  
 For the purpose of data comparison, only the turbulent flow data was considered here, since most of interest that satisfy the  $Gr_{c}$  criteria [2,3] enabling lateral cross flow area  $\lambda_{s} = \frac{A_{s}}{A_{c}}$  be in this fl(10) region width  $\frac{D_{R}}{P}$ . Further the validity of this new swirl mod21 is accomplished where more data is available.

where  
 Figures 9 and 10 show twelve inch wire wrap pitch data.  $\lambda_{s}$  = distance between the duct wall and outermost cal transvers fuel rod, i.e., the velocity at a particular point within the subchannel. The transverse velocity shape we seek assume that  $\lambda_{s}$  can be approximated by PERENERGY CODE. Since this code utilizes only subchannel averaged transverse velocities, some question exists regarding which data is most applicable for this purpose. The  $\lambda_{s}$  points A, B and C perhaps do the best job since they contain little of the internal subchannel then Eq. (10) becomes compared to points D and E) that are modeled by another empirical constant, the enhanced eddy diffusivity  $\alpha_{e}$ . Future work should include a more detailed experimental look into the subchannel transverse velocity flow field (11) that is true lumped  $\overline{D_{R}}$  average  $\overline{D_{R}}$  transverse velocity can be found.

Figure 11 shows a replot of Fig. 9 on a normalized scale. Also included are two averages, again normalized. The dashed line probably represents the best average of the two since it uses data points that are far from the corner and the most fully developed hydrodynamically.

Figures 12, 13 and 14 are similar to Figs. 9, 10 and 11 respectively except they are for the six inch wire wrap pitch. replacing Eqs. (5) and (11) into Eq. (9) yields

All MIT data is arbitrarily extrapolated to zero at  $\alpha = 0^\circ$ , i.e., the point at  $C_{1} = B_{2}$  (the wire wrap passes through the gap between the fuel pin and duct wall). Thus the range of whereability of MIT data extends from  $45^\circ < \alpha < 315^\circ$ . Future efforts should try to fill in this range of data uncertainty,  $-45^\circ < \alpha < 45^\circ$ .

Equation (13) is a wire bundle velocity  $2\sqrt{3}$  their six inch wire wrap lead bundle which design primary  $\sqrt{3} N_{RING}$  and axial pressure profiles may not

$$\left[ \left( \frac{D_R}{P} \right)^2 + \left( \frac{D_R}{P} \right)^2 \right] \left[ \frac{P}{D_R} - \frac{1}{2} \right]$$

The conversion factor in Eq. (13) is presented graphically in Fig. 7 as a function of  $P/D_R$  and the number of fuel rods,  $N$ .

## 2. Swirl flow model (Kerry Basehore)

The present version of SUPERENERGY [1] requires the input of a correlated empirical constant,  $C_1$  which is the ratio of the transverse velocity in the bundle periphery to the bound average axial velocity. ENERGY [2,3,4] has a similar constant  $C$ , which is a ratio of the superficial velocities encountered in the porous body model. These constants are discussed in some detail in the preceding section. Both models assume that this input parameter and therefore the transverse velocity or swirl flow is invariant with edge subchannel axial and radial positioning. Experimental studies, most notable the WARD 11:1 air flow experiments [5,6,7] and the MIT laser doppler anemometer water tests [8], have shown that this assumption is incorrect.

Work started this quarter on reducing the available swirl flow data and incorporating it into the SUPERENERGY code. Data from all sources was graphed on a common base for ease in comparison. The convention used was that suggested by the WARD 11:1 documents [5,6,7]:

$$\frac{V_T}{V_B \cdot \tan \theta} \text{ versus } \alpha$$

where

$V_T$  = transverse velocity in the bundle periphery

$V_B$  = bundle average axial velocity

$\tan \theta$  = tangent of the angle of projection of the wire wrap centerline on the axis of the rod

$\alpha$  = wire wrap position on the rod circumference.  
The zero position is when the wire is crossing the gap between the fuel rod and the duct wall.

This definition implies that when

$$\frac{V_T}{V_B \tan \theta} = 1,$$

then the flow is following the wire wrap tangentially. For more discussion see Ref. 5.

## MIT-61 pin bundle data [8]

The MIT data was collected at several points radially (see Fig. 8) from a 61 pin water bundle at two flow rates (one turbulent, the other laminar) and wire wrap lead lengths of six and twelve inches. For the purpose of data comparison, only the turbulent flow data was considered here since most cases of interest that satisfy the  $Gr_c^*$  criteria [2,3] enabling use of forced convection SUPERENERGY will be in this flow regime. Expansion to laminar data analysis can be undertaken after the validity of this new swirl model is accomplished and more data is available.

Figures 9 and 10 show twelve inch wire wrap pitch data. In this case the transverse velocity plotted is the local transverse velocity, i.e., the velocity at a particular point within the subchannel. The transverse velocity shape we seek is one which can be used with the SUPERENERGY CODE. Since this code utilizes only subchannel averaged transverse velocities, some question exists regarding which data is most applicable for this purpose. The gap points A, B and C perhaps do the best job since they contain little of the internal subchannel mixing effects (as compared to points D and E) that are modeled by another empirical constant, the enhanced eddy diffusivity  $\epsilon_1^*$ . Future work should include a more detailed experimental look into the subchannel transverse velocity flow field so that a true lumped or average transverse velocity can be found.

Figure 11 shows a replot of Fig. 9 on a normalized scale. Also included are two averages, again normalized. The dashed line probably represents the best average of the two since it uses data points that are far from the corner and the most fully developed hydrodynamically.

Figures 12, 13 and 14 are similar to Figs. 9, 10 and 11 respectively except they are for the six inch wire wrap pitch.

All MIT data is arbitrarily extrapolated to zero at  $\alpha=0^\circ$ , i.e., the point at which the wire wrap passes through the gap between the fuel pin and duct wall. Thus the range of reliability of MIT data extends from  $45^\circ < \alpha < 315^\circ$ . Future efforts should try to fill in this range of data uncertainty,  $-45^\circ \leq \alpha \leq 45^\circ$ .

## French - 19 pin bundle data [9]

Lafay et al., took some visual measurements of the transverse velocity in their six inch wire wrap lead bundle which was designed primarily to investigate radial and axial pressure profiles in a wire wrap bundle. While these profiles may not

be as precise as laser doppler anemometer or pitot tube measurements, they do serve to point out gross data errors that may occur with the more sophisticated acquisition techniques. The French data are shown on Figs. 12 and 14.

#### WARD 11:1 Air Flow Tests [5,6,7]

One of the important results of the WARD tests was a detailed measurement of the cross flow profile in the gap as a function of wire wrap angle. Of particular interest in the data reduction done here is the transverse velocity profile for the edge subchannels as reported in Ref. 6 are reproduced in Fig. 15. The profile will vary to a small degree (see Ref. 10) depending on the method used to select the characteristic transverse velocity. Three possible choices are the gap averaged velocity, maximum velocity in the gap region or the gap centerline velocity. The average velocity is plotted here since it appears to be most reasonable choice physically. This choice in reality is not that important anyhow, since as can be seen the range of measurement is quite small,  $-66.7^\circ < \alpha < 49^\circ$ , and offers no hint as to the profile in the center region of Fig. 10.

Through comparison of the various sets of data it was decided to use the French visual data shown in Fig. 14 for the six inch lead velocity profile, and the hybrid curve shown in Fig. 16 for the twelve inch lead velocity profile. These can be updated as more reliable data becomes available. Each of these curves was numerically integrated, and the average was found by changing the coordinate system so that the average is designated as 1.00 it is possible to use the curves only as forcing functions in conjunction with the empirical constant  $C_1$  which will specify the magnitude. Some work has been started in checking this new swirl model against existing heated pin data. These results will be reported upon their completion next quarter.

Recommendations under consideration for future MIT laser doppler anemometer measurements are:

1. Repeat existing data in an attempt to determine reproducibility, also taking more data points per lead length.
2. Extend the range of the measurements to include a four inch lead with geometry similar the CRBR blanket assembly.
3. Extend the range of measurement to include other flow rates in order to determine  $Re$  effects.

## TASK ID: 2.1 Analytical Model Development - Transient

## 2.1 SUPERENERGY (Stuart Glazer)

During the past quarter, much effort was devoted to the evaluation of the requirements for transient analysis codes, as well as some of the numerical methods and analysis techniques currently available. Following is a report listing the results, and recommendations for future effort. Plant

## 1.0 Introduction

Many transient events are postulated to occur during the knowledge of primary coolant and fuel temperatures in the core region of a liquid metal fast breeder reactor during transient events is necessary to verify component design temperature requirements, verify reactor safety, establish allowable burnup limitations, and evaluate rod and assembly bowing and associated loads on the core support structure. Simplified assumptions and computation techniques currently in use produce necessarily conservative estimates of these temperatures. As fuel cost is highly sensitive to burnup restrictions, one major goal of the core designer is to reduce the conservatism of these estimates so that limits on fuel burnup may be safely extended. Significant core thermal transients, as well as some transient mechanisms, such as variable fuel rods in LMFBR's, unlike the bare rods in PWR's, are spirally wound with a spacer wire and packed in arrays in hexagonal ducts. Further, interassembly heat transfer effects are extremely important in LMFBR's owing to the very severe power gradients existing in the radial blanket region. Therefore, to refine estimates of coolant and fuel temperatures throughout the core, computer codes must accurately model intraassembly heat transfer at the very detailed sub-channel level, and must evaluate interassembly heat transfer effects for at least a symmetrical 1/12 core sector. Considered here which result in coolant flow in the forced convection. A large number of computer codes have been developed to date which analyze coolant temperatures in LMFBR's under steady state conditions. Some of these are: COBRA [11], THI-3D [12], COTEC [13], CORTAC [14], SUPERENERGY [15], and ENERGY I, II, and III [16]. A chart summarizing the available codes and their capabilities has been prepared by Dr. N. Todreas of MIT and is included here as Table 1 for reference. Codes such as COBRA and THI-3D, which solve the momentum, continuity, and energy equations simultaneously, require long computational running times and large amounts of memory, even for the solution of the steady state temperature field. Use of this type of code to predict temperature fields during transient events requires such long computational running time as to be totally impractical.



The ENERGY series of codes, developed initially at MIT by E. Khan, and extended with the steady state multiassembly code SUPERENERGY by B. Chen, have exhibited very good agreement with the data [17]. In particular, the SUPERENERGY code, restricted to problems where intra-assembly buoyancy forces are negligible in relation to the viscous forces, requires relatively modest amounts of core storage for even the largest cases, and extremely fast running times. This is due to the explicit finite difference scheme used, and the fact that the ENERGY model permits uncoupling of the ENERGY, momentum, and continuity equations for those cases where the buoyant forces are unimportant. E. Khan developed a modified Grashoff number criterion specifically to determine when decoupling of the 3 equations is permissible. Flow under these conditions is termed forced convection in the context of the ENERGY model. In cases of forced convection, temperature differences caused by radial power skews are assumed not to significantly affect the flow field.

The memory and computational time requirements of the SUPERENERGY code makes its extension to cover transient events in single and many coupled assemblies in cases of forced convection highly desirable. It will be shown in section 5 that it is not possible to provide predictions of the coolant temperature field at the subchannel level for all assemblies in 1/12 core sector studies. Two different versions of a transient SUPERENERGY code are therefore proposed to deal with individual aspects of the problem.

Chapter 2 describes broad classes of transient events postulated to occur in the design life of the Clinch River Breeder Reactor Plant, and defines the capabilities and operational characteristics considered essential for a useful transient computer code. Chapter 3 describes limitations and capabilities of currently available transient analysis codes. Chapter 4 evaluates several numerical methods, with particular application to the extension of the steady state SUPERENERGY code to cover transients. Chapter 5 proposes specific modifications to the ENERGY model for each of the 2 versions of the code; one intended for evaluation of interassembly heat transfer in 1/12 core sector studies, and one intended for detailed single assembly studies. Finally, Chapter 6 discusses the work to be done and additional questions to be resolved in the process of providing a complete package of transient analysis codes applicable in the forced convection flow regime.

## 2.0 Requirements for Transient Analysis Codes

### 2.1 CRBRP Core Transients

The transient version of SUPERENERGY under development is designed for use with liquid metal fast breeder reactors. The transients defined in this section are solely representative of events considered possible at various times during the design life of the Clinch River Breeder Reactor Plant (CRBRP)

Many transient events are postulated to occur during the life of the CRBRP. Although thermal effects, and operational, structural, and safety consequences must be determined for all of these, a small number of events have been identified as "worst case" transients, i.e., those events imposing the most severe thermal conditions on the reactor core for a large number of similar events. The list of transients contained in this section were determined with the assistance of Dr. Ron Coffield at Westinghouse Advanced Reactors Division. The events described herein are not intended to represent either a complete list of "umbrella" events, and may not reflect the final event definitions. They are intended to identify some of the major causes of significant core thermal transients, as well as some transient mechanisms, such as variation of coolant flow rate, rod power production, and inlet coolant temperature with time, and to define even duration times. This data is necessary to establish the capabilities for a transient analysis code.

The list of transients and event descriptions is contained in Table 2. Since current efforts are directed toward development of a code capable of thermal analysis under conditions of forced convection as defined in section 1.0, only those transient events or parts of transient events will be considered here which result in coolant flow in the forced convection regime at all times.

It can be seen from Table 2 that a useful transient analysis code must include the capability to analyze transients resulting in either single or combined variation of coolant flow rate, increases and decreases of power production of various rates, and also variation in coolant inlet temperatures. Event duration and transient energy storage within fuel rods affect dictate that the code be able to analyze transients lasting in the range of at least 1/2-2 minutes. Changes in bundle geometry resulting from severe thermal transients are not within the scope of this analysis.

## 2.2 CRBRP Core Transient Analysis Requirements

The CRBRP core consists of 377 [18] fuel, blanket, and primary and secondary control assemblies. All fuel, breeding, and control rods are contained within hexagonal stainless steel ducts of uniform flat to flat dimensions. Individual fuel and blanket bundles include groupings of 61 and 217 pins. Severe thermal gradients occurring in the core during reactor operation currently call for symmetric movement of certain assemblies during the refueling cycles to assure more uniform thermal exposure. A code which can model the thermal and hydraulic effects with a 1/12 core sector is considered sufficient [19] to accurately model interassembly heat transfer during most types of transient events. As a design goal therefore, the transient analysis code under development should be able to couple a maximum of up to 39 assemblies, the number of assemblies in a 1/12 core sector, to attain good estimates of interassembly heat transfer, with at least a coarse nodal structure.

Detailed transient analysis of individual bundles requires that the code must be capable of providing temperature profiles at several axial sections throughout the bundle on a subchannel basis. The largest bundle, the 217 pin assembly, contains 438 subchannels in the coolant. In addition, to account for the transient thermal energy capacity of the fuel rods and ducts which significantly dampen the response of the coolant to rapid thermal transients, it is necessary to accurately model each fuel pin and duct wall to evaluate the transient heat flux absorbed from or released to the coolant.

In addition to the functional characteristics already discussed, the code should offer maximum flexibility to the user in terms of specification of input parameters, forcing functions, and output. It has been determined from discussions with core designers at Westinghouse that when in the multi-assembly analysis role, the code should permit the following degree of specificity:

- A. For each bundle type (i.e., 61 pin fuel, 217 pin fuel, etc.)
  1. Complete description of all bundle geometric parameters
  2. Empirical constants  $\epsilon^*$  and  $C_1$
  3. Complete description of the following forcing functions:
    - a. normalized rod power generation vs. time
    - b. normalized bundle flow rate vs. time

3.2 COBRA

c. normalized axial power profile

The COBRA family of codes were originally designed to calculate coolant inlet temperatures vs. time for a sub-

assembly for fuel assemblies in PWR's. It therefore evaluates two phase fluid flow which is not necessary in the currently identified bundle type fluid metal fast breeder reactors.

2. Bundle identification numbers, wire wrapped pins in hexagonal ducts, and as such, is an extremely useful design tool at available.

3. Neighboring bundles with new or extremely complex geometries. It does not, however, have the capability to specify boundary conditions on each boundary face, i.e., each face for single subchannel, or sector boundaries for core sector.

COBRA III solves the continuity equation for heat flux boundary conditions can be either adiabatic, isothermal, or profile read in by user. profile read from previous case results on magnetic tape elements in the fuel and clad regions. This is a significant departure from previous pin power profiles required fuel to coolant heat transfer as a function of time to be specified as initial (time = 0) average rod power value, to be multiplied by the radial, axial, and temporal power profiles to obtain individual rod power continuity equations.

5. Normalized radial pin power profiles required fuel to coolant heat transfer as a function of time to be specified as initial (time = 0) average rod power value, to be multiplied by the radial, axial, and temporal power profiles to obtain individual rod power continuity equations.

COBRA III solves the continuity equation for heat flux boundary conditions can be either adiabatic, isothermal, or profile read in by user. profile read from previous case results on magnetic tape elements in the fuel and clad regions. This is a significant departure from previous pin power profiles required fuel to coolant heat transfer as a function of time to be specified as initial (time = 0) average rod power value, to be multiplied by the radial, axial, and temporal power profiles to obtain individual rod power continuity equations.

COBRA III solves the continuity equation for heat flux boundary conditions can be either adiabatic, isothermal, or profile read in by user. profile read from previous case results on magnetic tape elements in the fuel and clad regions. This is a significant departure from previous pin power profiles required fuel to coolant heat transfer as a function of time to be specified as initial (time = 0) average rod power value, to be multiplied by the radial, axial, and temporal power profiles to obtain individual rod power continuity equations.

2. COBRA V has as a goal analysis of interassembly heat transfer effects and some information as to individual bundle thermal and hydraulic performance for a 1/12 sector. Maximum permissible size of time step, generation and lumping within individual bundles. COBRA V is still under development, so that axial locations of desired printouts of the code capabilities must await its formal release.

4. Axial locations of desired printouts of the code capabilities must await its formal release.  
5. Times at which printouts are required

6.3.3 FORE-TII (20) Transient-duration

7. Number of nodes per fuel pin of the code FORE-II. FORE-II is a coupled point kinetics-thermal hydraulic code with the capability for interassembly heat flux results and maps and other parameters in the coolant, fuel, and moderator.

In detailed single assembly studies, essentially all of the above data is also required.

### 2.3 Core Storage and Computational Time Requirements

An obvious design goal is to minimize both core storage and computational running times for all cases. Specifically, to permit running on many of the large computer systems currently in use in industry and government research laboratories, the largest multiassembly problems and the largest single bundle cases should require a maximum of 2000 K bytes of core storage. Also, for practical consideration, the largest and longest cases should probably not require in excess of 2 hours of running time on a high speed computer, such as a Control Data 7600. This is a softer limit than than on core storage, as the permissible running time can be determined by each user on a case by case basis.

### 3.0 Available Transient Codes

In this section, brief descriptions will be given of some general computer codes currently used in the evaluation of core transients. It will be shown that none of these codes can practically be used to evaluate coolant and fuel temperatures in large bundles on a subchannel basis while considering interassembly heat transfer effects.

#### 3.1 CORTAC

The code CORTAC [14] was developed by Argonne National Laboratories and General Electric to analyze the effects of core transients on the core restraint systems of liquid metal fast breeder reactors. Structural and thermal analysis of the core restraint system is accomplished by coupled reactor kinetics, core thermal hydraulics, and structural deformation analyses. The core region is modeled as a series of annular rings of assemblies. Each of the annular rings may be further subdivided into up to 9 additional annular regions. Up to 30 axial sections may be specified.

While the above physical model of the reactor core is adequate to perform structural analyses of the core restraint system, it is not sufficient to provide detailed thermal and hydraulic data for a single bundle on a subchannel basis. It is also not sufficient to provide data about individual assemblies during multiassembly studies. Thus, CORTAC cannot be considered sufficient to provide the core analysts the data necessary to set and evaluate fuel burnup requirements nor realistically analyze the safety implications of certain severe transients with respect to the fuel.

### 3.2 COBRA

The COBRA [11] series of codes were originally designed to provide detailed thermal and hydraulic data on a sub-channel basis for fuel assemblies in PWR's. It therefore contains extensive capability to evaluate two phase fluid flow which is not necessary in the currently identified transients occurring in liquid metal fast breeder reactors. The code is structured to permit analysis of a wide variety of bundle geometries, is not limited to wire wrapped pins in hexagonal ducts, and as such, is an extremely useful design tool in evaluation of bundles with new or extremely complex geometries. It does not, however, have the capability to evaluate multiple assembly clusters.

COBRA III-C/MIT is a modified version of COBRA III altered to reduce running time and allow large number of radial nodes. Both versions include a finite difference fuel model with an arbitrary number of annular elements in the fuel and clad regions. This is a significant departure from previous versions of COBRA which required fuel to coolant heat transfer as a function of time to be specified as input.

COBRA III solves the momentum, energy, and continuity equations simultaneously by using a mixture of explicit and implicit numerical methods permitting unconditional spatial and temporal stability. The complexity of the calculations, combined with the numerical techniques used, result in excessive computational time and core storage requirements. It is uneconomical, and in many cases impossible, to run transients of necessary duration for the full subchannel representation of 217 pin and 61 pin bundles in the CRBRP.

COBRA V has as a goal analysis of interassembly heat transfer effects and some limited information as to individual bundle thermal and hydraulic performance for a 1/12 core sector. This code will require some homogenization and lumping within individual bundles. COBRA V is still under development, so that further evaluation of the code capabilities must await its formal release.

### 3.3 FORE-III [20]

Many transient analyses performed to date at Westinghouse ARD were done using a modified version of the code FORE-II. FORE-II is a coupled point kinetics-thermal hydraulic code with the capability of providing extremely detailed temperature maps and other system parameters in the coolant, fuel,

and clad for a single fuel rod, as a function of time. Boundary conditions which must be input are currently evaluated at Westinghouse with the use of steady state subchannel codes such as COTEC. Although some statistical and other data necessary to evaluate safety and burnup criteria can be determined from FORE-II, it is not capable of producing temperature fields on a subchannel basis for an entire fuel bundle or of determining inter and intra-assembly heat transfer effects. The code cannot be expanded to a subchannel code since core storage requirements currently approach the capacity of the computer. The running time is extremely fast, and runs approximately as long as the transient event duration.

### 3.4 Other Codes

Other specialized or test codes exist for determination of transient temperatures. One such code, COTECT [24], an experimental transient version of COTEC, was an attempt at determining the feasibility of expanding the CORTAC code into a 3-D transient version. Results indicated the impracticability of such a conversion. Hence, the COTECT code is not considered acceptable for general use.

## 4.0 Comparison of Fuel and Coolant Models and Numerical Methods

### 4.1 Energy Model and Steady State SUPERENERGY Code Numerical Methods

The ENERGY method models interchannel heat transfer as the result of both thermal diffusion and turbulent eddy diffusion. For the specific case of forced convection flow conditions, the velocity profile within the bundle is assumed known. Flow in the interior region of the bundle is assumed to be purely axial, and is currently apportioned to each subchannel type using E. Novendstern's friction drop correlations. In the peripheral region of the bundle, consisting of all the edge and corner subchannels immediately adjacent to the duct, the flow is postulated to contain both the axial component, as well as a circumferential component taken to be a percentage of the axial flow.

The assumption of known velocity profile under forced convection conditions is particularly significant, in that it permits uncoupling of the energy equations from the momentum and continuity equations, and causes vast simplifications in the computational procedure. In the discussion of analytical methods for conversion of SUPERENERGY to a transient code, it will be assumed that forced convection flow conditions, as defined in section 1.0, prevail. The transient codes developed as a result of this study will be applicable only to transients which remain in the forced convection flow regime at all times.

4.2 Modifications for Transient SUPERENERGY Code

4.2.1 Coolant Model

4.2.1.1 Single Temperature per Node Model

Currently, the steady-state SUPERENERGY code uses an explicit, finite difference marching scheme to determine axial and spatial temperature profiles. A single temperature is assigned to each subchannel at every axial step, representing the coolant temperature at the end of the axial step. The single temperature per node model shown in Fig. 17(a) is exemplified by the following explicit equation, describing the steady state temperature at the next axial level in an interior subchannel surrounded by 3 interior subchannels.

Nomenclature

(4-5)

$$T_{j+1}^j = T_j^j + \frac{Q_o \Delta z}{C_p V_{j+1}} + \frac{(p-d)z}{\rho C_p A_1} (k + \rho C_p \epsilon_{H_1}) \left[ \frac{T_1^j + T_2^j + T_3^j + 3T_o^j}{\eta_1} \right]$$

where  $A_1$  is the area of the subchannel,  $V_{j+1}$  is the volume of the subchannel,  $\eta_1$  is the hydraulic diameter, and  $V_o$  is the circumferential velocity component.

(4-1)

4.2.1.2 Bender Method

is defined in [22].

The simplest extension for the transient case of the explicit finite difference marching scheme with a single temperature per node is a finite difference marching scheme explicit both axially and temporally, with the single temperature assigned per node. Equation (4-1) extended to the transient case in this manner becomes

$$T_o^{ij} = T_o^{i,j-1} + \frac{Q_o \Delta t}{C_p A_1} + \frac{(p-d) \Delta t}{\rho C_p A_1} (k + \rho C_p \epsilon_{H_1}) \left[ \frac{T_1^{ij} + T_2^{ij} + T_3^{ij} + 3T_o^{ij}}{\eta_1} \right]$$

Bender [13] indicates that for the case of a single isolated coolant channel, in contact with only one fuel rod, the

remaining equation is a function of position,  $x$ , and time,  $t$ , within one axial section

of given subchannel.

$$\rho C_p A \frac{\partial T_o(x,t)}{\partial t} = \frac{\partial}{\partial x} \left[ \frac{k A}{H_1} (T_w(x) - T_o(x)) \right] - \rho C_p V A \frac{\partial T_o(x,t)}{\partial x} \quad (4-5)$$



where  $\Delta t$  is the time step, and  $i$  is the timestep index.

The primary advantages of this method are extreme simplicity, minimization of core storage requirements, and speed. The major disadvantage is the stability limits which must be observed. Note that in order for equation 4-2 to be considered strictly correct, the timestep must never be taken larger than the time required for the coolant to pass completely through a node. This time period is called the node sweep time. This restriction is necessary in order that the last term in equation 4-2, the convective term, result in coolant being convected into the current node only from the coolant node immediately upstream. It would be physically incorrect to permit the coolant to be drawn from more than one node upstream of the current node, as the effect of intermediate nodes on the coolant temperature would be lost. Therefore, in order to insure the node sweep time criteria is always observed, we require that

$$V\Delta t \leq \Delta z \quad (4-3)$$

or

$$\Delta t \leq \frac{\Delta z}{V} \quad (4-4)$$

where  $\Delta t$  is the timestep

$\Delta z$  is the axial step length

$V$  is the smallest axial coolant velocity in any sub-channel of the bundle.

Note that the node sweep time criteria also applies in the circumferential direction. In the edge and corner nodes, which

lie exclusively in a flow region postulated to contain a circumferential component of velocity, an additional term would be added to equation 4-2 representing the transient convection of energy into the current node from the adjacent edge or corner node. Care must be taken to insure that in addition to equation 4-4,

$$\Delta t \approx \frac{\Delta l}{V_{\theta}} \quad (4-5)$$

where  $\Delta l$  is the lateral extent of the adjacent edge or corner node,  $V_{\theta}$  is the circumferential velocity component.

#### 4.2.1.2 Bender Method

Another finite difference formulation in use in codes such as CORTAC is one which specifies two nodal temperatures; the node average temperature and the node outlet temperature, as shown in Fig. 17(a). Although this formulation is potentially more accurate than the assignment of a single temperature per coolant node, it has a disadvantage of requiring twice as much storage.

Bender [13] indicates that for the case of single isolated axial coolant channel, in contact with only one fuel rod, the governing equation for determination of coolant temperature as a function of position,  $z$ , and time,  $t$ , within one axial section is given as:

$$\rho C_p A \frac{\partial T_c(t, z)}{\partial t} = \frac{1}{R_{wc}} [T_w(t) - T_c(t)] - \rho C_p V A \frac{\partial T_c(t, z)}{\partial z} \quad (4-5)$$

where  $T_c(t, z)$  = coolant temperature  
 $\bar{T}_c(t)$  = node average coolant temperature  
 $T_w(t)$  = node average fuel rod wall temperature  
 $R_{wc}$  = thermal resistance between the clad and the coolant.

Bender further notes that

$$\bar{T}_c(t) = \frac{1}{\Delta z} \int_0^{\Delta z} T_c(t, z) dz \quad (4-6)$$

and

$$\frac{\partial T_c(t, z)}{\partial z} = \frac{T_L(t) - T_{in}(t)}{\Delta z} \quad (4-7)$$

where  $T_L(t)$  = node outlet temperature  
 $T_{in}(t)$  = node inlet temperature, which equals the outlet temperature from the upstream node.

In order to determine a valid expression for  $T_L(t)$ , Bender solved a reduced form of equation (4-5) by Laplace transform methods, where the heat transfer from the fuel rod to the coolant is replaced by a time varying heat flux,  $q''$ . From this, the coolant temperature as functions of both position and time was explicitly determined. Evaluating this solution at  $z = \Delta z$ , the node outlet, and expanding the result to be applicable to a coolant subchannel in the core, Bender obtains the general solutions for the coolant nodal outlet temperature as a function of time:

$$T_L^{i+1,j} = T_L^{i,j} - 2(T_L^{i,j} - \bar{T}_c^{i,j}) \frac{V\Delta t}{\Delta z} + \sum_{k=1}^N \frac{1}{R_{c_k}} (\bar{T}_k^{i,j} - \bar{T}_c^{i,j}) \Delta t + \frac{\dot{q}'''_{i+1} \Delta t}{\rho C} \quad (\text{for } \Delta t < \frac{\Delta z}{V}) \quad (4-8)$$

$$T_L^{i+1,j} = T_L^{i,j} + \left( \frac{T_{in}^{i+1,j} - T_{in}^{i,j}}{\Delta t} \right) \left( \Delta t - \frac{\Delta z}{V} \right) + \sum_{k=1}^N \frac{1}{R_{c_k}} (\bar{T}_k^{i,j} - \bar{T}_c^{i,j}) \Delta t + \frac{\dot{q}'''_{i+1} \Delta z}{\rho C V} \quad (\text{for } \Delta t > \frac{\Delta z}{V}) \quad (4-9)$$

where:  $i$  is the timestep index

$j$  is the axial step index

$k$  is the index for neighboring subchannels

$R_{c_k}$  = thermal resistance between node  $k$  and the current coolant node.

The general form for the coolant node average temperature is also given by an adaptation of equation 4-5 to finite difference form:

$$\bar{T}_c^{i+1,j} = \bar{T}_c^{i,j} + \sum_k \frac{1}{R_{wc}} (\bar{T}_k^{i,j} - \bar{T}_c^{i,j}) \Delta t \quad (4-10)$$

$$+ \frac{\dot{q}'''_{i+1} \Delta t}{\rho C} - (T_L^{i,j} - T_{in}^{i,j}) \frac{V\Delta t}{\Delta z} \quad (4-10)$$

Bender compared the accuracy of his particular solutions for the coolant outlet temperature as a function of time with some other heuristic algorithms commonly in use at the time, namely

$$T_L(t + \Delta t) = T_L(t) + [\bar{T}_c(t + \Delta t) - \bar{T}_c(t)] \quad (4-11)$$

and

$$T_L(t + \Delta t) = \bar{T}_c(t + \Delta t) + [\bar{T}_c(t + \Delta t) - \bar{T}_{in}(t + \Delta t)] \quad (4-12)$$

It was shown that in all cases considered, the exact solution obtained by Bender produced results of higher accuracy than expression (4-11) and (4-12).

In addition, Bender introduced a solution procedure of Levy [24] which permits extension of the timestep,  $t$ , in explicit finite difference equations without instability. As reported in the paper by Levy, however, this technique will only produce acceptable accuracy if the temporal stability criteria, as derived for example, by Dusingberre [25], would not normally be exceeded without the method for the majority of nodes in the bundle cross-section. Levy's procedure was derived for the specific purpose of permitting the inclusion of a small number of physically small nodes in a finite difference network containing many larger nodes. As shown by Dusingberre, the timestep stability criteria varies directly with node volume. Since overall network stability is governed by the stability of the least stable node, Levy's method was capable of reducing overall computational time by permitting selection of timesteps normally suitable for most of the larger nodes. Levy reports, however, that even though unconditional stability for all timesteps results with his method, solution accuracy is good only when the timestep selected is normally stable for most of the nodes in the network.

The Bender method was originally investigated because of the promise of unconditional temporal stability of the explicit finite difference equations. The Levy method does not in general permit large increases in the size of the timestep with acceptable accuracy. Bender does point out the importance of the node sweep time, and develops specialized expressions which are valid for

4.2.2.3. Lumped Energy Partial Solution Technique  
 the nodal outlet temperatures for  $\Delta t$  less than the sweep time and

Early in the investigation into the characteristics of approximate expressions for the case of  $t$  greater than the sweep time. Various methods of solution of transient heat fluxes from the time. Timesteps larger than the sweep time cannot strictly be used in a finite difference scheme (see section 4.2.1.1). Other storage requirements could potentially impose a more severe restriction on code performance than the completely explicit methods, such as that employed by Fox and Yackle [16] have been developed which provide alternate definition of the coolant outlet temperature as a function of time. Doubling of the storage requirements, added complexity and lack of increase of stability rapid and efficient calculation of transient heat fluxes from suggest rejection of the dual temperature specification per node fuel pins, while requiring minimal core storage requirements. formulation in favor of that described in section 4.2.1.1. In the previous project report [12] results of this investigation were reported. The mass of the entire fuel pin over

of the single versus dual temperature per node formulation is axial segment was lumped in two studies into one and two finite difference nodes, respectively, and transient energy balances methods for various transient test cases will be carried out. Only if the dual temperature approach yields significant improvements such as to alter the heat capacity of the elements. Empirical factors were calibrated against the finite

difference fuel model of BOCAL III-C-MTR in such a way as to match the transient heat flux from the rod as well as possible.

The finite difference lumped energy balance for the single node model is:

#### 4.2.2 Fuel Models

##### 4.2.2.1 Analytic Solutions

While a number of totally analytic methods [27] exist for determination of both temperature distributions and heat fluxes valid at all times, such techniques are in general not applicable to the current problem. All such methods necessarily require a priori specification of the heat transfer coefficient, power generation, and coolant temperature. In a transient SUPERENERGY code, the heat transfer coefficient is determined from the input specification of coolant flowrate and an experimental correlation for heat transfer coefficient in liquid metals as a function of local Nusselt number. Transient power generation is also specified in the input. The coolant temperature as a function of time is not known a priori. Hence, as the coolant temperature is calculated at each timestep, the analytic solution for transient temperature distribution and heat flux may be advanced at most by only one timestep as long as care is taken to insure correct initial conditions at each calculation point. Hence, even though core storage requirements are minimized, the advantages of the analytic approach are lost.

##### 4.2.2.2 Hybrid Solution

Nijsing and Eifler have developed a hybrid solution technique [28] which permits accurate and computationally simple solutions to the transient temperature problems in fuel rods. The hybrid method breaks up the fuel pin cross section into several radial annular nodes, similar to a finite difference

nodalization. The analytic transient energy equation is written for each node, so that the temperature of each node as a function of time may be determined in closed form. This solution technique is not advantageous in the current problem for the same reasons as the analytic solutions (see section 4.2.2.1).

#### 4.2.2.3 Lumped Empirical Solution Technique

Early in the investigation into the characteristics of various methods of solution of transient heat fluxes from the fuel pins, it was recognized that computational time and the storage requirements could potentially impose a more severe restriction on code performance than the completely explicit coolant solution scheme. It was therefore decided to investigate whether a weighted lumped parameter approach would permit rapid and efficient calculation of transient heat fluxes from fuel pins, while requiring minimal core storage requirements. In the previous project report [19] results of this investigation were reported. The mass of the entire fuel pin over an axial segment was lumped in two studies into one and two finite difference nodes, respectively, and transient energy balances written for these nodes. Empirical factors,  $\Gamma$ , were applied in such a way as to alter the heat capacity of the elements. These empirical factors were calibrated against the finite difference fuel model of COBRA III-C-MIT in such a way as to match the transient heat flux from the rod as well as possible.

The finite difference lumped energy balance for the single region model is:



$$m C_p \Gamma \frac{dT}{dt} = q''' V - h A_s (T - T_c) \quad (4-13)$$

where

- $m$  = fuel rod mass
- $C_p$  = specific heat
- $T$  = temperature of the (single node) fuel pin
- $h$  = heat transfer coefficient from the surface
- $A_s$  = fuel rod surface area
- $T_c$  = coolant temperature
- $q'''$  = volumetric heat flux
- $V$  = volume of fuel pin.

Similar equations used in the two region lumped model are given in [29]. Note that in the formulation of the single region lumped model, equation (4-13), the thermal resistance of the fuel clad interface does not explicitly appear. This resistance was included in the finite difference code used for calibration, and hence, its effect is included in the empirical constant,  $\Gamma$ . Results presented in [29] indicate that neither the single nor the dual lumped node approach provides acceptable matches in transient heat fluxes, especially in the relatively massive blanket bundle pins. Additionally, it is considered possible that the empirical constants are functions of fuel rod properties, pin geometry, and transient characteristics. The advantages of this method, including extreme computational speed and minimal core storage requirements, were offset by poor accuracy in some cases, and the need for extensive additional parametric analysis and evaluation of the empirical constants. The use of

this method in the transient SUPERENERGY code was therefore re-  
jected, and further development beyond that reported in [29] has  
not been suspended. It has been programmed and tested in conjunction with

the 4.2.2.4 bundle test version of transient SUPERENERGY, estimated

4.2.2.4 Collocation Method  
A new highly accurate procedure developed to  
determine the transient temperature distribution in fuel pins  
utilizes a collocation method with Hermite cubic splines [30],  
[31], [32]. The detailed formulation of the equations pertaining  
to the general case of transient response of the fuel and clad  
regions of a fuel rod with temperature dependent properties, is  
contained in [30] and will not be presented here. Simply, the  
technique involves nodalization of the fuel rod into annular and

circumferentially symmetric elements in the fuel and clad regions.

The temperature distribution in each region is assumed to be  
of a specific form, namely, cubic Hermite polynomials. Sub-

stitution of the assumed temperature distribution into the  
governing partial differential equation and boundary and initial  
conditions, and then substitution of these conditions back into

4.2.3 Dynamic Storage Replacement Scheme  
the governing equation yields a set of simultaneous equations for  
the complete temperature distribution, determinate to within a

set of constants. It can be shown that the number of constants  
at every axial level, for both the current timestep and the  
previous timestep, is equal to twice the number of nodes in the fuel and clad  
region. Therefore, all the constants may be uniquely determined

by requiring the governing differential equations to be satis-  
fied exactly with the assumed temperature distribution at two  
adjacent and previous axial levels. The Gauss-Legendre quadrature points of

order two are chosen as these two collocation points so as to maximize accuracy.

It can be seen that at each step, the simultaneous solution of a set of equations is necessary in order to determine heat fluxes and temperature distributions. A transient version of SUPERENERGY, capable of determining temperature distributions in a 7 pin bundle of fixed geometry, was written as a test vehicle for evaluation of various coolant and fuel models. Comparison of running times using the simple explicit single lumped region fuel model discussed in section 4.2.2.3, with a modified version of a collocation code written by Yeung [33] with constant properties, indicates the collocation procedure is slower by an order of magnitude. Rough estimates for the running time of far larger bundles during long transients would prohibit the use of the collocation technique. Therefore, even though extremely high accuracy has been demonstrated with the collocation method using variable fuel and clad properties, the use of this procedure is tentatively rejected in favor of some other very simple and fast explicit fuel model.

#### 4.2.2.5 - Finite Difference Method

The finite difference method, as used in codes such as COBRA III-C, assumes circumferentially symmetric nodalization of the fuel and clad into annular elements. Discussions with Dr. Ron Coffield of Westinghouse ARD have indicated that 3 nodes in the clad and 7 nodes in the fuel region would normally be sufficient for a "high accuracy" solution. Fully explicit

solutions to the finite difference model are possible, and are described, for example, by Bender [23]. While this method has not currently been programmed and tested in conjunction with the 7 pin bundle test version of transient SUPERENERGY, estimates of running time based on extending the single region explicit fuel model described in section 4.2.2.3 indicate the finite difference method will be much faster than the collocation procedure. Storage requirements will be very large, but estimates of these requirements made in section 5.1.3 and 5.2.3 indicates sufficient storage available in industrial and government computers for even the largest anticipated cases. Evaluation of the finite difference procedure in the test case, and investigation of the effect of temperature dependent properties on solution accuracy is necessary before final selection is made. If running time and accuracy of the explicit finite difference fuel model compare favorably with the collocation procedure, the finite difference fuel model will probably be selected for use in the transient SUPERENERGY code.

#### 4.2.3 Dynamic Storage Replacement Scheme

Initial investigation of Eq. (4-2) indicates a need to store one value of coolant temperature for each subchannel at every axial level, for both the current timestep and the previous timestep. This would seem necessary as the explicit scheme requires knowledge of the current and surrounding subchannel temperatures at the current timestep, at both the current and previous axial levels. Schematic representation

of this method of temperature storage is shown in Fig. 18a.

It may be seen from Figs. 18a that storage of temperatures at the current timestep more than one axial level upstream is unnecessary. An alternate storage method is therefore proposed shown in Figs. 18b and 18c. In this method, temperatures at the next timestep are calculated and placed in temporary storage until the calculational procedure has marched two levels downstream. Then, the next timestep temperatures are dynamically replaced into the (single) main array as shown. With estimates of 18-36 axial levels in assemblies, the reduction in core storage requirements is significant.

## 5.0 Analysis Method for Detailed Single Bundle and Multiassembly Studies

It is proposed to write two options within the transient SUPERENERGY code; one which provides detailed temperature fields within a single large bundle while accounting for either user defined or previously calculated interassembly heat transfer, and one version which is capable of considering a 1/12 core sector of 39 highly "lumped" assemblies while determining and storing interassembly heat transfer data. Both versions of the code are described below.

### 5.1 Single Bundle Studies

#### 5.1.1 Basic Model

The primary purpose of a single assembly study should be

to provide extremely detailed spatial and temporal coolant and fuel temperature fields for design, analysis, and safety verification, while considering interassembly heat transfer effects. Therefore, the basic subchannel coolant nodal structure will not be changed in the single bundle version of the transient SUPERENERGY code, with two exceptions; it is proposed to eliminate the corner subchannels, and the subchannels within the interassembly gaps between 2 neighboring assemblies. The major purpose of these moves is to enhance axial stability criteria, permit use of fewer axial steps, and hence reduce computational running time.

Strict stability criteria exist for each subchannel type in the coolant and in the fuel which specify the maximum permissible axial step size, and the maximum permissible timestep size, due to the explicit nature of the proposed computation scheme. As reported in [22], axial stability criteria of the gap edge and corner subchannels nearly always governed the overall stability of bundles in the steady state case. To eliminate the need for an excessive number of very small axial steps, K. Basehore developed an alternative procedure which eliminates the need to calculate temperatures in the gap and duct regions. Heat transfer between assemblies is modelled as occurring solely by conduction between edge and corner subchannels of adjacent bundles. The duct walls of the 2 facing assemblies, as well as the sodium in the interassembly gap region, are taken to be effective resistances to heat

transfer.

It has been found through examination of stability criteria, that the small physical size of the corner subchannels makes them the next most limiting subchannels after the gap edge and corner subchannels. It becomes possible to significantly increase the axial step size by eliminating the corner subchannels as separate entities, and instead combine 1/2 of the areas of the corner subchannel into each of the two neighboring edge subchannels. Preliminary results from test cases run with the 7 pin bundle test code previously discussed has indicated very little loss in accuracy by this move. In many cases, the temperature of the coolant in the corner subchannel is predicted by the steady state SUPERENERGY code to be very close to the temperature of the surrounding edge channels due to both conduction and the circumferential coolant velocity component assumed to occur in the peripheral subchannels. Therefore, unless further investigation yields significant loss of accuracy, only interior and edge subchannel temperatures will be computed.

Further moves to permit even larger axial step sizes would be desirable, but are not essential at this point. Current estimates are that axial step sizes of the order of 1 inch would be permissible for a variety of bundle geometry and coolant flowrate conditions. This would result in 36 axial levels in a 3 foot bundle, and will probably be considered acceptable from an accuracy, storage, and running time standpoint. It is important to realize that owing to the explicit marching scheme used

in the code, where temperatures are determined by the temperatures of immediately adjacent nodes, it is possible for thermal effects to propagate radially inward by 1 node for every axial step taken. A 217 pin bundle would require at least 18 axial sections for the effects of an externally applied heat flux to penetrate to the center of the bundle.

#### 5.1.2 Timestep Selection

The code will be set to automatically determine the largest permissible timestep. In all cases, the smallest of the following criteria will be used to select the timestep:

1. node sweep time
2. stability criteria of the most restrictive coolant or fuel node
3. maximum time step size as input by the user.

#### 5.1.3 Estimates of Computational Time and Storage Requirements

Detailed estimates of running time and core storage required are currently underway and will be reported in the next quarterly progress report. Rough estimates can be made on storage requirements, however. Major arrays, which contain all coolant and fuel node temperatures at all axial sections in bundle, are assumed to impose the primary storage requirement for the purposes of this calculation. Then, the number of bytes of core storage required is determined approximately as:

$$B = [N_c + (N_p \times N_f)] \times N_a \times N_b$$



where

- B = # bytes of storage required
- $N_c$  = # subchannels in the coolant
- $N_p$  = # fuel pins in the bundle
- $N_f$  = # nodes in each fuel pin cross-section
- $N_a$  = # axial sections in the bundle
- $N_b$  = # bytes/computer word.

For the largest bundle now considered for use in the CRBRP core, the 217 pin bundle,

$$N_c \approx 440, N_p = 217, N_f \approx 10, N_a \approx 36, N_b \approx 8$$

The number of bytes of core storage required is then:

$$B \approx [440 + (217 \times 10)] \times 36 \times 8$$

$$\approx 750 \text{ K bytes}$$

Allowing for all other program arrays, a total storage requirement estimated at 1000 K bytes would appear to be fairly realistic for the case of a 217 pin bundle. This estimate falls well within the design goal of 2000 K bytes as discussed in section 2.3.

## 5.2 Multiple Assembly Studies

### 5.2.1 Basic Model

Projections of core storage requirements alone listed in section 5.1.3 indicate that the design goal of 2000 K bytes would be grossly exceeded if the 39 bundles in a 1/12 core sector were modelled on a subchannel basis. Computational running times

would also be excessive. To efficiently run large transient multiple assembly studies therefore it is necessary to greatly reduce the detail of a subchannel and individual rod nodal structure of individual bundles. Such homogenization or lumping is acceptable if we realize that the primary purpose of this multiassembly code is to provide interassembly heat transfer rates as boundary conditions to the detailed single assembly code. In this sense, the multiassembly study results are used in a cascade method, enabling the designer or analyst to select particular individual bundles for detailed examination with the single assembly code described in section 5.1. Since the designer may not know a priori which particular assembly will be selected for later detailed study, maximum utility is achieved only if the multiassembly code stores on a secondary scratch storage medium, such as magnetic tape, all interassembly heat transfer rate data, at selected axial levels at selected points in time during the transient. The single assembly code can then use the stored interassembly heat transfer data for the particular bundle selected as thermal boundary conditions throughout the transient.

Bundle nodal structures in the multiassembly code must be detailed enough to indicate the presence of internal power skews, and exhibit the effect of interassembly heat transfer from each of the six bundle faces. The nature of the thermal exchanges in a wire wrapped bundle as incorporated already in the ENERGY model suggest that in the

multiassembly code, each assembly may be modelled as a lumped 7 pin bundle with no corner subchannels, as shown in Fig. 19. It is believed that this is the coarsest nodal structure which can exhibit both inter- and intra-assembly heat transfer effects. However, any one or several assemblies could have a more detailed representation as desired.

The 7 pin lumped bundle does not alter the basic ENERGY heat transfer model, in that it retains the two region flow field representation. The nodal structure permits the transfer of heat through the turbulent eddy diffusivity mechanism. It also retains the feature of energy transport around the bundle by means of the circumferential coolant flow around the periphery of the assembly. The relatively coarse nodal structure in the interior of the bundle is believed to be acceptable, as it has been shown that the circumferential convection of coolant around the bundle has dominant effects on inter- and intra-assembly heat transfer in most cases. The nodal structure should prove acceptable as one of the primary purposes of the code is to determine transient interassembly heat transfer rates. The single edge node in the bundle also facilitates the coupling of any size bundle to any other size bundle.

The proposed 7 pin lumped bundle model includes 12 averaged nodal temperatures in the coolant, and a maximum of 10 nodal temperatures in each of the 7 lumped fuel rods. The presence of the fuel rods is necessitated due to the important thermal moderating heat capacity effects in determining transient heat fluxes to the coolant. Interassembly heat transfer

rates as determined from the proposed model will be compared with results from more detailed models, and will be considered acceptable if no significant differences result.

### 5.2.2 Timestep Selection

The procedure for the dynamic selection of timesteps are as described in section 5.1.2.

### 5.2.3 Estimates of Computational Time and Storage Requirements

Detailed estimates of running time and core storage requirements are currently underway and will be reported in the next quarterly progress report. A rough estimate on the amount of core storage required will be made in manner of section 5.1.3. In the multiassembly code, storage required for the major arrays is approximately given by:

$$B \approx [N_c + (N_p \times N_f)] \times N_a \times N_{bd} \times N_b$$

where  $B$ ,  $N_c$ ,  $N_p$ ,  $N_f$ ,  $N_a$ , and  $N_b$  are defined in section 5.1.3, and  $N_{bd}$  is the number of coupled bundles. For 39 coupled assemblies,

$$N_c = 12, N_p = 7, N_f = 10, N_a \approx 18, N_b \approx 8, N_{bd} = 39$$

Then:

$$B \approx [12 + (7 \times 10)] \times 18 \times 39 \times 8$$

$$\approx 460 \text{ K bytes}$$

Allowing for program and miscellaneous storage, the total storage requirement for a 1/12 core sector with the cornerless 7 pin bundle assembly idealization could be taken to be approximately 700 K bytes. This too lies well within the design goal of 2000 K bytes specified in section 2.3. Note that if accuracy demands, individual assemblies could be modelled as 19 pin assemblies. For a 19 pin assembly,

$$N_c = 36, N_p = 19, N_f = 10, N_a = 18, N_b = 8, N_{bd} = 39,$$

and,

$$B \approx [36 + (19 \times 10)] \times 18 \times 39 \times 8$$

$$\approx 1250 \text{ K bytes.}$$

The total storage requirement with a 19 pin bundle model would therefore be approximately 1500 K bytes.

## 6.0 Future Development

Work is currently progressing on determination of axial step and time step stability criteria for 61 pin and 217 pin bundles of CRBRP geometry for the single and multiple assembly code models. This data will be used to make detailed projections of core storage and computational running times for various transients listed in table 2. This in turn will enable determination of the range of transients for which each of the

two codes are practically applicable.

In the next quarter, development will begin on the single assembly transient SUPERENERGY code. Upon completion, the code will be tested against existing transient codes such as COBRA III, and compared for accuracy of solution.

Work will be initiated in the near future on development of the multiassembly transient SUPERENERGY code. Results from the code utilizing the 7 pin bundle nodal structure will be compared with those from one using a 19 pin bundle nodal structure. Solution sensitivity to the particular lumped model used will be examined. Estimates as to accuracy, as well as running times, will be compiled for various transients.

Resolution of several questions will be necessary before release of either the single bundle or multiassembly transient computer code. Among those items to be examined are: 1) physical implications of elimination of the corner subchannels as separate entities, 2) sensitivity of coolant temperature distribution to temperature dependent properties in the fuel and clad, 3) necessity of inclusion of heat capacity in the duct walls. Additionally, attempts will be made to include in the capabilities of transient SUPERENERGY as many of those specified in Ref. 19 as possible.

Finally, very little detailed data is available to date on mixing effects during flow transients in rod bundles. If deemed necessary at some point in the future, it will be possible to utilize the Automated Data Acquisition System to measure the effects of transients on mixing parameters in 61 pin fuel, 61 pin blanket, or 217 pin fuel bundles.

REFERENCES

- [1] B.C. Chen, N.E. Todreas, "Prediction of Coolant Temperature Field in a Breeder Reactor Including Interassembly Heat Transfer," MIT Department of Nuclear Engineering, May 1975, December 1976; COO-2245-20TR Revision 1.
- [2] E.U. Khan, W.M. Rohsenow, A.A. Sonin, N.E. Todreas, "A Porous Body Model for Predicting Temperature Distributions in Wire Wrapped Fuel and Blanket Assemblies of a LMFBR," MIT Department of Mechanical and Nuclear Engineering, June 1975, COO-2245-16TR.
- [3] E.U. Khan, W.M. Rohsenow, A.A. Sonin, N.E. Todreas, "INPUT Parameters to the ENERGY code (to be used with the ENERGY Coded Manual)," MIT Departments of Mechanical and Nuclear Engineering, May 1975, COO-2245-17TR.
- [4] E.U. Khan, W.M. Rohsenow, A.A. Sonin, N.E. Todreas, "Manual for ENERGY I, II, III Computer Programs," Department of Mechanical and Nuclear Engineering, May 1975, July 1976 COO-2245-18TR Revision 1.
- [5] Westinghouse Electric Corp, "11:1 Scale Wire Wrapped Rod Bundle Air Flow Test, Interior Subchannels," WARD-D-0108, November 1975.
- [6] Westinghouse Electric Corp, "11:1 Scale Wire Wrapped Rod Bundle Air Flow Test, Side Subchannel, WARD-D- Jan. 1976.
- [7] Westinghouse Electric Corp, "11:1 Scale Wire Wrapped Rod Bundle Air Flow Test, Corner Subchannel," WARD-D-0154 July 1976
- [8] Y.B. Chen, K. Ip and N.E. Todreas, "Velocity Measurements in Edge Subchannels of Wire Wrapped LMFBR Fuel Assemblies," MIT Department of Nuclear Engineering, September 1974, COO-2245-11TR.
- [9] J. Lafay, B. Menant, J. Barroil, "Local Pressure Measurements and Peripheral Flow Visualization in a Water 19-Rod Bundle Compared with FLICA IIB Calculations: Influence of Helical Wire-Wrap Spacer System, April 1975, ASME 75-HT-22.
- [10] W.T. Sha, R.C. Schmitt, "A Wire Wrap Model," ANS Transactions, Vol. 24, pp. 334-345.

- [11] D. Rowe, "COBRA III-C: A digital Computer Program for Steady State and Transient Thermal Hydraulic Analysis of Rod Bundle Nuclear Fuel Elements," BNWL-1965, 1973.
- [12] W.T. Sha and R.C. Schmitt, "THI3D - A Computer Program for Steady State Thermal Hydraulics Multichannel Analysis," ANL-8112, July 1974.
- [13] M. Carelli, LMFBR Rod Bundle T&H Working Group Meeting, June 2-3, 1976 at MIT, oral presentation.
- [14] P.J. Fulford, J. Fox and T. Yackle, "CORTAC - A Core Restraint Transient Analysis Code: Preliminary Users Manual," ANL-CT-76-10, July 1975.
- [15] B. Chen and N. Todreas, "Prediction of Coolant Temperature Field in a Breeder Reactor Including Interassembly Heat Transfer," COO-2245-20TR, May 1975.
- [16] E. Khan, W. Rohsenow, A. Sonin and N. Todreas, "A Porous Body Model for Predicting Temperature Distributions in Wire Wrapped Fuel and Blanket Assemblies of a LMFBR," COO-2245-16TR, June 1975.
- [17] N.E. Todreas, "Thermal Analysis Methods for LMFBR Wire Wrapped Bundles," COO-2245-32TR, November 1976.
- [18] M. Carelli and R. Markley, "Preliminary Thermal-Hydraulic Design and Predicted Performance of the Clinch River Breeder Reactor Core," ASME technical publications, 75-HT-71, August 1975.
- [19] Meeting of ERDA/RDD, October 12, 1976, Discussion of Program to Extend COBRA IV to Provide Solution to "Whole Core" Thermal Hydraulic Transients in LMFBR's.
- [20] J. Fox, et al., "FORE-II: A Computational Program for the Analysis of Steady State and Transient Reactor Performance," GEAP-5273, September 1966.
- [21] J.N. Fox, "COTECT - A Transient Version of COTEC," SG016-MEF-028, March 1976.
- [22] K. Basehore and N. Todreas, "Development of Stability Criteria and an Interassembly Conduction Model for the Thermal Hydraulic Code SUPERENERGY," COO-2245-33TR, December 1976.
- [23] D. Bender, "An Explicit Unlimited Stability Approach to the Transient Conduction Equations," Proceedings of the Effective Use of Computers in the Nuclear Industry, CONF 690401, p. 561-585.



- [24] S. Levy, "Use of Explicit Method in Heat Transfer Calculations with an Arbitrary Time Step," (General Electric Technical Information Series), 68-C-282, 1968.
- [25] G. Dusinberre, "Heat-Transfer Calculations by Finite Differences," pp. 13-18, International Textbook Company 1961.
- [26] T. Yackle and J. Fox, "Computational Techniques for Reactor Core Transient Conduction-Convection Heat Transfer,"
- [27] J. Blair and W. Selander, "Temperature Transients in a Cylinder Due to a Time Varying Heat Transfer Coefficient," Atomic Energy of Canada Report #AECL-4126.
- [28] R. Nijsing and W. Eifler, "The Hybrid Method, A New Accurate Computation Method for Transient Temperature Distributions in Fuel Rods," Nuclear Eng. and Design, Vol. 32, 1975, p. 208-220.
- [29] N. Todreas, M. Golay and L. Wolf, "Coolant Mixing in LMFBR Rod Bundles and Outlet Mixing Transients," Progress Report, COO-2245-31, August 1976.
- [30] T. Chawla, G. Leaf, W. Chen and M. Grolmes, "The Application of the Collocation Method Using Hermit Cubic Splines to Non-Linear Transient One-Dimensional Heat Conduction Problems," ANL-75-33, July 1975.
- [31] T. Chawla, G. Leaf, W. Chen, and M. Grolmes, "The Application of the Collocation Method Using Hermite Cubic Splines to Non-Linear Transient One-Dimensional Heat Conduction Problems," Trans. ASME, Journal of Heat Transfer, 76-HT-B, November 1975, p. 562-569.
- [32] T. Chawla, G. Leaf, and W. Chen, "Collocation Method Using B Splines for One Dimensional Heat or Mass Transfer Controlled Moving Boundary Problems," Nuclear Engineering and Design, Vol. 35, 1975, p. 163-180.
- [33] M. Yeung, "The Application of the Collocation Method Using Hermite Cubic Polynomials to LWR Fuel Pin Transient Conduction Problems," Report in Nuclear Engineering Department, September 1975.

TABLE I  
CODE APPLICATIONS

	SUBCHANNEL		HEAT FLUX B.C.	SINGLE ASSEMBLY		CLUSTER OF ASSEMBLIES	WHOLE CORE
	ADIABATIC B.C.			ADIABATIC B.C.	HEAT FLUX B.C.		
	INTER- IOR	EDGE					
STEADY STATE FORCED	FATHOM- 360 MIT-WOLF			COTEC ENERGY I THI-3D COBRA-IIIC	SUPER- ENERGY COBRA V	TRITON SUPERENERGY COBRA V	TRITON SUPERENERGY/ HEXFLOW COBRA V
MIXED CONVECTION				ENERGY II, III THI-3D COBRA IIIC	COBRA V	COBRA V	COBRA V
TRANSIENT FORCED				SUPER- ENERGY I COBRA V	SUPER- ENERGY I COBRA V	SUPER- ENERGY I COBRA B	SUPER- ENERGY I COBRA B
MIXED CONVECTION				COBRA B	COBRA V	COBRA V	COBRA V
WITH FLOW REVERSAL				COBRA V	COBRA V	COBRA V	COBRA V

TABLE 2  
SELECTED CRBRP CORE TRANSIENTS

Transient	Description	Type of Forcing Functions			Estimated Total Transient Duration (Minutes)
		Power Change	Flow Change	Inlet Temp Change	
U-1	<p>Reactor Trip (Scram)</p> <p>Occurs dur to PPS trip level exceeded</p> <p>t = 0.0 sec: PPS trips</p> <p>t = 0.0200 sec: control rods inserted, power drop rapidly</p> <p>t = 0.500 sec: main sodium pumps trip, flow coasts down as:</p> <p>t = 2.500 sec: flow <math>\approx</math> 80% full flow</p> <p>t = 5.500 sec: flow <math>\approx</math> 50% full flow</p> <p>t = 30.000 sec: flow <math>\approx</math> 10% full flow</p>	✓	✓		1
U-2b	<p>Uncontrolled Rod Withdrawal from 100% Power</p> <p>t = 0.0 sec: step increase in reactor power to 115% full power, maintained for transient duration</p> <p>t = 300.00 sec: manual reactor trip occurs</p> <p>NOTE: Other less severe scenarios include various ramp rates of reactivity insertion from 0.1¢/sec to 20¢/sec. This event is umbrella event.</p>	✓		✓	6
U-16	<p>Operating Basis Earthquake</p> <p>Reactivity insertion occurs as a result of core compaction</p> <p>Also, loss of offsite electrical power is assumed. Diesel generators assumed to permit main sodium pumps to keep flow at pony motor level</p>	✓	✓		

(Continued)

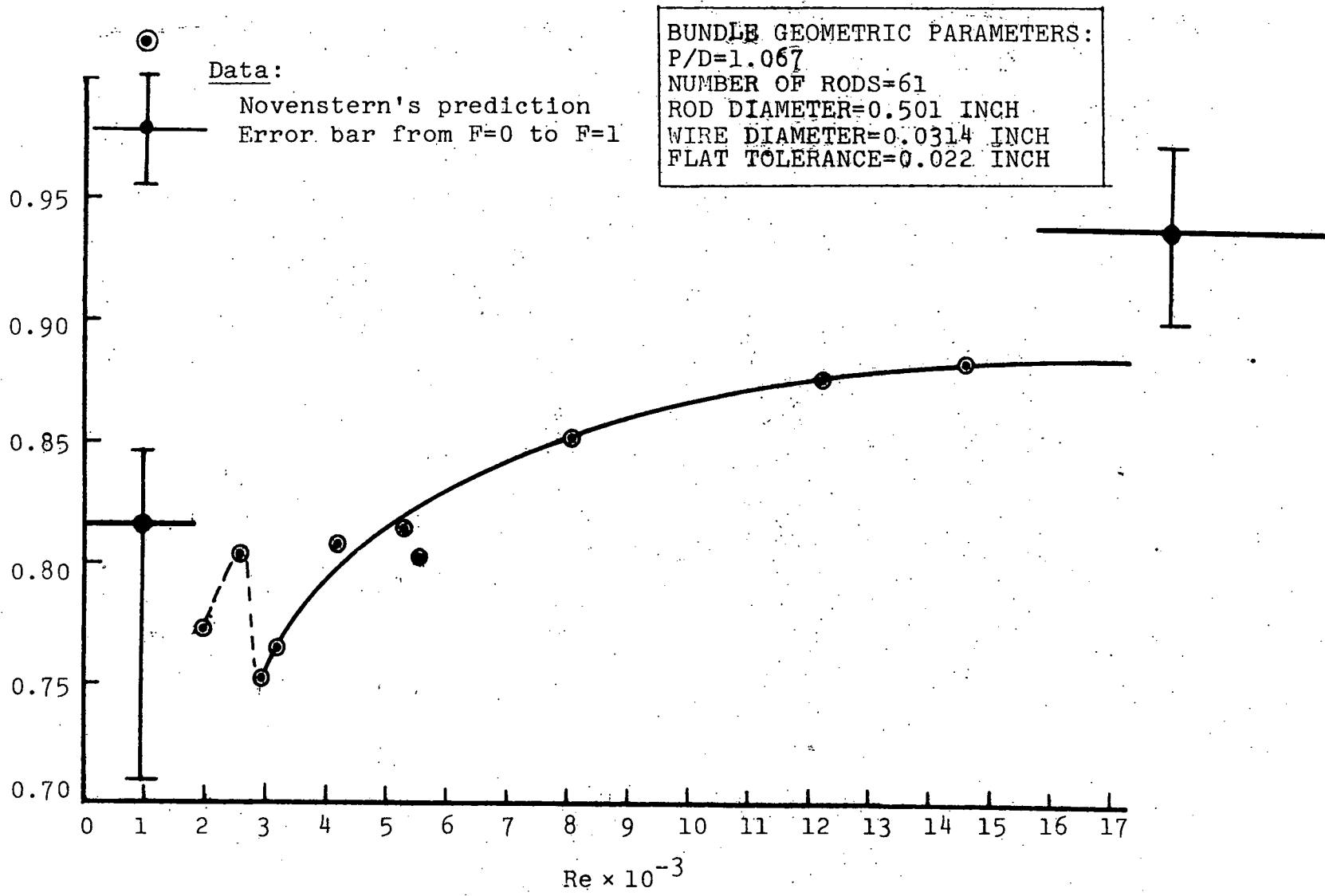
Table 2. (continued)

TRANSIENT	DESCRIPTION	TYPE OF FORCING FUNCTIONS UP UNTIL SCRAM			ESTIMATED TOTAL TRANSIENT DURATION (MINUTES)
		POWER CHANGE	FLOW CHANGE	INLET TEMP. CHANGE	
U-16 (cont.)	<p>t = 0.0 sec: earthquake hits, electrical power to pumps lost, flow begins to coast down to pony motor flow (10% full flow)</p> <p>t = 0.5 sec: step reactivity insertion of 30¢. Also, automatic reactor trip initiated. Rate of control rod insertion slowed due to core misalignment</p>	✓	✓		2
E-16	<p>Loss of offsite Electrical Power</p> <p>t = 0.0 sec: all electrical power to reactor lost, including diesel power. Main sodium pumps coast down, eventual natural circulation of <math>\approx</math> 3-3-1/2% full flow established</p> <p>t = 0.500 sec: reactor trip initiated</p>	✓	✓		2
F-1	<p>Safe Shutdown Earthquake</p> <p>Reactivity insertion occurs as a result of core compaction</p> <p>Also, loss of offsite electrical power is assumed. Diesel generators assumed to permit main sodium pumps to keep flow at pony motor level.</p> <p>t = 0.0 sec: earthquake hits, electrical power to pumps lost, flow begins to coast to pony motor flow</p> <p>t = 0.500 sec: step reactivity insertion of up to 60¢ occurs. Also, automatic reactor trip initiated. Rate of control rod insertion slowed due to core misalignment.</p>	✓	✓		2

(continued)

Table 2. (continued)

TRANSIENT	DESCRIPTION	TYPE OF FORCING FUNCTIONS UP UNTIL SCRAM			ESTIMATED TOTAL TRANSIENT DURATION (MINUTES)
		POWER CHANGE	FLOW CHANGE	INLET TEMP. CHANGE	
F-1 (cont.)	Note: This is an especially severe transient, due to both severe structural damage, and the fact that maximum power could reach 230% of full power for short time before scram. Thermal effects could be very severe.				
	Large Reactivity Insertions For purpose of PPS analysis only, large reactivity insertions of up to \$2.00/sec are studied. Ramp rates this large are assumed extremely unlikely faults, and are not postulated to occur.	✓			1



67

Figure 1 Interior Channel Flow Split versus Reynold Number

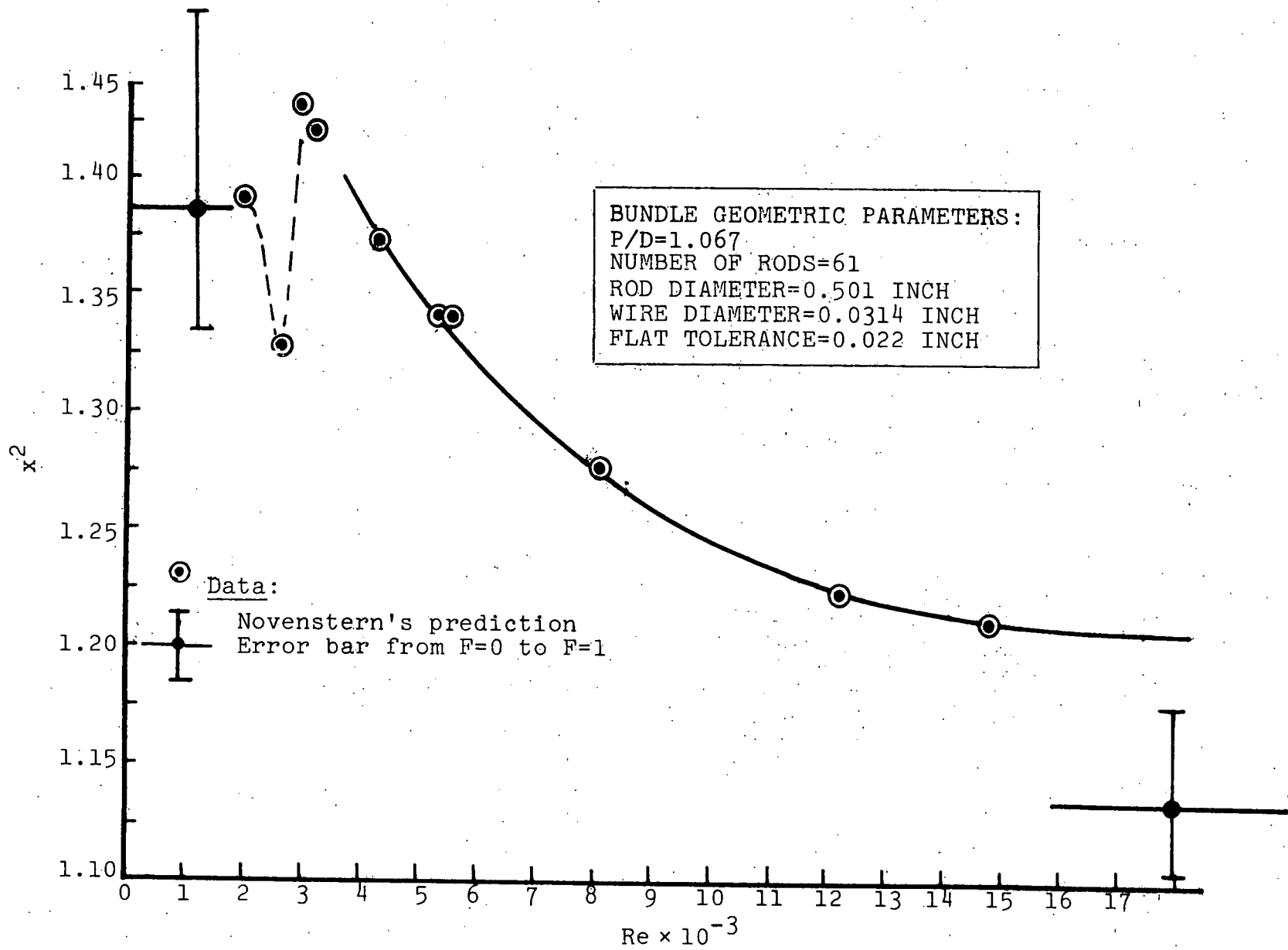


Figure 2 Edge Channel Flow Split versus Reynolds Number

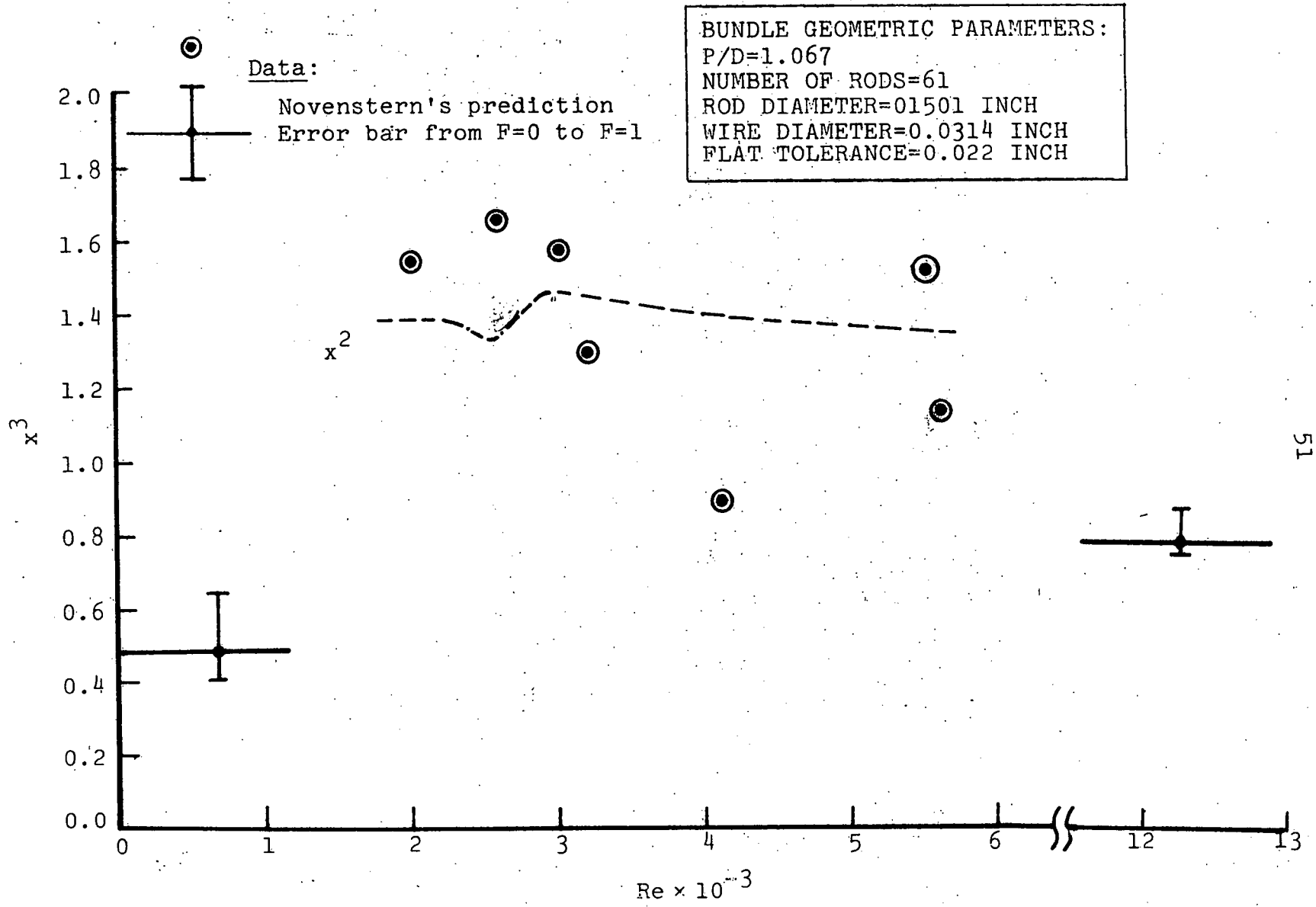


Figure 3. Corner Channel Flow Split versus Reynolds Number



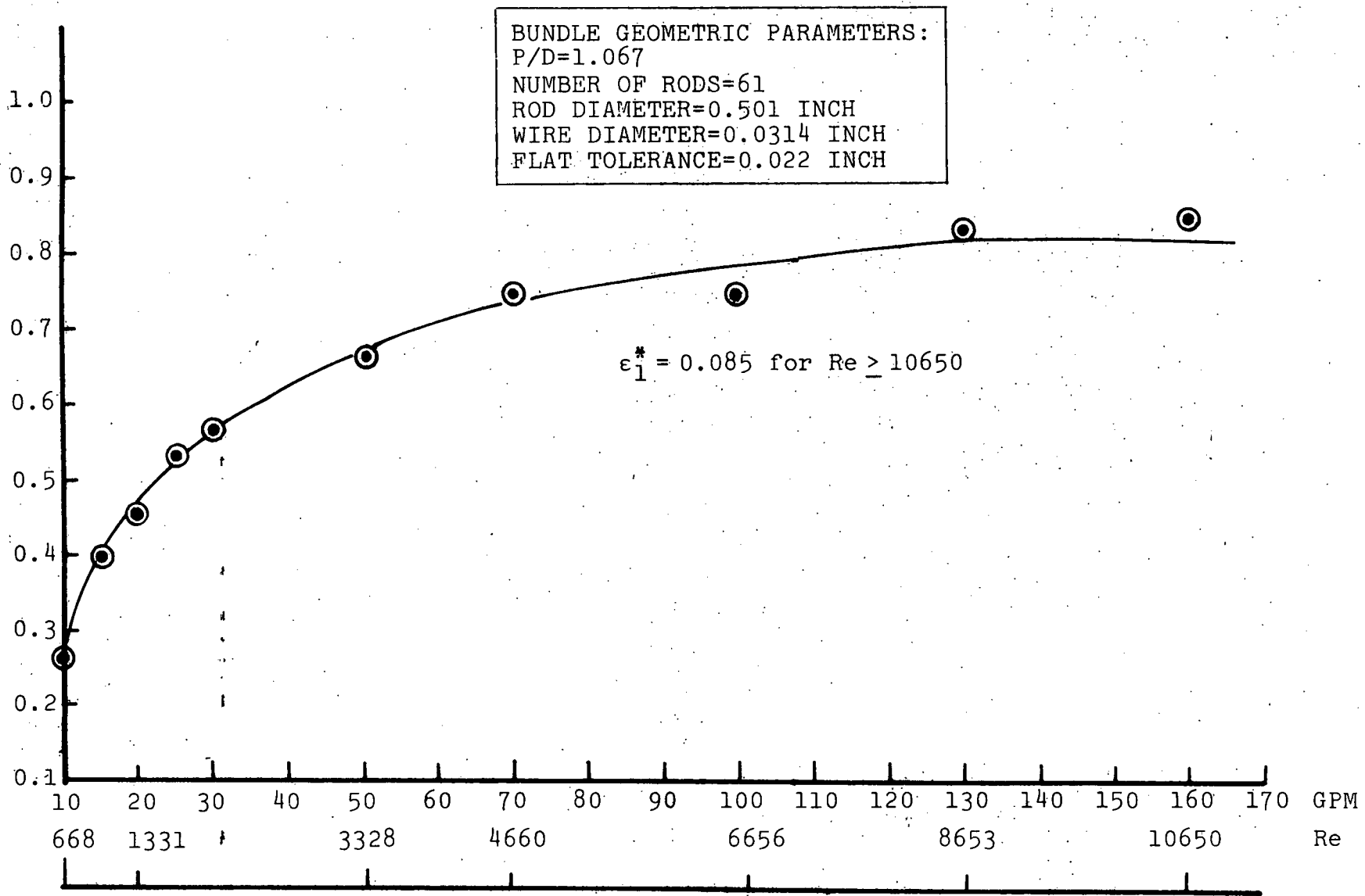


Figure 4  $\epsilon_1^*$  versus Reynolds Number

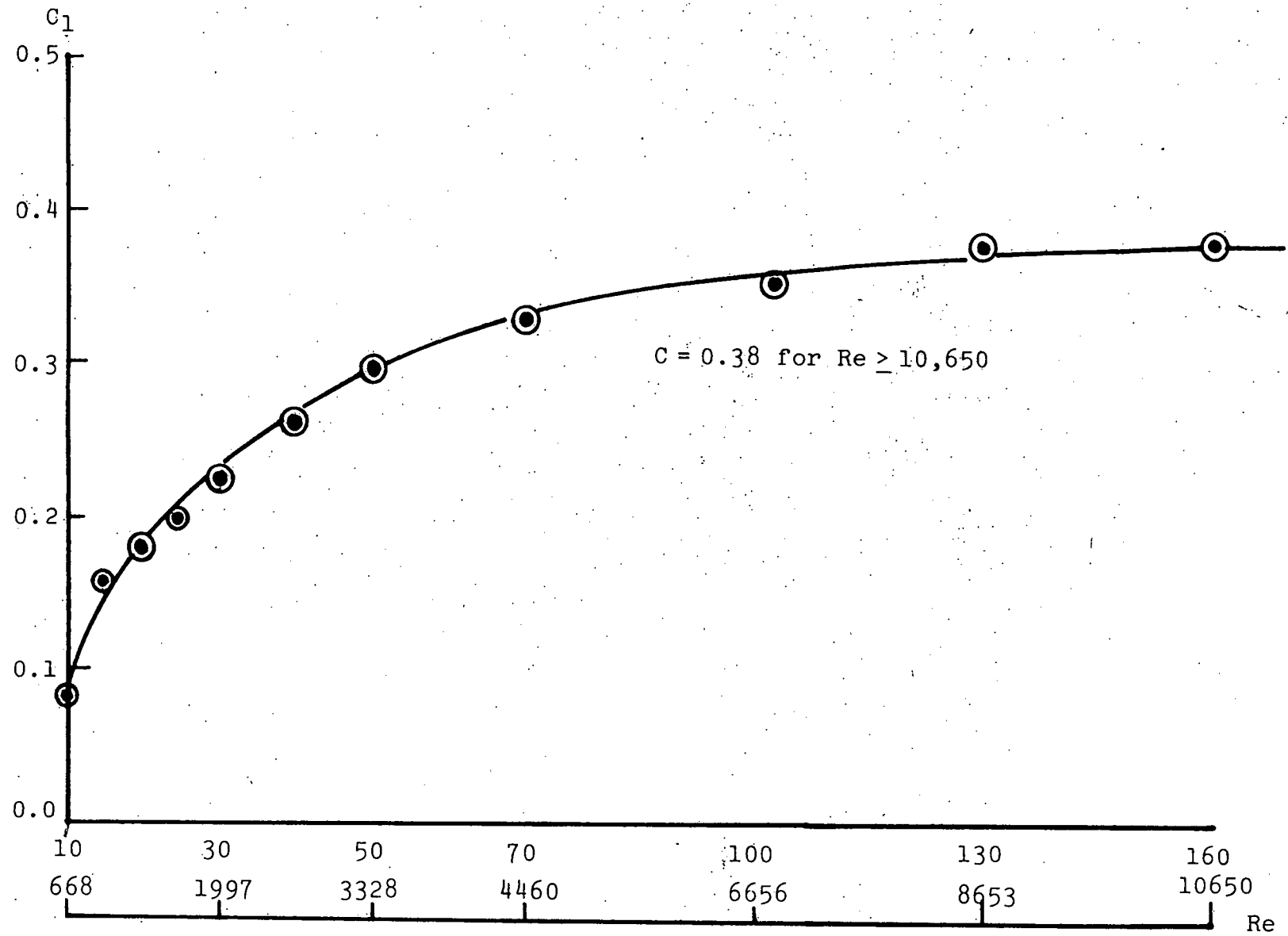


Figure 5  $C_1$  versus  $Re$  for Blanket Assembly

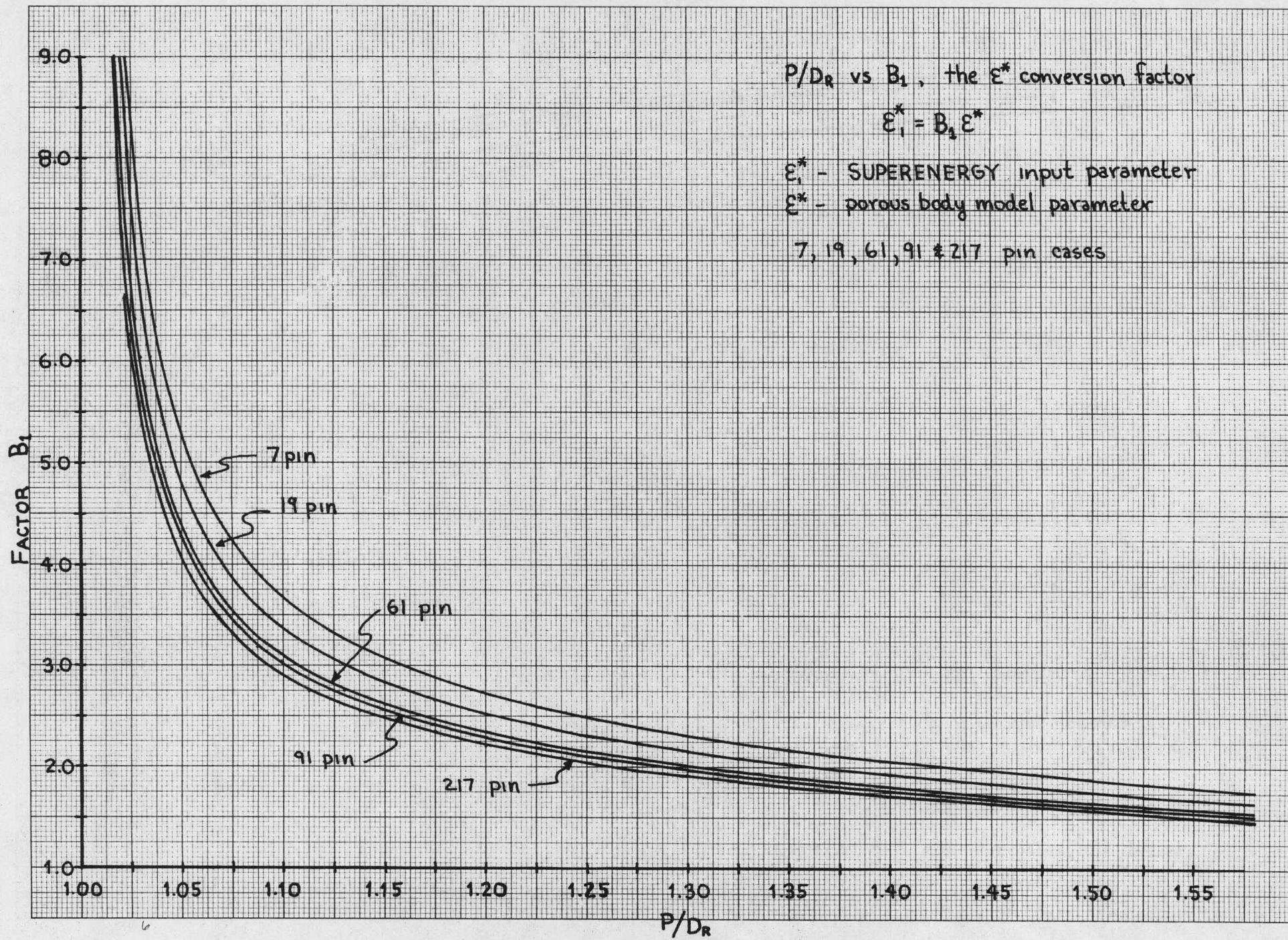


Figure 6



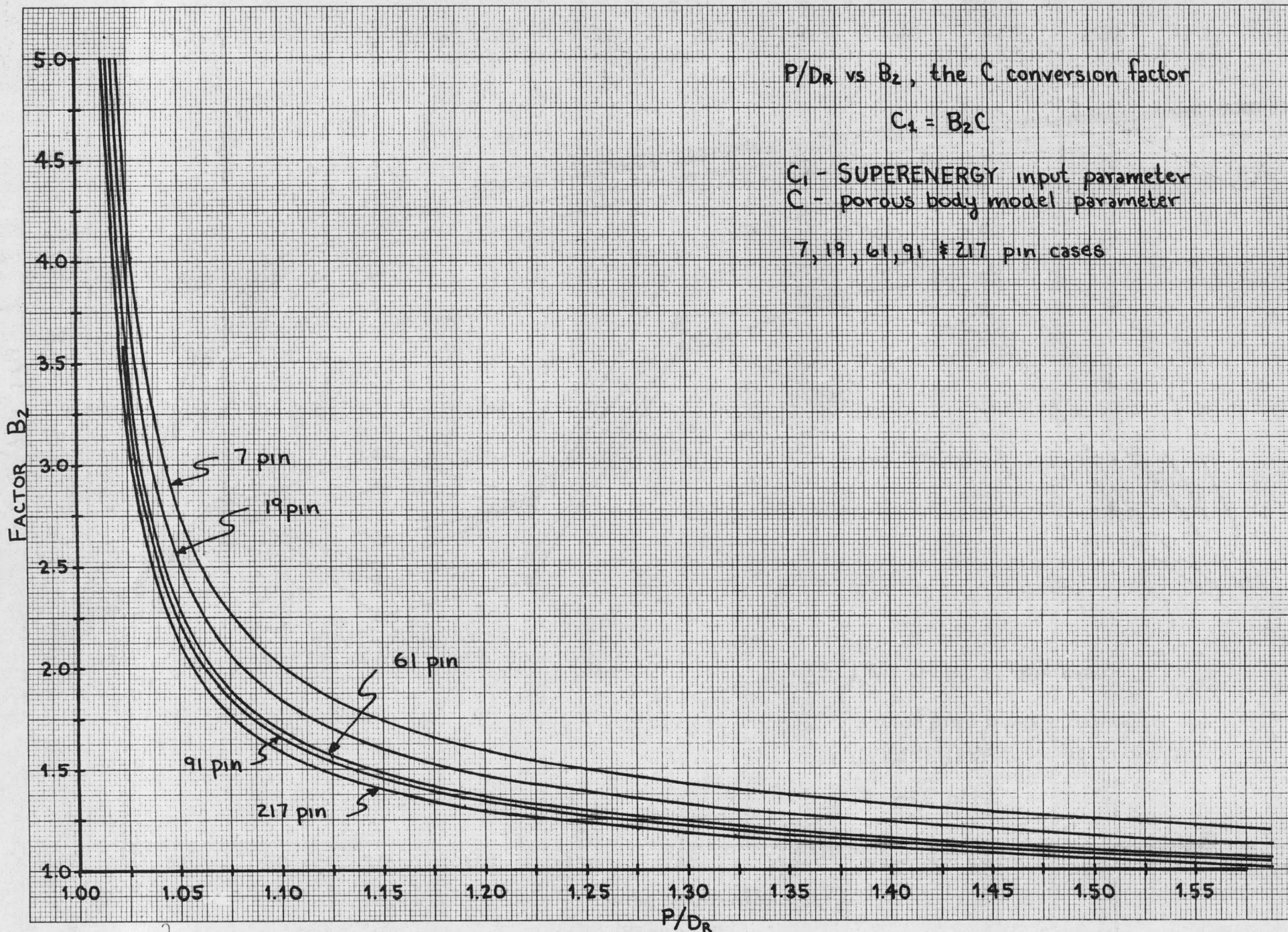


Figure 7

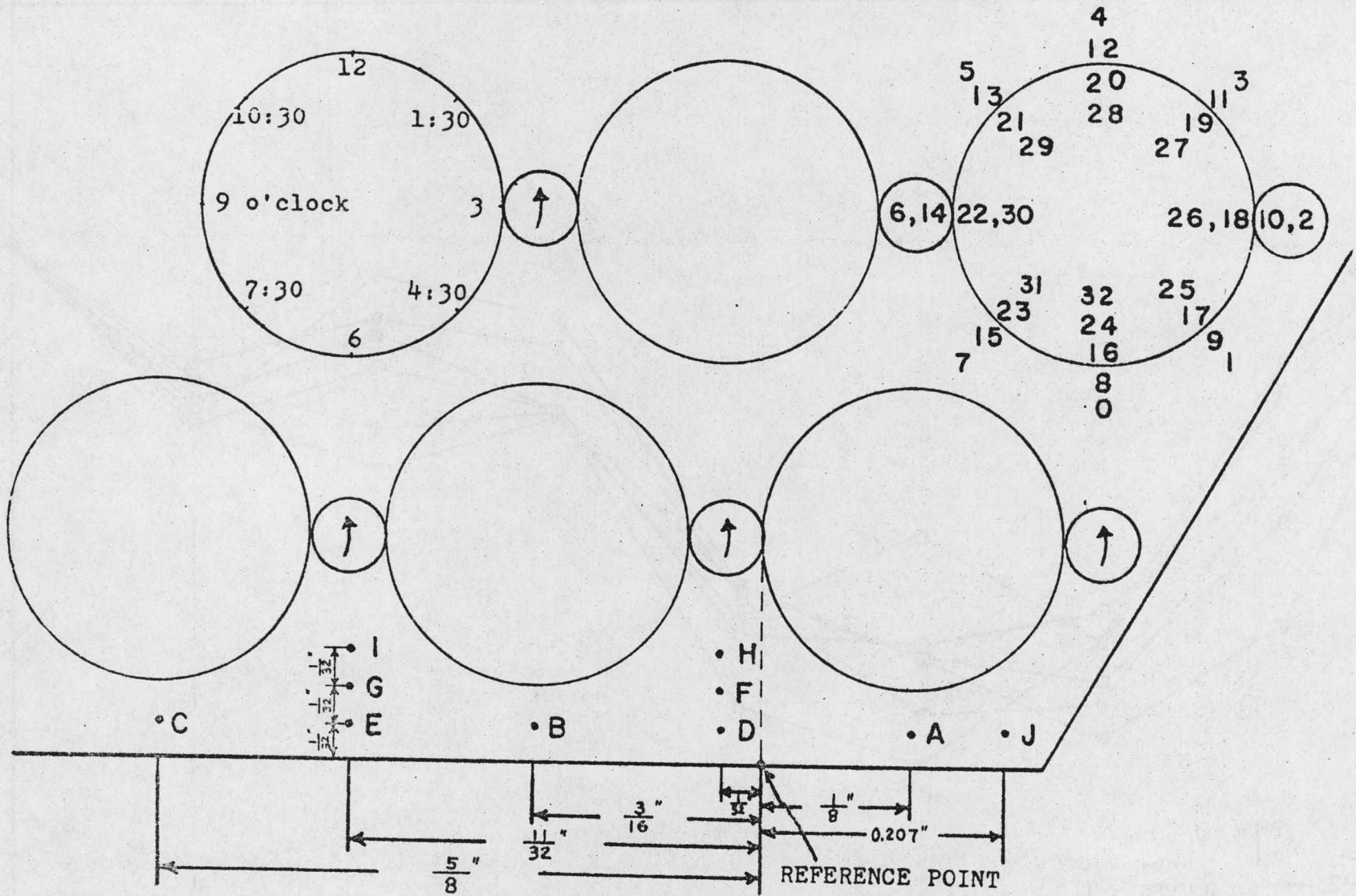


FIGURE 4.2 LOCATIONS OF MEASURING POINTS

Figure 8

Fig 8



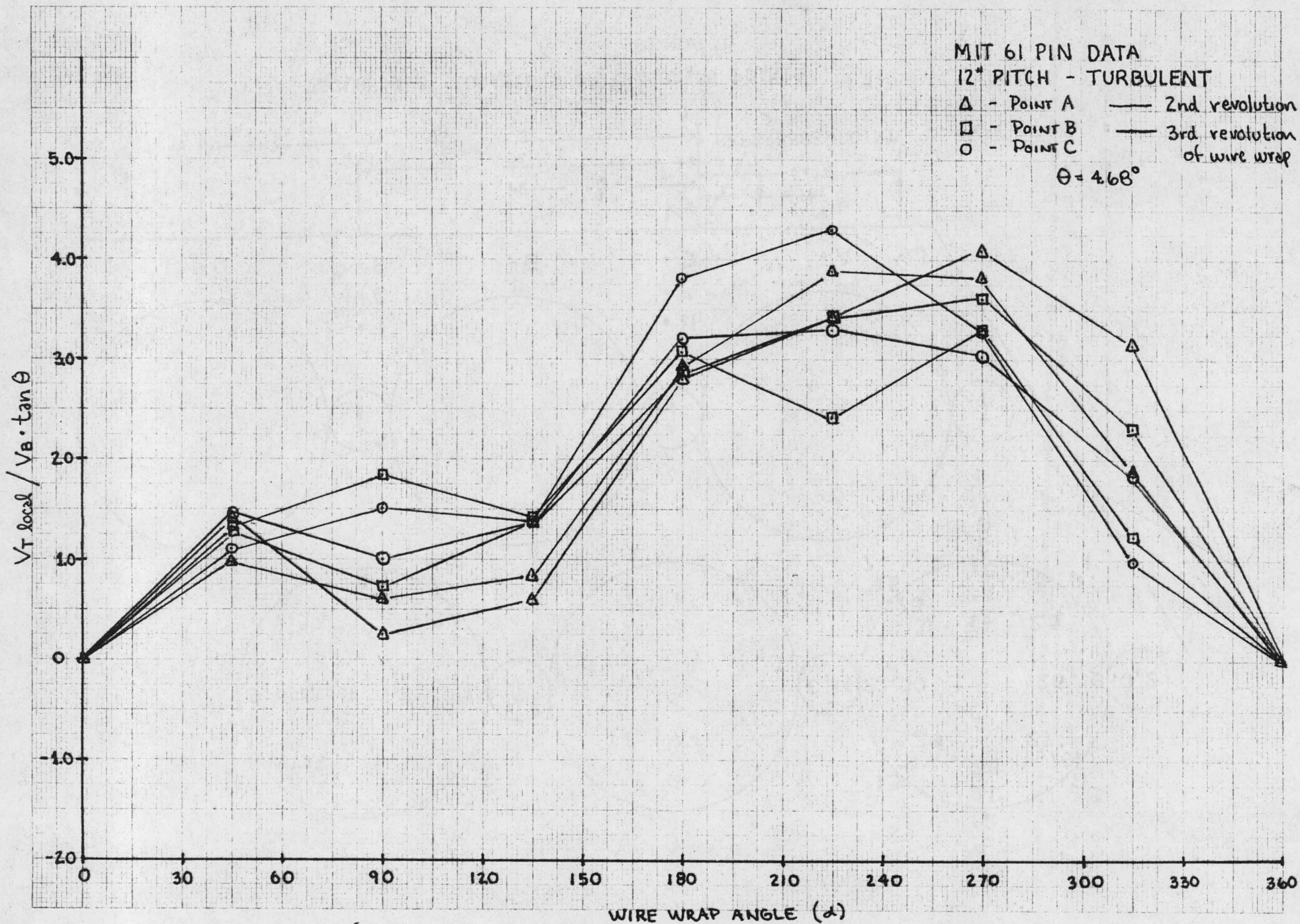


Fig 9

Figure 9

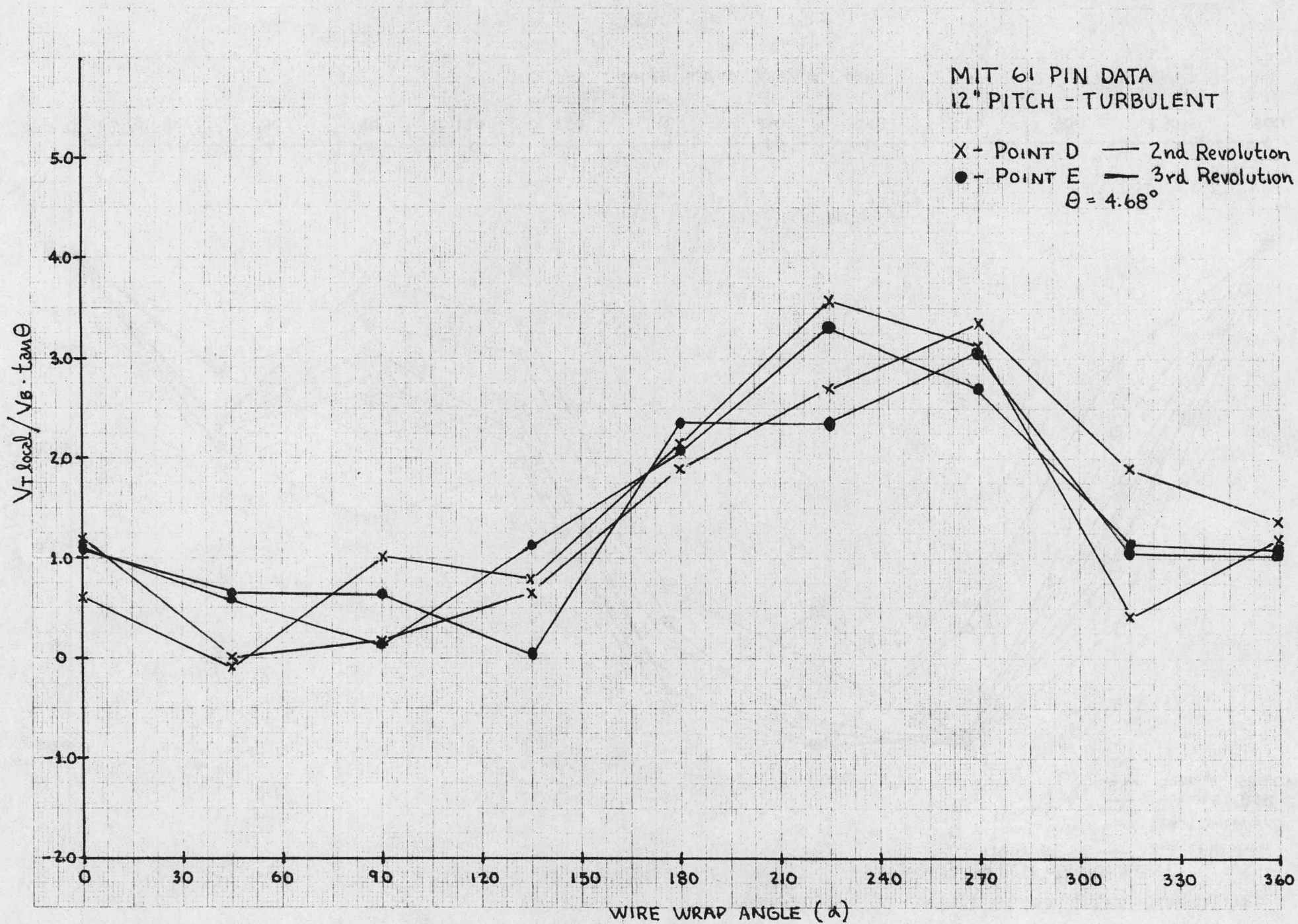


Fig 10

WIRE WRAP ANGLE ( $\alpha$ )  
Figure 10



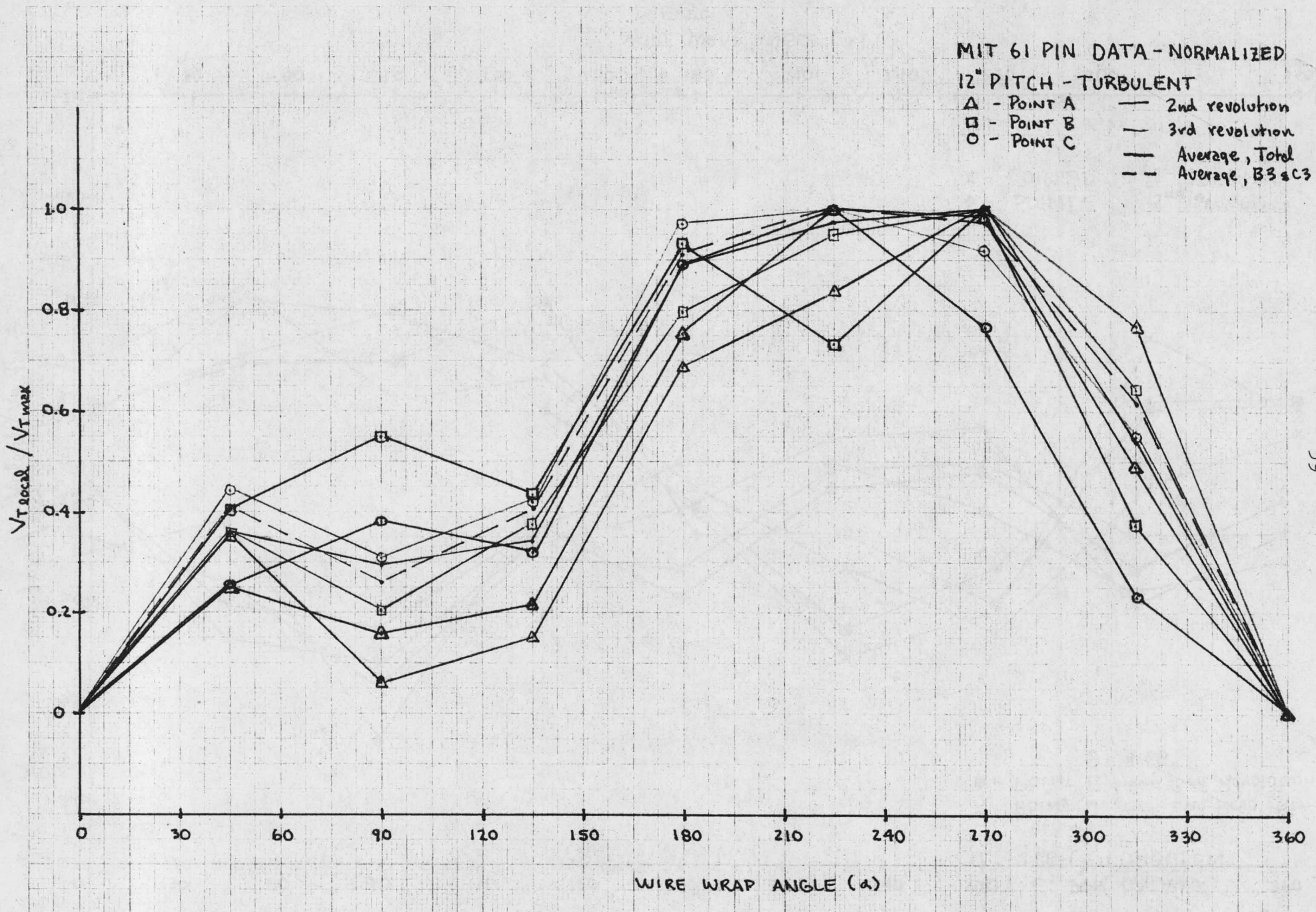


Fig 11.

Figure 11



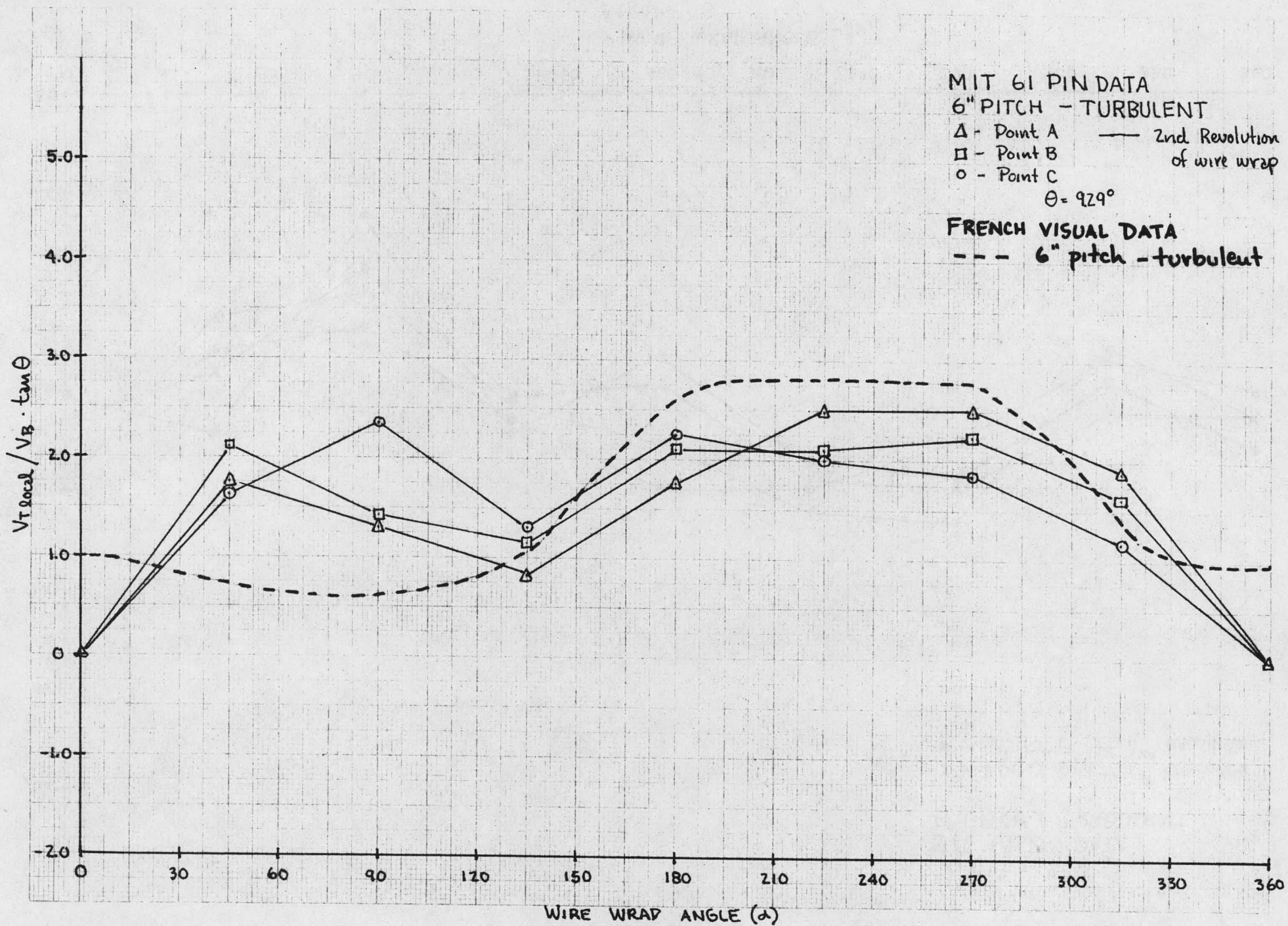
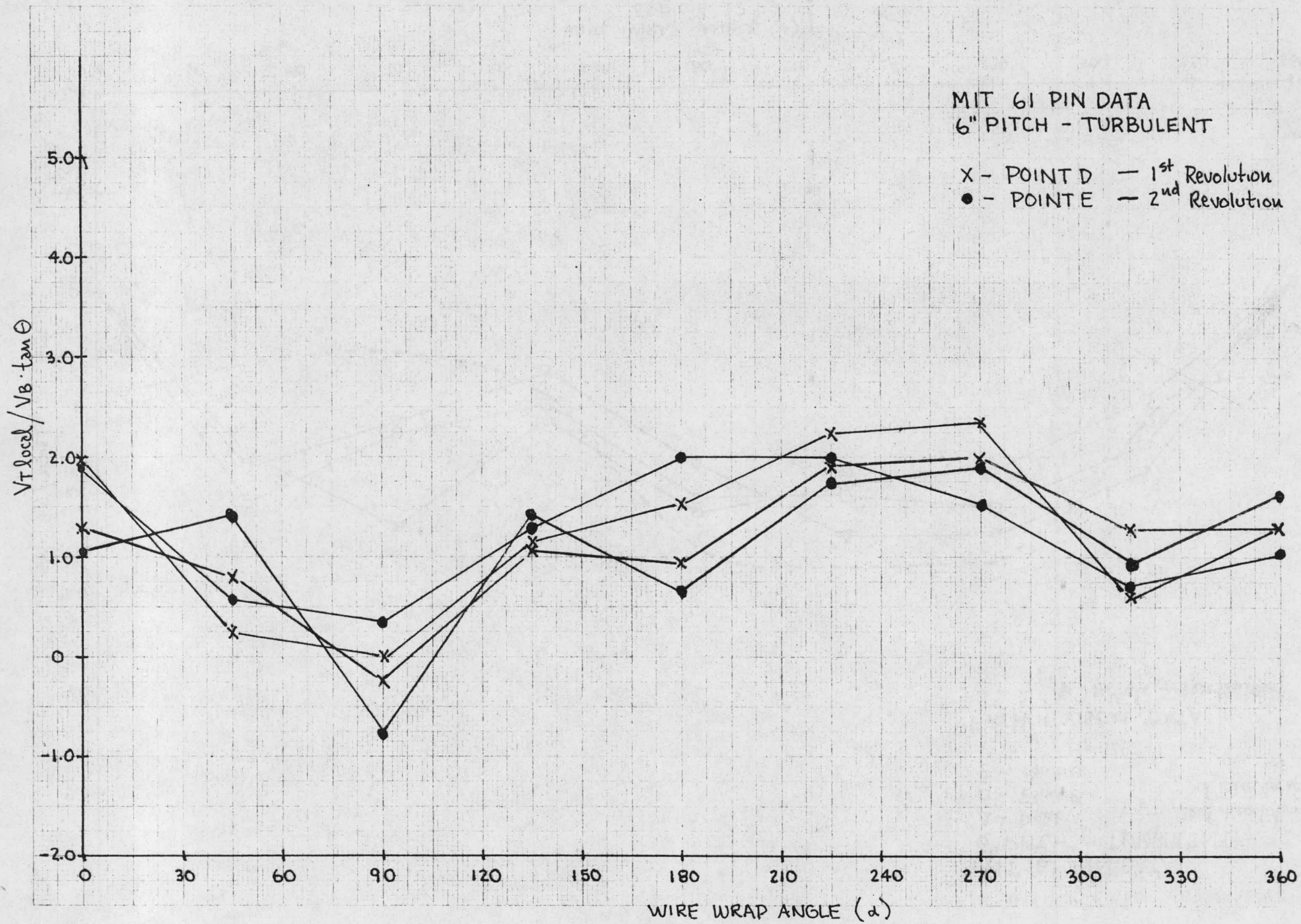


Fig 12

WIRE WRAP ANGLE (α)  
 Figure 12



61

Fig 13

Figure 13



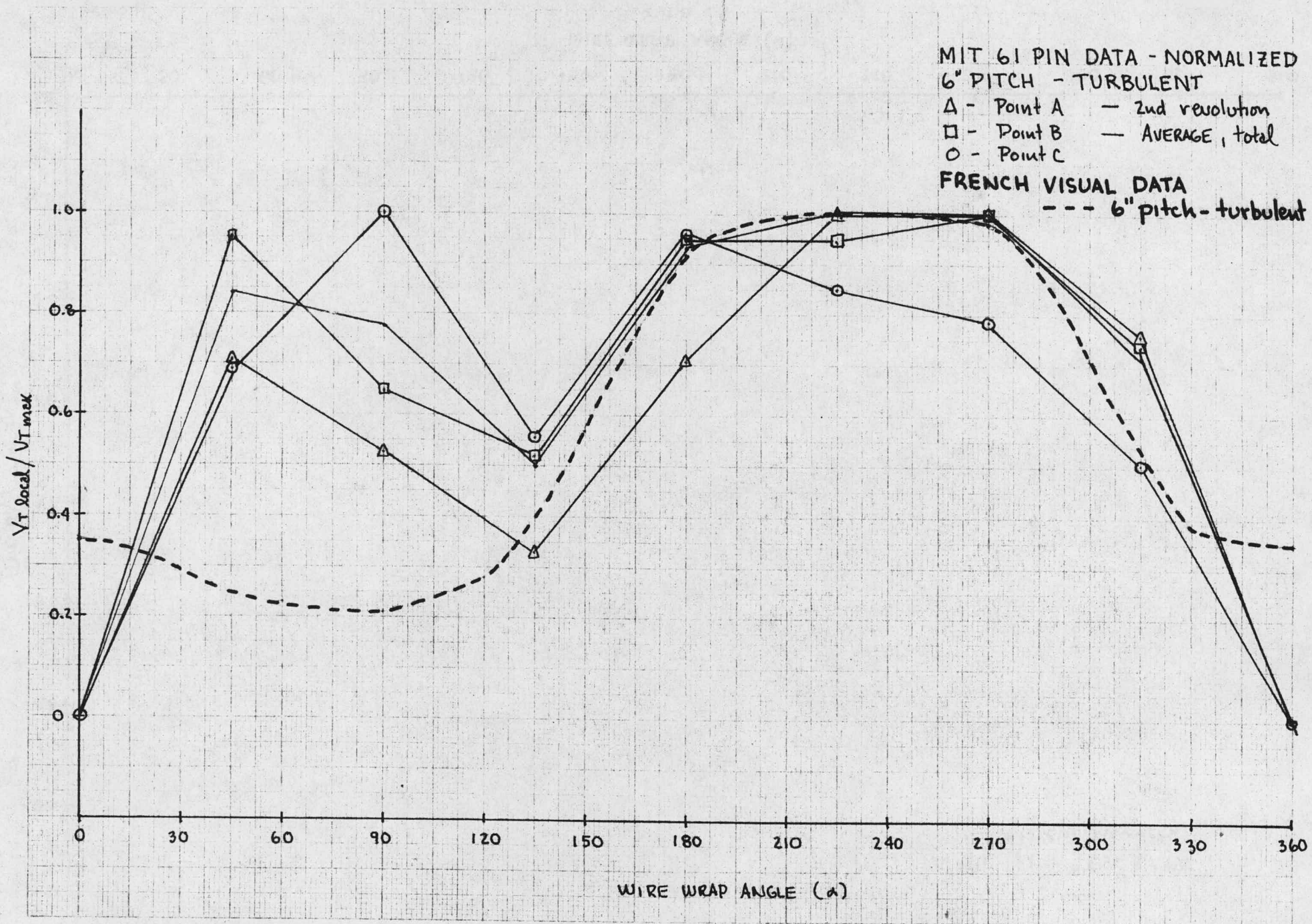


Fig 14.

Figure 14

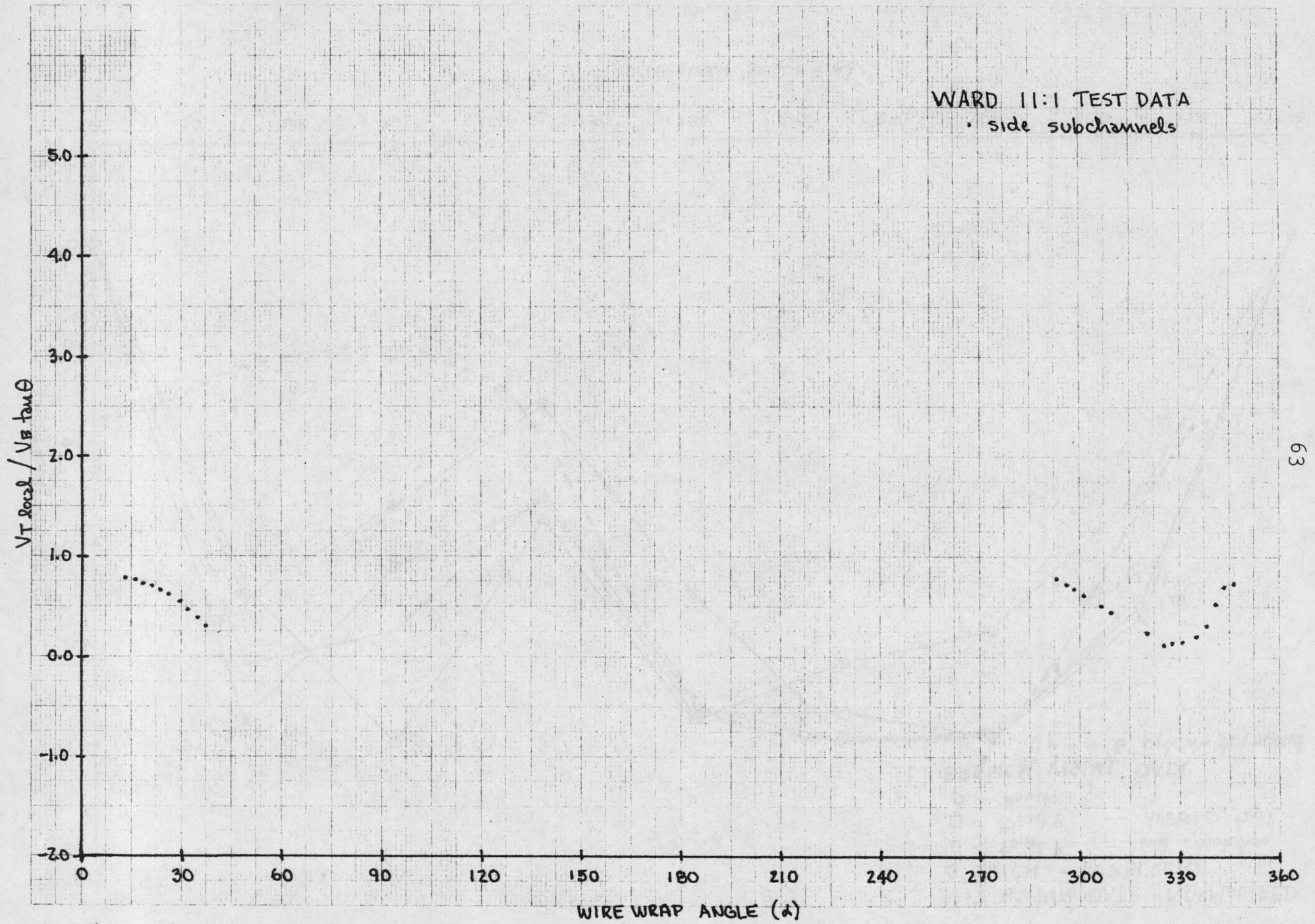


Fig 15

Figure 15



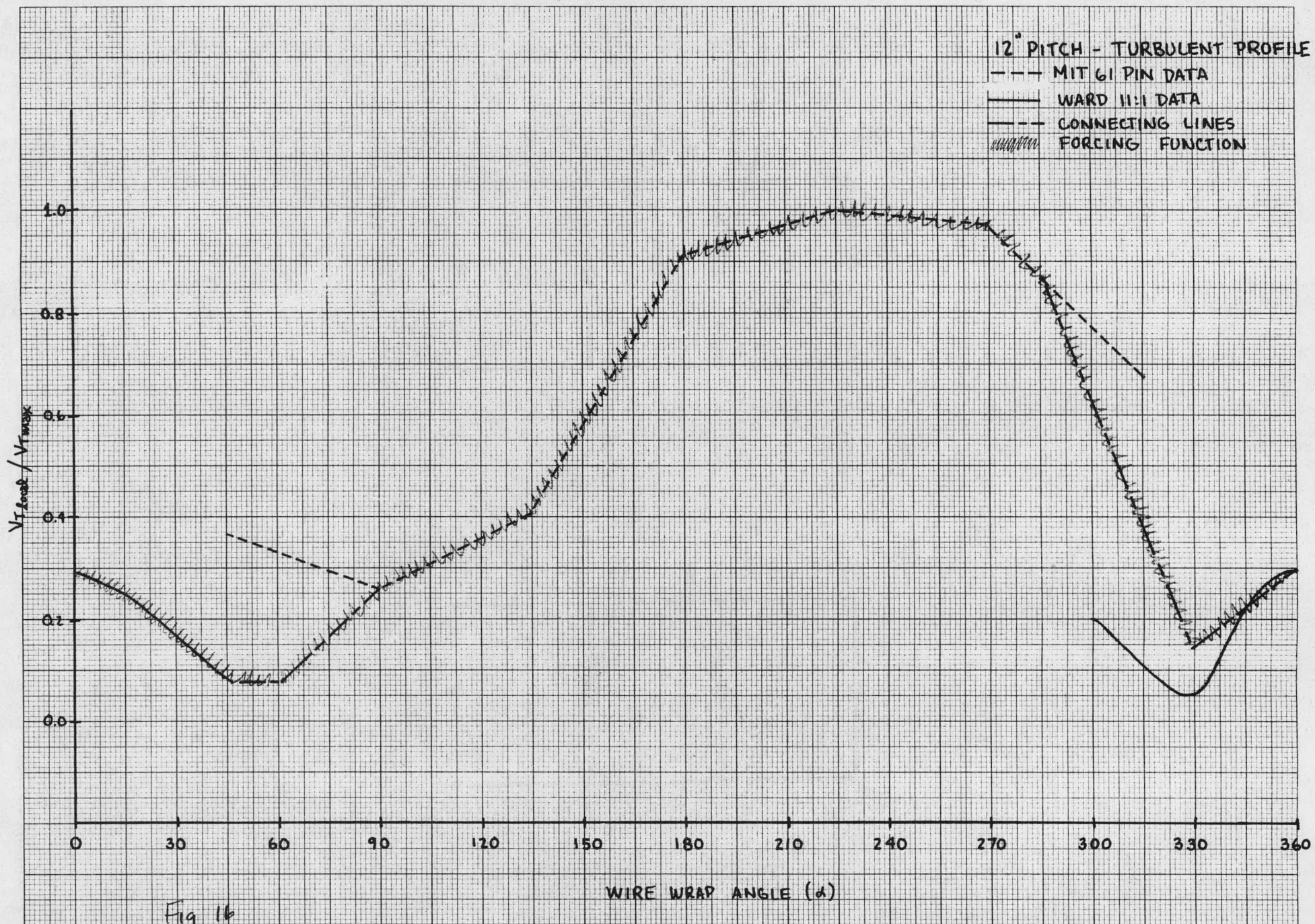
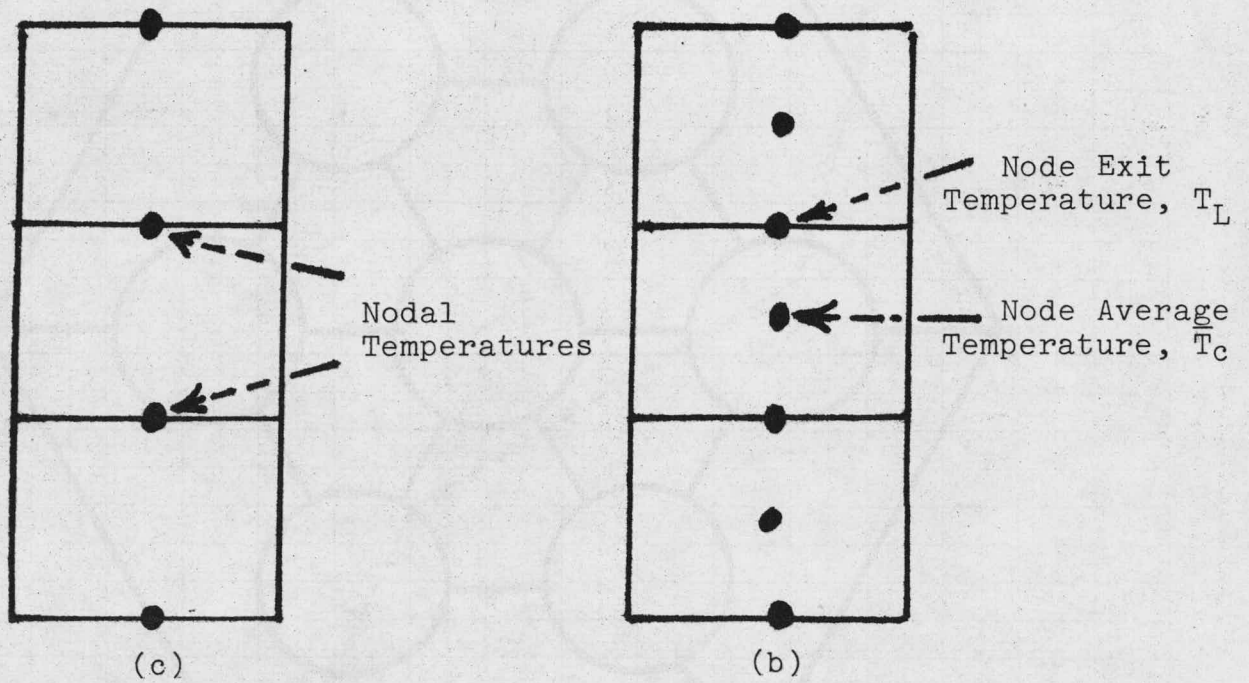


Fig 16

Figure 16

Figure 17

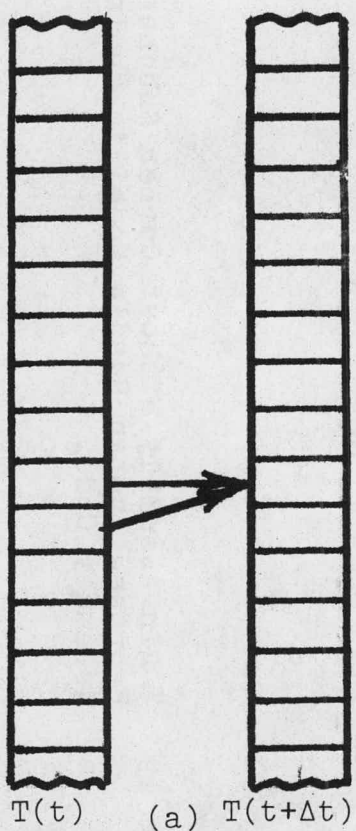


(c)  
 Nodal Temperatures Defined at  
 End of Node. Entire node assumed  
 at 1 temperature

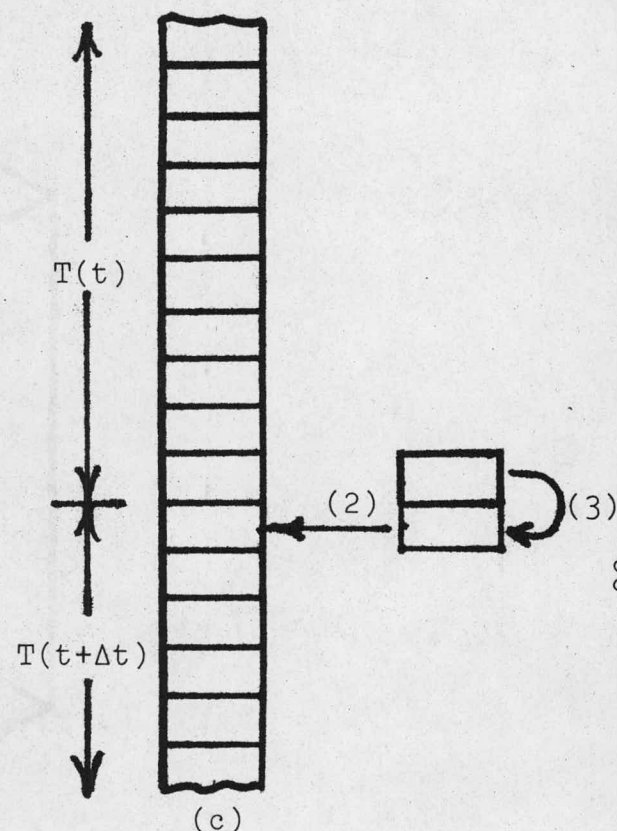
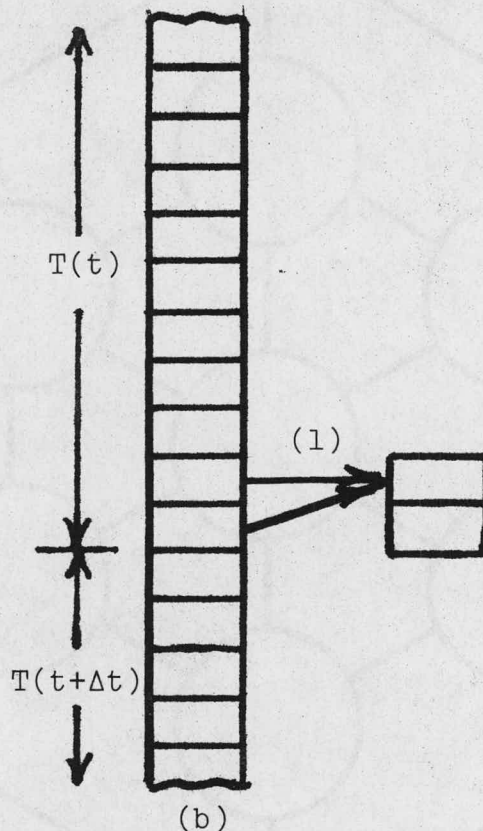
(b)  
 Dual Temperature per  
 Node Model: Node average  
 and node exit temperatures.



Figure 18



Dual Main Arrays Used for Storage of Coolant Temperatures



Dynamic Replacement of Storage into (Single) Main Array. Step (1), in (b) shows temporary storage of  $T(t+\Delta t)$  at the current axial step. At completion of calculation of  $T(t+t)$  for entire axial step,  $T(t+t)$  at previous axial step is replaced into main array, (2). Step (3) indicates "pushing down" of  $T(t+t)$  at current axial step in temporary storage. Calculation of  $T(t+t)$  at next axial step now continues as procedure marches up bundle.

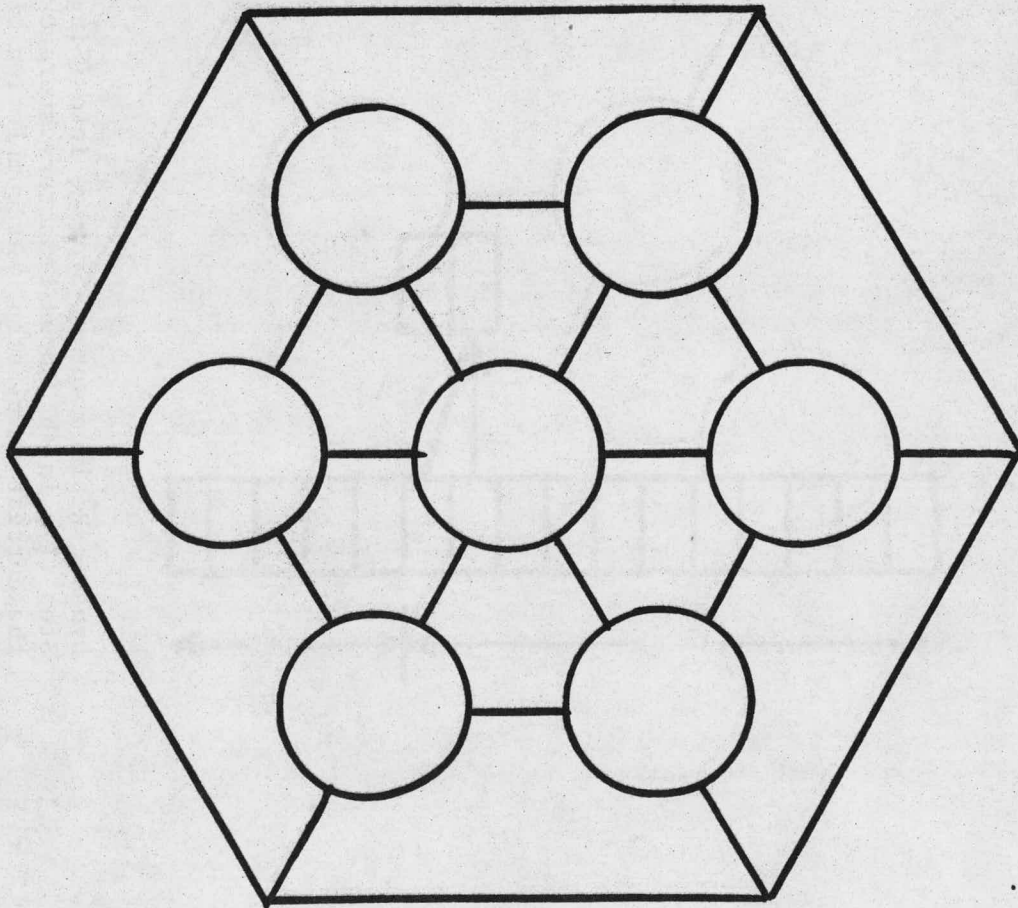


Fig. 19 7 Pin Assembly Without Corner Subchannels - Proposed Lumped Bundle Model in an Inter-assembly Code.



## TASK II: SUBCHANNEL GEOMETRY (BARE RODS)

TASK IIA: Assessment of Available Data

Nothing to report this quarter.

TASK IIB: Experimental Subchannel Water Mixing Investigation  
(Joseph M. Kelly)

Bulk mixing coefficients were measured for single plane water flows in a simulated rod bundle with a pitch to diameter ratio of 1.10. A tracer technique employing Rhodamine B as the tracer and measuring fluorescence was used. Isokinetic sampling was achieved by using a pressure balance method. The results were corrected for both entrance effects and diversion cross-flows.

Our results showed a change in Reynolds number behavior as the laminar sublayer began to "choke" the turbulent mixing. This, and a review of other mixing experiments, suggested that secondary flows do not compensate for laminarization and that turbulent mixing decreases as the pitch to diameter ratio decreases for values of P/D less than 1.05 in a manner similar to that predicted by Ramm et al.

Concentration profiles were measured through the clearance gap and the values of the gradient were used to calculate the gap averaged circumferential eddy diffusivity for mass.

TASK IIC: Experimental Subchannel Local Parameter  
Measurements (Wall Shear Stress Measurement  
and Laser Doppler Anemometry)TASK IIC.1: Wall Shear Stress Measurements (Mohammed Fakory)

As it was shown in the last progress report, use of a Preston tube was selected to measure wall shear stress. In order to measure the total pressure point by point in the peripheral direction around the rod, some changes were necessary to the selected test section. These changes are done and the test section is ready to be set up. After considering several viewpoints it was decided to use air flow in the experiments. A brief summary of these considerations follows:

Water Flow Advantages

1) One of the advantages of water flow is that we have larger Preston tube differential pressure (total local pressure - static pressure) than in the case of

air flow. The ratio of the differential pressure for the same Re number is of order

$$\frac{\Delta P_{\text{air}}}{\Delta P_{\text{H}_2\text{O}}} \sim \left[ \frac{\mu_{\text{air}}}{\mu_{\text{H}_2\text{O}}} \right]^2 \left[ \frac{\rho_{\text{H}_2\text{O}}}{\rho_{\text{air}}} \right] = \left[ \frac{3.827 \cdot 10^{-7}}{1.925 \cdot 10^{-5}} \right] \left[ \frac{1.935}{0.00548} \right] = 0.14$$

A typical ratio using the Patel correlation is

$$\frac{P_{\text{air}}}{P_{\text{H}_2\text{O}}} = 0.1405$$

2) In the case of water flow, the laminar sublayer is thicker so it is possible to use larger diameter probe respect to air flow.

#### Air Flow Advantages

1) The dissolved air in the water causes creation of air bubbles at the entrance of a small diameter probe and thus causing a false differential pressure.

2) Air flow requires a simpler transducer than water flow, there is no zeroing problem, and no zero set point shift.

3) The following error estimation shows that although as above  $\Delta P_{\text{air}} < \Delta P_{\text{H}_2\text{O}}$ , the measured wall shear stress error in the case of air flow is less or at most is the same as in the case of water flow.

The preferred Patel correlation for finding the wall shear stress is

$$y^* = 0.8287 - 0.1381 \eta^* + 0.143 \eta^{*2} - 0.006 \eta^{*3}$$

where

$$\eta^* = \log_{10} \left( \frac{\Delta P d^2}{4 \rho v^2} \right), \quad y^* = \log_{10} \left( \frac{\tau_w d^2}{4 \rho v^2} \right)$$

This formula gives  $\tau_w$  within + 1.5%. Considering both instrument error and correlation error we have in the case of water flow

$$\frac{\Delta \tau_w}{\tau_w} = 0.432\% + 1.5\% = 1.932\% \quad (\text{Re} = 25000)$$

And in the case of air flow:

$$\frac{\Delta \tau_w}{\tau_w} = 0.32\% + 1.5\% = 1.89\% \quad (\text{Re} = 25000)$$

Therefore probes, accessory devices, and instruments were designed and calculated on the basis of air flow. Hopefully gathering of experimental data will be initiated during January.

#### TASK IIC.2 Laser Doppler Anemometry Measurements (John Bartzis)

No measurements were obtained this quarter since the LDA system was being used for Task III.

#### TASK IID: Analytical Model Development - Subchannels (John Bartzis)

##### 1.1 The Differential Equations

###### 1.1.1 The Equations

Since we are going to use a 2-equation turbulent model, the equations of continuity, momenta, turbulent kinetic energy, energy dissipation are to be solved. The modeling of the above equations is discussed in Ref. 1.

The momentum and transport equations can be put in the general form

$$\left. \begin{array}{l} | \left\langle \begin{array}{c} \leftarrow \text{Convection} \rightarrow * \leftarrow \text{Diffusion} \rightarrow \leftarrow \text{Source} \rightarrow \\ \nabla \phi \underline{V} + \nabla \underline{T}_\phi = \nabla S_\phi + S_\phi^* \\ \underline{T}_\phi = (T_{\phi r}, T_{\phi \theta}) \\ \underline{S}_\phi = (S_{\phi r}, S_{\phi \theta}) \end{array} \right\rangle \\ (1-1) \end{array} \right\}$$

The separation of diffusion term into a  $T_\phi$  term and an  $S_\phi$  term which is treated as a source term has been on the ground that  $T_\phi$  includes only the terms that depend explicitly on  $\phi$ .

###### 1.1.2 The Solution Domain

The equations are to be solved within the characteristic triangle of the infinite rod bundle as shown in Fig. 1.

The secondary flow quantities (i.e.,  $v_r$ ,  $v_\theta$ ,  $p/p$ ) are going to be solved in the whole flow area of the characteristic

triangle whereas the  $v_z$  momentum equation and the  $k, \epsilon$  transport equations are going to be solved only in the outer region of the flow (i.e.,  $y_B^+ \geq 25-30$ ). As pointed out in Ref. 1 (p. 56) the exclusion of the wall region is made due to the following reasons:

- a) The sharp gradients of the hydrodynamic quantities within the wall region need a relatively high number of points to describe the hydrodynamic field sufficiently well.
- b) The strongly anisotropic turbulent kinetic equation makes a turbulent model based on the Kolmogorov-Prandtl hypothesis questionable. However, on the other hand, the prescription of the quantities themselves within the wall region is relatively not difficult since the main parameters of dependence are the wall shear stress, the distance from the wall and the fluid viscosity.

The approach of excluding the all region from the domain of solution has been used by several authors (see e.g., [2], [3]) and in the efforts preceding this work at MIT [4].

#### 1.1.2.1 Wall Layer Thickness Prescription

The wall layer thickness is defined from the relation

$$\frac{y_B \bar{u}^*}{\nu} \approx 30 \quad (1.2)$$

where  $\bar{u}^*$  is the average friction velocity

$$\text{i.e. } \bar{u}^* = \left( \frac{\tau_w}{\rho} \right)_{\text{avg}}^{1/2}$$

$y_B$  is the wall layer thickness

$\nu$  is the fluid kinematic viscosity.

In case the bulk velocity  $v_b$  is given instead of  $\bar{u}^*$  we use the friction factor relation, i.e.;

$$\bar{u}^* = \sqrt{\frac{f}{2}} v_b \quad (1.3)$$

For the friction factor estimation we will use Ibragimov's expression [5] which has also been used in Ref. 6. This expression is as follows:

$$\frac{f}{f_0} = \left( 0.58 + 0.42 e^{-\gamma} \right) \left[ 1 + 0.1 \left( \frac{2\bar{Y}}{D} \right)^{4/3} \right]$$

where  $\gamma = 0.21 \frac{P}{D} \left( \frac{A}{\bar{Y}^2} \right)^{1/4} \left( \frac{1}{\sqrt{3}} - \frac{1}{2} \right) \frac{D}{\bar{Y}}$

$$\bar{Y} = \frac{1}{A} \iint_A y r \, dr \, d\theta = \frac{1}{2} \left( \frac{3}{\pi\sqrt{3}} \frac{P}{D} - 1 \right) D$$
(1.2)

A is the flow area within the characteristic triangle and

$$f_0 = 0.046 \operatorname{Re}^{-0.2}$$
(1.4)

is the friction factor for circular pipe.

### 1.1.3 Boundary Conditions

The boundary conditions are given in Table Ib. The nature of the boundary conditions at the symmetry lines is profound. We will discuss below the boundary conditions at the near wall boundary (i.e., at the position  $y_B$ ).

#### 1.1.3.1 Near Wall Boundary Conditions

##### 1.1.3.1.1 Axial Velocity

Along the  $y_B$  circumferential line we will make the widely used assumption of logarithmic profile, i.e.,

$$v_z(y_B, \theta) = \frac{u^*(\theta)}{\kappa} \ln E \frac{u^*(\theta) y_B}{\nu}$$
(1.5)

where  $\kappa$  and  $E$  are constants

According to Ref. 4,  $\kappa \approx 0.419$ ,  $E \approx 9.8$

The velocity profile in the region  $0 \leq y \leq y_B$  needed for calculation of the bulk velocity is taken as follows

$$\frac{v_z(\gamma, \theta)}{u^*(\theta)} = \frac{u^*(\theta) \gamma}{\nu} \quad \text{for } \frac{u^*(\theta) \gamma}{\nu} \leq 5 \quad (1.6a)$$

$$\frac{v_z(\gamma, \theta)}{u^*(\theta)} = \alpha + \beta \ln \frac{u^*(\theta) \gamma}{\nu} \quad \text{for } 5 \leq \frac{u^*(\theta) \gamma}{\nu} \leq \frac{u^*(\theta) \gamma_B}{\nu} \quad (1.6b)$$

where

$$\beta = \frac{v_z(\gamma_B, \theta) / u^*(\theta) - 5}{\ln \frac{\gamma_B u^*(\theta)}{5\nu}} \quad (1.6c)$$

$$\alpha = \frac{1}{5} \left[ v_z(\gamma_B, \theta) / u^*(\theta) + 5 - \beta \ln \frac{5\gamma_B u^*(\theta)}{\nu} \right] \quad (1.6d)$$

The expressions for  $\alpha$ ,  $\beta$  come from the velocity continuity condition at the points

$$\frac{\gamma u^*(\theta)}{\nu} = 5 \quad \text{and} \quad \frac{\gamma u^*(\theta)}{\nu} = 30$$

#### 1.1.3.1.2 Turbulent Kinetic Energy

As we have pointed out in Ref. 1, p. 58 the near wall boundary lies within the dynamic equilibrium subregion where the importance of the convection and diffusion mechanism are minor.

Thus the transport equation for  $k$  can be reduced to

$$\left( -\overline{v_r' v_z'} \right)_{\gamma=\gamma_B} \left( \frac{\partial v_z}{\partial r} \right)_{\gamma=\gamma_B} \approx \epsilon_B \quad (1.7)$$

where  $\epsilon_B$  is the energy dissipation at  $\gamma=\gamma_B$ .

On the other hand the axial momentum equation neglecting the lateral gradient as small compared with the radial gradient is reduced to

$$\frac{1}{r} \frac{\partial}{\partial r} \left( r \overline{v_r' v_z'} \right) - \nu \frac{\partial^2 v_z}{\partial r^2} = \frac{4}{D_H} (\overline{u^*})^2 \quad (1.8)$$

where  $D_H$  is the hydraulic diameter and  $\overline{u^*}$  is the average friction velocity.

Integrating Eq. (1.8) over  $y_B$  and neglecting the friction effect at  $y_B$  we obtain

$$\left( - \overline{v_r' v_z'} \right)_{y=y_B} = \frac{r_1}{r_2} [u^*(\theta)]^2 - 2 \frac{r_2^2 - r_1^2}{r_2 D_H} (\overline{u^*})^2 \quad (1.9)$$

where

$$r_1 = D/2$$

$$r_2 = D/2 + y_B$$

Since

$$\left( \frac{\partial v_z}{\partial r} \right)_{y=y_B} = \frac{u^*(\theta)}{k y_B}$$

and

$$c_\mu \frac{k_B^2}{\epsilon_B} \left( \frac{\partial v_z}{\partial r} \right)_{y=y_B} = \left( - \overline{v_r' v_z'} \right)_{y=y_B}$$

we find finally

$$\epsilon_B = \left( - \overline{v_r' v_z'} \right)_{y=y_B} \frac{u^*(\theta)}{k y_B} \quad (1.10)$$

$$k_B = \frac{1}{\sqrt{c_\mu}} \left( - \overline{v_r' v_z'} \right)_B \quad (1.11)$$

## 1.2 Grid

We have tried to make the grid space as uniform as possible. The reason is that although grid nonuniformity can improve the accuracy of the problem in some cases usually it has a negative effect on rate of convergence and stability [8]. On the other hand a uniform grid makes the numerical equations easier to handle. So in the  $\theta$  direction a uniform spacing  $\Delta\theta$  is used, i.e.,

$$\Delta\theta = \theta_j - \theta_{j-1} = \frac{\pi}{6 \times (JN-1)} \quad (1.12)$$

where  $JN$  is the number of mesh points in the  $\theta$ -direction. With respect to the  $r$ -direction, the spacing along the gap (i.e.,  $\theta=0$ ) is also taken uniform, i.e.,

$$r_i - r_{i-1} = \left[ \frac{P}{2} - \left( \frac{D}{2} + Y_B \right) \right] / (M-2); \quad i \leq M$$

$$M = IN - (JN - 1) \quad (1.13)$$

where

$M$  is the number of points along  $\theta=0$  line

$IN$  is the number of points along  $\theta=30^\circ$  line, and

$Y_B$  is the wall boundary thickness

For  $i > M$  the spacing cannot be uniform since it is defined from the zero shear stress line as shown in Fig. 2.

In this case

$$r_{i=M+j-1} = \frac{P}{2 \cos \theta} - \frac{P}{2}; \quad M < i \leq IN \quad (1.14)$$

The grid is shown in Fig. 2.

So by the above procedure the mesh points  $(i,j)$  have been defined. However at these points only the scalar parameters  $k$ ,  $\epsilon$ , and  $p$  the axial velocity  $v_z$  and auxiliary quantities (e.g., eddy viscosities, mixing length) will be calculated. The



parameters  $v_r(i,j)$  and  $v_\theta(i,j)$  will be defined in a slightly different position as shown in Fig. 4. This procedure is similar to that adopted in TEACH code [9].

### 1.3 The Finite Difference Equations

The finite difference equations are obtained by integration of Eq. (1.1) over the control volume. The control volume surrounding the point under consideration is shown in its general form in Fig. 3.

After integration over the control volume and taking into consideration the Divergence Theorem Eq. (1.1) becomes

$$\oint_{CS} \phi \underline{v} \cdot \underline{n} \, dl + \oint_{CS} T_\phi \underline{n} \, dl = \oint_{CS} S_\phi \underline{n} \, dl + \iint_{CV} S_\phi^* \, dA \quad (1.15)$$

where by  $\int_{CS} \int_{CV}$  we denote the integration over the boundary of the control volume, and  $\underline{n}$  is the unit vector perpendicular to the surface boundary as shown in Fig. 3. Let

$$A_e = \text{length (ne, se)}$$

$$A_w = \text{length (nw, sw)}$$

$$A_n = \text{length (ne, nw)}$$

$$A_s = \text{length (se, sw)}$$

$$V_p = \text{area (ne, se, sw, nw, ne)}$$

$$(1.16)^*$$

The value of above quantities for the various angles  $\phi$  are given in Table II. Equation (1.15) can be written

$$\begin{aligned} & A_e \phi_e v_{re} - A_w \phi_w v_{rw} + A_n \phi_n v_{\theta n} - A_s \phi_s v_{\theta s} + \\ & + T_{\phi re} A_e - T_{\phi rw} A_w + T_{\phi \theta n} A_n - T_{\phi \theta s} A_s = \\ & = S_{\phi re} A_e - S_{\phi rw} A_w + S_{\phi \theta n} A_n - S_{\phi \theta s} A_s + \\ & + S_{\phi p}^* V_p \end{aligned} \quad (1.17)$$

(\*)The nomenclature used in Fig. 3 is almost the same as that used in Ref. 2.

In Eq. (1.19) the following approximation has been made

$$\iint_{CV} S_{\phi}^* dA \approx S_{\phi P}^* V_P \quad (1.18)$$

where

$S_P^*$  is the value of  $S_{\phi}^*$  at point P

$V_P$  is the control volume surface

The continuity equation gives after integration over the control volume

$$A_e v_{re} - A_w v_{rw} + A_m v_{\theta m} - A_s v_{\theta s} = 0 \quad (1.19)$$

In Eq. (1.17) we can distinguish the Convection term, Diffusion term and Source term as follows:

Diffusion term:

$$DT = T_{\phi re} A_e - T_{\phi rw} A_w + T_{\phi \theta m} A_m - T_{\phi \theta s} A_s \quad (1.20a)$$

Convection term:

$$CT = A_e v_{re} \phi_e - A_w v_{rw} \phi_w + A_m v_{\theta m} \phi_m - A_s v_{\theta s} \phi_s \quad (1.20b)$$

Source term:

$$ST = S_{\phi re} A_e - S_{\phi rw} A_w + S_{\phi \theta m} v_{\theta m} - S_{\phi \theta s} v_{\theta s} + S_{\phi P}^* V_P \quad (1.20c)$$

Thus Eq. (1.17) can be written

$$DT + CT = ST$$

1.3.1 Diffusion Term1.3.1.1 Scalar Quantities k, ε and the Axial Velocity V<sub>z</sub>

From the Table Ia we have

$$\begin{aligned}
 T_{\phi r} &= - \frac{\nu_{rz}^{eff}}{\sigma_{\phi}} \frac{\partial \phi}{\partial r} \\
 T_{\phi \theta} &= - \frac{\nu_{\theta z}^{eff}}{\sigma_{\phi}} \frac{\partial \phi}{r \partial \theta}
 \end{aligned}
 \tag{1.21}$$

We can make the following approximations

$$\begin{aligned}
 T_{\phi re} &= - \frac{(\nu_{rz}^{eff})_E + (\nu_{rz}^{eff})_P}{2\sigma_{\phi}} \frac{\phi_E - \phi_P}{r_E - r_P} \\
 T_{\phi rw} &= - \frac{(\nu_{rz}^{eff})_W + (\nu_{rz}^{eff})_P}{2\sigma_{\phi}} \frac{\phi_P - \phi_W}{r_P - r_W} \\
 T_{\phi \theta n} &= - \frac{(\nu_{\theta z}^{eff})_N + (\nu_{\theta z}^{eff})_P}{2\sigma_{\phi}} \frac{\phi_N - \phi_P}{r_P \Delta \theta} \\
 T_{\phi \theta s} &= - \frac{(\nu_{\theta z}^{eff})_S + (\nu_{\theta z}^{eff})_P}{2\sigma_{\phi}} \frac{\phi_P - \phi_S}{r_P \Delta \theta}
 \end{aligned}
 \tag{1.22a}$$

$$\tag{1.22b}$$

Thus Eq. (1.7a) becomes

$$DT = (DE + DW + DN + DS)\phi_P - DN \cdot \phi_N - DS \cdot \phi_S - DE \cdot \phi_E - DW \cdot \phi_W$$

(1.23)

where

$$DE = \frac{BE}{\sigma_\phi} \left[ (\nu_{rz}^{\text{eff}})_E + (\nu_{rz}^{\text{eff}})_P \right]$$

(1.24a)

$$DW = \frac{BW}{\sigma_\phi} \left[ (\nu_{rz}^{\text{eff}})_W + (\nu_{rz}^{\text{eff}})_P \right]$$

(1.24b)

$$DN = \frac{BN}{\sigma_\phi} \left[ (\nu_{\theta z}^{\text{eff}})_N + (\nu_{\theta z}^{\text{eff}})_P \right]$$

(1.24c)

$$DS = \frac{BS}{\sigma_\phi} \left[ (\nu_{\theta z}^{\text{eff}})_S + (\nu_{\theta z}^{\text{eff}})_P \right]$$

(1.24d)

$$BE = \frac{A_e}{2(r_E - r_P)}$$

(1.25a)

$$BW = \frac{A_w}{2(r_P - r_w)}$$

(1.25b)

$$BN = \frac{A_n}{2r_P \Delta\theta}$$

(1.25c)

$$BS = \frac{A_s}{2r_p \Delta\theta} \quad (1.25d)$$

The values of DE, DW, DN, DS, BE, BW, BN, BS are given in Table III.

### 1.3.1.2 The Velocity $V_r$

From Table I we see that

$$T_{\phi r} = -2\nu \frac{\partial V_r}{\partial r} \quad (1.26)$$

$$T_{\phi\theta} = -\nu_{r\theta}^{eff} \frac{\partial V_r}{r \partial \theta}$$

we make the following approximations

$$\begin{aligned} T_{\phi rE} &= -2\nu (V_{rE} - V_{rP}) / (r_E - r_P) \\ T_{\phi rW} &= -2\nu (V_{rP} - V_{rW}) / (r_P - r_W) \\ T_{\phi\theta n} &= -\nu_{r\theta n}^{eff} (V_{rN} - V_{rP}) / r_P / \Delta\theta \\ T_{\phi\theta s} &= -\nu_{r\theta s}^{eff} (V_{rP} - V_{rS}) / r_P / \Delta\theta \end{aligned} \quad (1.27)$$

Thus the diffusion term is

$$DT = (DE + DW + DN + DS)v_{rp} - DN \cdot v_{rN} - DS \cdot v_{rS} - DE \cdot v_{rE} - DW \cdot v_{rW}$$

(1.28)

where

(1.29a)

$$DE = BE \cdot v \quad (1.29b)$$

$$DW = BW \cdot v$$

$$DN = BN \left[ (v_{r\theta}^{\text{eff}})_{Ne} + (v_{r\theta}^{\text{eff}})_e + (v_{r\theta}^{\text{eff}})_w + (v_{Nw}^{\text{eff}})_{Nw} \right] \quad (1.29c)$$

$$DS = BS \left[ (v_{r\theta}^{\text{eff}})_{se} + (v_{r\theta}^{\text{eff}})_e + (v_{r\theta}^{\text{eff}})_w + (v_{r\theta}^{\text{eff}})_{sw} \right] \quad (1.29d)$$

$$BE = \frac{2A_e}{r_E - r_P} \quad (1.30a)$$

$$BW = \frac{2A_w}{r_P - r_W} \quad (1.30b)$$

$$BN = BS = \frac{A_n}{4r_P \Delta\theta} \quad (1.30c)$$

The values of DE, DW, DN, DS, BE, BW, BN, BS are given in Table III.

### 1.3.1.3 The Velocity $v_\theta$

From Table I we have

$$T_{\phi r} = -v_{r\theta}^{\text{eff}} r^2 \frac{\partial}{\partial r} \left( \frac{v_\theta}{r} \right) \quad (1.31a)$$

$$T_{\phi\theta} = -2v \frac{\partial v_\theta}{\partial \theta} \quad (1.31b)$$

We make the following approximations

$$\begin{aligned}
 T_{\phi re} &= v_{r\theta e}^{\text{eff}} r_e^2 \left[ \frac{\frac{v_{\theta E}}{r_E} - \frac{v_{\theta P}}{r_P}}{r_E - r_P} \right] \\
 T_{\phi rw} &= v_{r\theta w}^{\text{eff}} r_w^2 \left[ \frac{\frac{v_{\theta P}}{r_P} - \frac{v_{\theta W}}{r_W}}{r_P - r_W} \right] \\
 T_{\phi \theta n} &= -2v \left[ \frac{v_{\theta N} - v_{\theta P}}{\Delta\theta} \right] \\
 T_{\phi \theta s} &= 2v \left[ \frac{v_{\theta P} - v_{\theta S}}{\Delta\theta} \right]
 \end{aligned} \tag{1.32}$$

Thus Eq. (1.20a) becomes

$$DT = (DN + DS + DE \cdot \frac{r_E}{r_P} + DW \cdot \frac{r_W}{r_P}) v_{\theta P} - DE \cdot v_{\theta E} - DW \cdot v_{\theta W} - DN \cdot v_{\theta N} - DS \cdot v_{\theta S} \tag{1.33}$$

where

$$\begin{aligned}
 DE &= BE \left[ \left( \nu_{r\theta}^{\text{eff}} \right)_{nE} + \left( \nu_{r\theta}^{\text{eff}} \right)_{sE} + \left( \nu_{r\theta}^{\text{eff}} \right)_s + \left( \nu_{r\theta}^{\text{eff}} \right)_n \right] \\
 DW &= BW \left[ \left( \nu_{r\theta}^{\text{eff}} \right)_{nW} + \left( \nu_{r\theta}^{\text{eff}} \right)_{sW} + \left( \nu_{r\theta}^{\text{eff}} \right)_s + \left( \nu_{r\theta}^{\text{eff}} \right)_n \right]
 \end{aligned} \tag{1.34}$$

$$DN = DS = BN \cdot v$$

$$BE = \frac{r_e^2 A_e}{4r_e(r_e - r_p)}$$

$$BW = \frac{r_w^2 A_w}{4r_w(r_p - r_w)}$$

$$BN = BS = \frac{2A_m}{\Delta\theta}$$

(1.35)

The values of DE, DW, DN, DS, BE, BW, BS are given in Table III.

### 1.3.2 The Convection Term

Recall that the convection term is given by the Eq. (1.20) i.e.,

$$CT = A_e v_{re} \phi_e - A_w v_{rw} \phi_w + A_m v_{\theta n} \phi_m - A_s v_{\theta s} \phi_s \quad (1.20b)$$

where

$\phi$  is given in Table Ia

From Eq. (1.20b) it is evident that the common substitution

$$\phi_e = \frac{\phi_E + \phi_P}{2}$$

etc., can produce a finite difference equation with negative coefficients which can produce nonconvergence in the solution. Since our ultimate purpose is to obtain a finite difference equation with positive coefficients and on the other hand as much accurate as possible we proceed as follows:



Let

$$\phi_e = \phi_P + \left( \frac{\partial \phi}{\partial r} \right)_P (r_e - r_P) \quad (1.36a)$$

$$\phi_m = \phi_P + \left( \frac{\partial \phi}{\partial \theta} \right)_P \frac{\Delta \theta}{2} \quad (1.36b)$$

$$\phi_w = \phi_P - \left( \frac{\partial \phi}{\partial r} \right)_P (r_P - r_w) \quad (1.36c)$$

$$\phi_s = \phi_P - \left( \frac{\partial \phi}{\partial \theta} \right)_P \frac{\Delta \theta}{2} \quad (1.36d)$$

Substituting Eqs. (1.26) into (1.20b) and taking into consideration continuity Eq. (1.19) we end up with

$$CT = \left[ A_e v_{re} (r_e - r_P) + A_w v_{rw} (r_P - r_w) \right] \left( \frac{\partial \phi}{\partial r} \right)_P + \frac{A_n \Delta \theta}{2} (v_{\theta n} + v_{\theta s}) \left( \frac{\partial \phi}{\partial \theta} \right)_P \quad (1.37)$$

In Eq. (1.24) we have taken into consideration the fact that  $A_n = A_s$

We further approximate

$$\left( \frac{\partial \phi}{\partial r} \right)_P = \begin{cases} \frac{\phi_E - \phi_P}{r_E - r_P} & \text{if } A_e v_{re} (r_e - r_P) + A_w v_{rw} (r_P - r_w) < 0 \\ \frac{\phi_P - \phi_w}{r_P - r_w} & \text{otherwise} \end{cases} \quad (1.38)$$

$$\left( \frac{\partial \phi}{\partial \theta} \right)_P = \begin{cases} \frac{\phi_N - \phi_P}{\Delta \theta} & \text{if } v_{\theta P} \leq 0 \\ \frac{\phi_P - \phi_S}{\Delta \theta} & \text{otherwise} \end{cases} \quad (1.39)$$

Under these circumstances the convection term can be written

$$CT = (C_E + C_W + C_N + C_S) \phi_P - C_E \phi_E - C_W \phi_W - C_N \phi_N - C_S \phi_S \quad (1.40)$$

where

$$C_E = 0.5 \left\{ \left| A_e v_{re} (r_e - r_P) + A_w v_{rw} (r_P - r_w) \right| - A_e v_{re} (r_e - r_P) - A_w v_{rw} (r_P - r_w) \right\} / (r_E - r_P) \quad (1.41a)$$

$$C_W = 0.5 \left\{ \left| A_e v_{re} (r_e - r_P) + A_w v_{rw} (r_P - r_w) \right| + A_e v_{re} (r_e - r_P) + A_w v_{rw} (r_P - r_w) \right\} / (r_P - r_w) \quad (1.41b)$$

$$CN = A_m \frac{|v_{\theta n} + v_{\theta s}| - v_{\theta n} - v_{\theta s}}{4} \quad (1.41c)$$

$$CS = A_s \frac{|v_{\theta n} + v_{\theta s}| + v_{\theta n} + v_{\theta s}}{4} \quad (1.41d)$$

The value for CE, CW, CN, CS at a particular point (i,j) and for  $\phi = k, \epsilon, v_z, v_r$  are given in Table IV

The convection term for the component  $v_{\theta}$  itself is slightly different (\*) than (1.40) as in the case of the diffusion term, i.e.,

$$CT = \left( CE \frac{r_p}{r_e} + CW \frac{r_p}{r_w} + CN + CS \right) v_{\theta p} -$$

$$- CE \cdot v_{\theta e} - CW \cdot v_{\theta w} - CN v_{\theta n} - CS v_{\theta s}$$

The values of CE, CW, CN, CS for  $v_{\theta}$  are given also in Table IV.

### 1.3.3 Source Term

Recall that the source term is given by (1.20c) i.e.,

$$ST = S_{\phi r e} A_e - S_{\phi r w} A_w + S_{\phi \theta n} A_n - S_{\phi \theta s} A_s + S_{\phi}^* V_p \quad (1.20c)$$

The form of the source term for each quantity is different in character so we examine ST for each quantity separately.

#### 1.3.3.1 Axial Velocity $v_z$

From Table I we see that

$$ST = S_p^* V_p = \frac{4}{DH} \left( \frac{\tau_w}{\rho} \right)_{avg} V_p$$

(\*) Eq (1.40) is valid for  $v_{\theta}$  instead of  $v_{\theta}$  as Table Ia shows

where

$\left(\frac{\tau}{\rho}\right)_{\text{avg}}$  is the average shear stress, and  
DH is the hydraulic diameter.

### 1.3.3.2 Kinetic Energy k

From Table Ia

$$ST = S_P^* V_P = \left[ \left( \nu_{rz}^T \right)_P \left( \frac{\partial v_z}{\partial r} \right)_P^2 + \left( \nu_{\theta z}^T \right)_P \left( \frac{\partial v_z}{r \partial \theta} \right)_P^2 - \epsilon_P \right] V_P \quad (1.44)$$

For reasons of numerical stability as we will see later the energy dissipation term can be transferred as follows:

Since

$$\nu_{rz}^T = C_\mu \frac{k^2}{\epsilon}$$

$$\epsilon = \frac{C_\mu k^2}{\nu_{rz}^T}$$

Thus

$$ST = \left[ \left( \nu_{rz}^T \right)_P \left( \frac{\partial v_z}{\partial r} \right)_P^2 + \left( \nu_{\theta z}^T \right)_P \left( \frac{\partial v_z}{r \partial \theta} \right)_P^2 \right] V_P - S_P \cdot k_P \quad (1.45)$$

where

$$S_P = \frac{C_\mu k_P}{\left( \nu_{rz}^T \right)_P} \quad (1.46)$$

1.3.3.3 Energy Dissipation

From Table Ia

$$ST = \left\{ c_1 \frac{\varepsilon}{k} \left[ v_{rz}^T \left( \frac{\partial v_z}{\partial r} \right)^2 + v_{\theta z}^T \left( \frac{\partial v_z}{r \partial \theta} \right)^2 \right] - c_2 \frac{\varepsilon^2}{k} \right\} \quad (1.47)$$

Since

$$\frac{\varepsilon}{k} = c_\mu \frac{k}{v_{vz}^T} \quad (1.48)$$

Then

$$ST = c_1 \frac{c_\mu k_P}{(v_{rz}^T)_P} \left\{ (v_{rz}^T)_P \left( \frac{\partial v_z}{\partial r} \right)_P^2 + v_{\theta z}^T \left( \frac{\partial v_z}{r \partial \theta} \right)_P^2 \right\} - S_P \varepsilon_P \quad (1.49)$$

where

$$S_P = c_2 c_\mu \frac{k_P v_P}{(v_{rz}^T)_P} \quad (1.50)$$

1.3.3.4 Radial Velocity  $v_r$ 

From Table I we have

$$S_{\phi r} = -(\overline{v_r^2} + \frac{p}{\rho})$$

$$S_{\phi \theta} = v_{r\theta}^{\text{eff}} r \frac{\partial}{\partial r} \left( \frac{v_\theta}{r} \right)$$

$$S_\phi^* = \frac{v_\theta^2 + \overline{v_\theta^2}}{r} - \frac{2v}{r} \left( \frac{\partial v_\theta}{r \partial \theta} + \frac{v_r}{r} \right) \approx \frac{\overline{v_\theta^2}}{r}$$

Thus Eq. (1.20c) becomes

$$\begin{aligned}
 ST = & A_w \left[ \overline{v_{rw}'^2} + (p/\rho)_w \right] - A_e \left[ \overline{v_{re}'^2} + (p/\rho)_e \right] \\
 & + (v_{r\theta}^{eff})_m r_p \left[ \frac{\partial}{\partial r} \left( \frac{v_\theta}{r} \right) \right]_m A_n - v_{r\theta}^{eff} r_p \left[ \frac{\partial}{\partial r} \left( \frac{v_\theta}{r} \right) \right]_s A_s \\
 & + \frac{(\overline{v_\theta'^2})_p}{v_p} V_p
 \end{aligned} \tag{1.51}$$

The ST value for the point (i,j) is given in Table IV.

#### 1.3.3.5, Velocity $v_\theta$

From Table I we have

$$S_{\phi r} = -v_{r\theta}^{eff} \frac{\partial v_r}{\partial \theta} \tag{1.52}$$

$$S_{\phi \theta} = 2v v_r - r \overline{v_\theta'^2} - \frac{rp}{\rho} \approx -r(\overline{v_\theta'^2} + \frac{p}{\rho}) \tag{1.53}$$

Thus Eq. (1.20c) can be approximated

$$\begin{aligned}
 ST = & v_{r\theta e}^{eff} \left( \frac{\partial v_r}{\partial \theta} \right)_e A_e - v_{r\theta w}^{eff} \left( \frac{\partial v_r}{\partial \theta} \right)_w A_w \\
 & + r_p A_n \left[ (\overline{v_\theta'^2})_s + (p/\rho)_s - (\overline{v_\theta'^2})_n - (p/\rho)_n \right]
 \end{aligned} \tag{1.54}$$

The ST value for the point (i,j) is given in Table IV.

### 1.3.4 General Form of FDE

The general form of the differential equations of all the quantities under consideration, has as follows

$$(AP + SP)\phi_P = AE + \phi_E + AN \cdot \phi_N + AW \cdot \phi_W + AS \cdot \phi_S + SU \quad (1.55a)$$

where

$$\left. \begin{aligned} AE &= CE + DE \\ AW &= CW + DW \\ AN &= CN + DN \\ AS &= CS + DS \end{aligned} \right\} (1.55b)$$

$$AP = \begin{cases} \frac{r_P}{r_E} CE + \frac{r_E}{r_P} DE + \frac{r_P}{r_W} CW + \frac{r_W}{r_P} DW + AN + AS & \text{for } v_\theta \\ AE + AW + AN + AS & \text{Otherwise} \end{cases} \quad (1.55c)$$

where CE, CW, CN, CS, DE, DW, DN, DS, SU, SP are given in Tables III, IV and V

### 1.3.5 The Boundary Conditions

#### 1.3.5.1 Quantities k, $\epsilon$ , $v_z$

##### 1.3.5.1.1 Boundary I and II (Fig. 1)

According to Table Ib

$$\left(\frac{\partial \phi}{\partial \theta}\right)_{I,II} = 0 \quad (1.56)$$

where

$$\phi = k, \epsilon \text{ or } v_z$$

Numerically Eq. (1.55) is translated to

$$\phi_{i,j} = \phi_{i,j+1} \quad \text{for Boundary I} \quad (1.57)$$

$$\phi_{i,j} = \phi_{i,j-1} \quad \text{for Boundary II}$$

1.3.5.1.2 Boundary III

From Table Ib we have

$$\left(\frac{\partial \phi}{\partial n}\right)_{\text{III}} = 0 \quad (1.58)$$

Integrating over the triangular control volume shown in Fig. 5 and taking into consideration Eq. (1.58) we end up with

$$(AP + SP')\phi_P = AW \cdot \phi_W + AN \cdot \phi_N + SU' \quad (1.59)$$

$$AW = DW + CW'$$

$$AN = DN + CN'$$

$$AP = AW + AN$$

Where DW, DN are given from Table III and IV respectively

$$\left. \begin{aligned} CN' &= -AN(v_\theta)_{i,j+1}/2 \\ CW' &= A_W(v_r)_{i,j}/2 \\ SU' &= SU \frac{V_P'}{V_P} \\ SP' &= SP \frac{V_P'}{V_P} \end{aligned} \right\} (1.60)$$

and  $A_e$ ,  $A_n$ ,  $V_P$  are given from Table II.  $SU$ ,  $SP$  are given from Table V.

$V_P'$  is the area of the triangular control volume under consideration, i.e.,

$$(V_P')_j = \left[ (r_{i+1} + r_i) \sin \Delta\theta - (r_i + r_{i-1}) \Delta\theta \right] \frac{r_i + r_{i+1}}{8} \quad (1.61)$$



It is evident from Eq. (1.60) that we have substituted for

$$\phi_e = \frac{\phi_E + \phi_P}{2}$$

and similarly for  $\phi_w$ ,  $\phi_n$ ,  $\phi_s$ .

### 1.3.5.1.3 Wall Region

#### 1.3.5.1.3.1 Axial Velocity

At the  $y_B$  line we will demand continuity of the velocity and the velocity gradient.

The velocity gradient can be calculated numerically with accuracy  $O(\Delta r^2)$  from the relation

$$\left(\frac{dv_z}{dr}\right)_{2,j} = \frac{r_4 - r_2}{(r_3 - r_2)(r_4 - r_3)} (v_z)_{3,j} - \frac{r_3 - r_2}{(r_4 - r_2)(r_4 - r_3)} (v_z)_{4,j} - \frac{r_4 + r_3 - 2r_2}{(r_3 - r_2)(r_4 - r_2)} (v_z)_{2,j} \quad (1.62a)$$

since

$$(v_z)_{2,j} = \frac{u_j^*}{K} \ln E \frac{u_j^* y_B}{\nu} \quad (1.62b)$$

and

$$\left(\frac{dv_z}{dr}\right)_{2,j} = \frac{u_j^*}{K y_B} \quad (1.62c)$$

we can solve Eqs. (1.62) for  $u_j^*$  and  $(v_z)_{2,j}$  numerically

### 1.3.5.1.3.2 Turbulent Kinetic Energy and Energy Dissipation

$k_{2,j}$  and  $\epsilon_{2,j}$  are calculated from the algebraic relations given in Table Ib

### 1.3.5.2 $v_r$ Velocity

#### 1.3.5.2.1 Boundary I and II (Fig. 1)

According to Table IB

$$\left(\frac{\partial v_r}{\partial \theta}\right)_{I,II} = 0 \quad (1.63a)$$

thus numerically Eq. (1.63) is translated

$$\left. \begin{aligned} (v_r)_{i,j} &= (v_r)_{i,j+1} \quad \text{for Boundary I} \\ (v_r)_{i,j} &= (v_r)_{i,j-1} \quad \text{for Boundary II} \end{aligned} \right\} (1.63b)$$

#### 1.3.5.2.2 Boundary III Fig. 1)

From Table Ib we have

$$V_{\text{sec}} n = 0 \quad (1.64)$$

Numerically Eq. (1.64) can be expressed as we can see from Fig. 5b

$$(A_e)_{i-1} (v_r)_{i,j} = (A_n)_{i-1} (v_\theta)_{i-1,j} \quad (1.65)$$

where  $A_e$  and  $A_n$  are given in Table III

#### 1.3.5.2.3 Wall

From Table Ib we have

$$(v_r)_{i,j} = 0 \quad (1.66)$$

from the continuity equation, since

$$\frac{\partial v_\theta}{\partial \theta} = 0 \quad \text{at the wall}$$

$$\frac{\partial rv_r}{\partial r} = 0$$

which gives

$$(v_r)_{i,j} = 0 \quad (1.67)$$

as well

### 1.3.5.3 v<sub>θ</sub> Velocity

#### 1.3.5.3.1 Boundaries I and III

From Table 1b we have

$$(v_\theta)_{I,II} = 0 \quad (1.68)$$

Numerically we can approximate\* (with accuracy of  $O(\frac{\Delta\theta}{2})$ )

$$\left. \begin{aligned} (v_\theta)_{i,2} &= 0 \\ (v_\theta)_{i,N} &= 0 \end{aligned} \right\} (1.69)$$

where N is the maximum number of points for v<sub>z</sub> along the tangential direction.

#### 1.3.5.3.2 Boundary III

From Table 1b

$$\frac{\partial v_{sec}}{\partial n} = 0 \quad (1.70)$$

This relation leads to (see Ref. 6)

$$\frac{\partial(rv_\theta)}{\partial r} = \frac{\partial v_r}{\partial \theta} \quad (1.70a)$$

Numerically Eq. (1.70) as we can see from Fig. 5c can be expressed

\*More accurate schemes for Eq. (1.68) have led to instabilities.

$$\frac{r_i (v_\theta)_{i,j} - r_{i-1} (v_\theta)_{i-1,j}}{r_i - r_{i-1}} = \frac{(v_r)_{i,j} - (v_r)_{i,j-1}}{\Delta\theta} \quad (1.71)$$

### 1.3.5.3.3. Wall

From Table Ib

$$(v_\theta)_{1,j} = 0 \quad (1.72)$$

REFERENCES

- [1] John Bartzis and N. Todreas, "Coolant Mixing in LMFBR Rod Bundles and Outlet Mixing Transients," Quarterly Progress Report, Task IID, COO-2245-28.
- [2] B.E. Launder and Ying, "Prediction of Flow and Heat Transfer in Ducts of Square Corss Section," The Institution of Mech. Eng. Proceedings, Vol. 187, 37/93, pp. 455-461, (1972).
- [3] D. Naot, et al., "Numerical Calculations of Reynolds Stresses in a Square Duct with Secondary Flow," Wärme-Stoffubertragung 7 (1975) pp. 151-
- [4] P. Carajilescov and N. Todreas, "Experimental and Analytical Study of Axial Turbulent Flow in an Interior Subchannel of a Bare Rod Bundle," 75-WA/HT-57 (1976).
- [5] M.U. Ibrajirmov et al., "Calculation of Hydraulic Resistivity Coefficients for Turbulent Fluid Flow in Fluid Flow in Channels of Noncircular Cross Section," Soviet Atomic Energy Vol. 23, No. 4, pp. 1042-1047 (1967).
- [6] P. Carajilescov, "Experimental and Analytical Study of Axial Turbulent Flows in an Interior Subchannel of a Bare Rod Bundle," MIT Ph.D. Thesis, 1975.
- [7] Gosman, et al., "Heat and Mass Transfer in Recirculating Flows," Academic Press, London 1969.
- [8] J.G. Bartzis, "Partially Blocked Flow between Parallel Plates," Euratom Internal Report, Ispra 1975.
- [9] A.D. Gosman, "Listing of the TEACH-T Computer Program and Sample Output," The Pennsylvania State University, August 1975.

Table Ia THE DIFFERENTIAL EQUATIONS

General Form:

$$\nabla\phi V + \nabla T\phi = \nabla S\phi + S_{\phi}^*$$

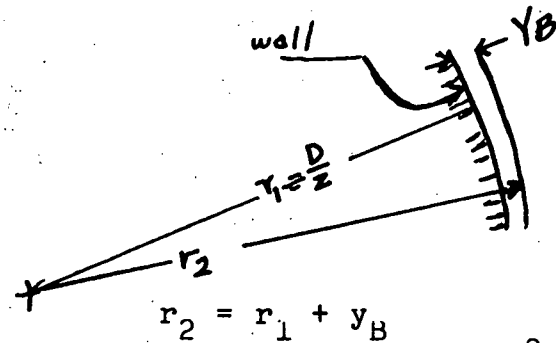
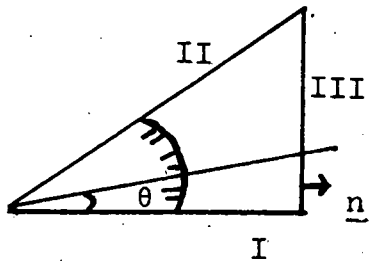
$\phi$	$T\phi$		$S\phi$		$S^*$
	$T\phi r$	$T\phi\theta$	$S\phi r$	$S\phi\theta$	
$v_r$	$-2v \frac{\partial v_r}{\partial r}$	$-\frac{v_{r\theta}^{eff}}{r} \frac{\partial v_r}{\partial \theta}$	$-\frac{v_r^2}{r^2} - p/\rho$	$+v_{r\theta}^{eff} r \frac{\partial}{\partial r} \left( \frac{v_{\theta}}{r} \right)$	$\frac{v_{\theta}^2 + v_r^2}{r} - \frac{2v}{r} \left( \frac{\partial v_{\theta}}{r\partial\theta} + \frac{v_r}{r} \right)$
$r v_{\theta}$	$-v_{r\theta}^{eff} r^2 \frac{\partial}{\partial r} \left( \frac{v_{\theta}}{r} \right)$	$-2v \frac{\partial (r v_{\theta})}{r\partial\theta}$	$+v_{r\theta}^{eff} \frac{\partial v_r}{\partial \theta}$	$+2v_{r\theta} - r v_{\theta}^2 - \frac{r p}{g}$	0
$v_z$	$-v_{rz}^{eff} \frac{\partial v_z}{\partial r}$	$-v_{r\theta}^{eff} \frac{\partial v_z}{r\partial\theta}$	0	0	$-\frac{d(p/\rho)}{dz} = \frac{4\bar{u}^2}{D_H}$
$k$	$-\frac{v_{rz}^{eff}}{\sigma_k} \frac{\partial k}{\partial r}$	$-\frac{v_{r\theta}^{eff}}{\sigma_k} \frac{\partial k}{r\partial\theta}$	0	0	$v_{rz}^T \left( \frac{\partial v_z}{\partial r} \right)^2 + v_{r\theta}^T \left( \frac{\partial v_z}{r\partial\theta} \right)^2 - \epsilon$
$\epsilon$	$-\frac{v_{rz}^{eff}}{\sigma_{\epsilon}} \frac{\partial \epsilon}{\partial r}$	$-\frac{v_{r\theta}^{eff}}{\sigma_{\epsilon}} \frac{\partial \epsilon}{r\partial\theta}$	0	0	$C_1 \frac{\epsilon}{k} \left[ v_{rz}^T \left( \frac{\partial v_z}{\partial r} \right)^2 + v_{r\theta}^T \left( \frac{\partial v_z}{r\partial\theta} \right)^2 \right] - C_2 \frac{\epsilon^2}{k}$

Table Ib. BOUNDARY CONDITIONS

PARAMETER	I	II	III	NEAR WALL REGION	
$v_z$	$\frac{\partial v_z}{r \partial \theta} = 0$	$\frac{\partial v_z}{r \partial \theta} = 0$	$\frac{\partial v_z}{\partial r} = \frac{\partial v_z}{r \partial \theta} \operatorname{tg} \theta$	Logarithmic Profile	
$v_r$	$v_r = 0$	$v_r = 0$	$n \cdot v_{\text{sec}} = 0$	$v_r  _{\text{wall}} = 0$	
$v_\theta$	$v_\theta \neq 0$	$v_\theta = 0$	$\frac{\partial v_{\text{sec}}}{\partial n} = 0$	$v_\theta  _{\text{wall}} = 0$	
$k$	$\frac{\partial k}{r \partial \theta} = 0$	$\frac{\partial k}{r \partial \theta} = 0$	$\frac{\partial k}{\partial r} = \frac{\partial k}{r \partial \theta} \operatorname{tg} \theta$	$k = \frac{v_r v_z}{\sqrt{c_u}}$	
$\epsilon$	$\frac{\partial \epsilon}{r \partial \theta} = 0$	$\frac{\partial \epsilon}{r \partial \theta} = 0$	$\frac{\partial \epsilon}{\partial r} = \frac{\partial \epsilon}{r \partial \theta} \operatorname{tg} \theta$	1-EQ.	2-EQ.
				$\epsilon = c_D \frac{k^{3/2}}{l}$ Algebraic	$\epsilon = \frac{u_*}{ky} (v_r v_z)$

CONSTANTS

- $c_D \approx 0.4$
- $c \approx 0.08$
- $k \approx 0.4$



(\*) 
$$\frac{v_r v_z}{r} = \frac{r_1}{r_2} u_* (\theta)^2 \frac{r_2^2 - r_1^2}{r_2 D_H} \left( \frac{r_1 \omega}{p} \right)_{\text{avg}}$$

$\phi$	$A_e$	$A_w$	$A_i$	$A_s$	$V_p$
$v_z$ $k$ $\epsilon$ $rv_{\theta\theta}$	$\frac{r_i + r_{i+1}}{2} \Delta\theta$	$\frac{r_i + r_{i-1}}{2} \Delta\theta$	$\frac{r_{i+1} - r_{i-1}}{2}$	$\frac{r_{i+1} - r_{i-1}}{2}$	$r_i \Delta\theta \frac{r_{i+1} - r_{i-1}}{2}$
$v_r$	$r_i \Delta\theta$	$r_{i-1} \Delta\theta$	$r_i - r_{i-1}$	$r_i - r_{i-1}$	$\frac{r_i + r_{i-1}}{2} (r_i - r_{i-1}) \Delta\theta$

Table II Control volume (Fig 1) Lengths and surface



TABLE III: THE DIFFUSION COEFFICIENTS

	$\phi = k, \epsilon, v_z$	$v_r$	$v_\theta$
BE	$0.25 \frac{r_{i+1} + r_i}{r_{i+1} - r_i} \Delta\theta$	$\frac{4r_i}{r_{i+1} - r_{i-1}} \Delta\theta$	$\frac{(r_i + r_{i+1})^3}{32r_{i+1}(r_{i+1} - r_i)}$
BW	$0.25 \frac{r_i + r_{i-1}}{r_i - r_{i-1}}$	$\frac{4r_{i-1}}{r_i - r_{i-2}} \Delta\theta$	$\frac{(r_i + r_{i-1})^3}{32r_{i-1}(r_i - r_{i-1})}$
BN BS	$0.25 \frac{r_{i+1} - r_{i-1}}{r_i} \Delta\theta$	$\frac{r_i - r_{i-1}}{2(r_i + r_{i-1})} \Delta\theta$	$\frac{r_{i+1} - r_{i-1}}{\Delta\theta}$
DE	$\frac{BE}{\sigma_\phi} \left[ \left( v_{rz}^{eff} \right)_{i+1,j} + \left( v_{rz}^{eff} \right)_{i,j} \right]$	BE $\cdot v$	BE $\left[ \left( v_{r\theta}^{eff} \right)_{i+1,j} + \left( v_{r\theta}^{eff} \right)_{i+1,j-1} + \left( v_{r\theta}^{eff} \right)_{i,j-1} + \left( v_{r\theta}^{eff} \right)_{i,j} \right]$
DW	$\frac{BW}{\sigma_\phi} \left[ \left( v_{rz}^{eff} \right)_{i+1,j} + \left( v_{rz}^{eff} \right)_{i,j} \right]$	BW $\cdot v$	BW $\left[ \left( v_{r\theta}^{eff} \right)_{i-1,j} + \left( v_{r\theta}^{eff} \right)_{i-1,j-1} + \left( v_{r\theta}^{eff} \right)_{i,j-1} + \left( v_{r\theta}^{eff} \right)_{i,j} \right]$
DN	$\frac{BN}{\sigma_\phi} \left[ \left( v_{\theta z}^{eff} \right)_{i,j+1} + \left( v_{rz}^{eff} \right)_{i,j} \right]$	BN $\left[ \left( v_{r\theta}^{eff} \right)_{i,j+1} + \left( v_{r\theta}^{eff} \right)_{i,j} + \left( v_{r\theta}^{eff} \right)_{i-1,j} + \left( v_{r\theta}^{eff} \right)_{i-1,j+1} \right]$	BN $\cdot v$

TABLE III: THE DIFFUSION COEFFICIENTS (Continued)

	$\phi = k, e, v_z$	$v_r$	$v_\theta$
DS	$\frac{BS}{\sigma} \left[ (v_{\theta z}^{\text{eff}})_{i,j-1} + (v_{\theta z}^{\text{eff}})_{i,j} \right]$	$BS \left[ (v_{r\theta}^{\text{eff}})_{i,j-1} + (v_{r\theta}^{\text{eff}})_{i,j} \right]$ $(v_{r\theta}^{\text{eff}})_{i-1,j} + (v_{r\theta}^{\text{eff}})_{i-1,j-1}$	BS $\cdot v$
$\sigma$	0	0	1

Diffusion Term  $DT = \left[ DE \left( \frac{r_{i+1}}{r_i} \right)^\sigma + DW \left( \frac{r_{i-1}}{r_i} \right)^\sigma + DN + DS \right] \phi_{i,j} - DE \phi_{i+1,j} - DW \phi_{i-1,j} - DN \phi_{i,j+1} - DS \phi_{i,j-1}$

(Concluded)

TABLE IV: THE CONVECTION COEFFICIENTS

Coeff	$\phi = k, \epsilon, v_z$	$\phi = v_r$	$\phi = v_\theta$
$A_1$	$\left[ (r_i + r_{i+1})(r_{i+1} - r_i)(v_r)_{i+1,j} \right. \\ \left. + (r_i + r_{i-1})(r_i - r_{i-1})(v_r)_{i,j} \right] \\ \cdot \frac{\Delta\theta}{8}$	$\left\{ r_i(r_i - r_{i-1}) \left[ (v_r)_{i+1,j} + (v_r)_{i,j} \right] \right. \\ \left. + r_{i-1}(r_i - r_{i-1}) \left[ (v_r)_{i-1,j} + (v_r)_{i,j} \right] \right\} \\ \cdot \frac{\Delta\theta}{4}$	$\left\{ (r_i + r_{i+1})(r_{i+1} - r_i) \left[ (v_r)_{i+1,j} + (v_r)_{i+1,j-1} \right] \right. \\ \left. + (r_i + r_{i-1})(r_i - r_{i-1}) \left[ (v_r)_{i,j} + (v_r)_{i,j-1} \right] \right\} \\ \cdot \frac{\Delta\theta}{16}$
$A_2$	$\frac{(r_{i+1} - r_{i-1})}{8} \left[ (v)_{i,j} + (v)_{i+1} \right]$	$\frac{r_i - r_{i-1}}{8} \left[ (v_\theta)_{i,j+1} + (v_\theta)_{i-1,j+1} \right. \\ \left. + (v_\theta)_{i,j} + (v_\theta)_{i-1,j} \right]$	$r_i \frac{r_{i+1} - r_{i-1}}{16} \left[ (v_\theta)_{i,j+1} + 2(v_\theta)_{i,j} + (v_\theta)_{i,j-1} \right]$
CE	$( A_1  - A_1) / (r_{i+1} - r_i)$	$( A_1  - A_1) / (r_{i+1} - r_{i-1})$	$( A_1  - A_1) \frac{r_{i+1}}{r_{i+1} - r_i}$
CW	$( A_1  + A_1) / (r_i - r_{i-1})$	$( A_1  + A_1) / (r_i - r_{i-1})$	$( A_1  + A_1) \frac{r_{i-1}}{r_{i+1} - r_i}$
CN	$( A_2  - A_2)$	$ A_2  - A_2$	$ A_2  - A_2$
CS	$ A_2  + A_2$	$ A_2  + A_2$	$ A_2  + A_2$
$\sigma$	0	0	1

Convection term  $CT = \left[ CE \left( \frac{r_i}{r_{i+1}} \right)^\sigma + CW \left( \frac{r_i}{r_{i+1}} \right)^\sigma + CN + CS \right] \phi_{i,j} - CE \phi_{i+1,j} - CW \phi_{i-1,j} - CN \phi_{i,j+1} - CS \phi_{i,j-1}$

TABLE V: SOURCE TERMS

$\phi$	SU	SP
$v_z$	$\frac{4V}{DH} \left( \frac{\tau_w}{\rho} \right)_{\text{avg}}$	0
k	$v_p (v_{rz}^T)_{i,j} \left[ \left( \frac{\partial v_z}{\partial r} \right)_{i,j} \right]^2 + (v_{\theta z}^T)_{i,j} \left[ \left( \frac{\partial v_z}{r \partial \theta} \right)_{i,j} \right]^2$	$\frac{C_{\mu} k_{i,j} v_p}{(v_{rz}^T)_{i,j}}$
$\epsilon$	$C_1 C_{\mu} \frac{k_{i,j} v_p}{(v_{rz}^T)_{i,j}} \left\{ (v_{rz}^T)_{i,j} \left[ \left( \frac{\partial v_z}{\partial r} \right)_{i,j} \right]^2 + (v_{\theta z}^T)_{i,j} \left[ \left( \frac{\partial v_z}{r \partial \theta} \right)_{i,j} \right]^2 \right\}$	$\frac{C_2 C_{\mu} k_{i,j} v_p}{(v_{rz}^T)_{i,j}}$
$v_r$	$r_{i-1} \Delta \theta \left[ \overline{(v_r^2)}_{i-1,j} + (p/\rho)_{i-1,j} \right] - r_i \left[ \overline{(v_r^2)}_{i,j} + (p/\rho)_{i,j} \right]$ $+ \frac{(v_{r\theta}^{\text{eff}})_{i,j} + (v_{r\theta}^{\text{eff}})_{i,j+1} + (v_{r\theta}^{\text{eff}})_{i,j-1} + (v_{r\theta}^{\text{eff}})_{i-1,j}}{8}$ $\cdot (r_i + r_{i-1}) \left[ \frac{(v_{\theta})_{i,j+1}}{r_i} - \frac{(v_{\theta})_{i-1,j+1}}{r_{i-1}} \right]$ $- \frac{(v_{r\theta}^{\text{eff}})_{i,j} + (v_{r\theta}^{\text{eff}})_{i,j-1} + (v_{r\theta}^{\text{eff}})_{i-1,j-1} + (v_{r\theta}^{\text{eff}})_{i-1,i}}{8}$ $\cdot (r_i + r_{i-1}) \left[ \frac{(v_{\theta})_{i,j}}{r_i} - \frac{(v_{\theta})_{i-1,j}}{r_{i-1}} \right]$ $+ \frac{2}{r_i + r_{i-1}} v_p \left[ \frac{\overline{(v_{\theta}^2)}_{i,j} + \overline{(v_{\theta}^2)}_{i-1,j}}{2} \right]^2$	0

TABLE V: SOURCE TERMS (Continued)

$\phi$	SU	SP	
$v_\theta$	$\frac{(v_{r\theta}^{\text{eff}})_{i+1,j} + (v_{r\theta}^{\text{eff}})_{i+1,j-1} + (v_{r\theta}^{\text{eff}})_{i,j-1} + (v_{r\theta}^{\text{eff}})_{i,j}}{4} \frac{r_i + r_{i+j}}{2} [(v_r)_{i+1,j} - (v_r)_{i+1,j-1}]$	0	
	$- \frac{(v_{r\theta}^{\text{eff}})_{i-1,j} + (v_{r\theta}^{\text{eff}})_{i-1,j-1} + (v_{r\theta}^{\text{eff}})_{i,j-1} + (v_{r\theta}^{\text{eff}})_{i,j}}{4} \frac{r_i + r_{i-1}}{2} [(v_r)_{i,j} - (v_r)_{i,j-1}]$		
	$+ \frac{r_i (r_{i+1} - r_{i-1})}{2} [(v_\theta^{\prime 2})_{i,j-1} + (p/\rho)_{i,j-1} - (v_\theta^{\prime 2})_{i,j} - (p/\rho)_{i,j}]$		

Source Term  $ST = SU - SP \phi_p$

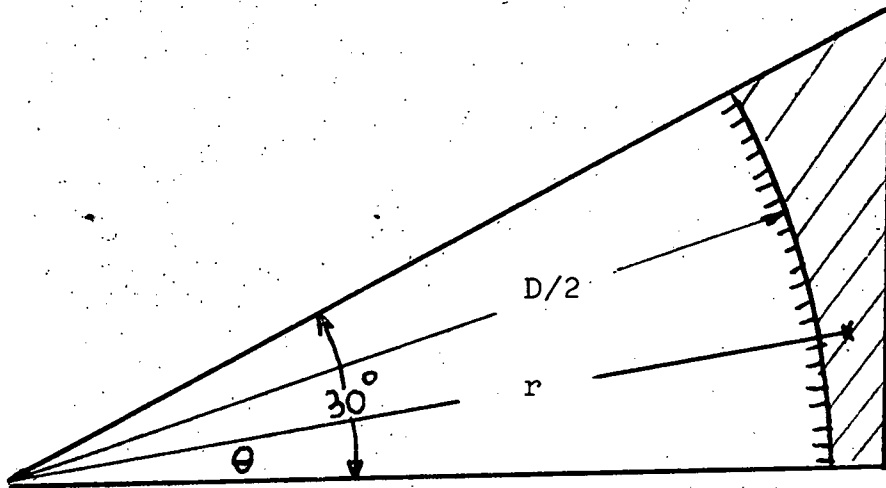


Fig. 1 Characteristic triangle for the study of fully developed flow in an infinite triangular array of bare rods

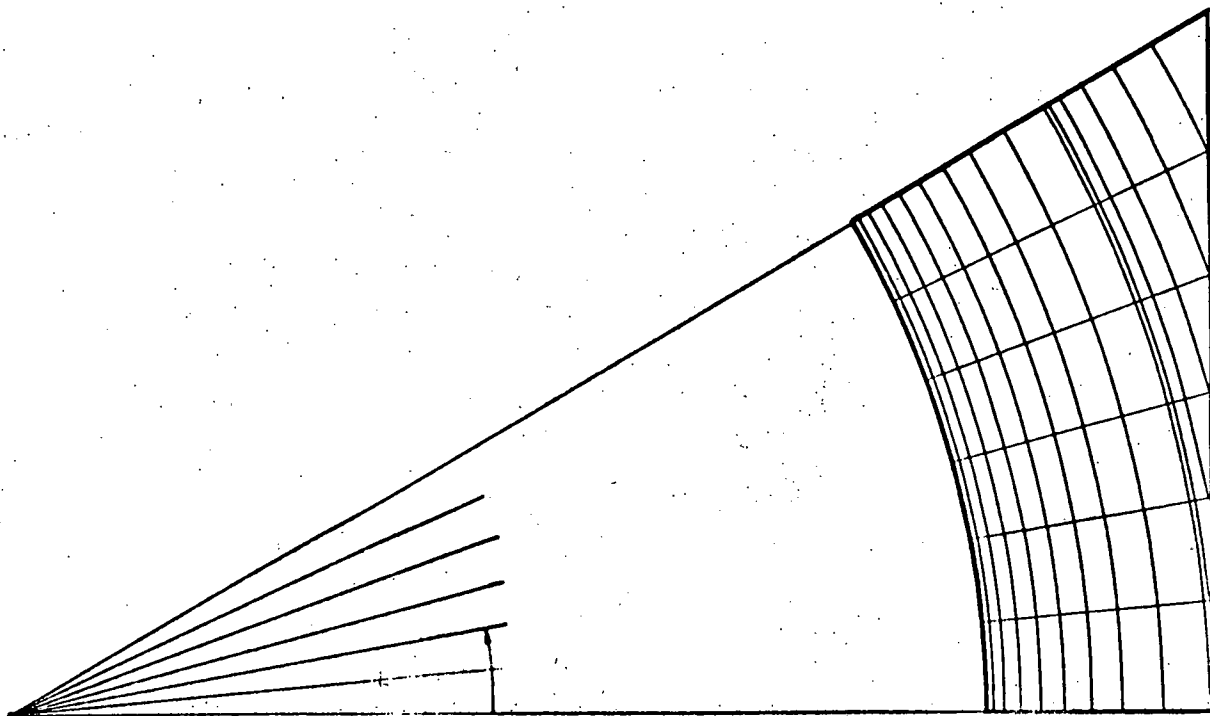


Fig. 2 Grid for Numerical Procedure

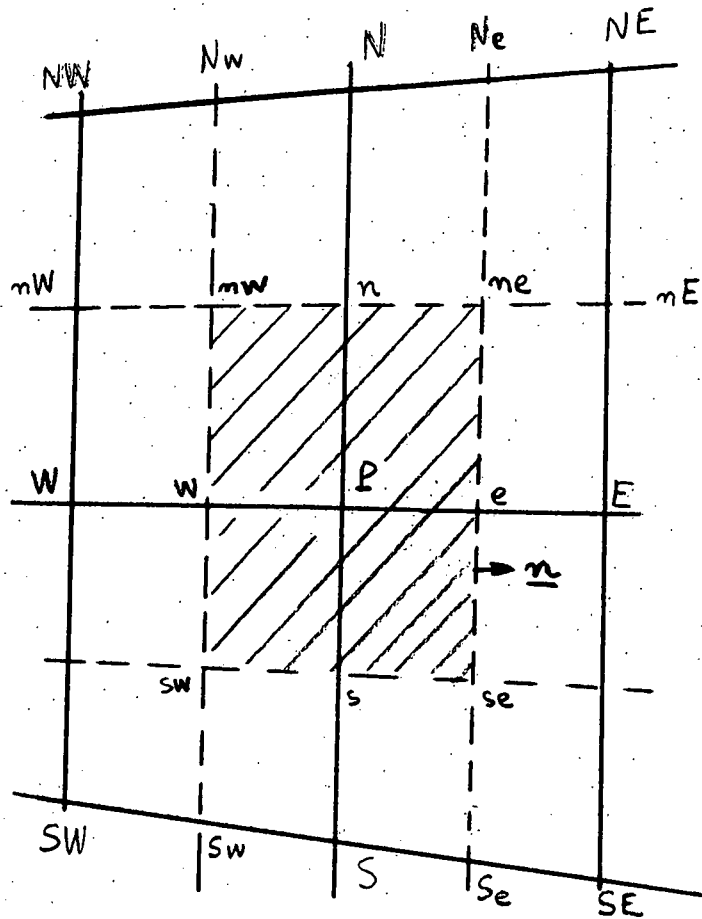


Fig. 3 Control Volume



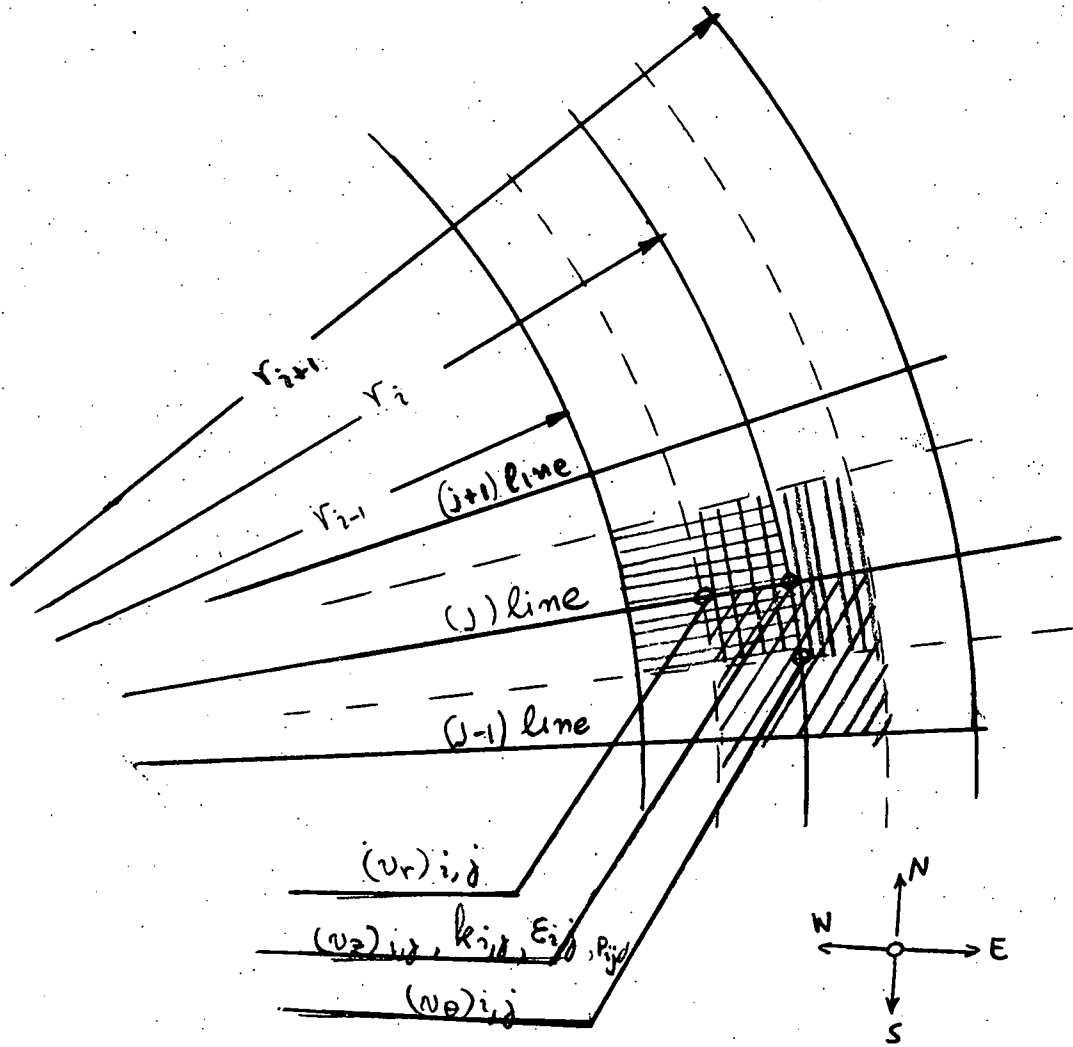
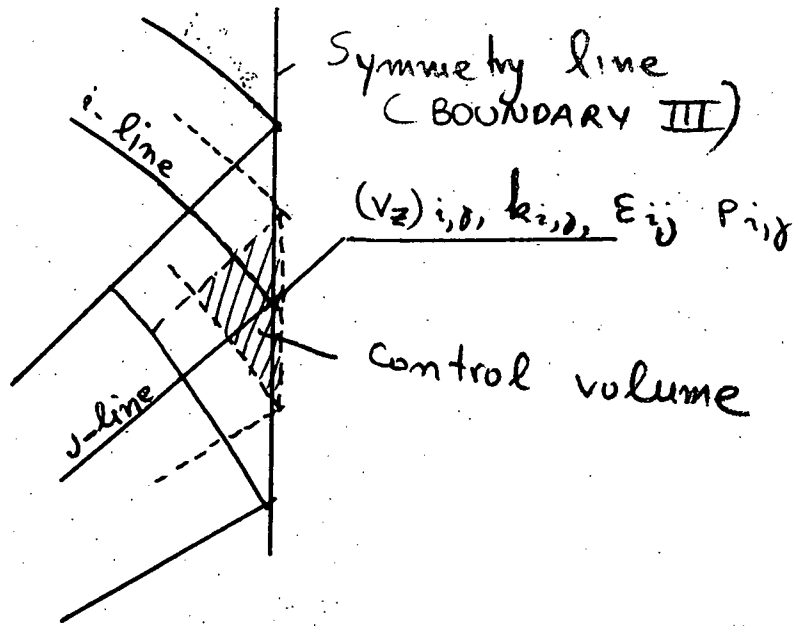
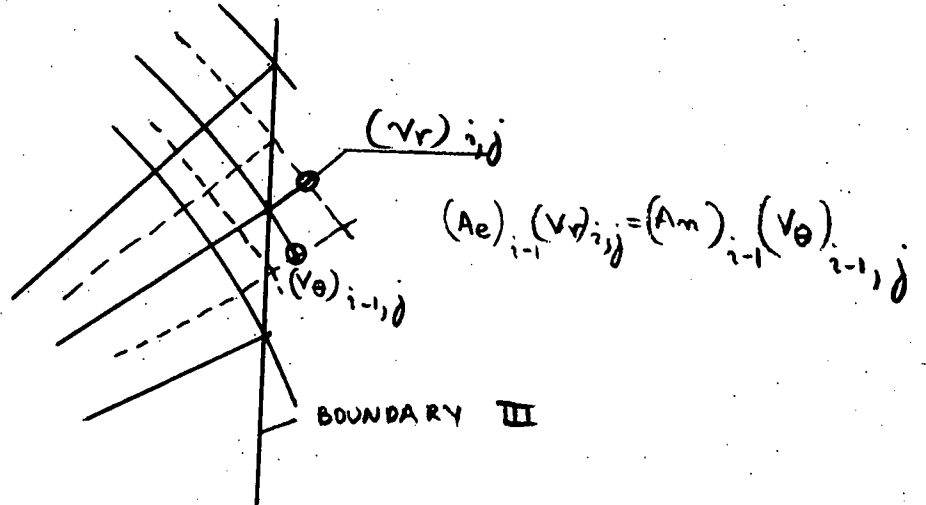


Fig. 4 Relative positions of the control volumes at the points  $P=(i,j)$

(a)



(b)



(c)

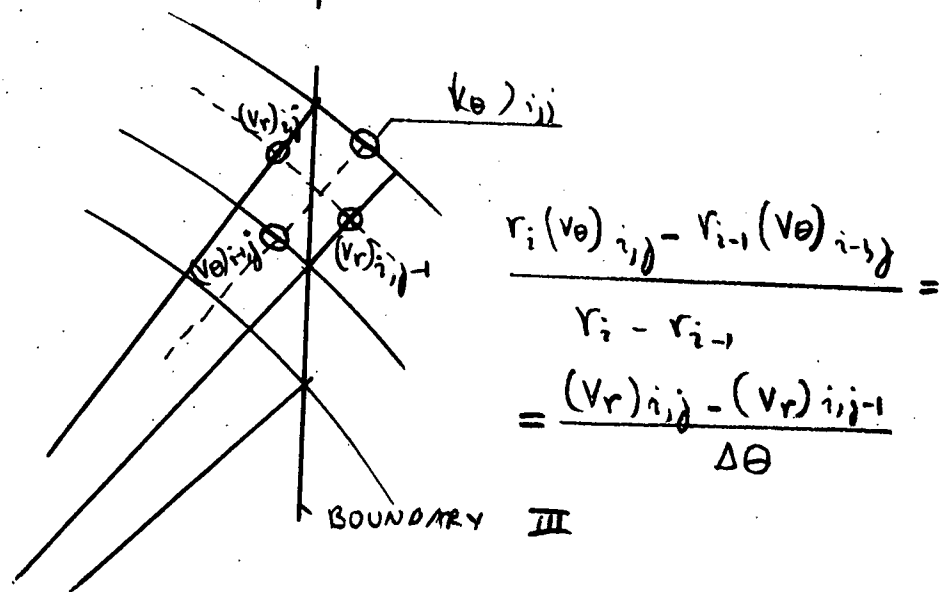


Fig. 5 Boundary Conditions in Boundary III

## TASK III. LMFBR OUTLET PLENUM FLOW MIXING

## III.A. Velocity Field Analysis (Yi Ben Chen)

The planned program of steady state velocity field measurements has been completed. The measurements involve obtaining steady state mean flow velocity and turbulence field mass in small-scale LMFBR outlet plenum flow cells, using water. Candidate turbulence model computer codes are used to predict the experimental results, and their success in doing so is taken as a measure of their respective validities. The results of the measurements and the validating calculations are presented and analyzed in Appendix III.A., in the paper, "Validation of Turbulence Models for LMFBR Outlet Plenum Flows" which will be presented at the 1977 National Heat Transfer Conference, and which has been submitted for publication by the Journal of Fluids Engineering.

III.B. Combined Temperature and Velocity Measurements  
(Vincent P. Manno)

The efforts of the last quarter centered on acquiring all the required components of the integrated measurement system. Currently, the acquisition procedures have been completed and all needed equipment is on hand. Among the major items purchased and received are the following: mirrors, a beamsplitter, LDA (Laser Doppler Anemometer) transmitting optical unit and LDA frequency shifter optical unit. The transmitting optics unit purchased is a model 910 assembly manufactured by Thermo-Systems, Inc. (TSI). The unit is a transducer which splits an incoming light beam (the light source being utilized is a He-Ne laser) into two beams which are focused at a particular point in the flow where the velocity is to be measured. These intersecting beams are the "probes" of the anemometer and the Doppler frequency shift caused by the flow velocity is recorded by a photodetector which is a photomultiplier tube in this case. The unit has the versatility of three different intersection focal lengths (120mm, 250mm, and 600mm) which allows greater ease in alignment procedures.

The frequency shifter purchased adds a significant feature to the velocity measurement system. Inherent in the LDA system is a directional ambiguity in the output signal of the apparatus. This is caused by the fact that flows perpendicular to the beam intersection yet moving in opposite directions will produce the same output signal. In other words, if the system is aligned to measure the vertical velocity component, it will produce the same signal whether the flow direction is up or down. The frequency shifter (TSI model 980) shifts the frequency of one of the LDA measurement beams by a specified frequency as to alleviate the directional ambiguity. Its mode of operation consists of an acousto-optic cell (Bragg cell) with an RF driver

and associated frequency downmixing electronics. The cell is mounted in front of the transmitting optics before the focusing lense which directs the beam intersection. Associated with the model 980 optical unit is the model 985 control and power unit which is already part of the equipment inventory of this task and is shared among the various sub-tasks using LDA systems. Other shared LDA equipment used in this experiment include the photomultiplier tube and power source, frequency tracker, and control unit all of which when combined with the laser source and transmitting optics comprise the complete LDA system.

At present the complete temperature measurement system is in place and operable including the photodiode. The flow circuit is also complete and operable. The experimental area's electrical system has been upgraded to provide proper power for the various electronic components and laser. The LDA transmitting system has been assembled and positioned on the optical bench. The next quarter's work will consist of installing the LDA detection and control units and aligning the system. The system alignment is a crucial step in the experiment since the velocity and temperature measurements must be made at the same point in the flow. The alignment procedure while being straightforward is time consuming and has just begun.

As was specified in the previous progress report, the development of a proper flow seeding scheme is being investigated. The flow seed is a suspended particle in the flow which provides light scattering centers which produce the Doppler frequency shift characteristic of a particular velocity. The desired qualities of the seed are the ability to follow the flow truly and the ability to significantly scatter light. The natural contamination of air is sometimes sufficient for production of good LDA data but whether that is the case in this experiment has not been ascertained. The reason for the uncertainty is that the criteria are empirical in nature; that is, one must perform some initial LDA measurements and examine the results in order to evaluate the performance of the particular seed. Since the LDA system is still not operable and the possibility of a seeding system exists, some preliminary investigations have been undertaken. The first tested was ordinary tobacco smoke injected at the air blower intake but this scheme was immediately seen to be inadequate for many reasons. First of all, the large volume flow rate (@ 30 cubic feet per minute) necessitated the presence of great amounts of smoke which seemed beyond the capacity of typical sources and secondly, the system would have called for a ventilation system-which was not available. The second seed tested was powder (actually commercial baby powder) which also had unwelcomed qualities. The most negative aspect of this particular seed was the fact that it adhered to the test section walls rendering them occluded, which interfered greatly with the optical measurement system. Also, the power was injected into the system at the air blower intake where the only natural suction of the flow circuit exists. As can be ascertained from

the flow circuit description presented in the previous progress report, the flow exits the blower and after being divided into two flow legs (one to be heated and the other to remain ambient) is directed into a heater. Therefore this seeding scheme had the unfortunate quality of depositing powder on the heater filaments and it was feared this contamination would degrade the heater's continued operation. Therefore, the powder seed concept was abandoned.

The final seeding scheme tested used plastic micro-balloons which are basically hollow plastic spheres with diameters on the order of ten microns. These spheres (product name is Phenolic Microballons) have the attractive quality of very little adherence to the test cell walls. Also, their chemical composition would be less detrimental to the heater's operation. The only negative feature is that they burst at elevated temperatures (@400F). This characteristic could cause substantial attrition in seed density in the flow leg that passes through the heater. Two possible solutions are being investigated. One possible answer would be to create a suction in the circuit after the heater by using a "Venturi" or reduced flow area section and the other avenue of investigation will be to actually measure the attrition rate through the heater in order to determine whether the depletion can be compensated for by overseeding the flow. Finally, concurrent with these tests an air filtering system was installed and successfully tested which consists of directing the two exiting jets from the test section into a crude air filter which utilizes a standard ventilation system filter. The goal of the next quarter in regard to the seeding problem is to establish whether a seeding system is actually needed and to install a workable one if called for.

Therefore, the experimental efforts of the next quarter will be directed toward aligning and testing the complete measurement system. After testing the system the actual measurements will be made using the 1/15 scale FFTF outlet plenum test section described in the previous progress report. The output of the measurement system is the product of the DC analog voltages of the temperature and velocity systems. Represented mathematically, the output arise as:

$$\text{output} = \int_0^{\tau} (\bar{u} + u') (\bar{T} + T') d\tau \quad (1)$$

where  $\bar{U}$  = mean velocity,  $U'$  = velocity, fluctuation about the mean  
 $\bar{T}$  = mean temperature,  $T'$  = temperature fluctuations about the mean, and  
 $\tau$  = resolution time of system

The integral can be evaluated with the result

$$\int_0^T (\bar{u} + u') (\bar{T} + T') d\tau = \langle \bar{u} \bar{T} \rangle + \langle u' \bar{T} \rangle + \langle \bar{u} T' \rangle + \langle u' T' \rangle = (\bar{u} \cdot \bar{T}) + \langle u' T' \rangle \quad (2)$$

since the second and third terms both equal to zero-by definition- and the first term is merely the product of the two time averaged values of T and U. Now we note that the eddy diffusivity of heat is defined in the following manner:

$$\epsilon_H \equiv \frac{\langle u' T' \rangle + \langle u' T' \rangle}{\left( \frac{\partial \bar{T}}{\partial y} + \frac{\partial \bar{T}}{\partial x} \right)} \quad (3)$$

Therefore the quantity  $\langle u' T' \rangle$  which is the desired value can be easily computed from the system's output signal by subtracting the product of the time averaged temperature and velocity DC analog voltages from it. Mathematically, that is (using Eqs (1) and (2)) the result is obtained

$$\langle u' T' \rangle = \int_0^T (\bar{u} + u') (\bar{T} + T') d\tau - (\bar{u} \cdot \bar{T}) \quad (4)$$

Hence, the final measurement scheme must include evaluating the time averaged values of the temperature and velocity outputs using their respective measurement systems. These measurements will commence once the system is completely assembled and tested.

APPENDIX III.A

VALIDATION OF TURBULENCE MODELS FOR  
LMFBR OUTLET PLENUM FLOWS

by

Michael W. Golay

and

Yi Ben Chen

of

Massachusetts Institute of Technology  
Department of Nuclear Engineering  
Cambridge, Massachusetts 02139

Submitted to the

Heat Transfer During Reactor Transients Session of the  
National Heat Transfer Conference ASME and AICHE  
Salt Lake City, Utah

ABSTRACT

Small scale experiments involving water flows are used to provide mean flow and turbulence field data for LMFBR outlet plenum flows. Measurements are performed at Reynolds number (Re) values of 33000 and 70000 in a 1/15 - scale FFTF geometry and at Re = 35000 in a 3/80-scale CRBR geometry. The experimental behavior is predicted using two different two-equation turbulence model computer programs, TEACH-T and VARR-II. It is found that the qualitative nature of the flow field within the plenum depends strongly upon the distribution of the mean inlet flow field, importantly also upon the degree of inlet turbulence, and also upon the turbulent momentum exchange model used in the calculations. It is found in the FFTF geometry that the TEACH-T predictions agree well with the experiments, while the agreement of the VARR-II prediction is poorer, and in the CRBR geometry neither code provides a good prediction of the observed behavior.



In the Liquid Metal-cooled Fast Breeder Reactor (LMFBR), sodium is used as coolant to remove heat from the reactor core. Since sodium is a good heat transfer medium and has low heat capacity, the temperature difference between inlet and outlet of the core is much higher than that of the current design light water reactor (LWR). A typical value for this temperature rise is approximately 300 °F. During a reactor scram with (or without) flow coastdown, the cold sodium will issue from the reactor core, and will mix with hot sodium which had previously filled the reactor outlet plenum. Predicting the transient thermal response of the sodium in the outlet plenum is an important problem, since this thermal regime will dictate the thermal fatigue environment for the outlet nozzles, instrument trees, and other mechanical components which will be exposed to the reactor coolant flow. Two-equation turbulence model calculations are being used to predict the thermal histories which such components will experience. Thus, it is necessary, in order to insure the adequacy of the design of these components, that the design numerical simulations be both accurate and economical. Experimental verification of the accuracy of the resulting predictions is an essential component of that insurance.

The detailed analytical treatment of the coolant mixing in the outlet plenum is very difficult due to the complex nature of the resulting turbulent flow. The Navier-Stokes equation cannot be solved numerically because of small scale of turbulence, and due to the limited storage capacity and speed of existing computers.

Therefore, most of the problems in the turbulent flow are solved by using the time-averaged Navier-Stokes equations (or Reynolds equation). Due to the nonlinearity of the Navier-Stokes equations, one additional term, known as Reynolds stress, appears in the Reynolds equation. Much of the attention has been concentrated on how to model this parameter in terms of known quantities.

This is the so-called turbulence model approach. In general the LMFBR outlet plenum will display a recirculating flow pattern. The simplest model (e.g., Prandtl's mixing length theory) has been found to be inadequate in providing accurate predictions of this behavior.<sup>(1)</sup> Therefore, current design work has adopted the use of the two-equation turbulence model. This decision is based on the need for accuracy and for reasonably short computation times.

In our work two computer codes, namely TEACH-T<sup>(2)</sup> and VARR-II<sup>(3)</sup> are used. TEACH-T is a steady-state two-dimensional code which adopts turbulent kinetic energy and turbulent energy dissipation as two additional dependent variables. VARR-II is a time-dependent two-dimensional thermal hydraulic code. Different from TEACH-T, it solves turbulent kinetic energy and turbulent viscosity conservation equations in differential form. In addition, a heat conservation equation is also incorporated into the code for temperature prediction, and in order to provide buoyant force feedback to the vertical momentum equation. (See Appendix A for a more complete discussion of the two codes). The code TEACH-T has been modified to calculate flows in the reactor plenum geometry, and has been used to generate a prediction of the flows which would be observed in the validation experiments of this work. The code VARR-II is currently in use as a design tool in

the U.S. LMFBR demonstration reactor (Clinch River) program. Its predictions have not been verified experimentally in the flow geometry of interest. It is also being used in this work to predict the flow in the experimental test cell. Thus, by intercomparison of the results from these two competing turbulence model codes and the observed experimental data, one may identify sources of error in the predictions and make appropriate improvements in the turbulence models for the outlet plenum application.

In the experiments, small-scale Cartesian geometry test models of a diametrical section of the prototypic outlet plenum geometries are used. The experiments consist of measurements of appropriate turbulence model parameters in steady-state water flows. These data are then compared to predictions of the behavior of the experiment by each of the two-equation turbulence model codes.

A variable geometry outlet plenum test cell which stimulates two reactor cases, namely those of the Fast Flux Test Facility (FFTF) and the Clinch River Breeder Reactor Project (CRBRP), has been fabricated, and is shown in Fig. 1. Measurements of velocity, turbulent kinetic energy, and Reynolds stresses in the two perpendicular directions are obtained simultaneously by use of a DISA Mark-II two-channel Laser Doppler Anemometer<sup>(4)</sup> operating in the reference beam mode as shown in Fig. 2. Both velocity component signals have 40 MHz preshift devices and frequency down mixing to remove the ambiguity regarding the flow direction in low speed measurements. A 2-watt Spectra Physics Argon Laser is the light source.

The results obtained have shown significant discrepancies in the

agreements between the measurements and the code predictions in a spectrum of cases. The experimental errors are typically 20 percent for the Reynolds stress, 5 percent for the turbulence kinetic energy, and 2 percent for the mean velocity data. In all of the TEACH-T calculations the mean velocity field and the turbulence kinetic energy field at the plenum inlet are set equal to the values measured in the case of interest. In all of the VARR-II calculations the inlet mean velocity distributions are set equal to the measured values; however, the turbulence kinetic energy and Reynolds stress values are calculated internally in the program. In two cases (Figs. 11 and 22) a VARR-II data option is used which permits matching the turbulence kinetic energy at a single mesh point to the measured value.

The measured and predicted velocity field data for the cases investigated are shown in Figs. 3 through 18 for the 1/15 scale FFTF geometry and in Figs. 19 through 26 in the 3/90-scale CRBR geometry. In each of the Figures the data are normalized in terms of the maximum velocity value in the field. The range of cases examined is summarized in Table 1. It is seen consistently in examining the data that both the measured and predicted flow fields depend strongly upon both the inlet flow conditions (velocity distribution and turbulence level) and the turbulent momentum exchange in the flow. The results obtained are discussed in order of ascending Figure number.

The first set of data applies to the FFTF geometry at a Reynolds number ( $Re$ ) value of 33000 (defined with respect to the inlet duct width). As with the data obtained in other geometries

and at higher  $Re$  values it is seen that both codes predict velocity fields with inlet jets which persist spatially with greater momentum than are observed experimentally. Similarly the predicted vortex centers are significantly displaced from the observed vortex location and the predicted mean velocity values near the cell boundaries are significantly greater than those observed experimentally, while the opposite comparison is observed in the low flow speed region near the vortex center. The agreement with the experiment of the TEACH-T prediction is generally superior to that of the VARR-II prediction. This is because the former calculations are performed by matching the inlet velocity and turbulence kinetic energy values to those observed experimentally as is done in all of the TEACH-T calculations. It is seen in Fig. 6 and 7 that the turbulence parameter fields predicted by TEACH-T agree reasonably well at most positions with those observed experimentally (i. e., within the same order of magnitude), and those predicted by VARR-II are generally lower than the measured values by as much as an order of magnitude, typically. It is seen that the Reynolds stress agreement is poorer for both codes than is that for the turbulence kinetic energy, since in neither calculation are the inlet Reynolds stress values matched to the experimental values. The generally better agreement of the TEACH-T prediction reflects the value of specifying accurately the inlet velocity, and turbulence kinetic energy. Although it has not been tested it is expected that further improved agreement would be obtained by matching also the inlet Reynolds stress values in the calculations to those observed

experimentally.

In Figs. 8 through 13 data for the FFTF geometry at  $Re=70,000$  are shown. It is seen that the velocity field comparison between TEACH-T and the experiment is excellent throughout the flow field, reflecting the value of matching inlet flow and turbulence conditions, and reflecting the expected improvement in turbulence model predictions at higher  $Re$  values. As in the case at  $Re = 33,000$  the VARR-II calculation (Fig. 10) tends to predict too - little turbulent momentum exchange, with the resulting values of inlet jet and near-wall flow rates being higher than those observed experimentally by approximately 20 percent, and with the overall vortex shape being distorted from that observed experimentally. In Fig. 11 a calculation is presented which is identical to that in Fig. 10 except that the VARR-II data option of matching the turbulent kinetic energy at one inlet point is exercised. It is seen that the mean flow fields predicted in the two cases are virtually identical, and that the predicted turbulence fields (see Figs. 12 and 13) are affected by this turbulence data matching only in the inlet flow region. Thus, a more complete prescription of the inlet turbulence state is seen to be required in order to provide accurate turbulent momentum exchange predictions throughout the entire flow field. Even with the limited inlet flow turbulence kinetic energy matching it is seen throughout most of the flow field that the VARR-II predicted Reynolds stress and turbulence kinetic energy are lower than the experimental values by approximately an order of magnitude.

The qualitative dependence of the observed and predicted flow fields upon the inlet mean velocity distribution is shown in a startling fashion in Figs. 14 through 18. In this case in the FFTF geometry the inlet mass flow rate is maintained for  $Re = 70,000$ ; however, a partial inlet flow blockage is used to provide a velocity distribution which has a maximum near the outside edge of the inlet duct (See Fig. 14). This results in a mean flow map which is qualitatively different from that observed in the previous cases. The main flow is observed to pass through the lower portion of the plenum, with an upper region being occupied by a counter-rotating secondary flow. This is due to the high rate of mean flow shear above the inlet orifice with rapid entrainment of fluid in the plenum, accompanied by strong degradation of the inlet jet momentum. It is notable that both of the codes are able to predict the qualitative features of this flow, although neither code is successful in describing the experimentally observed flow field in detail, particularly in regard to the location and rate of circulation of the secondary flow vortex.

As with the previous cases the TEACH-T prediction of the turbulence parameters is much more successful than that of VARR-II, reflecting the more accurate inlet turbulence specification in the former case. The importance of this case lies in demonstrating that the qualitative nature of the mean flow field is strongly dependent upon the inlet mean velocity field. The implications for design calculations of the need for an accurate knowledge of these inlet conditions is clearly evident.

Data similar to those obtained in the 1/15-scale FFTF test cell have also been obtained for steady state water flows in a 3/30-scale Clinch River Breeder Reactor (CRBR) outlet plenum geometry (see Fig. 19). In this geometry the inlet orifice (i.e., the region above the reactor core) is much wider, and penetrates to a much greater height into the plenum, so that relative to the inlet orifice width the outlet plenum is much shorter and narrower than in the FFTF case. A mass flowrate equal to that at a Re value of 70,000 in the FFTF geometry results in a Re value of 35,000 in the CRBR geometry.

The CRBR data with the "normal" inlet mean flow distribution are shown in Figs. 19 through 23. Effectively in this geometry the inlet jet impacts against the upper plenum boundary in a much shorter distance than in the FFTF case and then rebounds to the outlet duct due to high upper plenum stagnation pressures, while in the FFTF geometry the mean flow is able to follow streamlines from the entrance to the exit in a fashion as would be encountered in a laminar flow.

This greater mean flow chaos is seen in the comparison of the measured mean flow field (Fig. 19) to the TEACH-T (Fig. 20) and VARR-II (Figs. 21 and 22) predictions. It is seen in the lower half of the plenum that the measurements and code predictions agree reasonably well, with the TEACH-T prediction agreeing excellently and with the VARR-II prediction being approximately 20% too high in the high velocity regions. In the upper half of the plenum it is seen that neither of the codes is able to predict the flow field qualitatively. As in previous cases the



VAPR-II prediction is insensitive to the matching of the turbulence kinetic energy to the experiment at a single inlet point, and the predicted turbulence kinetic energy field is typically too low by approximately an order of magnitude throughout most of the flow field (see Fig. 22).

In Figs. 24 through 26 CRBR flow data for  $Re = 35,000$  are shown for the case with a partial inlet flow blockage, resulting in a distorted inlet mean flow distribution (see Fig. 24). The striking feature is that neither code is able to predict the qualitative features of the mean flow anywhere except in the neighborhood of the inlet and outlet ducts. In a situation such as this one the highly chaotic mean flow distribution (with little net mass flow) in the upper plenum region is translated by the codes into a stagnant, or alternatively into a recirculating flow region. Thus, the net flow into and out of the plenum is predicted correctly, but the flow pattern within the plenum is described very inaccurately.

### Conclusions

From the FFTF cases having normal inlet flow conditions it is seen that excellent agreement is obtained between the TEACH-T predictions and the measurements. The inferior quality of the VARR-II predictions is attributable to the inability to match the inlet turbulence conditions to those in the experiment, as well as to possible errors in the turbulence model. The more important conclusions arise from the inability of either program to predict the qualitative flow behavior in either geometry when the distorted inlet conditions prevail. This indicates that the turbulence model used to describe turbulent momentum transfer within the flow may be less important than an accurate knowledge of the detailed inlet mean flow and turbulence field. It also implies that codes such as those used in this study should be used with great caution in which abrupt changes in shape situations arise (i.e., CRBR flows) or in which strong mean flow gradients are imposed. Within these limitations codes of the type used in this work can provide predictions which are useful for design purposes, although further work is required to determine the degree of accuracy of turbulent momentum exchange within a simple geometry well-specified flow.

Acknowledgement

This work was performed with financial support from  
the U. S. Energy Research and Development Administration.

References

1. Rodi, W., and Spalding, D.B., "A Two-Parameter Model of Turbulence and its Application to Free Jets," *Warme-und Stoffübertragung*, Vol. 3, 1970, pp. 85-95.
2. Notes on "Turbulent Recirculating Flow-prediction and Measurement," College of Engineering, The Pennsylvania State University. July 28-August 1, 1975.
3. Cook, J. L., P.I. Nakayama, "VARR-II. A Computer Program for Calculating Time Dependent Turbulent Fluid Flows with Slight Density Variation," WARD-D-0106. July 1975.
4. The DISA Mark II Laser Doppler Anemometer, DISA Electronics, Franklin Lakes, N. J., 1974.
5. Harlow, F. H. and Welch, J.E., "Numerical Calculation of Time-Dependent Viscous Incompressible Flow," *Phys. Fluids*, Vol. 8, 1965, pp. 182.
6. Welch, J.E., Harlow, F.H., Shannon, J. P., and Daly, B.J., "The MAC Method. A Computing Technique for Solving Viscous, Incompressible, Transient Fluid Flow Problems Involving Free Surfaces, LA - 3425, 1966, Los Alamos Scientific Laboratory.

TABLE 1

Figure Number

Geometry	Reynolds Number	Inlet Velocity Distribution	Measurement	TEACH-T Prediction	VARR-II Prediction No Turbulence Match	VARR-II Prediction With Turbulence Match	Reynolds Stress Comparison	Turbulence Kinetic Energy Comparison
FFTF	33,000	Normal	3	4	5	---	6	7
FFTF	70,000	Normal	8	9	10	11	12	13
FFTF	70,000	Distorted	14	15	16	---	17	18
CRBR	35,000	Normal	19	20	21	22	---	23
CRBR	35,000	Distorted	24	25	26	---	---	---

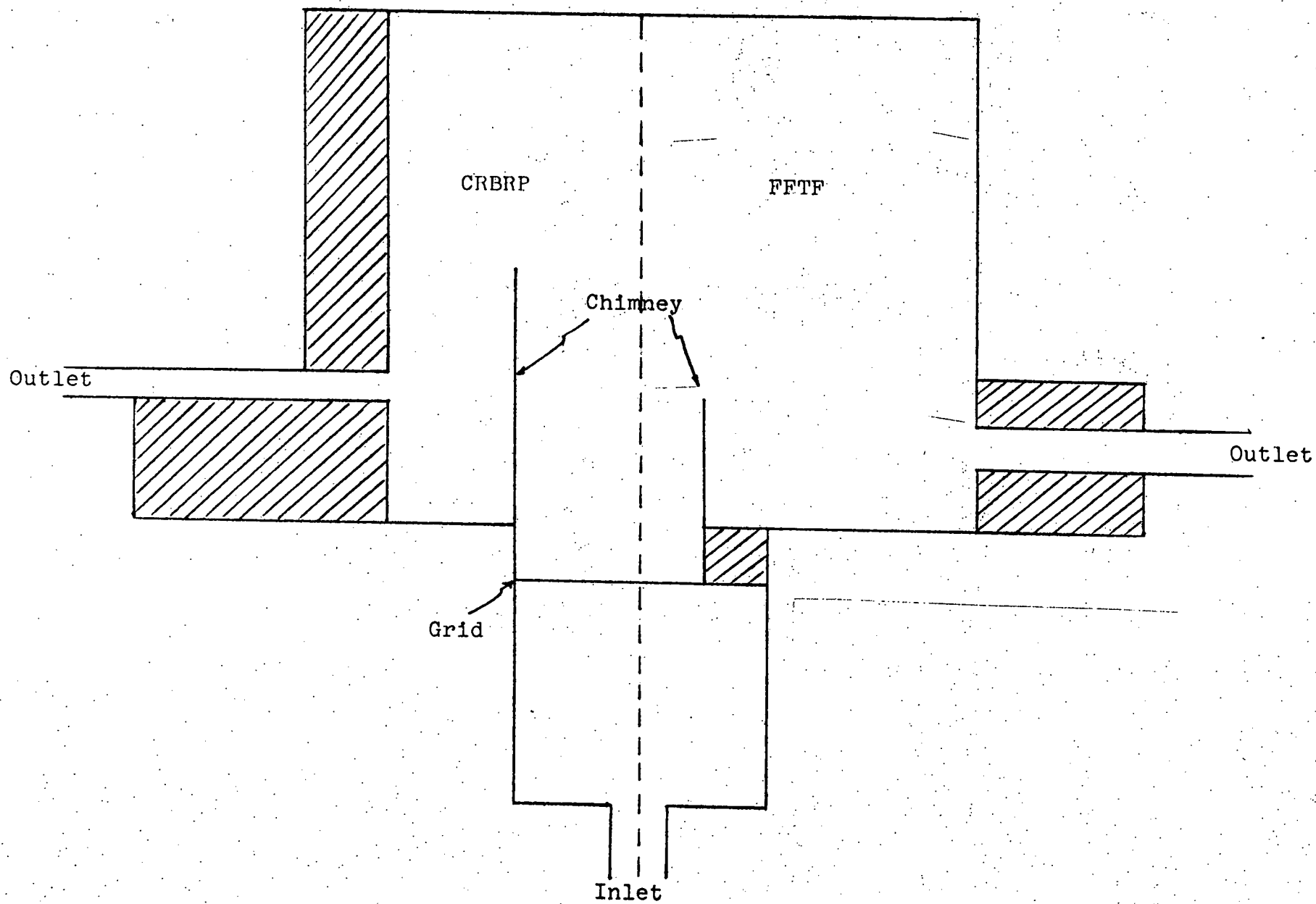


Fig. 1. Variable Geometry Outlet Plenum Test Cell

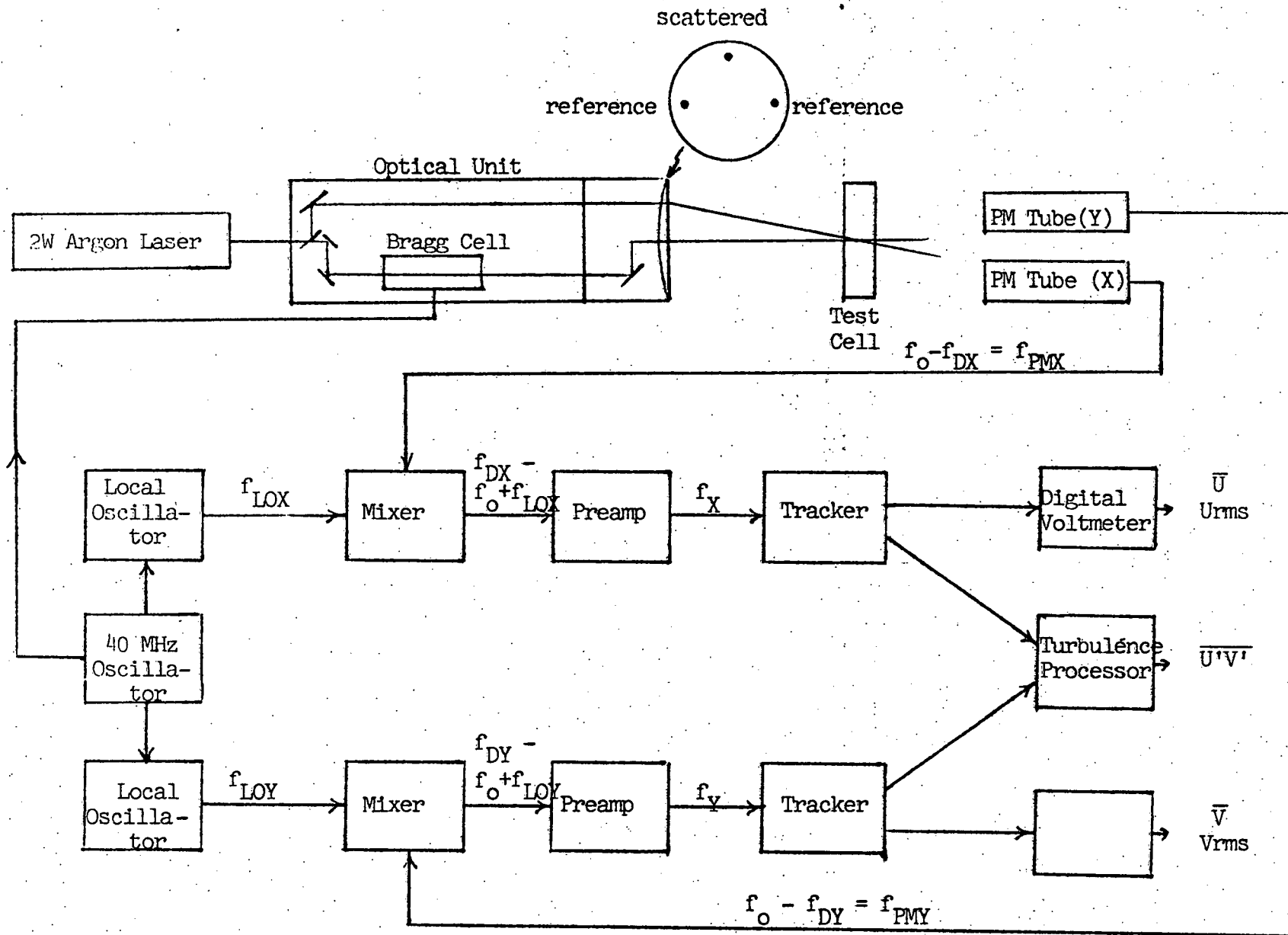


Fig.2. Layout of Instrument and Optical Unit

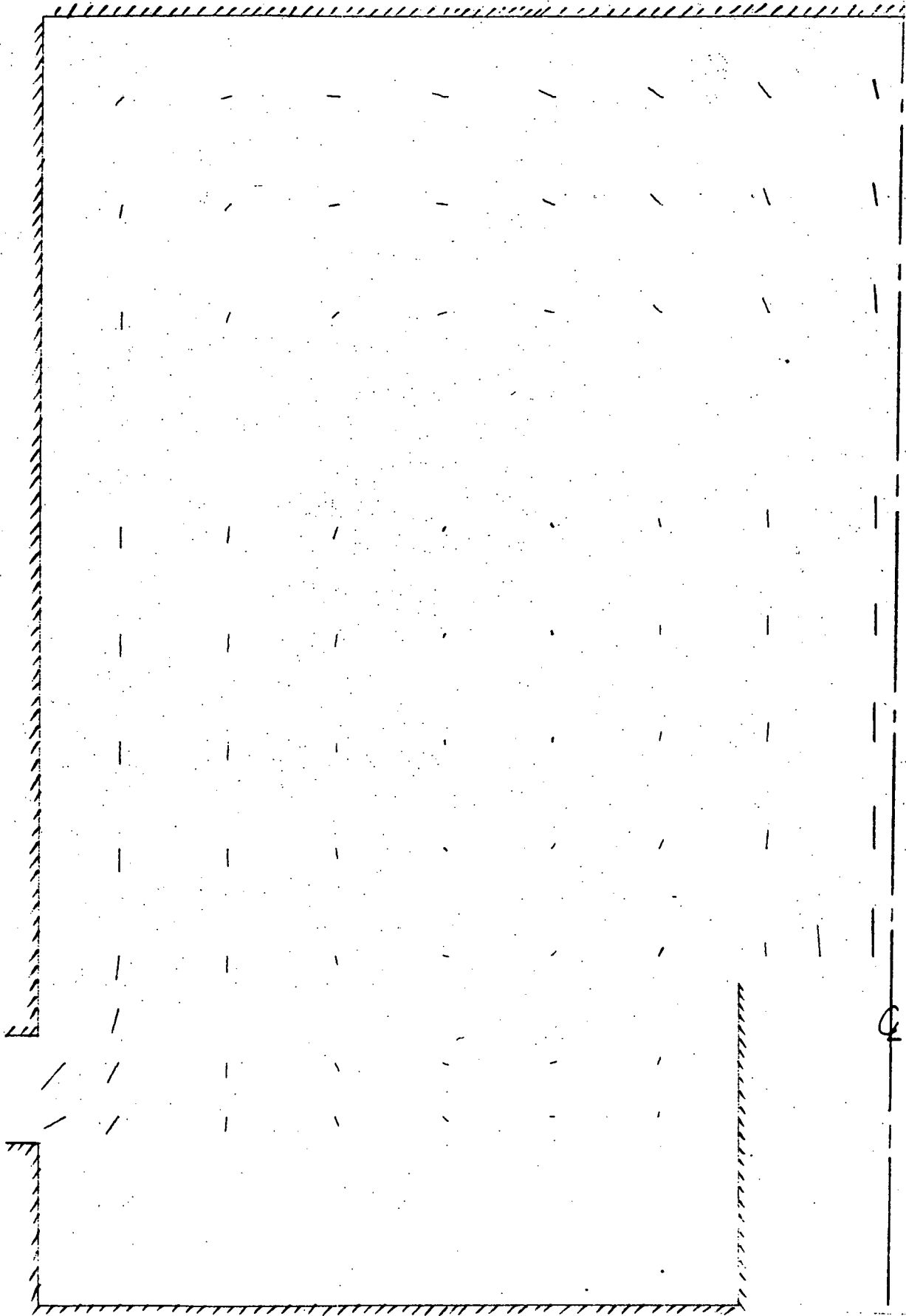


Fig. 3 Measured Mean Flow Field, FFTF Geometry,  $Re = 33000$



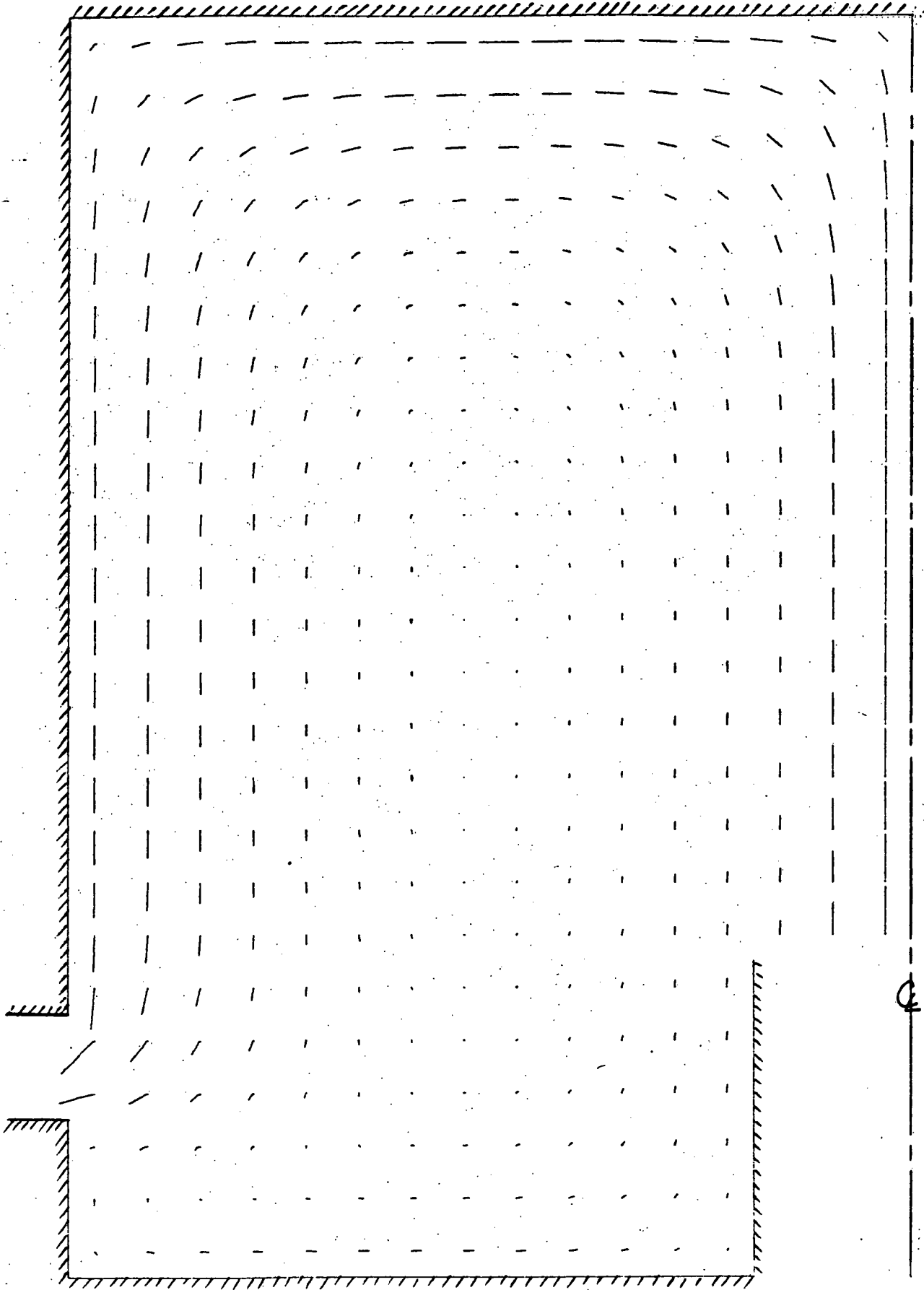


Fig. 4 TEACH-T Prediction, FFTF Geometry,  $Re = 33000$

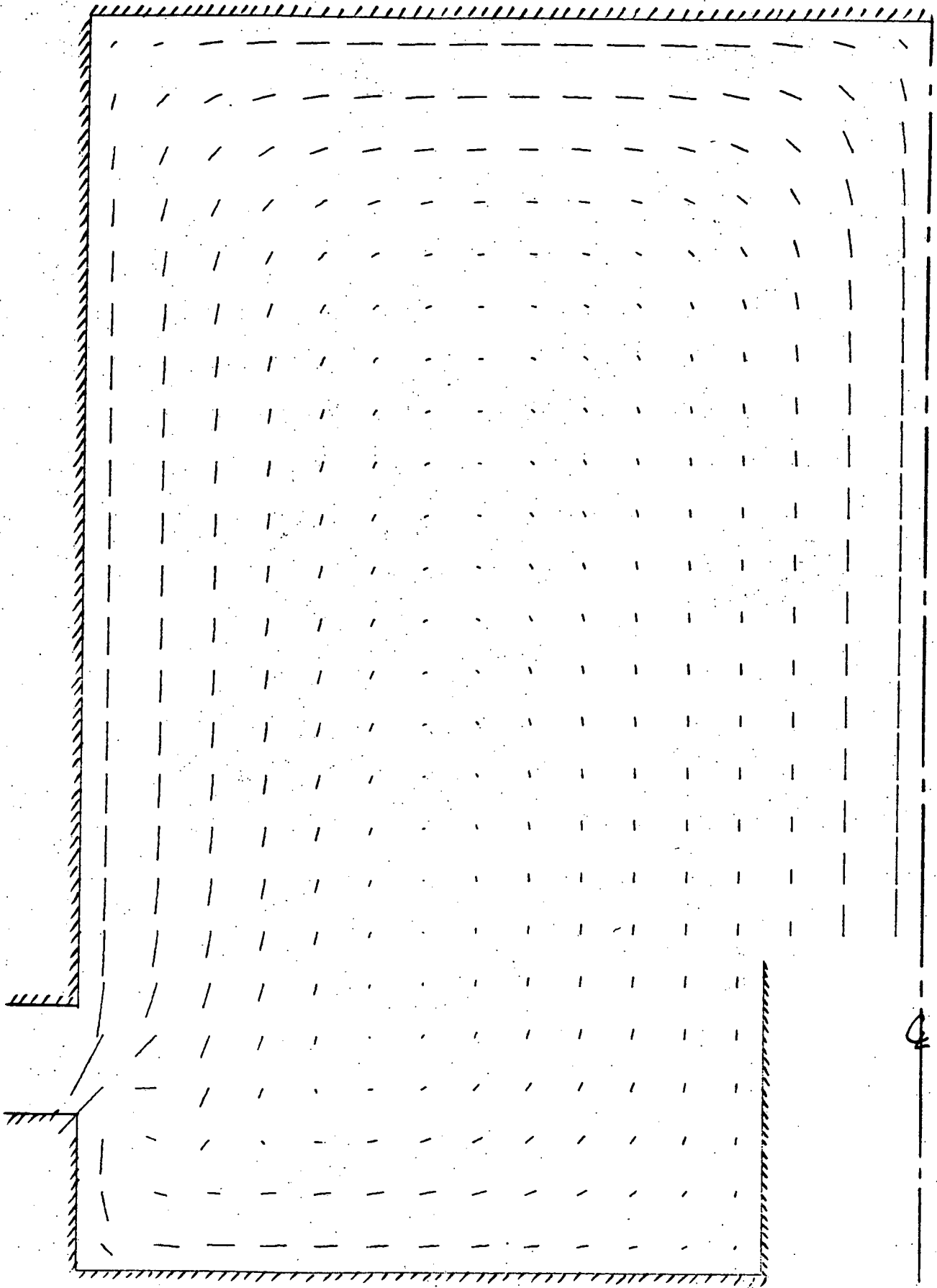


Fig. 5 VARR-II Prediction, FFTF Geometry,  $Re = 33000$

Fig. 6 Compared Calculated and Measured Turbulence Kinetic Energy Fields, FPIR Geometry, Re = 33000

	.096 [.089 .75 .081]	.093 [.088 .086 .044]	.028 .0051 .037	.029 .0075 .046	.034 .0085 .033	.038 .0085 .028	.035 .0097 .033	.018 .0040 .047	.011 .0035 .045	.0047 .0065 .048
	.027 .056 .051	.020 .027 .042	.017 .0061 .035	.019 .0053 .044	.024 .0080 .045	.030 .0047 .044	.035 .0052 .036	.026 .0027 .047	.018 .0026 .049	.0096 .0050 .043
	.015 .030 .049	.010 .018 .049	.0096 .0094 .046	.012 .0077 .043	.018 .0063 .050	.026 .0046 .047	.033 .0052 .055	.028 .0026 .055	.021 .0024 .055	.013 .0040 .044
	.013 .023 .043	.0091 .017 .046	.0080 .012 .046	.0084 .011 .039	.017 .0087 .044	.027 .0053 .052	.035 .0055 .060	.026 .0024 .063	.021 .0025 .065	.014 .004 .063
	.014 .023 .041	.012 .020 .042	.0096 .016 .046	.011 .015 .035	.022 .016 .037	.034 .0060 .039	.040 .0061 .059	.021 .0020 .098	.017 .0025 .093	.012 .0030 .087
	.013 .030 .039	.013 .027 .036	.018 .024 .037	.025 .020 .030	.039 .010 .035	.048 .0062 .043	.049 .0063 .064	.013 .0017 .110	.012 .0024 .120	.0090 .0030 .094
				.0084 .011 .113	.072 .0069 .089	.064 .0076 .095	.045 .0016 .102	.082 .0018 .110	.0085 .0026 .117	.0063 .0035 .091
← TEACH	.104 .119									
← VARR	.034 .106									
← Exp. results	.015 .085		.040 .0023 .080	.022 .0019 .086	.032 .0033 .073	.011 .0011 .031	.0062 .0020 .110	.0065 .0081 .105	.0042 .0044 .085	

Fig. 7 Compared Calculated and Measured Reynolds Stress Fields, FFTF Geometry, Re = 33000

202.	-255.	-99.8	-27.8	-11.1	-11.8	-19.6	-9.73	4.38	-1.36
428.	-418.	-1170	-3.38	4.53	4.40	2.35	5.65	2.88	.99
-28.6	-63.6	-28.6	-21.0	-38.2	-25.4	-25.4	-31.8	3.18	-22.3
4.72	-42.3	-45.0	-25.8	-14.4	-21.8	-46.9	-56.6	-35.8	-18.4
15.76	-78.50	-28.73	-8.85	-.75	-5.01	-11.46	-2.80	-3.57	-3.93
-24.2	-28.6	-47.1	-33.7	-53.4	-38.1	-25.4	-49.5	-25.4	+9.54
-2.99	-14.4	-19.8	-15.3	-10.4	-26.2	-58.2	-74.4	-48.9	-23.1
7.32	-22.57	-30.10	-9.38	-1.20	-9.53	-18.59	-9.91	-9.44	-6.87
-17.8	-12.7	-28.8	-22.3	-24.8	-25.4	-25.4	-25.4	~ 0	+12.7
.104	-8.92	-18.8	-8.03	-5.56	-28.8	-65.4	-73.0	-44.6	-24.3
14.42	-.17	-11.22	9.43	1.97	-12.73	-21.34	-11.31	-10.92	-7.15
-14.6	-3.82	-5.72	-20.4	-28.6	-29.6	-50.9	-40.8	-25.4	+6.36
-5.40	-12.1	-14.7	-1.51	-5.88	-34.4	-66.2	-45.3	-24.2	-12.1
+6.67	-1.62	+10.05	+23.68	-3.98	-13.71	-19.96	-7.66	-9.21	-6.20
-7.63	-18.4	-15.3	-11.4	-17.8	-15.9	-11.1	-95.4	-70.0	~ 0
-19.2	-26.4	-17.1	-18.0	-28.0	-36.6	-37.3	-6.05	-6.02	-8.41
-12.8	-34.0	-2.22	-14.88	-11.04	-7.68	-8.40	-2.95	-5.85	-4.64
-7.00	-12.1	-19.1	-10.2	-7.63	-25.4	-38.2	-70.0	-38.2	~ 0
			67.4	97.4	101.	57.8	8.43	2.64	-1.70
			+6.12	14.5	13.0	5.60	-.33	-2.54	-2.65
			-42.6	-14.0	-146.	-636	38.2	+28.6	12.7
			32.2	27.5	26.3	8.91	3.67	1.67	-0.03
			-.020	-3.93	-9.22	-.13	.22	-.17	-.35
			-26.7	17.8	76.3	58.9	57.2	+636	6.36

← TEACH  
 ← VARR  
 ← EXP. Results

X 10<sup>-1</sup>

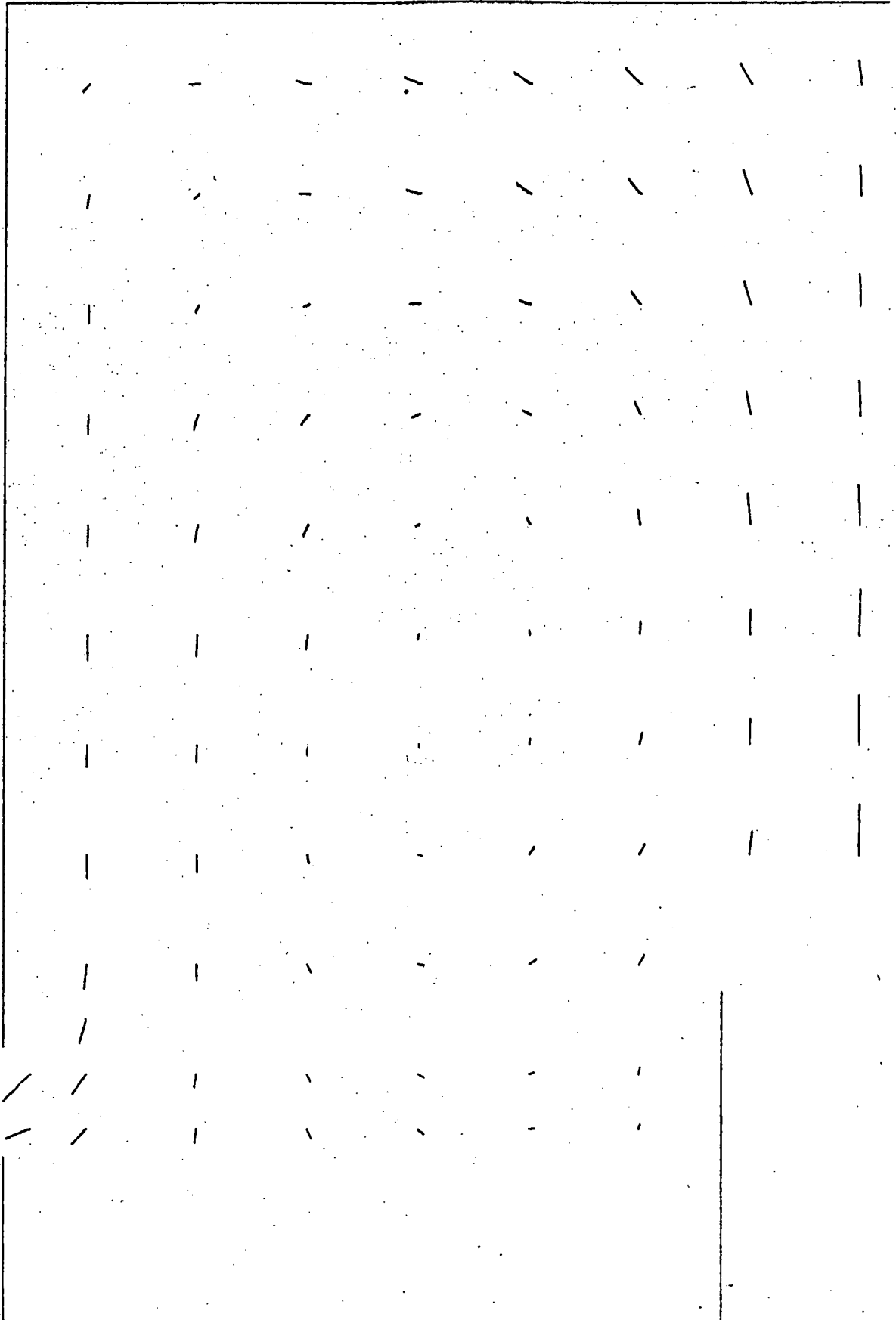


Fig. 8 Measured Mean Flow Field, FFTF Geometry,  $Re = 70000$

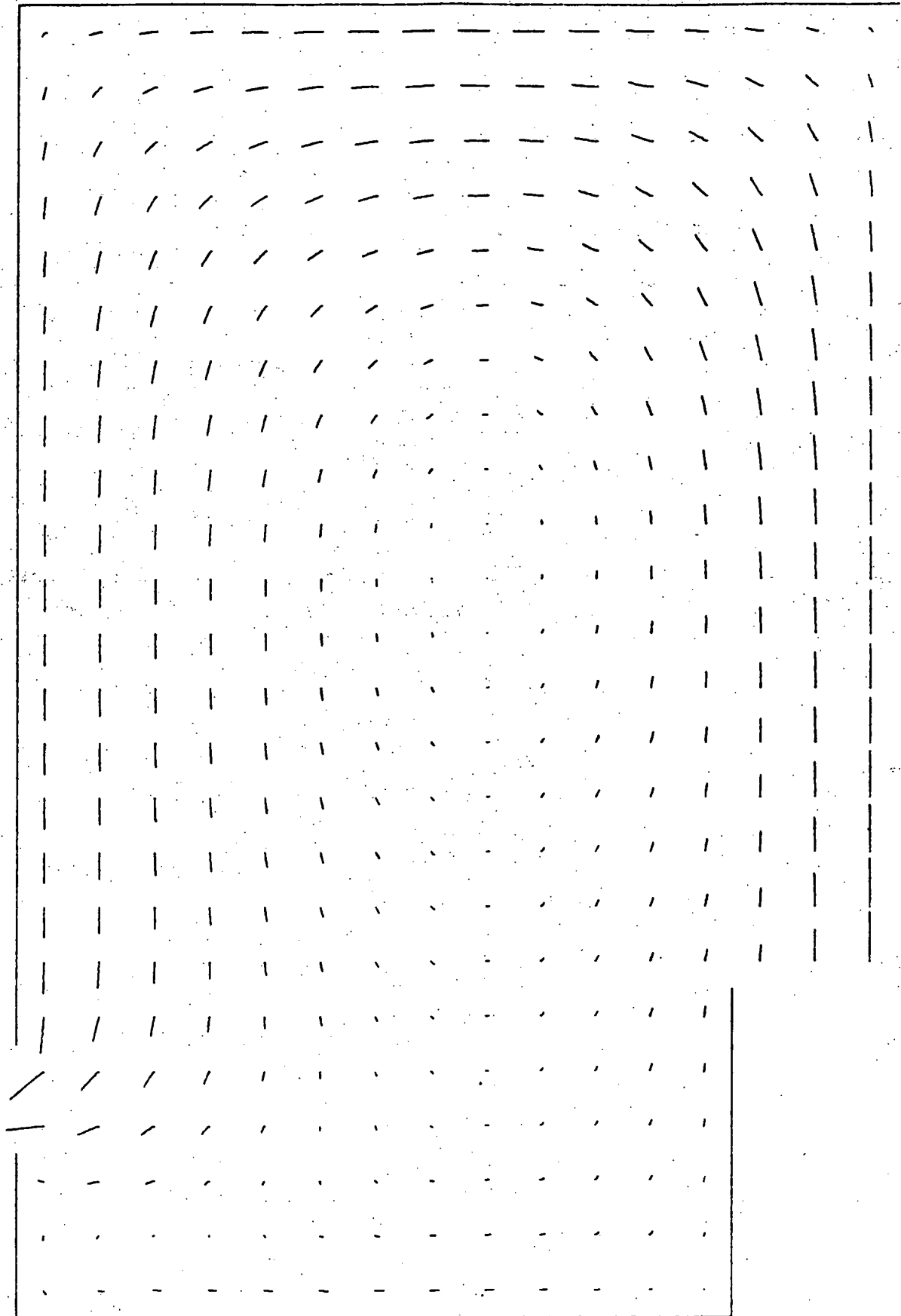


Fig. 9 TEACH-T Prediction, FFTF Geometry,  $Re = 70,000$

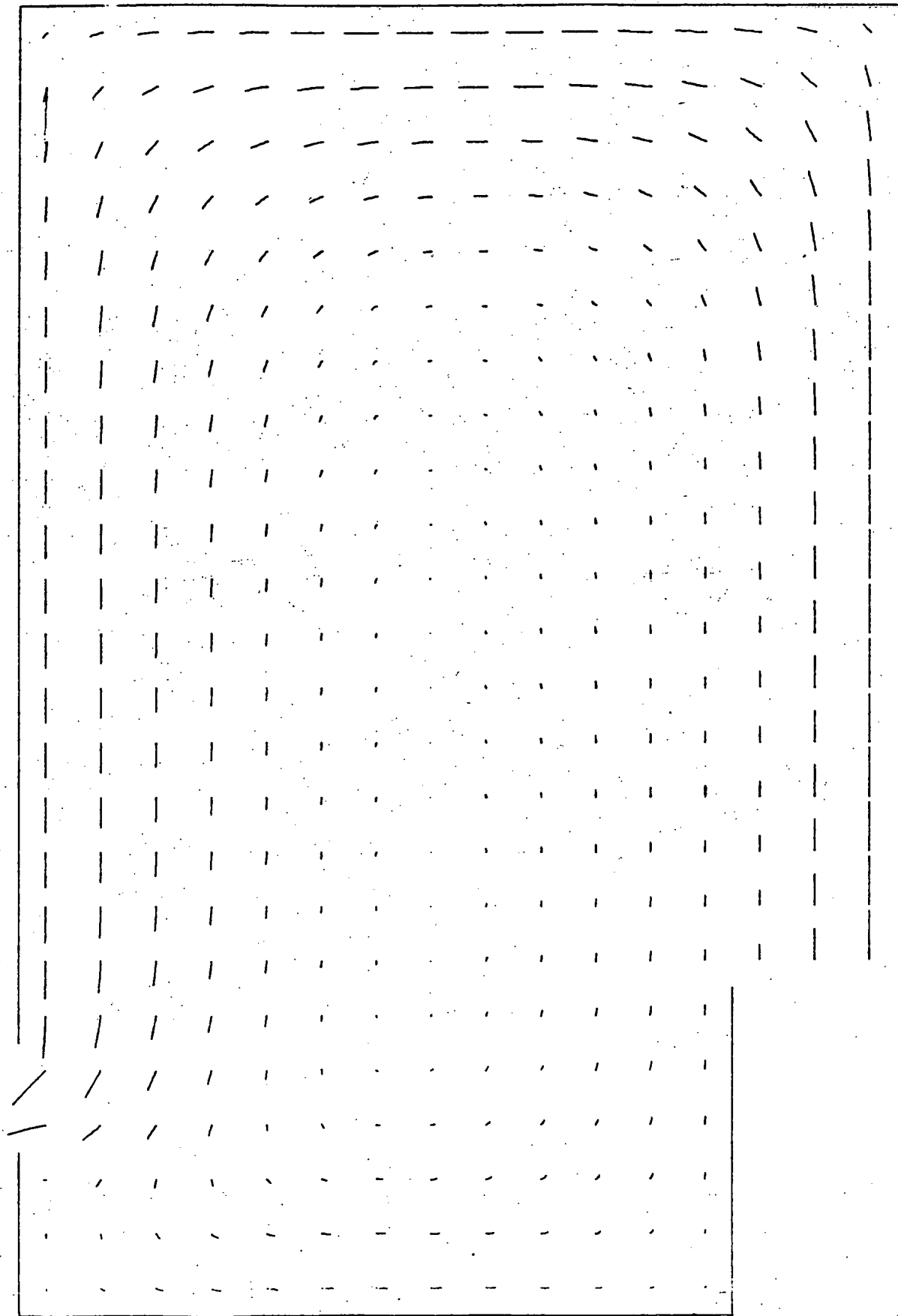


Fig. 10 VARR-II Prediction, FFTF Geometry,  $Re = 70000$

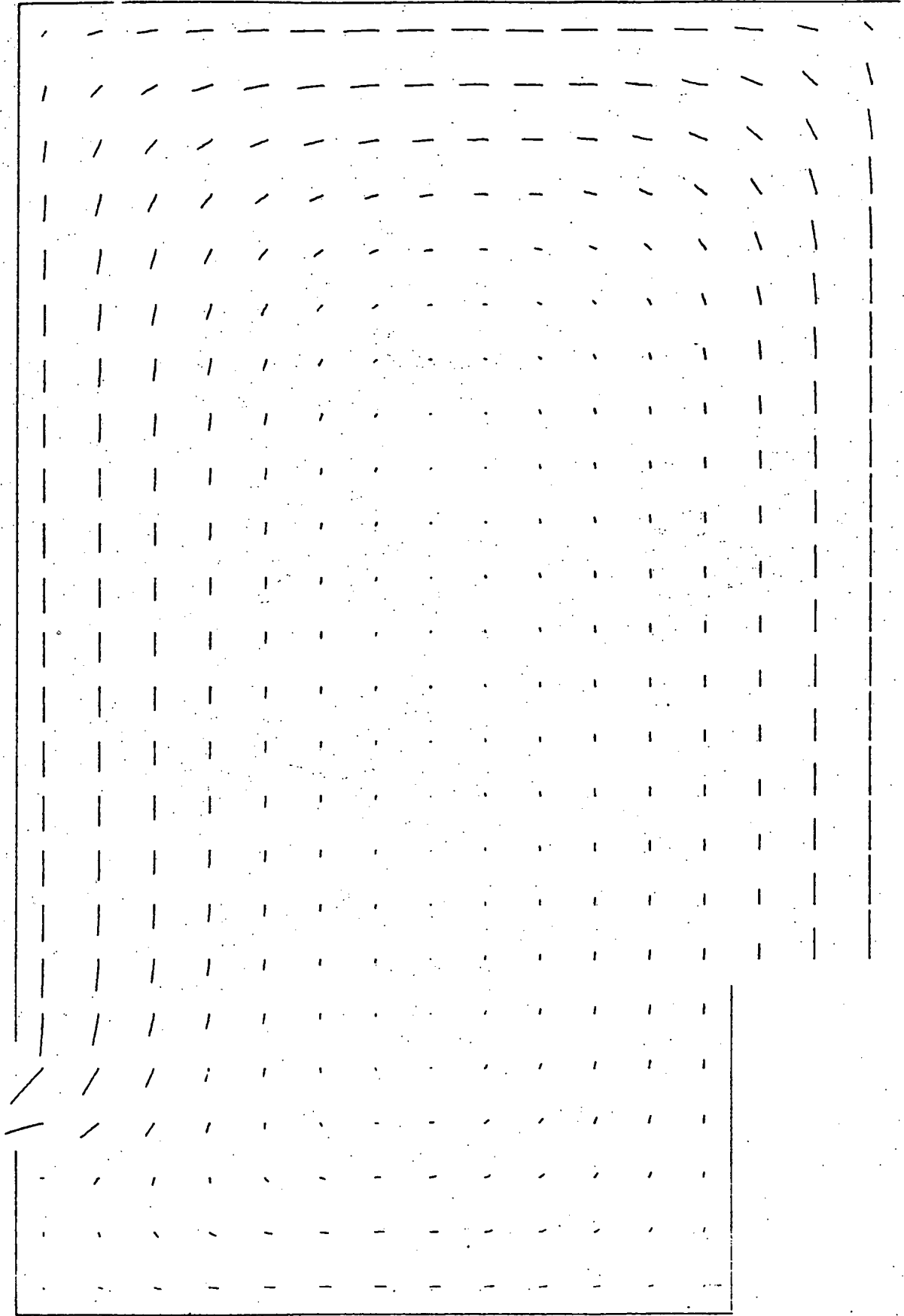


Fig. 11 VARR-II Prediction, FFTF Geometry,  $Re=70000$  Turbulent Kinetic Energy Matched at Inlet Centerline







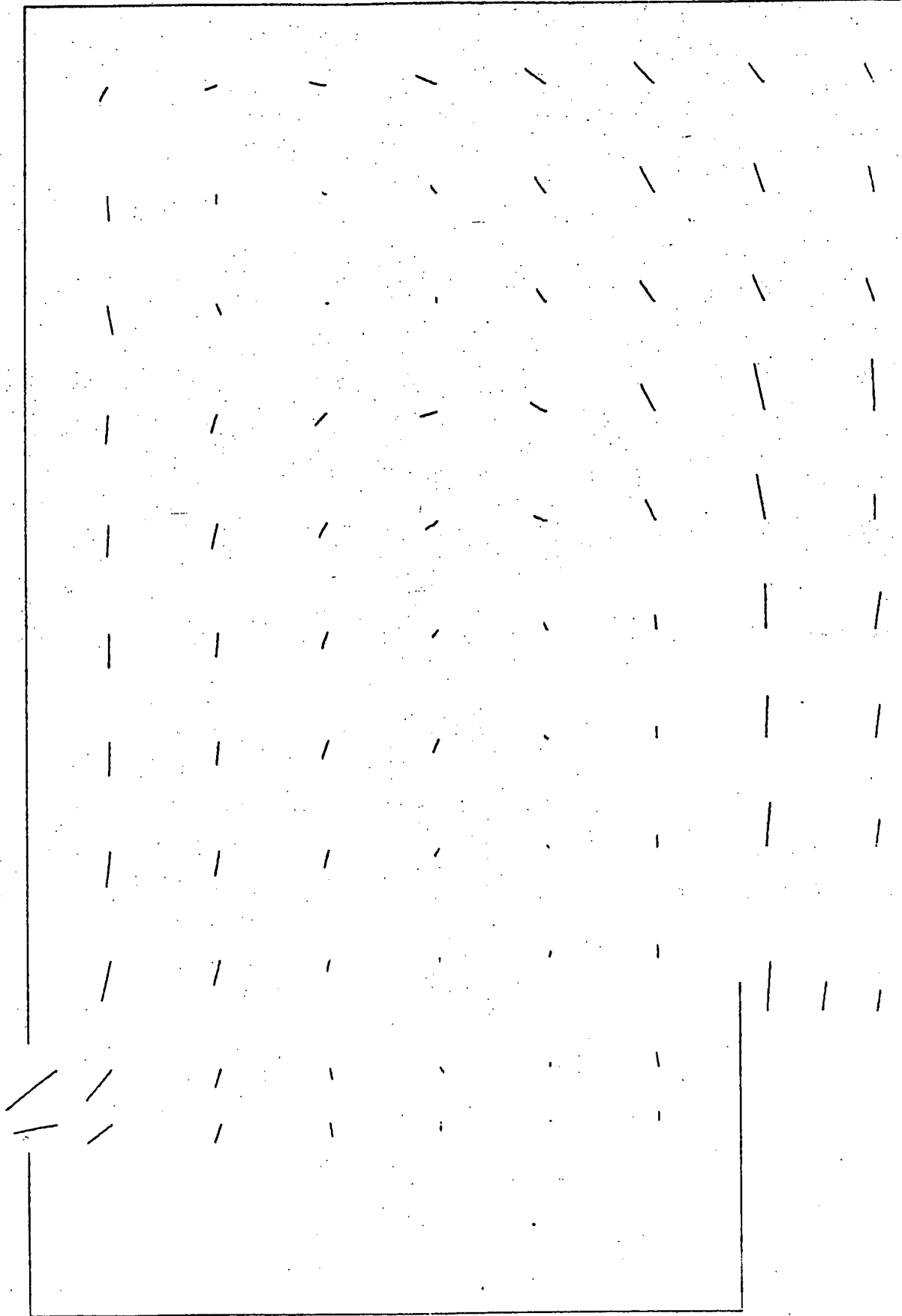


Fig. 14. Measured Mean Flow Field, FFTF Geometry,  $Re = 70000$  Distorted Inlet  
Mean Flow Distribution

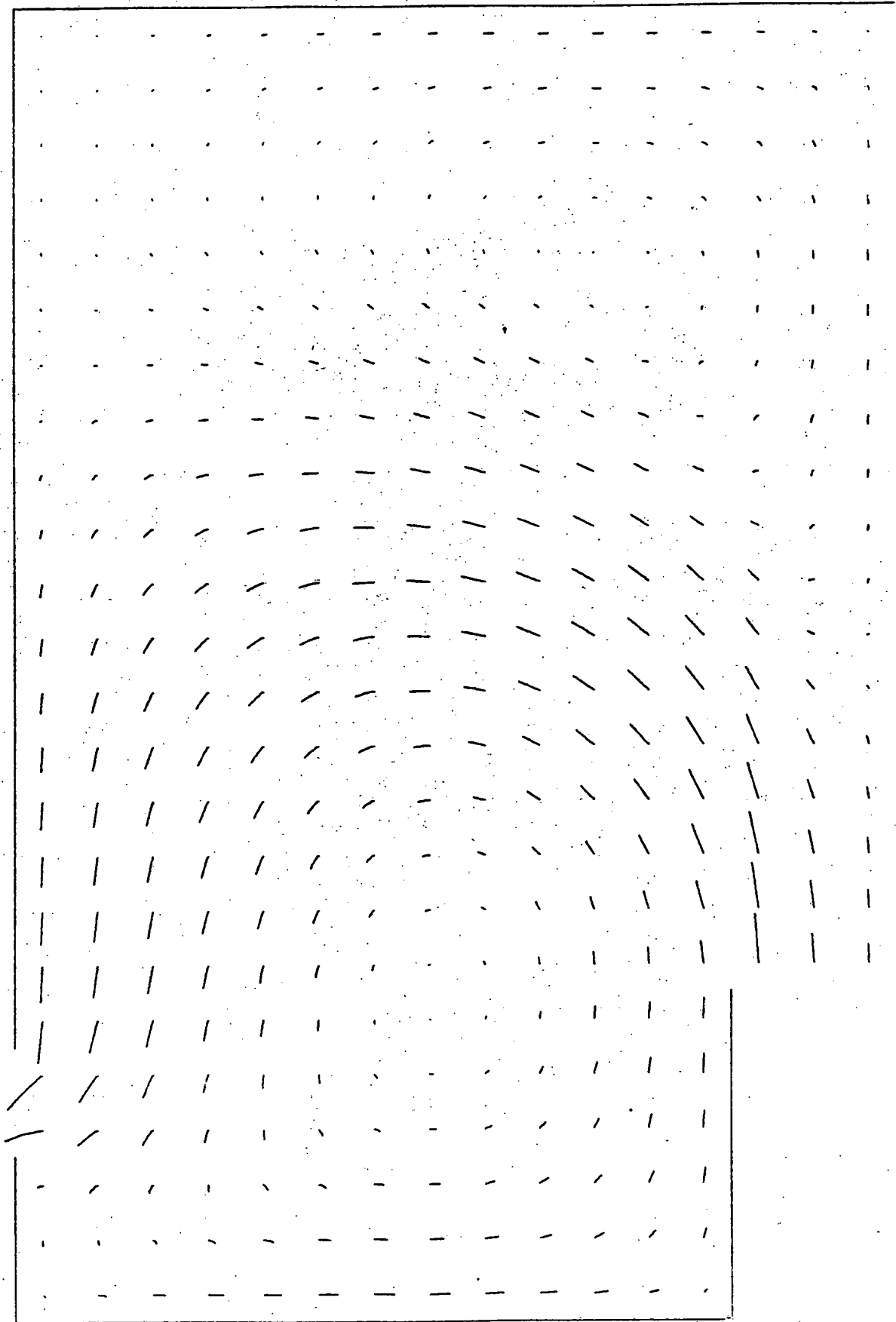


Fig. 15 TEACH - T Prediction, FFTF Geometry,  $Re = 70,000$  Distaled Inlet  
Mean Flow Distribution

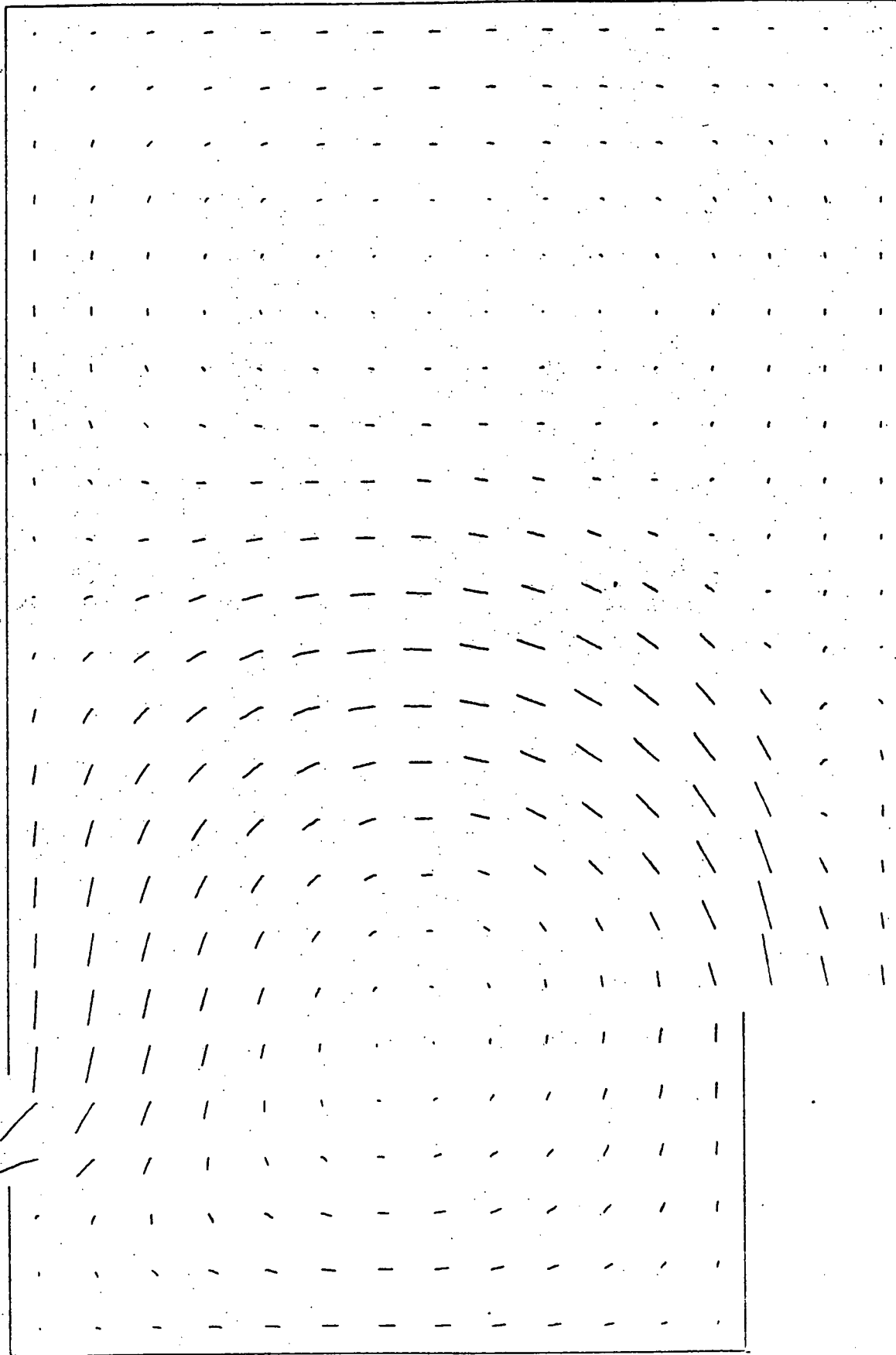
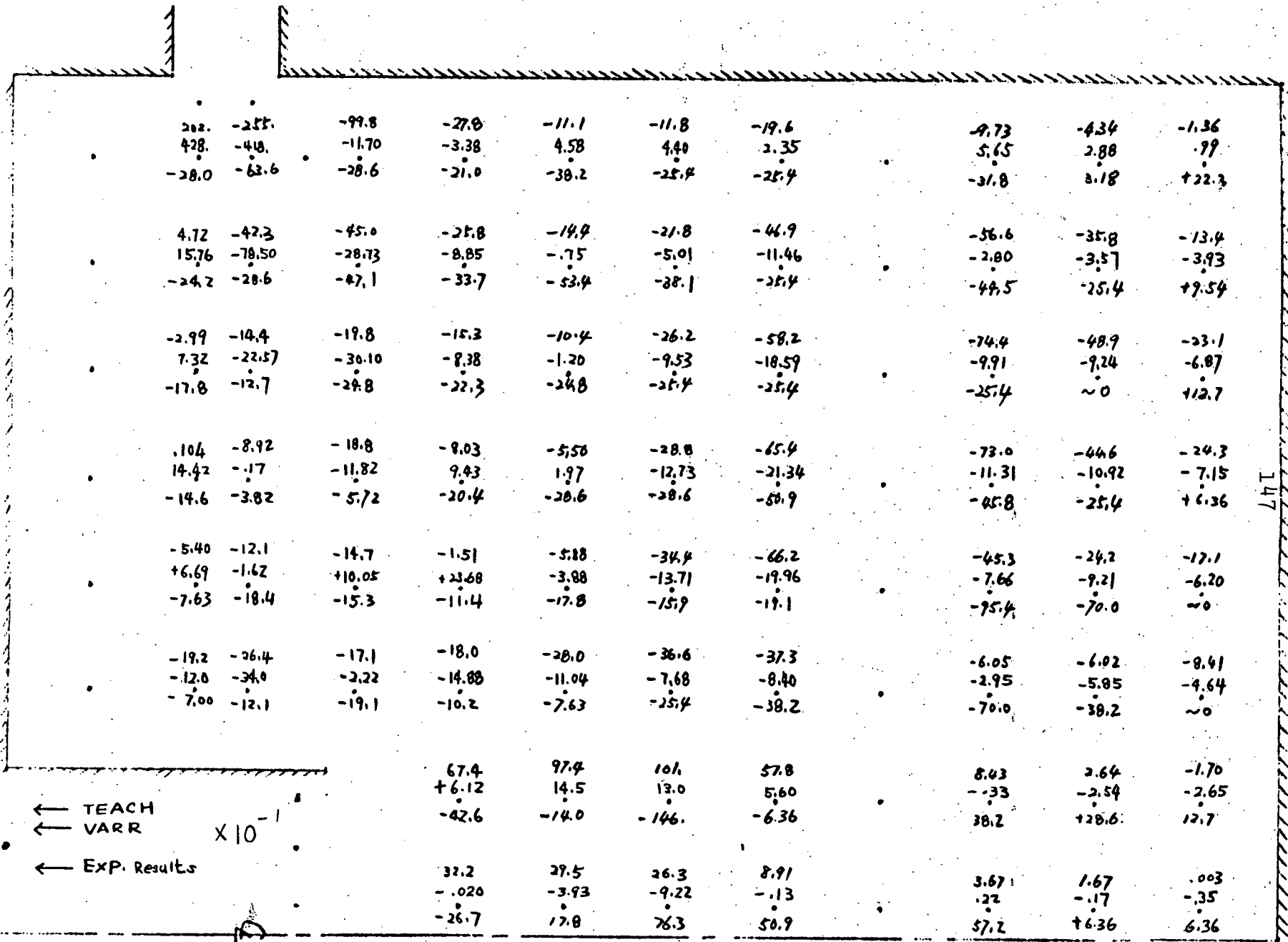


Fig. 16 VARR-II Prediction, FFTF Geometry,  $Re=70000$  Distorted Inlet Mean Flow Distribution



Fig. 18 Compared Calculated and Measured Reynolds Stress Fields, FIFTH Geometry, Re = 70000 Distorted Inlet Mean Flow Distribution



← TEACH  
 ← VARR  
 ← EXP. Results

x 10<sup>-1</sup>

147

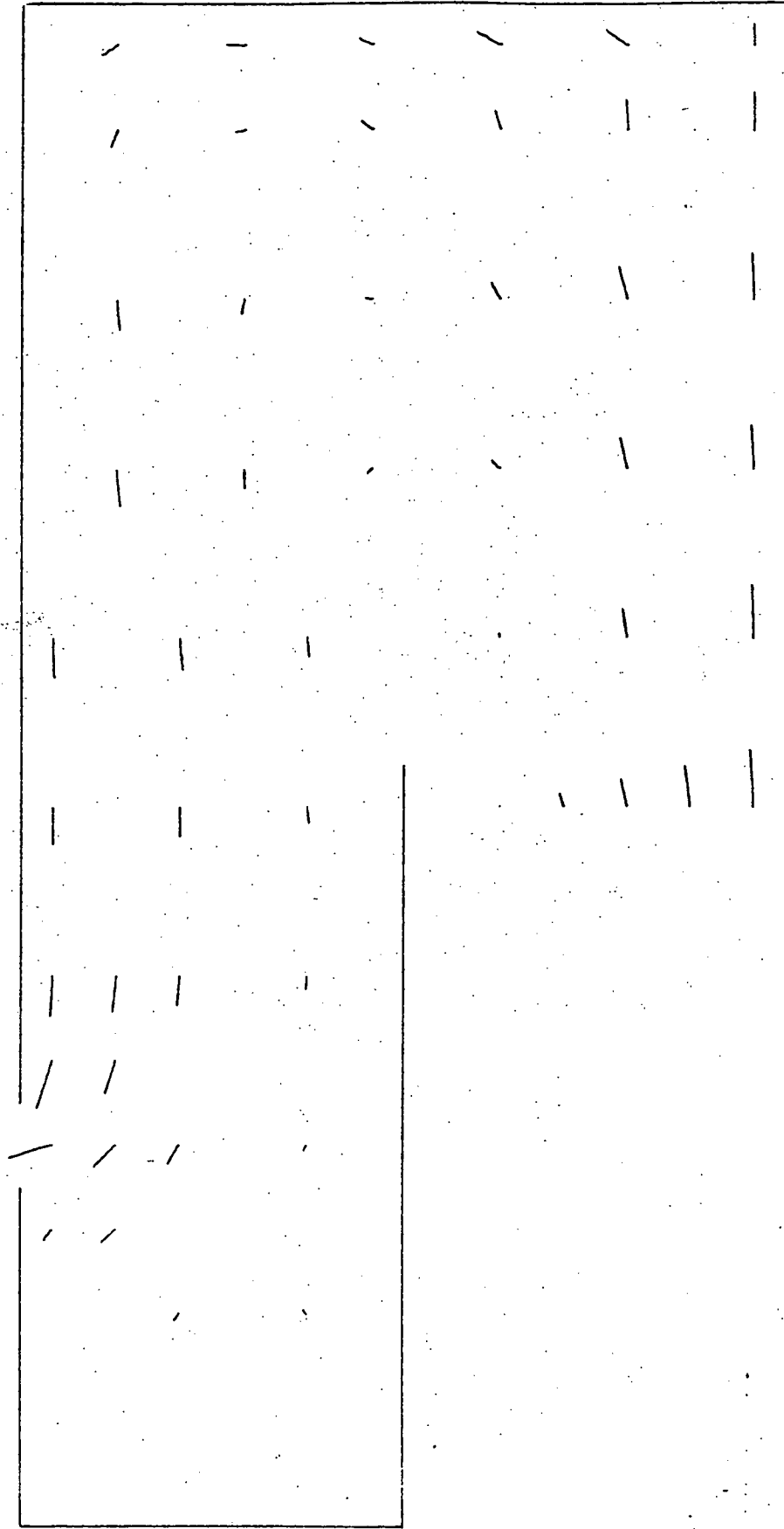


Fig. 19 Measured Mean Flow Field, CRBR Geometry,  $Re = 35000$



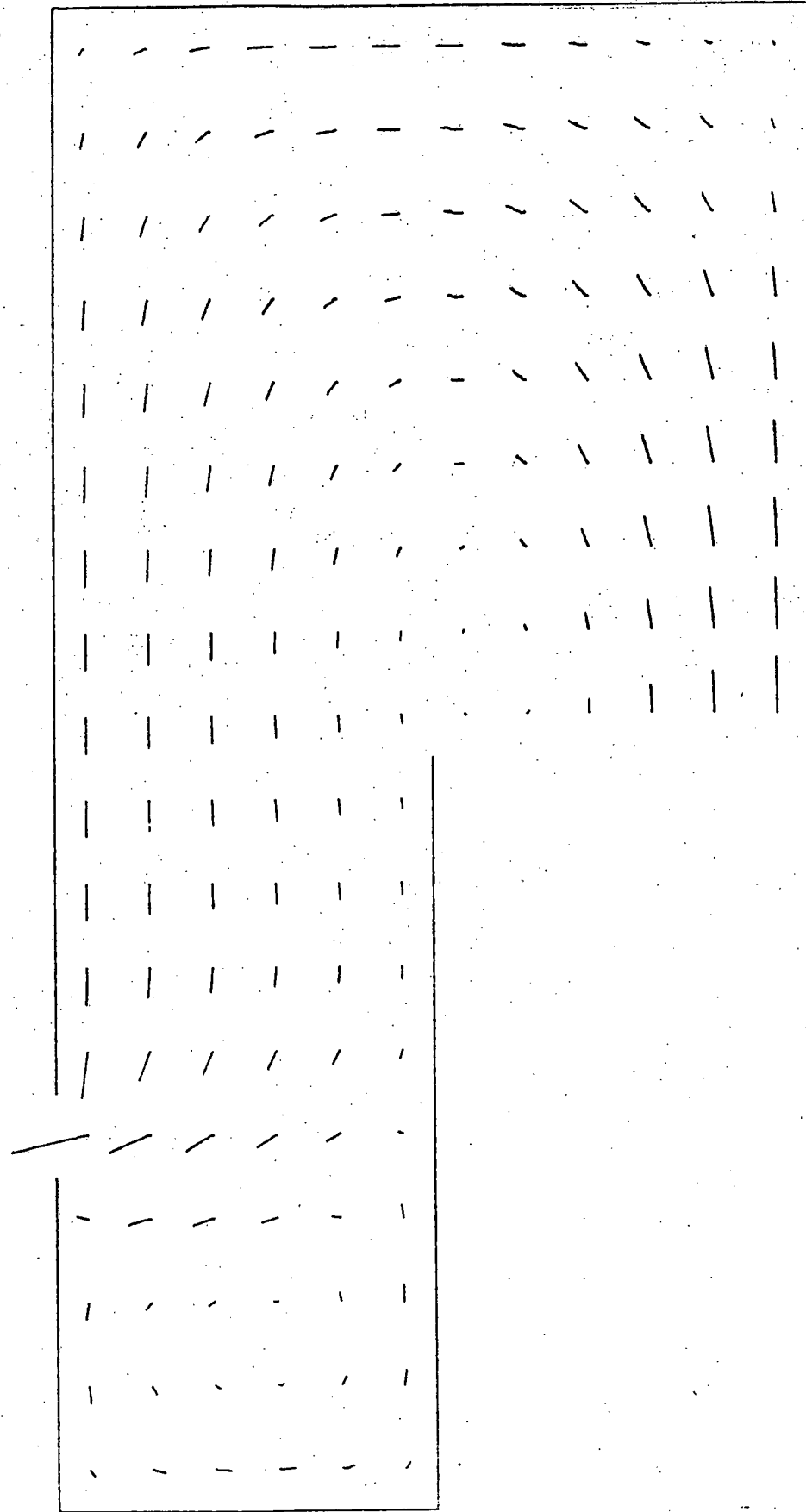


Fig. 20 TEACH-T Prediction, CRBR Geometry, Re - 35000

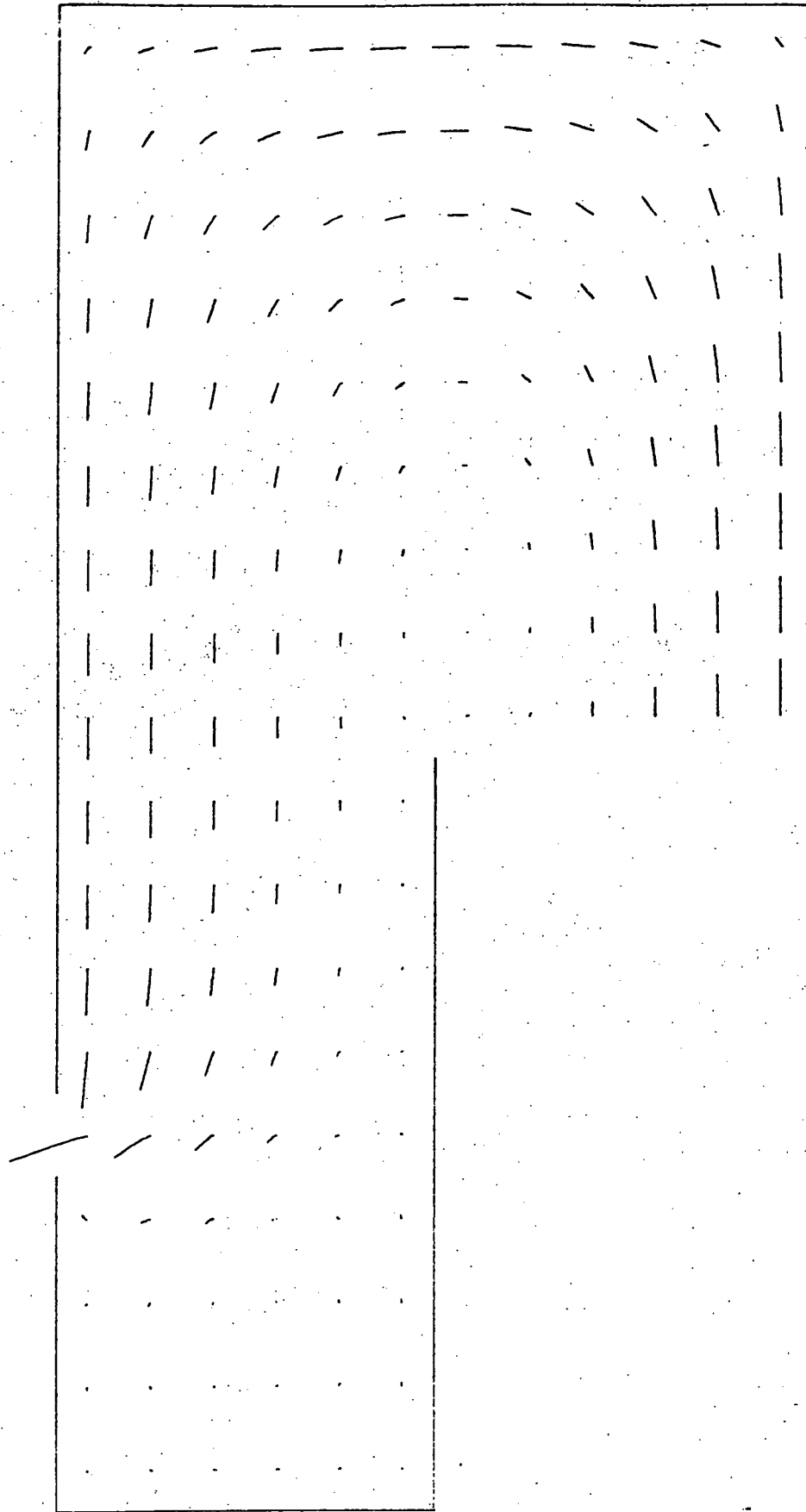


fig. 21 VARR-II Prediction, CRBR Geometry, Re=35000

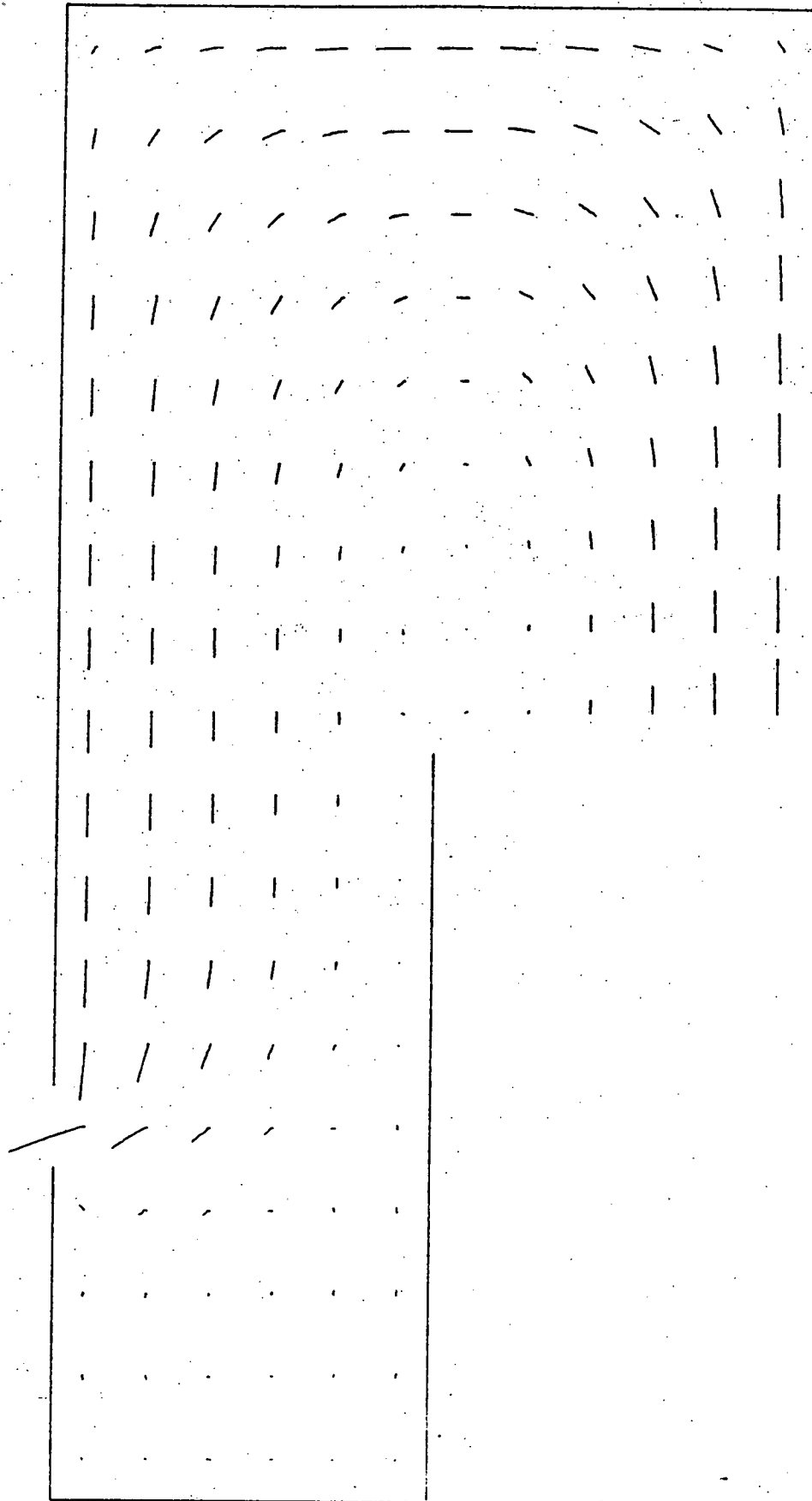


Fig. 22 VARR-II Prediction, CRBR Geometry,  $Re = 35000$  Turbulence Kinetic Energy Matched at Inlet Centerline

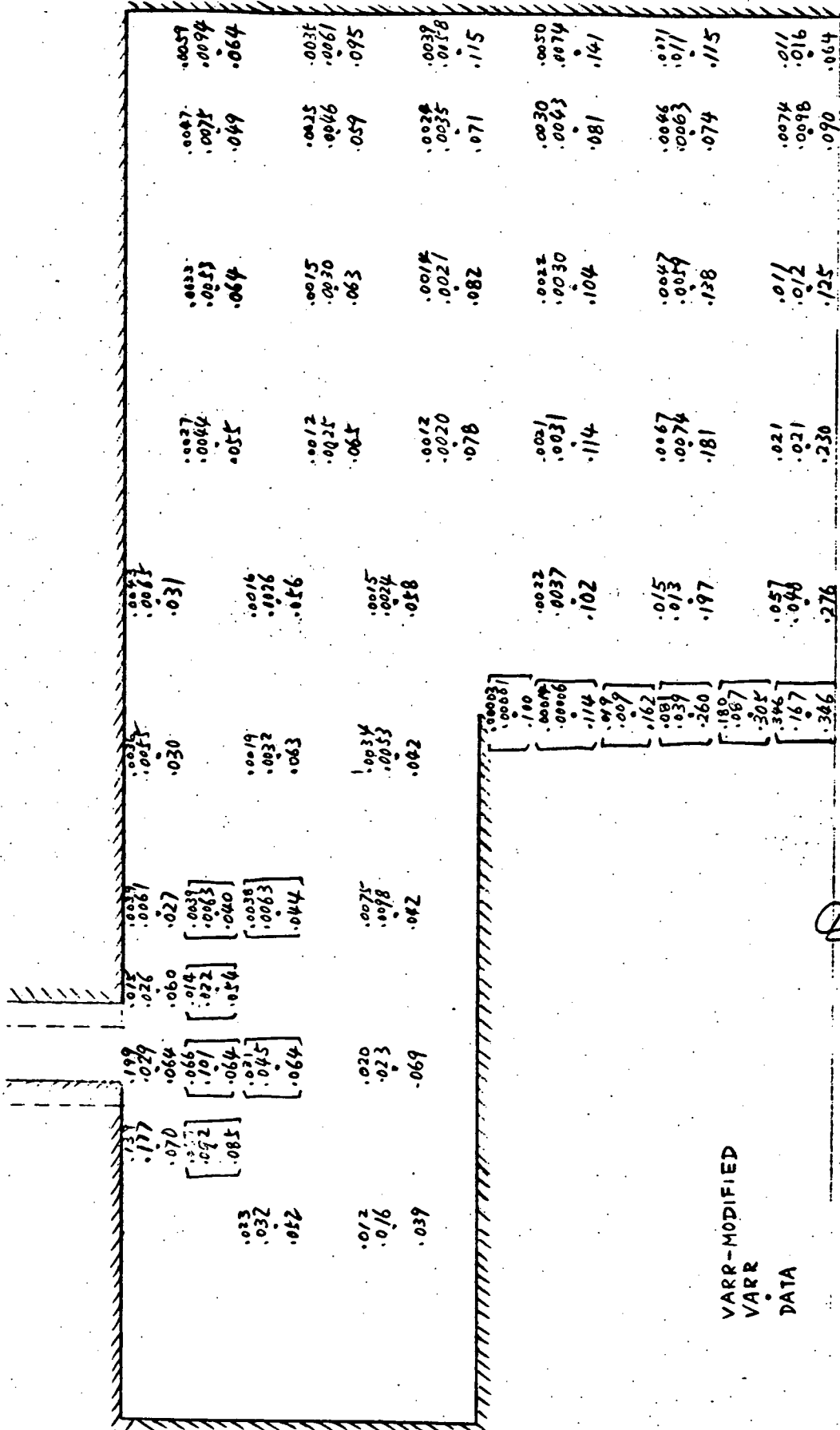


Fig. 23 Compared Calculated and Measured Turbulence Kinetic Energy Fields, CRBR Geometry,  $Re = 35000$



Fig. 24 Measured Mean Flow Field, CRBR Geometry, Distorted Inlet Mean Flow Distribution

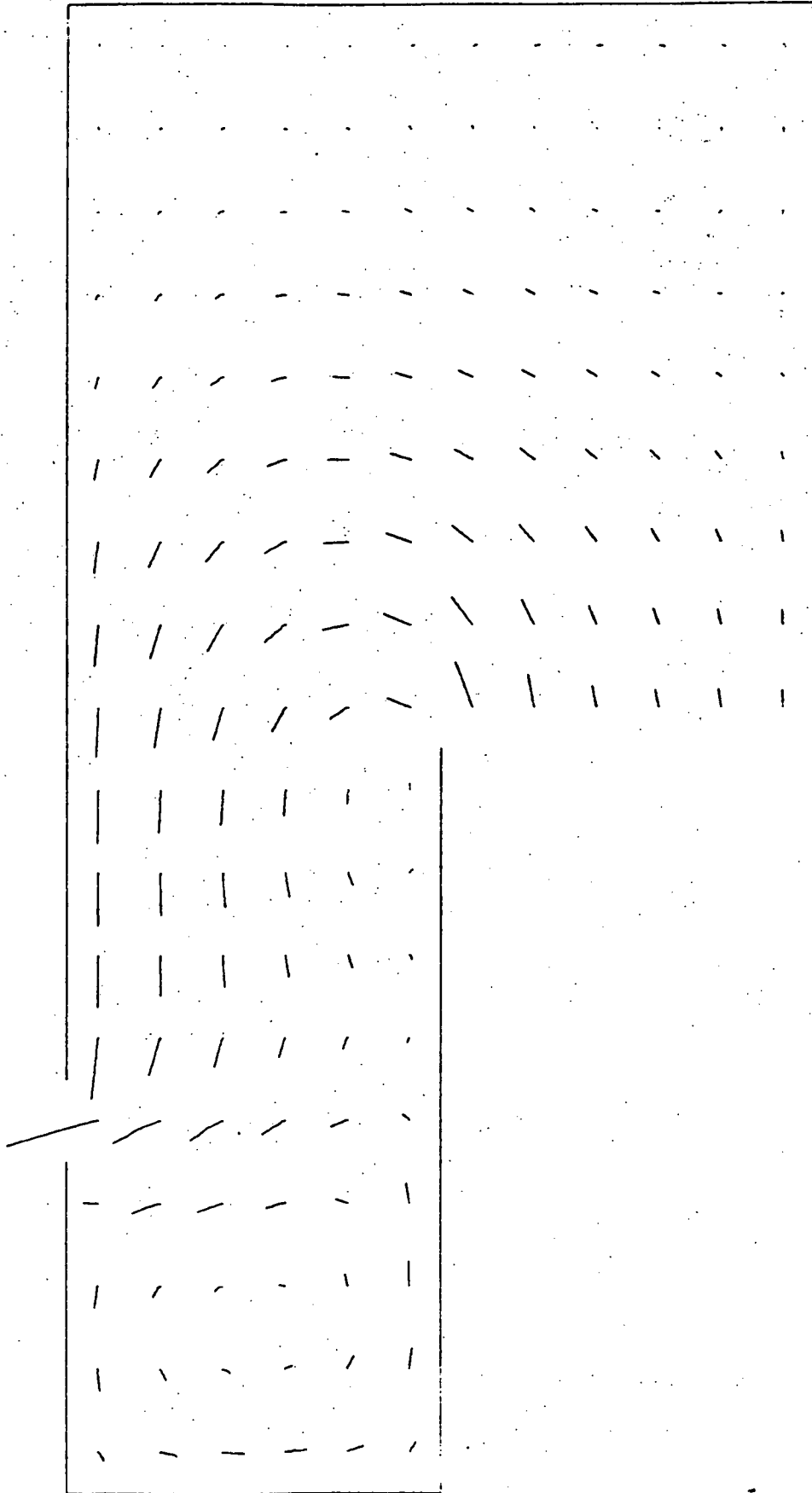


Fig. 25 TEACH-T Prediction, CRBR Geometry,  $Re = 35000$  Distorted Inlet Mean Flow Distribution

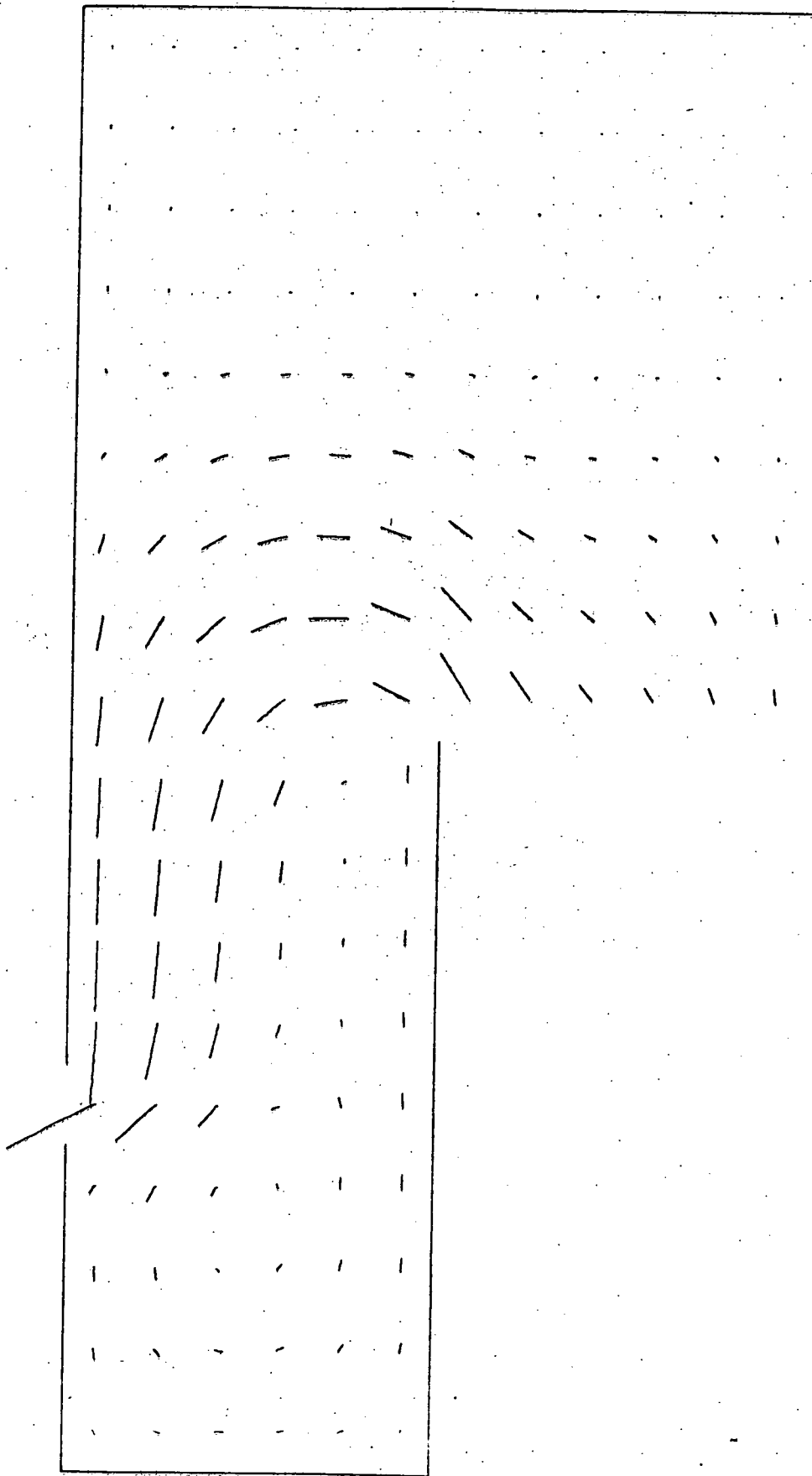


Fig. 26 VARR-II Prediction, CRBR Geometry,  $Re = 35000$  Distorted Inlet Mean Flow Distribution.

Appendix A - Turbulence Model Code Descriptions

The fundamental equations of the various turbulence model codes are outlined in this Appendix. These codes are used to provide the detailed analysis of the experiments, and the theoretically predicted velocity and turbulence distributions.

The basic conservation equations are the following:

$$\text{Mass: } \frac{\partial \rho}{\partial t} + \frac{\partial}{\partial x_j} (u_j \rho) = \frac{\partial \rho}{\partial x_j} \leftarrow \frac{\partial \rho}{\partial x_j} \quad (\text{A.1})$$

$$\text{Momentum: } \frac{\partial u_i}{\partial t} + \frac{\partial}{\partial x_j} u_i u_j = - \frac{\partial P}{\partial x_i} + \rho g_i - \frac{\partial}{\partial x_j} R_{ij} \quad \text{and (in VARR II)} \quad (\text{A.2})$$

$$\text{Heat: } \frac{\partial T}{\partial t} + u_j \frac{\partial T}{\partial x_j} = \frac{\partial}{\partial x_j} (\alpha + E \sigma_k) \frac{\partial T}{\partial x_j} + \frac{\dot{q}}{\rho c}, \quad \text{where} \quad (\text{A.3})$$

$\alpha$  = thermal diffusivity

$\rho$   $\equiv$   $\rho_{\text{local}} - \rho_0$  = local gas density deficit;

$\rho_{\text{local}}$  = local gas density

$\rho_0$  = ambient gas density,

$x_j$  = j-th spatial coordinate,

$t$  = time,

$u_j$  = j-th velocity coordinate,

$P$  = pressure,

$E$  = Ratio  $\left( \frac{\text{eddy heat diffusivity}}{\text{eddy momentum diffusivity}} \right)$



$T$  = temperature,

$g_j$  = gravitational acceleration component in  $j$ -th direction

$R_{ij} \equiv \frac{2}{3} k \delta_{ij} - \epsilon \left( \frac{\partial u_i}{\partial x_j} + \frac{\partial u_j}{\partial x_i} \right)$  or Reynolds Stress (A.4)

$k \equiv \frac{1}{2} \langle u_i' u_i' \rangle$  or turbulence kinetic energy (A.5)

$u_i^l$  =  $i$ -th turbulent fluctuating velocity component,

$\epsilon \equiv - \frac{\langle u_i' u_j' \rangle}{\left( \frac{\partial u_i}{\partial x_j} + \frac{\partial u_j}{\partial x_i} \right) - \frac{2}{3} k \delta_{ij}}$  or eddy diffusivity (A.6)  
of momentum

$\mu_t$  = turbulent viscosity,

$\sigma$  = turbulent momentum diffusivity,

$k$  = molecular momentum diffusivity,

$l_m$  = mixing length,

$\tau$  = shear stress,

$y$  = displacement normal to a boundary,

$R$  = duct radius,

$a, b, c, c_1, c_2$  = free parameters, and

$\delta_{ij}$  = the Kronecker delta function

Equations A.1 and A.2 are solved via coupled iteration upon the velocity divergence as in the marker and cell (MAC) method (55). Equation A.3 is solved explicitly at each time step in terms of variables known from the preceding time step and from Eqs. A.1 and A.2.

In order to solve Eqs. A.1 through A.3 knowledge of the turbulent diffusivities for heat ( $\epsilon_{v_T}$ ) and momentum ( $\nu_T$ ) is required. For this a variety of phenomenological "turbulence

models" have been devised in which appropriate time-averages of Eq. A.2 (weighted by velocities or velocity gradients) are used to provide conservation equations for the turbulence kinetic energy, viscous energy dissipation rate, etc. The order of a turbulence model is denoted by the number of differential conservation equations which must be solved in addition to Eqs. A.1 - A.3. In Table A.1 are summarized a spectrum of zero, one, and two-equation turbulence models which are currently in common use - including those used in TEACH-T and VARR-II. In the formulation of the turbulence conservation equations because of the quadratic nature of the convective terms of Eq. A.2 there are always created more statistically - defined variables than there exist equations for their solution. Thus, relationships between a sufficient set of extra variables must be postulated in order to permit solution of the equations. Thus, a combination of empirical knowledge and intuition is required in the formulation of a turbulence models, and it is the requirement for the arbitrary additional closure equations which accounts for the difference between turbulence models.

The TEACH-T program uses the turbulence kinetic energy - viscous dissipation rate two-equation model ( $K, \epsilon$ ), and the VARR-II program uses the turbulence kinetic energy - turbulent viscosity two-equation model ( $K, \sigma$ ) as described in Table A.1.

Table A.1

## Several Proposed Turbulence Models

MODEL	EQUATIONS (proposer)	ASSUMPTIONS (proposer)	APPLICATION	ADVANTAGES	DISADVANTAGES
ZERO EQ.	1. Mixing Length Theory (Prandtl) $-\rho \overline{u_1' u_2'} = \mu_t \frac{\partial \overline{u_1}}{\partial x_2}$ where $\mu_t = \rho l_m^2 \left  \frac{\partial \overline{u_1}}{\partial x_2} \right $ $l_m = l_m(x_1, x_2)$ , the mixing length, must be prescribed	1. $l_m \propto \delta$ , where $\delta \equiv$ width of 1/2 Jet 2. $l_m/R = 0.14 - 0.08(1 - X_2/R)^2 - 0.06(1 - X_2/R)^4$	Jet  Pipe	1. Simple, no additional differential equations need to be solved. 2. For boundary-layer flow, this theory made very good predictions. 3. Much experience has been accumulated	In situation where more than one characteristic length and time are involved (e.g., recirculating flow) the relation between the stress and velocity gradients are too complicated. This theory does not give a good result.
		3. $l_m \propto \left  \frac{\partial \overline{u_1}}{\partial x_2} / \frac{\partial^2 \overline{u_1}}{\partial x_2^2} \right $ (Von Karman)		It removes the necessity to prescribe the mixing length profile.	1. The prediction is not in agreement with measurement except in the vicinity of a wall 2. For certain flows the velocity profiles have inflection points (i.e., $\frac{\partial^2 \overline{u_1}}{\partial x_2^2} = 0$ ) this formula gives infinite mixing length.

Table A.1  
Several Proposed Turbulence Models

MODEL	EQUATIONS (proposer)	ASSUMPTIONS (proposer)	SUCCESSFUL APPLICATION	ADVANTAGES	DISADVANTAGES
ONE EQ.	<p>1. Turbulent Kinetic Energy Model (Prandtl)</p> $\overline{u_i' u_j'} = -\frac{\mu_t}{\rho} \left( \frac{\partial \bar{u}_i}{\partial x_j} + \frac{\partial \bar{u}_j}{\partial x_i} \right) + \frac{2}{3} \delta_{ij} k$ $\frac{Dk}{Dt} = \underbrace{-\frac{\partial}{\partial x_j} (\overline{u_j' k'})}_{\text{convection}} + \underbrace{\overline{u_j' \phi'}}_{\text{diffusion}} - \nu \frac{\partial k}{\partial x_j}$	<p>diffusion term = <math>\frac{\mu_t}{\rho k} \cdot \frac{\partial k}{\partial x_j}</math></p> <p>dissipation term = <math>\epsilon</math></p>			<ol style="list-style-type: none"> <li>Transport of length scale is not accounted for</li> <li>In practice, the model only offer very small advantages over the mixing length model</li> </ol>
	$\underbrace{\overline{u_i' u_j'} \frac{\partial \bar{u}_i}{\partial x_j}}_{\text{generation}} - \nu \underbrace{\left( \frac{\partial \bar{u}_i}{\partial x_j} \right)^2}_{\text{dissipation}}$ <p>where <math>k \equiv \frac{1}{2} \overline{u_i' u_i'}</math>, <math>\mu_t \equiv \rho k^{1/2} \ell</math></p> <p><math>\ell \equiv \ell(x_1, x_2, x_3)</math> prescribed algebraically</p>	<p>dissipation = <math>\frac{\rho k^{3/2}}{\ell} = \epsilon</math></p> <p>diffusion = <math>-\overline{v' k'} = Bk \sqrt{\frac{\tau_{\max}}{\rho}}</math></p> <p><math>B \equiv \frac{\tau_{\max}}{\rho u_c^2} g(y/\delta)</math></p> <p><math>\tau = a \cdot \rho k</math> (<math>a=0.3</math>)</p> <p>(BRADSHAW)</p>	boundary-layer flow	local shear stress is not related to the local mean velocity gradient	<ol style="list-style-type: none"> <li>Transport of length scale is not accounted for</li> <li>Shear stress <math>\sim</math> energy relation is of limited validity. In practice, applicable only to external boundary layers without velocity maxima.</li> </ol>

Table A.1  
Several Proposed Turbulence Models

MODEL	EQUATIONS (proposer)	ASSUMPTIONS (proposer)	SUCCESSFUL APPLICATION	ADVANTAGES	DISADVANTAGES
<p>TWO EQ.</p>	<p>1. k-ε Model</p> <p><math>\frac{Dk}{Dt}</math> - diffusion term + generation term + dissipation term (same as above)</p> $\frac{D\epsilon}{Dt} = -2\nu \frac{\partial \bar{u}_i}{\partial x_k} \underbrace{\left( \frac{\partial u'_i}{\partial x_\ell} \frac{\partial u'_k}{\partial x_\ell} + \frac{\partial u'_\ell}{\partial x_i} \frac{\partial u'_\ell}{\partial x_k} \right)}_a$ $\underbrace{\left( 2\nu \frac{\partial u'_i}{\partial x_k} \frac{\partial u'_i}{\partial x_\ell} \frac{\partial u'_k}{\partial x_\ell} - 2\left( \nu \frac{\partial^2 u'_i}{\partial x_k \partial x_\ell} \right)^2 \right)}_b$ $- \frac{\partial}{\partial x_k} \underbrace{\left( \overline{u'_k \epsilon'} + \frac{2\nu}{\rho} \frac{\partial p'}{\partial x_\ell} \frac{\partial u'_k}{\partial x_\ell} - \nu \frac{\partial \epsilon}{\partial x_k} \right)}_c$ <p>where <math>c \equiv \nu \left( \frac{\partial u'_i}{\partial x_j} \right)^2</math>    <math>\mu_c = \rho k^2 / c</math></p>	$a = \left( C_1 \frac{\overline{u'_i u'_i}}{k} + C'_1 \delta_{ik} \right) \epsilon$ $b = C_2 \epsilon^2 / k$ $c = \frac{\mu_c}{\sigma_\epsilon} \frac{\partial \epsilon}{\partial x_k}$	<p>boundary-layer flow recirculating flow</p>	<ol style="list-style-type: none"> <li>1. The exact equation for <math>\epsilon</math> can be derived from Navier-Stokes equations and <math>\epsilon</math> appears directly as an unknown in the equation for <math>k</math>.</li> <li>2. Gives satisfactory predictions for both boundary-layer flow and recirculating flow.</li> <li>3. It does not greatly increase the cost of computation over that with simple model</li> </ol>	<p>The empirical constants are difficult to predict.</p>

Table A.1

## Several Proposed Turbulence Models

MODEL	EQUATIONS (proposer)	ASSUMPTIONS (proposer)	SUCCESSFUL APPLICATION	ADVANTAGES	DISADVANTAGES
TWO EQ.	<p>2. k-<math>\sigma</math> Model (Stuhmiller)</p> $\frac{Dk}{Dt} = \frac{1}{2} \sigma \left( \frac{\partial \bar{u}_i}{\partial x_j} + \frac{\partial \bar{u}_j}{\partial x_i} \right)^2 + \frac{\partial}{\partial x_j} \Gamma \sigma \frac{\partial k}{\partial x_j} - \alpha \frac{(2k)^2}{\sigma}$ $\frac{D\sigma}{Dt} = \frac{\sigma^2}{4k} \left( \frac{\partial \bar{u}_i}{\partial x_j} + \frac{\partial \bar{u}_j}{\partial x_i} \right)^2 + \frac{\sigma}{k} \frac{\partial}{\partial x_j} \Gamma \sigma \frac{\partial k}{\partial x_j} - \frac{\sigma^3}{k^2} \frac{\partial}{\partial x_j} \Gamma_1 k \frac{\partial}{\partial x_j} \left( \frac{k}{\sigma} \right) - \alpha k$ $\rho \overline{u_i' u_j'} = \frac{2}{3} \delta_{ij} k - \sigma \left( \frac{\partial \bar{u}_i}{\partial x_j} + \frac{\partial \bar{u}_j}{\partial x_i} \right)$ <p>where <math>\Gamma</math>, <math>\alpha</math>, <math>\Gamma_1</math> are constants</p>		pipe flow recirculating flow	<ol style="list-style-type: none"> <li>1. The exact equation for <math>\sigma</math> can be derived from Navier-Stokes equation and <math>\sigma</math> appears directly as an unknown in the equation for <math>k</math>.</li> <li>2. Gives satisfactory predictions for both boundary-layer flow and recirculating flow.</li> <li>3. It does not greatly increase the cost of computation over that with simple model.</li> </ol>	The empirical constants are difficult to predict.

Table A.1

## Several Proposed Turbulence Models

MODEL	EQUATIONS (proposer)	ASSUMPTIONS (proposer)	SUCCESSFUL APPLICATION	ADVANTAGES	DISADVANTAGES
TWO EQ.	<p>3. k-k<sub>l</sub> Model (Rodi and Spalding)</p> $U \frac{\partial k}{\partial x} + v \frac{\partial k}{\partial y} = \frac{1}{y_l} \frac{\partial}{\partial y} \left( y_l \frac{v_t}{\sigma_k} \frac{\partial k}{\partial y} \right) + v_t \left( \frac{\partial u}{\partial y} \right)^2 - C_p \frac{k^{3/2}}{l}$ $U \frac{\partial k_l}{\partial x} + v \frac{\partial k_l}{\partial y} = \frac{1}{y_l} \frac{\partial}{\partial y} \left[ y_l \frac{v_t}{\sigma_{kl}} \left( \frac{\partial k_l}{\partial y} + C_{kl} l \frac{\partial k}{\partial y} \right) \right] + C_B v_t l \left( \frac{\partial u}{\partial y} \right)^2 - C_S k^{3/2}$ <p>where <math>C_D</math>, <math>C_S</math>, <math>C_B</math>, <math>\sigma_k</math>, <math>C_{kl}</math> and <math>C_{kl}</math> are constants</p>		Free Jet boundary-layer near wall	<ol style="list-style-type: none"> <li>1. The exact equation for <math>k_l</math> can be derived from Navier-Stokes equation and <math>k_l</math> appears directly as an unknown in the equation for <math>k</math>.</li> <li>2. Gives satisfactory predictions for both boundary-layer flow and free jet.</li> <li>3. It does not greatly increase the cost of computation over that with simple model.</li> </ol>	The empirical constants are difficult to predict.

TASK IV: THEORETICAL DETERMINATION OF LOCAL TEMPERATURE  
FIELDS IN LMFBR FUEL ROD BUNDLES

TASK IVA: Code Development for Solving the 2-D Multicell,  
Multiregion Energy Equations (Man Kit Yeung)

Summary

During the last quarter emphasis has been primarily focused on the application of the iterative analytical solution to determine 2-D temperature field in finite bundles of both square and hexagonal geometry. Further progress has been made to predict the "effective mixing length" for conduction heat transfer, a parameter which enters the subchannel formulation and application for LMFBRs. Both clad temperature distribution and the effective mixing length for conduction yield excellent agreements when compared with results in the open literature for the square array bundle. In addition parametric studies of conductivities and channel wall effects have been also investigated. A calculation with the accurately predicted effective mixing length for a 7-pin LMFBR bundle is performed with COBRA-IIIC. The calculational results reveal the excess conservatism in current design calculations due to the uncertainty of the effective conduction mixing length.

1. Clad Temperature Distributions in Hexagonal Rod Bundles

For subchannel calculations, it is generally assumed that the heat flux is uniform around the clad surface and the clad temperature is calculated by using the simple heat transfer coefficient method. However, this procedure is highly oversimplistic when applied to the side and corner cells because the high degree of geometric irregularities of the cells greatly enhance the azimuthal variations of the clad temperatures and heat fluxes. Information about a correct treatment of these phenomena is only available for single side and corner cell calculations with artificially imposed adiabatic boundary condition at the imaginary cell boundary [1]. The present study gives detailed clad and coolant temperature distributions in a finite hexagonal rod bundles.

A 30° symmetry section of a typical 7-pin fuel bundle as shown in Fig. 1 is studied in the first place. Analytical solutions of the temperature fields in all regions are obtained for thermally fully developed slug flow condition. Thermal and geometric parameters used in the analysis are presented in Table 1. The results of the calculation of the clad temperature distributions as function of the azimuthal angle for both the internal and corner cell are given in Fig. 2 at the axial



plane where the bulk coolant temperature is 1150°F, which represents a typical core exit temperature. Case 1 denotes the clad surface temperature distribution with the commonly imposed condition of uniform heat flux at the outside clad surface and case 2 denotes the multiregion analysis. It is evident that the latter indeed removes excess conservatism as compared to the single region analysis by reducing the clad temperature variation of the corner cell from approximately 185°F to 100°F. On the other hand the temperature variation of the internal cell is much less sensitive to the boundary condition because of its higher degree of symmetry for this 7-pin bundle case.

## 2. Calculation of Effective Conduction Mixing Length in Hexagonal Rod Bundles

Subchannel codes usually "lump" the assembly into a finite grid of subchannels, each of which is characterized by a bulk temperature, flow rate and pressure. Energy transport between adjacent channels is governed by the mechanisms of diversion cross-flow, turbulence mixing and conduction mixing. For LMFBR design calculations the energy transport by conduction constitutes a major contribution to the overall energy transport. This effect is even more pronounced for flows which are characterized by low Reynolds numbers. These flow situations especially arise in the case of a loss-of-flow accident and the like. Despite this importance only scattered information is available for internal cells but nothing is known for the bundle-wall-near regions of finite bundles.

The heat transfer rate due to conduction between adjacent subchannel  $i$  and  $j$  as calculated in subchannel codes is given by: [2]

$$Q_{ij} = k \frac{S_{ij}(\bar{T}_i - \bar{T}_j)}{l_{ij}} = k \frac{S_{ij}}{l_{ij}^*} (\bar{T}_i - \bar{T}_j) \frac{1}{L_{ij}} \quad (1)$$

Where  $S_{ij}$  is the length of the common boundary,  $l_{ij}$  is the effective conduction mixing length,  $l_{ij}^*$  is the centroid-to-centroid distance and  $L_{ij}$  is a dimensionless correction factor which represents the ratio of the effective conduction mixing length to the centroid-to-centroid distance ( $L_{ij} = l_{ij}/l_{ij}^*$ ). In subchannel calculations,  $L_{ij}$  is usually set to be unity due to the lack of knowledge of  $l_{ij}$  the local temperature field.

It is obvious that the lumped parameter subchannel codes will give reliable results only if reasonably correct effective mixing lengths are known. The calculation of the local temperature field thus provides a tool for the determination of the  $L_{ij}$ . With some rearrangements Eq. 1 can be written as:

$$L_{ij} = k \frac{S_{ij}}{l_{ij}^*} \frac{(\bar{T}_i - \bar{T}_j)}{\int_{S_{ij}} q'' ds} \quad (2)$$

where the channel averaged temperature and the heat transfer at the channel boundary can be calculated explicitly from the local temperature field of the coolant, and the ratio  $S_{ij}/l_{ij}^*$  which appears in Eq. (1) and Eq. (2) can be simply expressed by geometric parameters as:

$$\frac{S_{ij}}{l_{ij}^*} = \frac{\frac{1}{2} \left( \frac{P}{D} - 1 \right)}{\left[ \frac{\frac{1}{16} \left( \frac{2W}{P} \right)^2 \left( \frac{P}{D} \right) + \frac{1}{24\sqrt{3}} \left( \frac{2W}{D} \right)^3 - \frac{1}{16} - \frac{1}{2} \left( \frac{P}{D} \right)^3 - \frac{\sqrt{3}}{12} \pi \left( \frac{P}{D} \right)}{\frac{1}{4} \left( \frac{P}{D} \right) \left( \frac{2W}{D} \right) + \frac{1}{8\sqrt{3}} \left( \frac{2W}{D} \right)^2 - \frac{1}{12} \pi + \sqrt{3} \left( \frac{P}{D} \right)^2 - \frac{1}{2} \pi} \right]} \quad (3)$$

Fig. 3 shows  $L_{ij}$  as a function of the dimensionless wall distance for the corner region in case of  $P/D = 1.20$ . The results of both the single region and the multiregion analyses indicate that  $L_{ij}$  generally deviates quite substantially from unity, what is usually employed in subchannel codes such as COBRA-IIIC. [2]. The singularity indicates zero integral net heat transfer rate by conduction between the cells. The behavior of the curves for large  $2W/D$  values implies that the effect of the bundle wall diminishes and only  $P/D$  governs the asymptotic regime. The domain of the curve to the left of the singularity which results in  $L_{ij} > 1$  indicates a reversal of the heat flow direction.

For this regime of  $2W/D$  the net heat transfer is obviously from the corner channel into the internal channel due to the

decrease of the wall distance and reduction of flow area in the corner channel.

In order to demonstrate the effect of  $L_{ij}$  on subchannel calculations, three cases with different effective conduction mixing lengths were performed with COBRA-IIIC to compute the channel averaged temperatures for a bundle with geometric parameters of  $P/D=1.20$  and  $2W/D=1.24$ . The channel averaged temperatures at 36" from the core entrance for the cases with no conduction ( $L_{ij} = \infty$ ), the centroid-to-centroid distance as effective conduction mixing length ( $L_{ij}=1.0$ ), and the effective mixing length calculated from the analysis ( $L_{ij}=0.65$ ) are tabulated in Table 2. The case without the conduction mixing effect is essentially an isolated channel problem with respect to conduction and naturally yields the highest difference of averaged channel temperatures. Using the centroid-to-centroid distance without any correction leads to a reduction in  $\Delta T$  of about 20°F and using the analytically derived  $L_{ij}$  from Fig. 3 further decreases the temperature difference by another 9°F. Thus the advantage of an accurately determined  $L_{ij}$  becomes obvious.

It should be mentioned at this point that most ongoing efforts have been devoted to the diversion mixing area which obtains mixing effects of similar magnitude and it is felt that an equally significant gain in design margin is possible by properly accounting for the conduction effect.

### 3. Clad Temperature Distributions in Square Array Configurations

In addition to the analysis of hexagonal arrangements, a two cell section of a square cell arrangement as shown in Fig. 4 has been analyzed in parallel because the only concise information in the literature is available for the latter. Thus this case serves in order to check the validity of the developed code. The clad temperature distribution of the two cell calculation is compared to the result reported by France and Ginsberg [3]. In addition, the effect of changes in the flow split as well as multiregion analysis are also investigated to provide full understanding of the problem on hand.

As a first step only identical power source densities are considered in the fuel bundle. Slug flow is assumed within each cell and the variation in the velocity from cell to cell is given by [4].

$$\frac{U_i}{U_j} = \left( \frac{D_i}{D_j} \right)^{5/7} \quad (4)$$

where  $U_i$  and  $D_i$  are the cellular velocity and hydraulic diameter of cell  $i$ , respectively. This accounts approximately for the friction effect due to the presence of the channel wall and approximates the flow split. It should be noticed that, by virtue of Eq. 3 discontinuities in the velocity field at the interfaces of the cells are introduced. However, this is of no consequence for this analysis because the momentum equation is not solved at all. Furthermore, it should be recognized that instead of Eq. (4) Novendstern's approximation for the flow split in wire-wrapped bundles can be introduced or experimentally determined quantities may be used. This will be done in the next step of the code's development.

Calculational results are presented in Fig. 5 for a particular case with geometric parameters of  $P/D=1.20$  and  $2W/D = 1.24$ . Curve I denotes a special case with no flow split and uniform heat flux at the outside clad surface. The clad temperature distributions of both cells are compared to those of a finite difference solution by using the THTB code as given in [3]. It can be seen that the solution given by the present method has an accuracy which is comparable to that resulting from the finite difference method with 720 nodes in the coolant region. The excellent agreement adds further confidence to the accuracy of the iterative technique presently developed.

Curve 2 denotes the clad temperature distribution for a case with uniform heat flux at the outside clad surface and a flow split as calculated by Eq. (3). As can be seen from Fig. 5, the flow split due to the presence of the channel wall has completely reversed the temperature distribution. However, none of these curves represent the realistic clad temperature distribution due to the unrealistic boundary condition imposed at the outside clad surface. Only a multiregion analysis with flow split and accounting for the additional effects of the fuel and clad regions is capable to remove excess conservatism. Curve 3 summarizes the result of this calculation with some typical conductivity ratios ( $\kappa = 0.8327$ ,  $\kappa_w = 0.1538$ ). It is obvious that the heat flux and temperature redistributions result in a smaller circumferential temperature variation at the clad surface, i.e. a reduction of about  $60^\circ\text{F}$  to  $80^\circ\text{F}$  for normal operating conditions. Thus it becomes clear that an analytical tool should handle multiregion analysis together with the flow split in order to give realistic results.

#### 4. Calculation of Effective Conduction Mixing Lengths in Square Array Configuration

It is desirable to determine the effective conduction mixing length for the square cell bundle and compare the results to those given by France and Ginsberg in [4]. Again this will serve as an additional check for the validity of the present

calculational procedure. For the square array configuration the ratio  $S_{ij}/l_{ij}^*$  in Eq.(2) becomes:

$$\frac{S_{ij}}{l_{ij}^*} = \frac{\frac{P}{D}}{\frac{3}{2} \left(\frac{P}{D}\right) + \frac{1}{2} \left(\frac{2W}{D}\right) + 2 \left[ \frac{\frac{\pi}{\delta} \left(\frac{2W}{D} - \frac{P}{D}\right)}{\frac{P}{D} \left(\frac{P}{D} + \frac{2W}{D}\right)} - \frac{\pi}{2} \right]} \quad (5)$$

All other quantities in Eq. (2) are again evaluated from the local temperature field for the square array configuration. The results are presented in Fig. 6 with the effective conduction mixing length  $L_{ij}$  plotted vs. the quantity  $\mu$ , which is defined as:

$$\mu = \frac{\dot{M}_{\text{wall}}}{\dot{M}_{\text{internal}}} \quad (6)$$

where  $\dot{M}_{\text{wall}}$  and  $\dot{M}_{\text{internal}}$  are the mass flow rates for the cell next to the wall and the internal cell, respectively. Curve 2 in Fig. 6 denotes the result given by France and Ginsberg who used a boundary integral method for an eight cell configuration. For both cases the boundary condition of uniform heat flux at the clad outside surface has been used for comparison. The singular points as shown in Fig. 6 indicate that the net heat transfer between adjacent cells approaches zero. It can also be seen from Fig. 6 that  $L_{ij}$  generally deviates substantially from unity and exhibits strong dependence upon  $\mu$ , which itself is a function of geometry. However, the  $L_{ij}$  values for a 2-cell configuration indicate a fairly good agreement with those resulted from the 8-cell calculation except for the range where  $\mu < 0.95$ . This is because the effect on the flow in the interior cell due to the presence of the wall is more pronounced in a 2-cell configuration than in an 8-cell arrangement. On the other hand, the results indicate that even for the extreme case, a two cell model gives reasonable solutions as compared to the eight cell model. What this means is that a compromise between the gain in accuracy and additional computational efforts should be made.

#### 4. Conclusion and Discussion of Future Efforts

The iterative analytical method has demonstrated its applicability of both the calculation of the local temperature field and the determination of the effective conduction mixing length. The analysis serves as a tool to abridge the gap between the distributed parameter and lumped parameter analyses.

Moreover, it should be pointed out that the functional dependence of  $L_{ij}$  vs. wall distance for the hexagonal bundle is of particular interest because for the first time the effect of bundle wall displacement due to thermal and mechanical loads during its lifetime can be studied consistently with better knowledge of the variation of  $L_{ij}$  as a function of time.

Future effort will be directed towards the extension of the present analysis from a 7-pin bundle to larger bundles. However, by virtue of the results indicated by the clad temperature distributions given in Fig. 2, the circumferential temperature variations of the clad for most interior cells in a large bundle may be quite small due to their higher degree of symmetry. This suggests that the channel wall effect probably does not go beyond the second or third row and from the thermal stress analysis point of view only the first row from the wall is of prime interest. Thus the implication is that future work should be directed also to coupling subchannel and distributed parameter codes together.

TASK IVB: 3-D COUPLED TWO CELL SLUG FLOW HEAT  
TRANSFER ANALYSIS (Chung Nin Wong)

Summary

During the last quarter, the analytical method which has been described in the former progress reports has been extended in order to analyze the coupled corner and internal cells in three dimensions. To the author's knowledge this is the first time that results are presented for this geometry. All information hitherto available for 3-D analyses are limited to the coupling of two internal cells. Due to the similarity of the internal cells, these analyses are of no special engineering interest. The analysis of coupled corner and internal cells is of much more interest though because two cells with completely different thermal entrance behavior are considered.

Results are given for the outside clad temperature variations and are compared to the results given in previous reports. The heat flux distribution along the common boundary between the two cells is given as a function of the axial coordinate.

Furthermore, a sensitivity study has been performed to show the effect of the number of collocation points, the number of eigenvalues and the number of harmonies upon the solution.

In a next step, the effective conduction mixing length will be presented for the thermal entrance region and compared to that given in the preceding section for thermally fully developed conditions.

## 1. Short Outline of the Method

Before this problem has been attacked, the decision was made not to use the iterative scheme as outlined in the preceding section but instead to extend the already available analytical tool as described in the former progress reports. The only change which had to be made concerns the geometry of the coolant regime. Instead of studying the cells individually, the geometry as shown in Fig. 7 has to be considered; that is the two cells are treated as a whole new unit. This concept works well as long as the coolant channel geometry can be easily described by a rod centered polar-coordinate system located in one of the rods. Although this limits the application of the method to smaller regions it is felt that the most important bundle-wall-near regions together with the next row of interest cells can be effectively analyzed.

In order to make the analysis in its initial stage as simple as possible, the input parameters for both cells are assumed to be the same. Furthermore, the heat fluxes are assumed to be axially and azimuthally uniform in both pins.

With the assumptions made above the solution to the problem can still use the superposition of two solutions, namely, the fully developed and the thermal entrance solution, which have been outlined earlier.

## 2. Results

The same data, as already used in the last report, have been chosen here again for the test case:

$$P/D = 1.3 ; \quad 2W/D = 1.38 \quad D = 9 \text{ mm}$$

$$P_e = 372 ; \quad T_{in} = 415^\circ\text{C}$$

$$q'' = 104 \text{ W/cm}^2$$

Uniform heat flux in the axial and azimuthal directions. It should be recalled that these data reflect one of the experiments conducted at Karlsruhe.

For the presentation of the results the following abbreviations are used for the dimensionless groups:

$$\theta(\rho, \phi, \xi) = \frac{T(r, \phi, z) - T_{in}}{q'' r_1/k}$$

$$\rho = \frac{r}{P/2}$$

$$\xi = \frac{z D_n}{\left(\frac{P}{2}\right)^2 P_e}$$



The first results of this study are summarized in Figs. 8 to 5. Fig. 8 shows the comparison between the results of the single and two cell calculations for the clad temperature distribution of the corner cell under thermally fully developed conditions. Surprisingly, the two cell calculation results in even larger temperature variations around the clad as predicted by the single cell calculation. This complies perfectly with what has been already discovered with the 2-D analysis. The implication of this result is that under certain geometrical conditions the temperature variations are not getting smoothed out as one would intuitively think in the first place but instead become more pronounced.

Figs. 9 and 10 show the axial development of the peripheral temperature distributions for corner and internal cells. Whereas some remarkable changes in the profile can be noticed for the former the distribution in the latter does not change that much. What is interesting to see is that around  $\phi=180^\circ$  the temperature distribution around the corner and the internal pin are the same, because both channel geometries are the same in that regime. For  $\phi < 180^\circ$  the specific geometry of the coolant channel and the thermal entrance effect dominate the development of the temperature profile in the corner cell. At this point it must be mentioned that the temperature distribution in the neighborhood of  $\phi = 180^\circ$  is quite different from that predicted by the isolated single cell analysis. In the coupled two cell analysis this behavior is pretty much governed by the internal cell even at small  $z$ , i.e. there is a remarkable difference between the results obtained from the simplistic adiabatic boundary condition as compared to the realistic one. A good feeling about what happens along that imaginary boundary between the two cells can be obtained by calculating the heat flux along that line as a function of the axial distance. This is explicitly shown in Fig. 11. These results indicate that in the inlet regime of the coolant thermal heat is transferred from the corner to the internal cell. However about midway through the core this behavior reverses and heat flows from the internal cell towards the corner cell. This trend increases with increasing length of the channel. Naturally, the highest amount of energy is transferred across a line segment of this imaginary boundary which is characterized by the interval  $150 < \phi < 170$ , whereas for  $\phi > 170^\circ$  the transfer rate drops due to the similarity and symmetry of the coolant channel cross section in that regime. This figure shows that the assumption of zero heat flux along the interface between the cells as applied in the adiabatic single cell calculation is not valid in a strict sense. On the other hand, the curves indicate that the local transfer rate up to about midcore height is not very large either which suggests that at least in a certain axial regime the assumption of an adiabatic boundary condition can be somewhat justified. The change of the heat flux distribution as function of the axial coordinate can be explained in terms of the vastly different thermal entrance behaviors of the two cells.

### 3. Results of the Sensitivity Analysis

In order to assure the validity of the results shown in the previous section a sensitivity study has been performed. At this point it should be recalled that the complete analytical solution contains the summations over three integers ranging from either zero or one to infinity. It is obvious that the upper limit has to be cut down to a suitably chosen finite number of summation terms for computational purposes. This raises automatically the question what are the appropriate limits for these numbers for a specific problem on hand. With respect to the fully developed part of the solution it is felt that its validity has been already shown by comparing it to the iterative solution technique which itself was tested and compared favorably to a finite-difference solution. What remains then is to check the thermal entrance solution. For convenience the general form of this part of the total solution is repeated below

$$\theta_e(\rho, \phi, \xi) = \sum_{h=0}^{\infty} \sum_{m=1}^{\infty} [C_{n,m}]_n (\beta_{m\rho}) + D_{n,m} Y_n(\beta_{n\rho})] E_m e^{-\beta_m^2 \xi} \cos n\phi$$

As can be seen this equation contains a double summation. The first one sums over the number of harmonies kept in the solution and the second one sums over the number of eigenvalues.

Figs. 12 and 13 show the results for different upper limits in the above summation terms upon the peripheral clad temperature distribution. This comparison shows that selecting  $N_{eig}$  and/or  $N_n$  over a wide range does not greatly affect the clad temperature. Only for the fairly extreme case of  $N_{eig}=4$  and  $N_n=5$  are some small differences noticeable. However, the effects are much more pronounced for the coolant temperature. This becomes obvious from Fig. 14 where the heat flux distributions along the common boundary between the cells are compared. The selection of  $N_{eig}=4$  and  $N_n=5$  leads clearly to a fairly different distribution as compared to the standard  $N_{eig}=16$  and  $N_n=15$ . Obviously the strongest effect is introduced by the wrong selection of the harmonies to be kept in the solution. However, it should be noticed that due to the differentiation of the coolant temperature in order to get the heat flux, differences in the solutions are especially accentuated. This means that the heat flux as shown in Fig. 14 is indeed a very tight criterion to judge upon the accuracy of a solution.

In addition to the above mentioned selections there exists one more possibility to affect the solution, namely by choosing the number and distribution of points directly at the inlet of the coolant channel to satisfy the inlet boundary condition.

This selection mainly determines the coefficients  $E_m$ . The effects of two different selections upon the clad temperature is shown in Fig. 15. The solid line results by setting 5 points in the radial direction in the range  $0^\circ \leq \phi \leq 100$  and 7 in the range  $101^\circ \leq \phi \leq 180$  which gives a total of 269 points. The dotted line represents the results as obtained by setting 5 points in the range  $0^\circ \leq \phi \leq 140^\circ$  and 8 for  $141^\circ \leq \phi \leq 180^\circ$  which gives a total of 320 points. The azimuthal point distributions are indicated directly in the figure itself. The results therein show how sensitive the clad temperature is with respect to these two choices. At this point there is no direct way to decide what is the more accurate solution. However, experience tells us that it is appropriate to put more points in the region where the two cells are coupled together. Further increase of the number of points may lead to difficulties in the solution of the linear set of equations if no precautionary measures are taken. Overall this raises some doubts as to what limits the boundary least square method can be finally driven. Future studies will show whether the observed inaccuracies are indeed introduced by the solution method used for solving the set of linear equations. If this should be the case, a better method will be chosen out of the variety of available methods solving the general boundary least square problem.

#### 4. Future Work

Efforts in the next quarter will concentrate upon the evaluation of the effective conduction mixing length as a function of the axial distance. Curves will be fitted to these results and then implemented into COBRA-IIIC. The outcome of this study will then be compared to the results obtained from COBRA-IIIC by using the effective conduction mixing lengths resulting from the study of thermally fully developed conditions as derived in subtask IVA.

## TASK IVC: FULLY DEVELOPED LAMINAR MIXED CONVECTION (Jong-Yue Kim)

Summary

Work has been completed on this subject during the last quarter [5]. A topical report will be issued soon which in addition to the analytical results obtained in [5] will contain a review of experimental and other yet simplified analyses.

The undertaken efforts have been concentrated upon solving the laminar mixed convection problem in isolated single cells. The clad region has been considered, whereas the fuel region remained neglected. With respect to the peripheral heat flux distribution at the inside clad surface, two options were examined, namely

- a) a constant distribution
- and b) an azimuthally varying distribution

The latter served to simulate power tilts across the fuel region. The following parameters were changed in order to study their effects upon local and integral thermal and hydrodynamic quantities:

- 1) pitch-over-diameter ratio,  $P/D$
- 2) wall distance-to-diameter ratio,  $2W/D$
- 3) Rayleigh number,  $Ra$
- 4) clad-to-coolant thermal conductivity ratio
- 5) tilt parameter in the heat flux distribution

During the course of the analysis all efforts were undertaken to compare its results against publically available information. These comparisons turned out to show excellent agreements. Based upon these observations it is hoped that all the other results obtained in this study are valid, too.

## 1. Results

In what follows, only a small part of the overall results given in [5] will be presented. Although the internal cell has been as thoroughly examined as the edge (side) cell, results will be shown only for the latter here.

Fig. 16 and 17 show the dimensionless outside clad temperature distributions for  $P/D = 1.08$  and  $P/D = 1.2$ , respectively, for different values of  $2W/D$  and two values of the Ra-number, namely  $Ra=1$  and  $Ra=10^4$ . The values for  $2W/D$  were chosen such that they span a certain design range for the  $P/D$  under consideration. Furthermore, it should be noticed that  $Ra=1$  very closely resembles the forced laminar convection case as has been shown in [5] by comparing the results with those given by Hsu [6].

By comparing Figs. 16a and 17a it becomes apparent that designs with small  $P/D$  are much more sensitive against changes in the wall distance, which might occur during the operation due to bowing of the pin as well as the subassembly wall. That is, the temperature variations around the clad can become remarkably high if  $2W/D$  assumes values which deviates from the design values. Naturally, this effect is more pronounced for tighter pitches.

Independently of  $P/D$  Figs. 16b and 17b show that by increasing  $Ra$  always leads to a nearly flat temperature distribution at the surface which essentially means that free convection has a favorable effect upon the local distribution.

Fig. 18 shows the additional effect of a variable heat flux distribution. In the cases examined, the heat flux assumed its maximum towards the inside of the bundle and has its minimum adjacent to the subassembly wall. As can be observed these distributions lead to even higher temperature variations compared to the constant heat flux boundary condition and yet at  $Ra=10^4$  the variations have been totally eliminated.

Fig. 19a and 19b show the dimensionless heat flux ratios for the constant and the variable heat flux boundary cases, respectively. For  $Ra=1$ , the maximum of  $q''/q''$  is about 1.5 which steadily decreases when  $Ra$  increases. As shown in Fig. 19b for  $Ra=10^5$  all fluctuations have been smoothed out and the distribution follows essentially the boundary condition at the clad inside surface.

Fig. 20 shows how the direction of the flux tilt affects the dimensionless heat flux ratio for different Ra-numbers.

As with regard to the average Nusselt number,  $\bar{Nu}$ , as

function of Ra, Figs. 21 to 23 depict quite interesting behaviors which have not been reported in the open literature thus far. Over a certain range of the Ra-number,  $\bar{Nu}$  increases more or less dependent upon  $2W/D$ . However, at some critical Ra-number,  $\bar{Nu}$  sharply drops off and may assume even negative values before it asymptotically recovers to values around zero at very high Ra-numbers. This general behavior is explainable in terms of the differences of the average clad and coolant temperatures. The latter are strongly affected by the velocity field an example of which is given in Fig. 24. This figure discloses a very complicated structure of the velocity field for higher Ra-numbers. It is evident that regions exist with local downflow. This will naturally affect the overall pressure-drop characteristics of the coolant channel as shown in Fig. 25. Detailed discussions of these findings will be given in the forthcoming topical report.

Finally, Fig. 26 shows the feedback effect of the variable heat flux upon the velocity field. Naturally, for higher tilt parameters in the heat flux distribution the effects will become even more pronounced.

In conclusion, it should be recalled that all of the aforementioned results were obtained with the assumption of fully developed thermal and hydrodynamic conditions. Whether this is indeed justifiable under realistic conditions remains to be seen. However, it can be reasonably argued that the foregoing results establish upper limits and therefore are conservative.

## 2. Future Work

Dependent upon the future funding situation it is planned to couple several cells together in order to derive effective convection mixing lengths which are then inputted into the especially prepared COBRA-IIIC code together with the effective conduction mixing lengths as derived in subtasks IVA and IVB.

## REFERENCES

1. Hsu, C.J., "Multiregion Analysis of the Effect of Rod Displacement on Heat Transfer in Slug Flow Through Closely Packed Rod Bundles," Nucl. Sci. Engr., 47, 380 (1972).
2. Rowe, D.S., "COBRA-IIIC: A Digital Computer Program for Steady State and Transient Thermal-Hydraulic Analysis of Rod Bundle Nuclear Fuel Elements," BNWL - 1695. May 1973.
3. France, D.M. and Ginsberg, T., "Improved Point-Matching Techniques Applied to Multi-Region Heat Transfer Problems," ASME Journal of Heat Transfer, Vol. 94, May 1972.
4. France, D.M. and Ginsberg, T., "Comparison of Analytic and Lumped-Parameter Solutions for Steady-State Heat Transfer in Fuel-Rod Assemblies," Progress in Heat and Mass Transfer, Vol. 7.
5. J-Y. Kim: "Fully-Developed Mixed Convection Heat Transfer in the Finite Hexagonal Bundles," M.S. Thesis, Dept. Nuclear Engineering, MIT, Feb. 1977.
6. C-J. Hsu: "Laminar-and Slug Flow Heat Transfer Characteristics of Fuel Rods Adjacent to the Fuel Subassembly Walls," Nucl. Sci. Engrg.

TABLE 1

## Thermal and Geometric Parameters Used in Clad Temperature Calculations

Case 1 and 2	Pitch to diameter ratio	$(P/D) = 1.30$
	Wall distance to radius ratio	$(2W/D) = 1.38$
	Fuel Rod Radius	$(b) = 0.177"$
	Fuel Pellet Radius	$(a) = 0.159"$
	Power Density	$(q''') = 0.547 \times 10^8 \text{ BTU/ft}^3\text{-hr.}$
	Coolant conductivity	$(k_c) = 15.5 \text{ BTU/ft-hr}^\circ\text{F.}$
Case 2 only	Clad Conductivity	$(k) = 13.0 \text{ BTU/ft-hr}^\circ\text{F.}$
	Fuel Conductivity	$(k_f) = 2.0 \text{ BTU/ft-hr}^\circ\text{F.}$



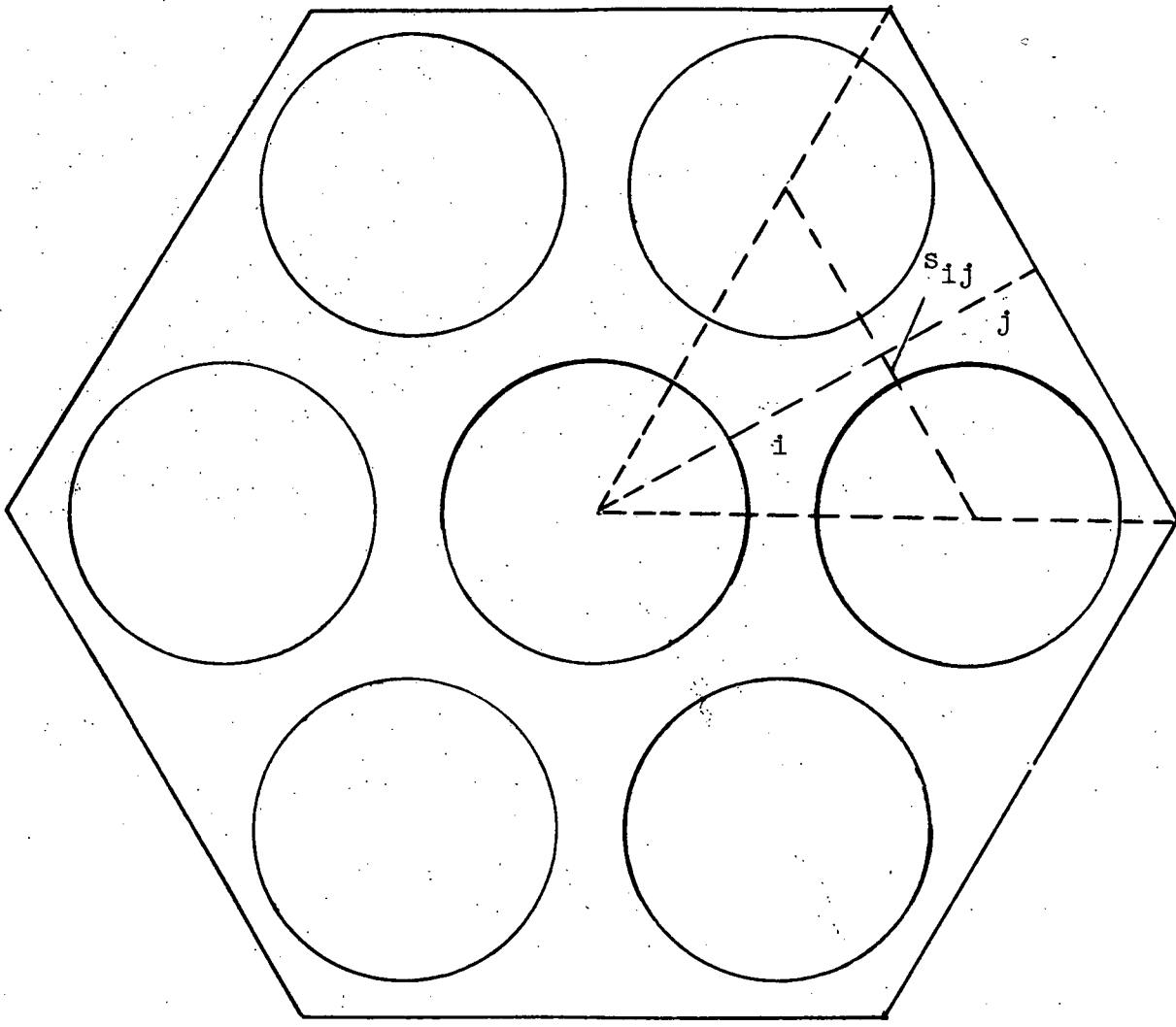


Fig. 1 Configuration of a 7 Pin Bundle

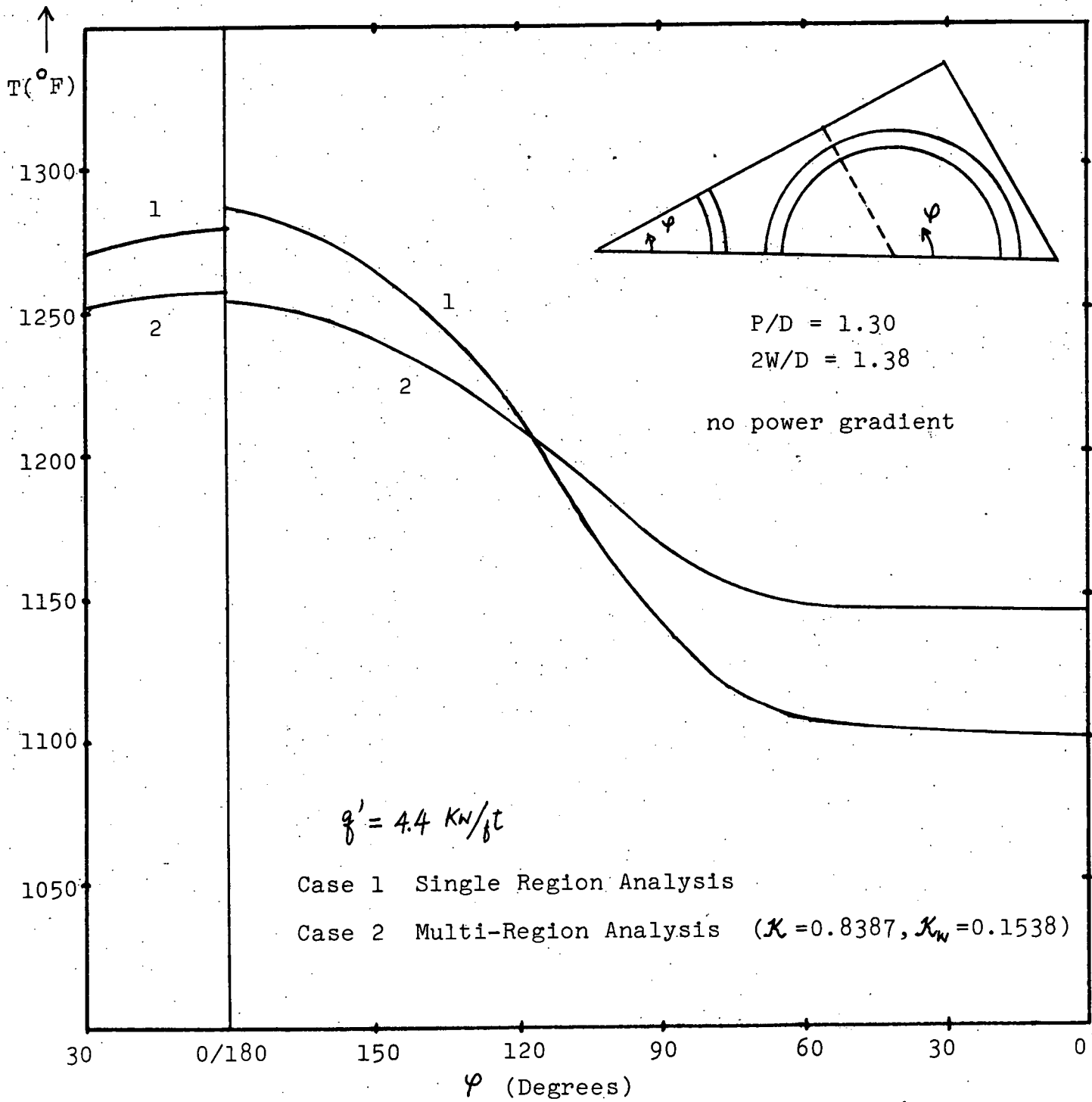


Fig. 2 Clad Temperature Distributions for a 7 Pin Bundle

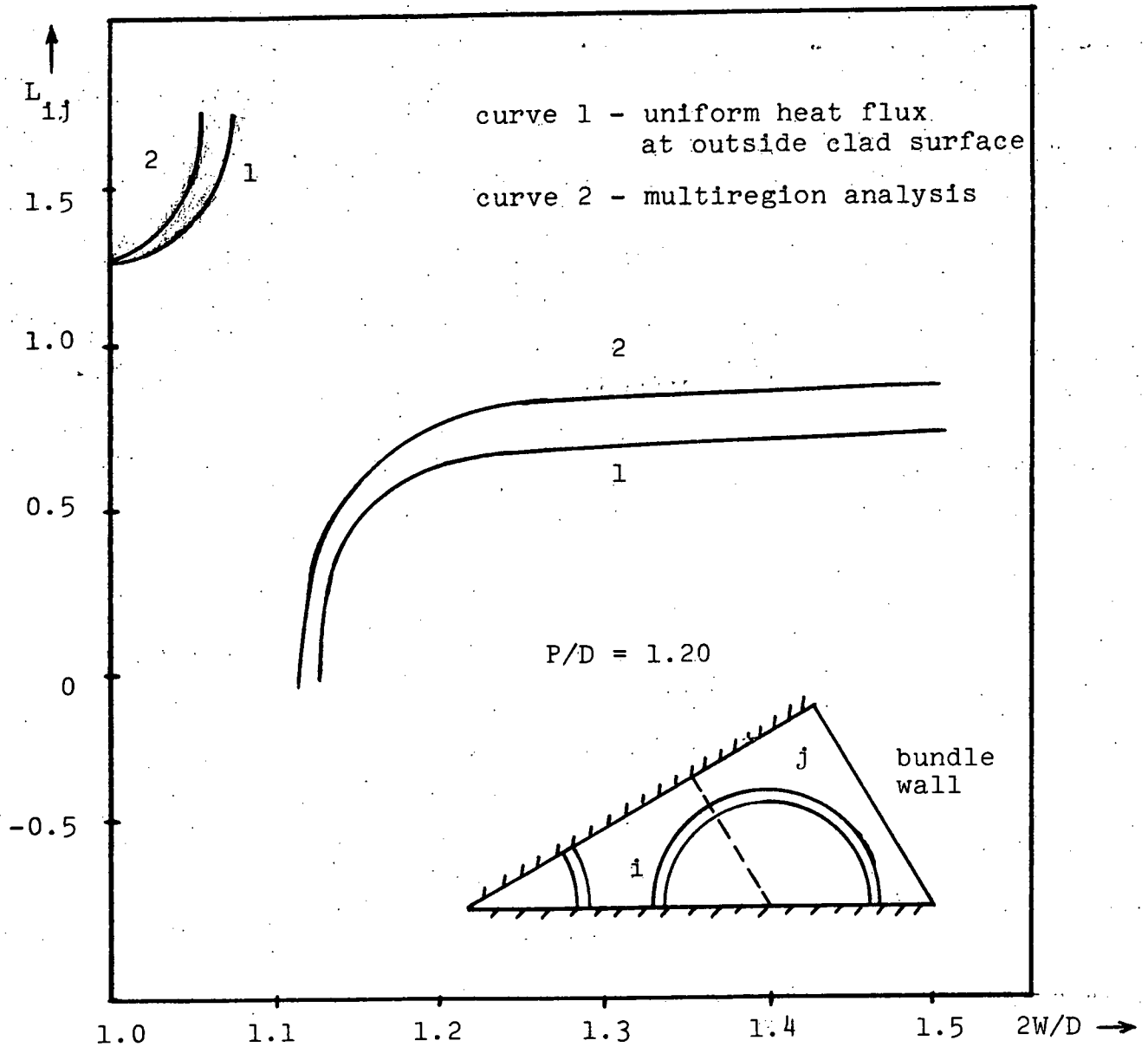


Fig. 3 Normalized Effective Conduction Mixing Lengths vs. Wall Distance in The Range of Interest

Table 2

Effect of different  $L_{ij}$ 's upon average cell temperatures and their differences as calculated by COBRA-IIIC at core exit  
 $P/D = 1.2$ ,  $2W/D = 1.24$   $\bar{q}'' = 0.3 \times 10^6$  BTU/ft<sup>2</sup>-hr

	$\bar{T}_{\text{internal}}$ °F	$\bar{T}_{\text{corner}}$ °F	$\Delta T$ °F
without conduction	1025.42	924.37	101.05
$L_{ij} = 1.0$	1011.74	931.46	80.28
$L_{ij} = 0.65$	1006.08	934.39	71.69

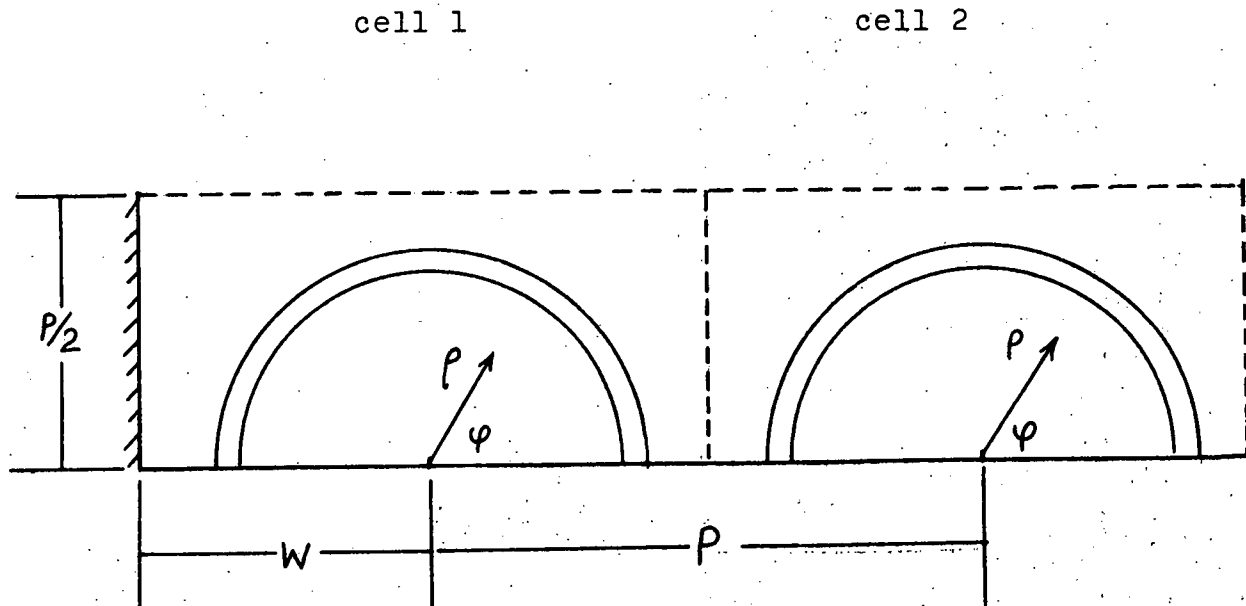


Fig. 4: A Two Cell Section of a Square Array Configuration

64

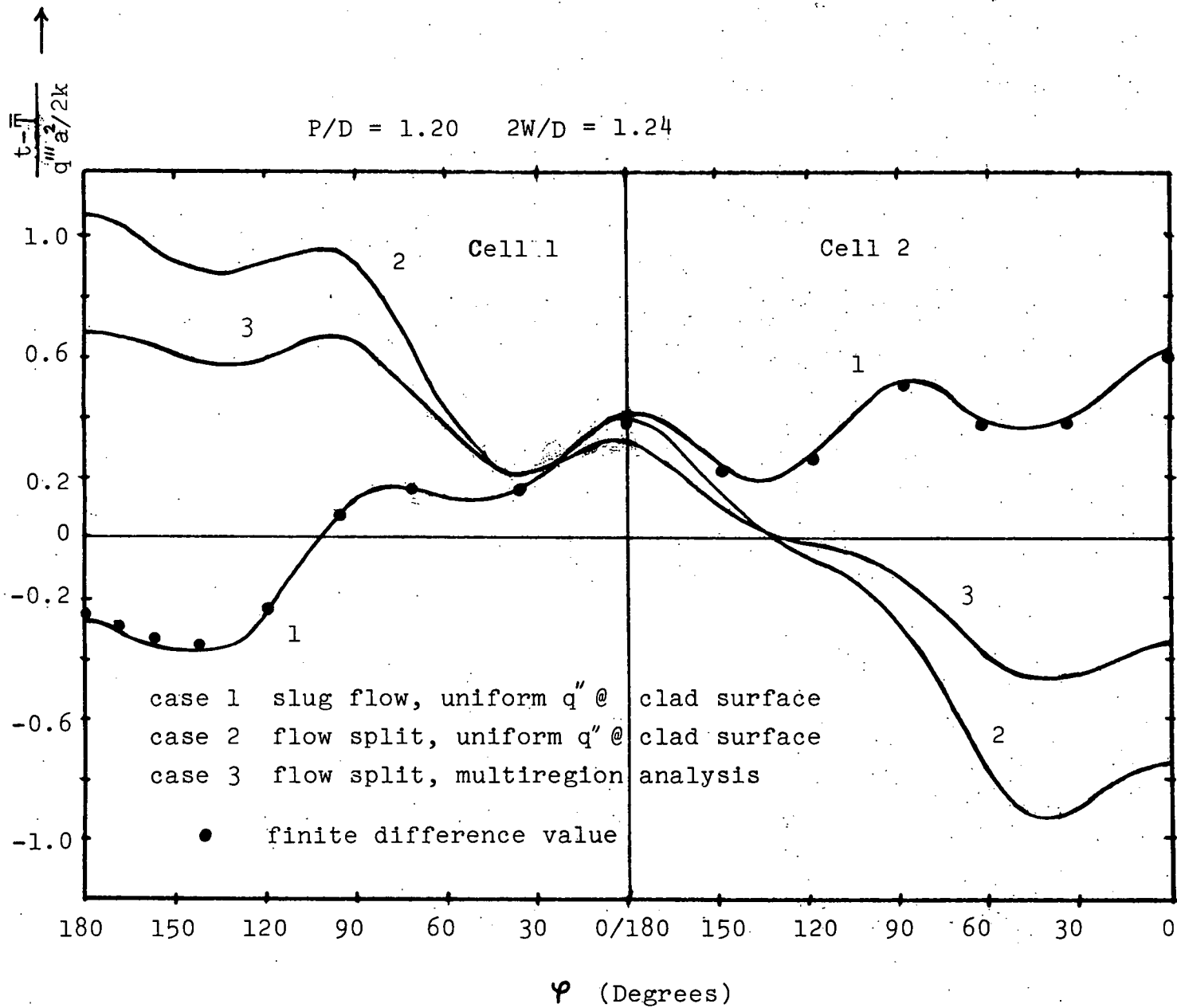
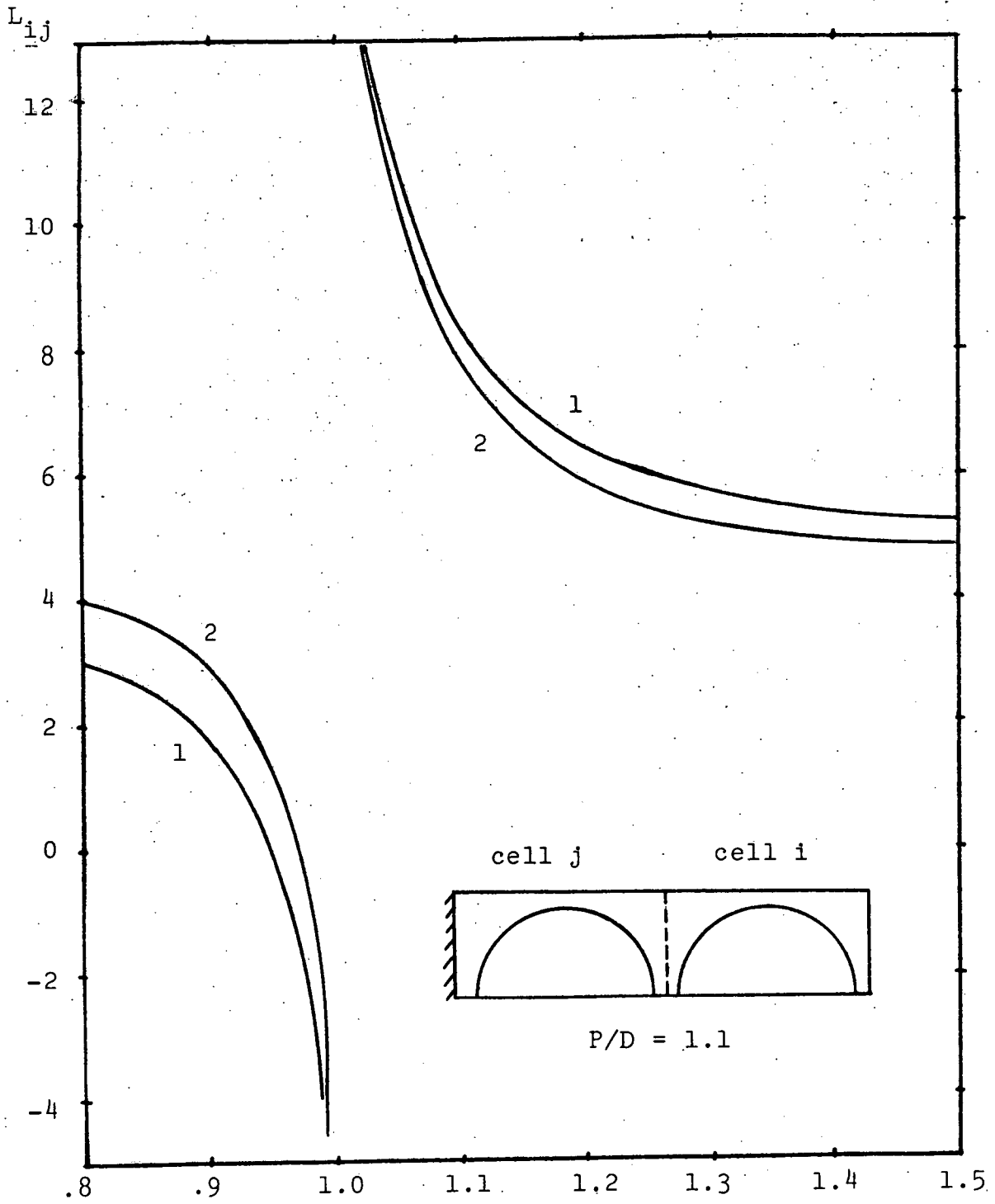


Fig.5 Clad Temperature Distributions of the Two-Cell Configuration

Fig. 6  $L_{ij}$  in Square Cell Configuration

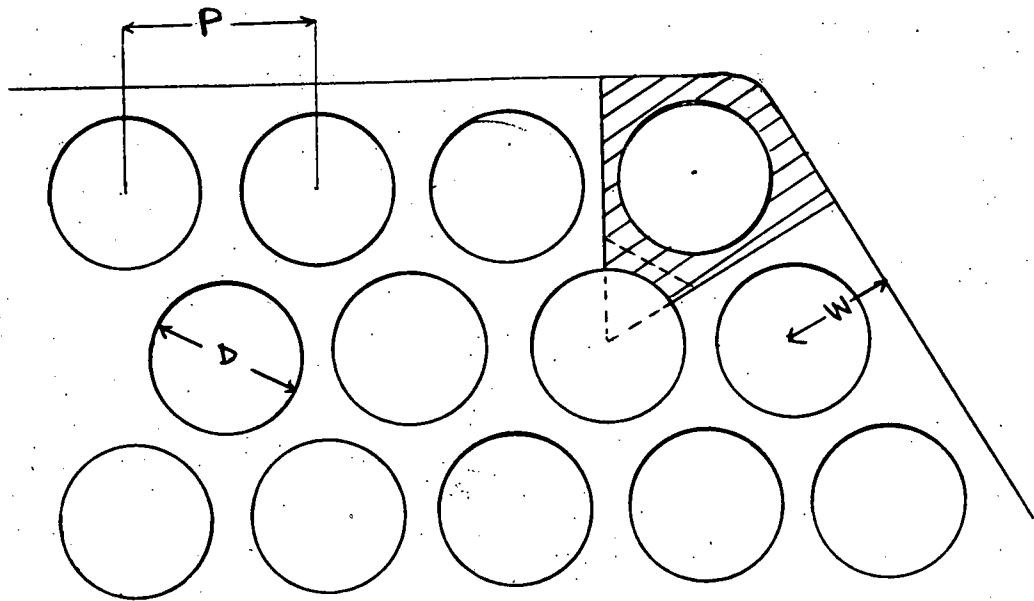


Fig. 7a: Geometry of the Coupled Two-Cell Analysis for the Corner Region.

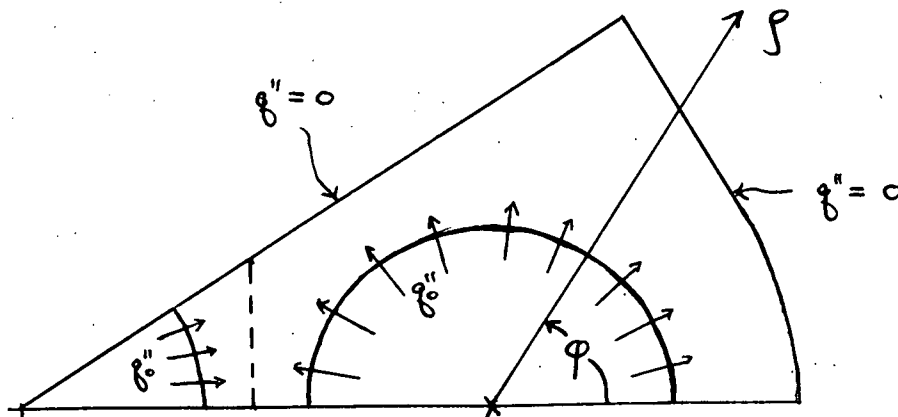


Fig. 7b: Thermal Boundary Conditions for the Coupled Two-Cell Analysis



$$\theta(\varphi, z) = \frac{T(r, \varphi, z) - T_{in}}{q'' r_c / k}$$

Conditions :  $P/D = 1.3$  ,  $2W/D = 1.38$   
 $D = 9 \text{ mm.}$  ,  $q'' = 104 \text{ W/cm}^2$   
 $T_{in} = 415^\circ\text{C}$  ,  $Pe = 372$

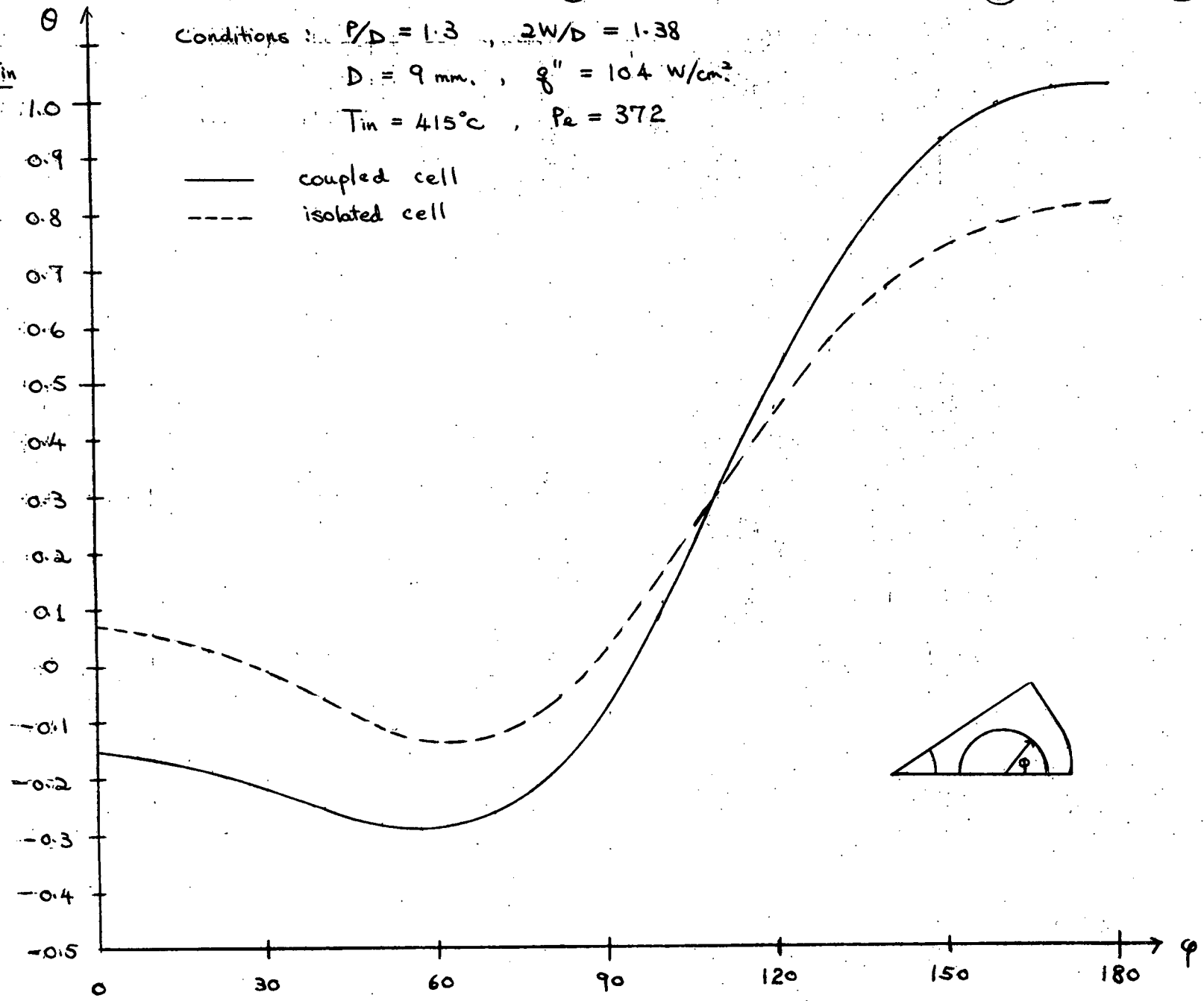


Fig. 8: Comparison of Corner Pin Clad Temperature Distributions for One and Two-Cell Analyses

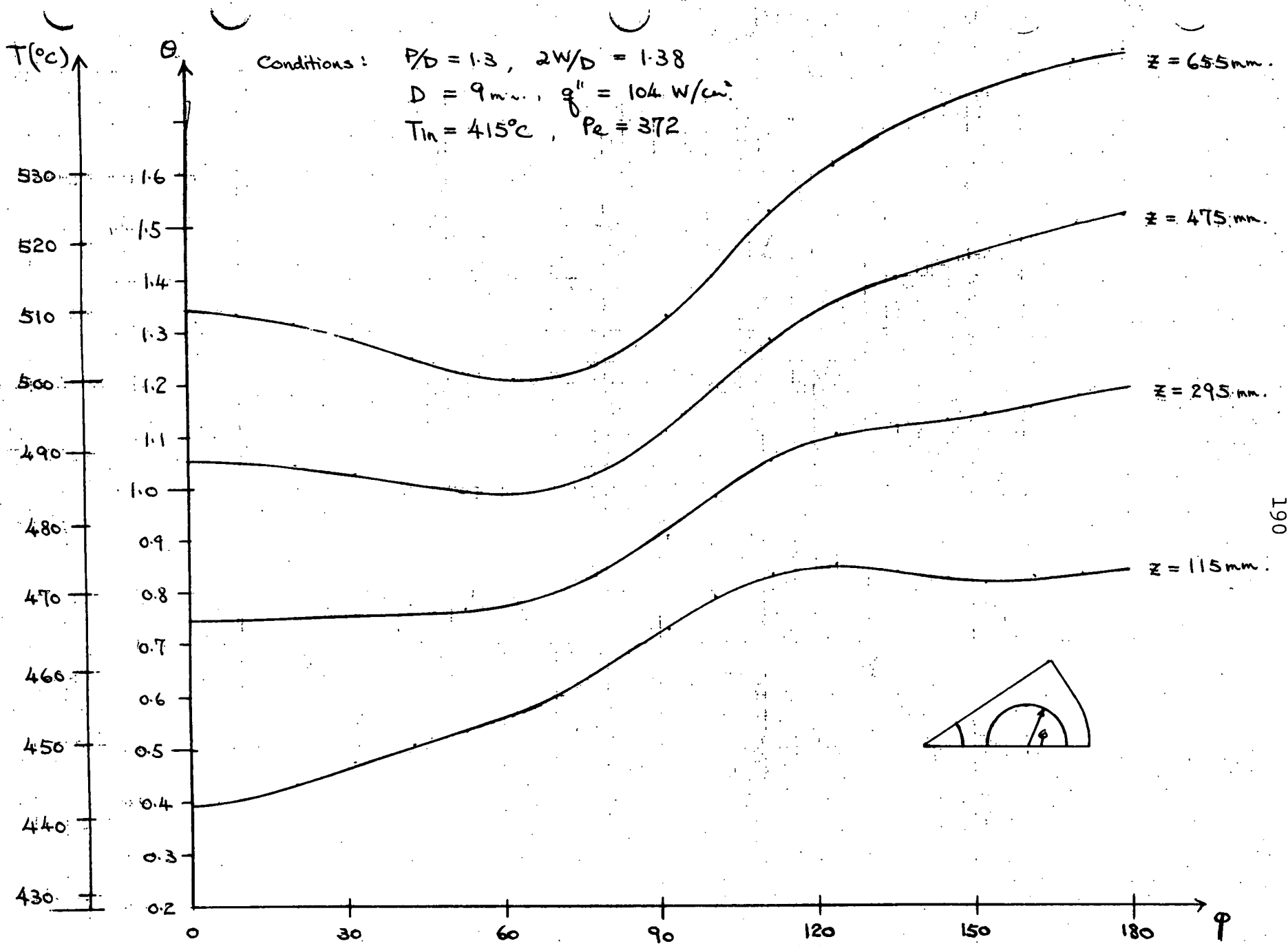


Fig. 9: Axial Development of Corner Pin Clad Temperature Distribution as Predicted by Coupled Two-Cell Analysis

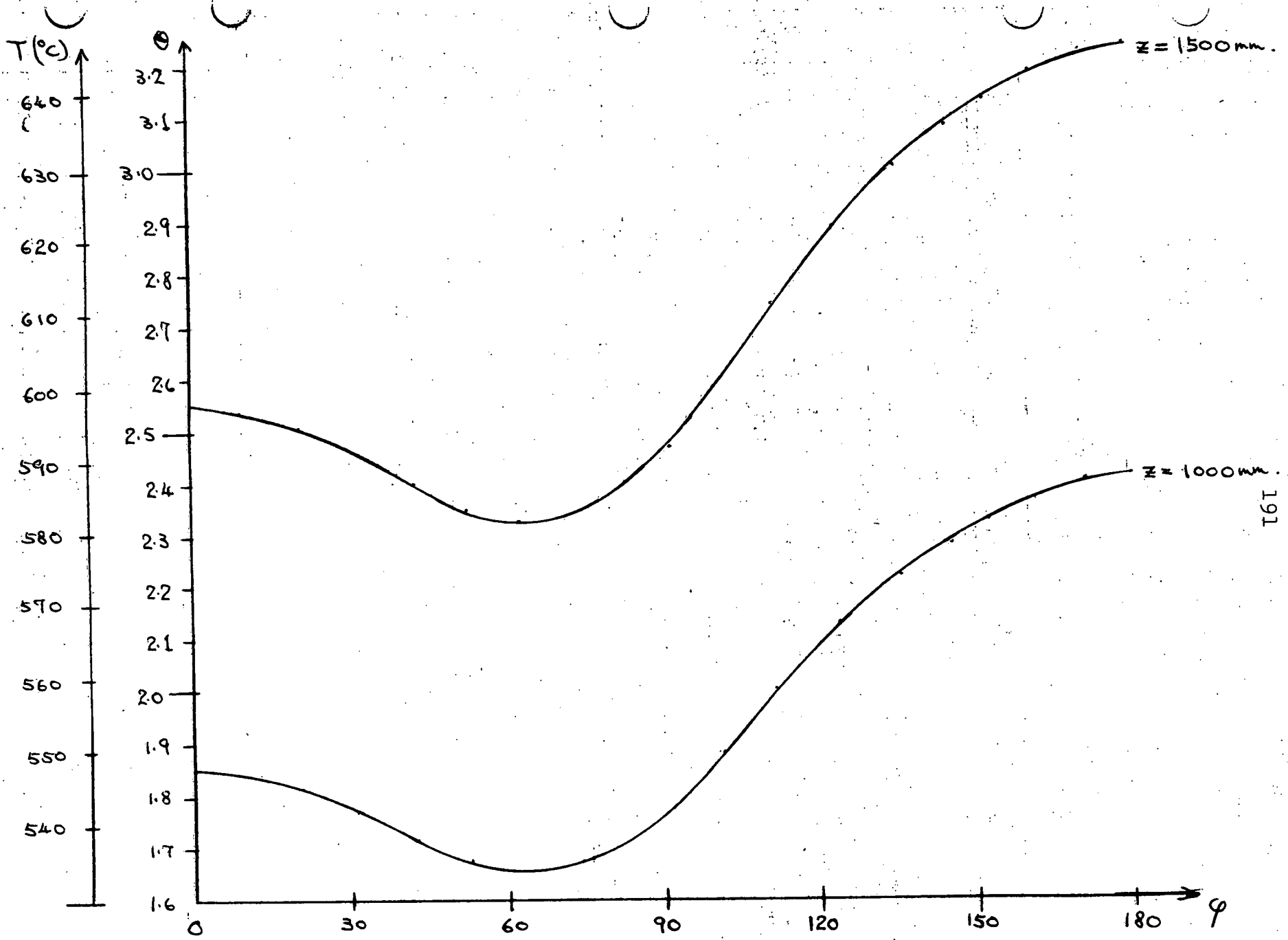
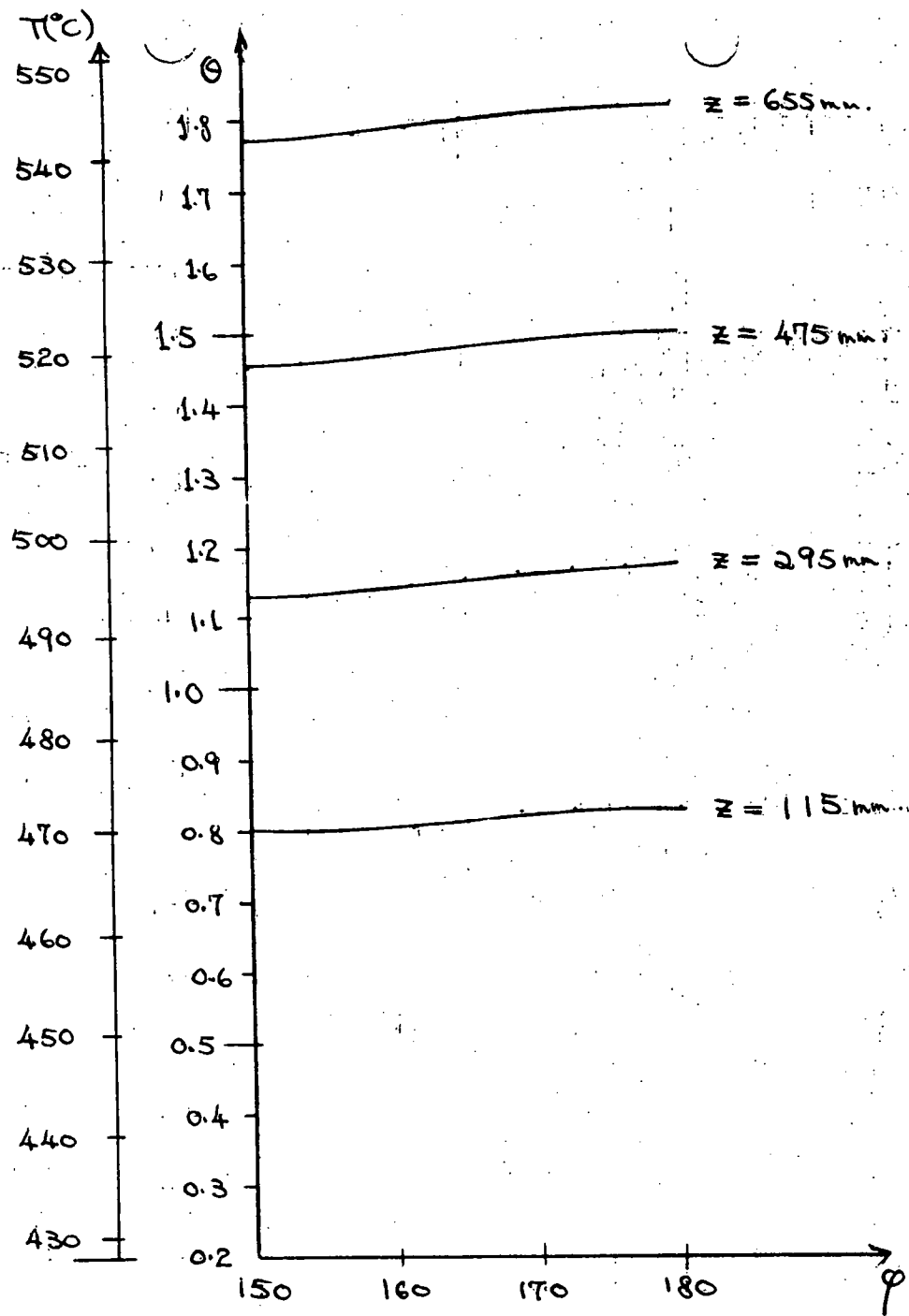


Fig. 9 (Continued)



Conditions:

$$P/D = 1.3$$

$$2W/D = 1.38$$

$$D = 9 \text{ mm.}$$

$$q_0'' = 104 \text{ W/cm}^2$$

$$T_{in} = 415^\circ\text{C}$$

$$P_e = 372$$

Fig. 10: Axial Development of Internal Pin Clad Temperature Distribution as Predicted by Coupled Two Cell Analysis

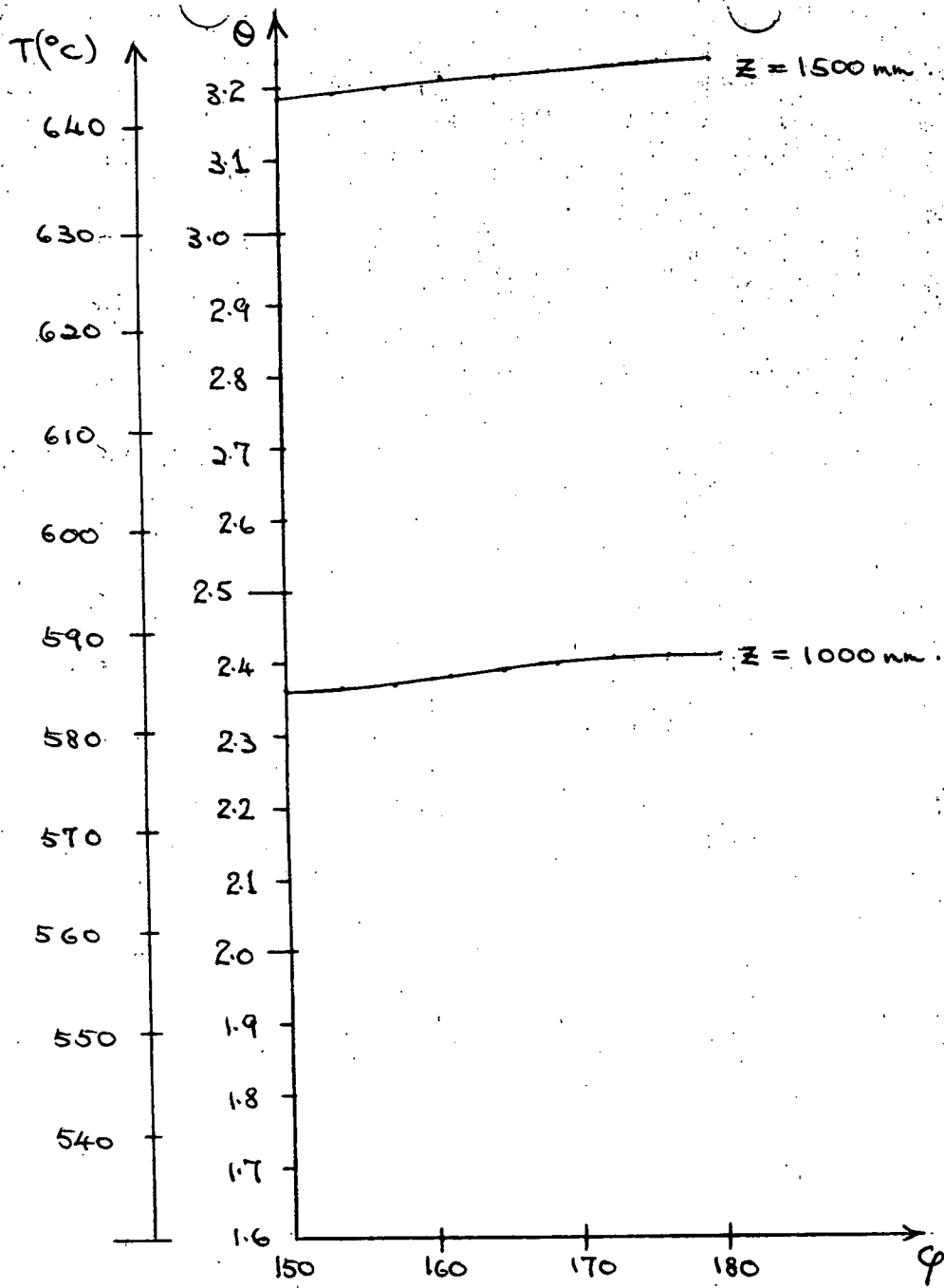


Fig. 10 (Continued)

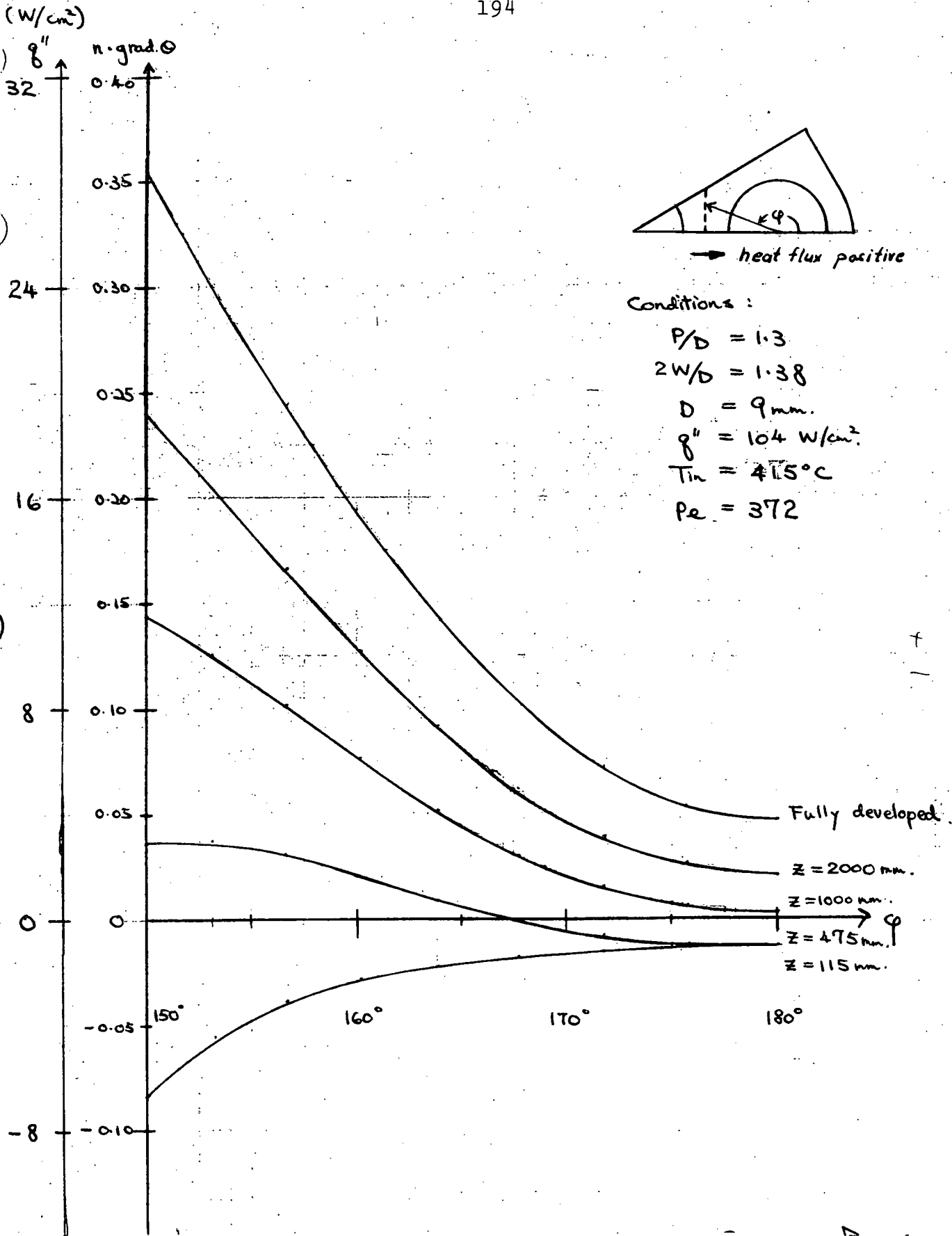


Fig. 11: Axial Development of the Heat Flux Distribution Along the Imaginary Common Boundary Between the Two Cells

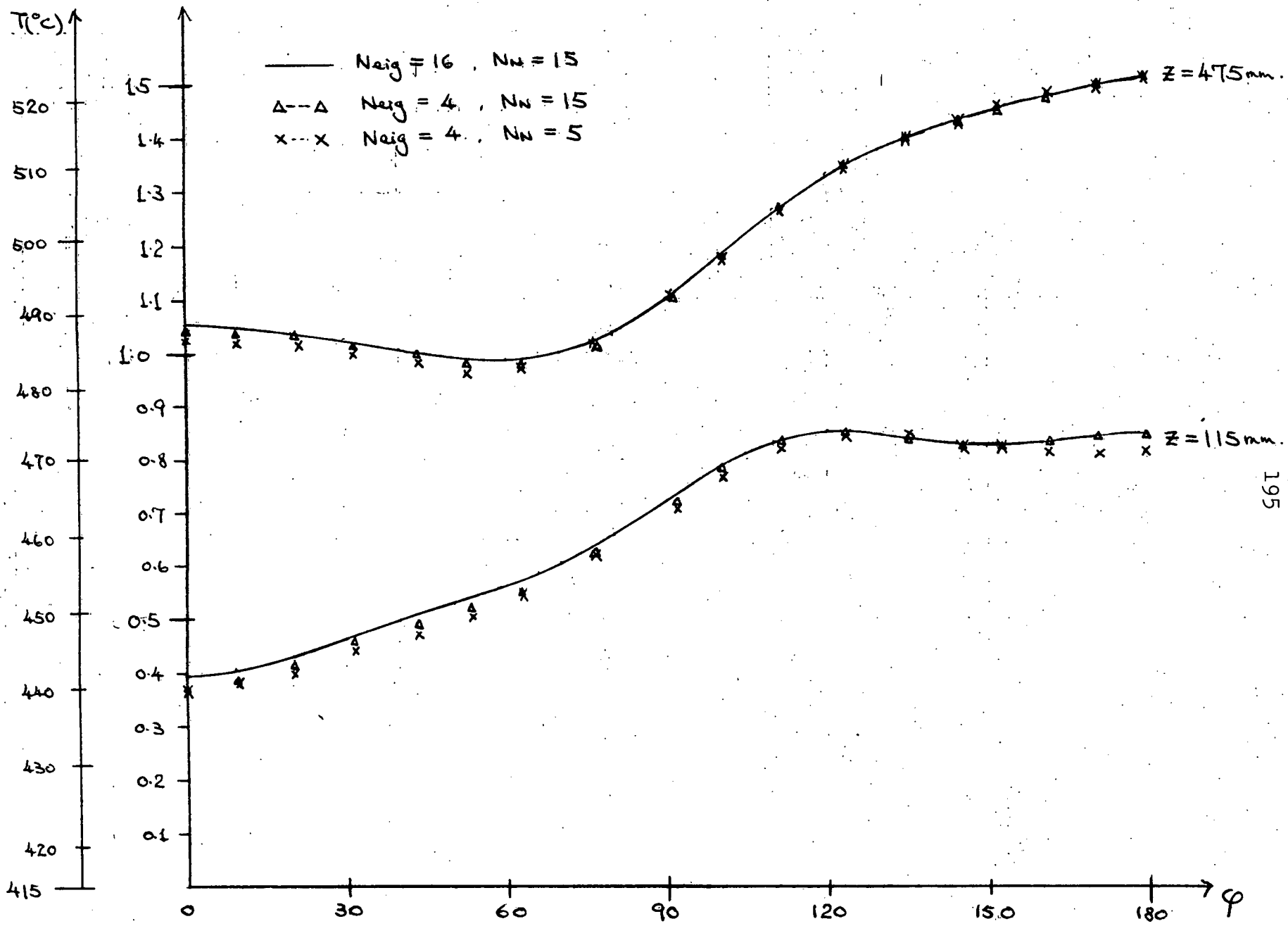


Fig. 12: Effect of Upper Limit in the Eigenvalues Upon the Corner Pin Clad Temperature Distribution

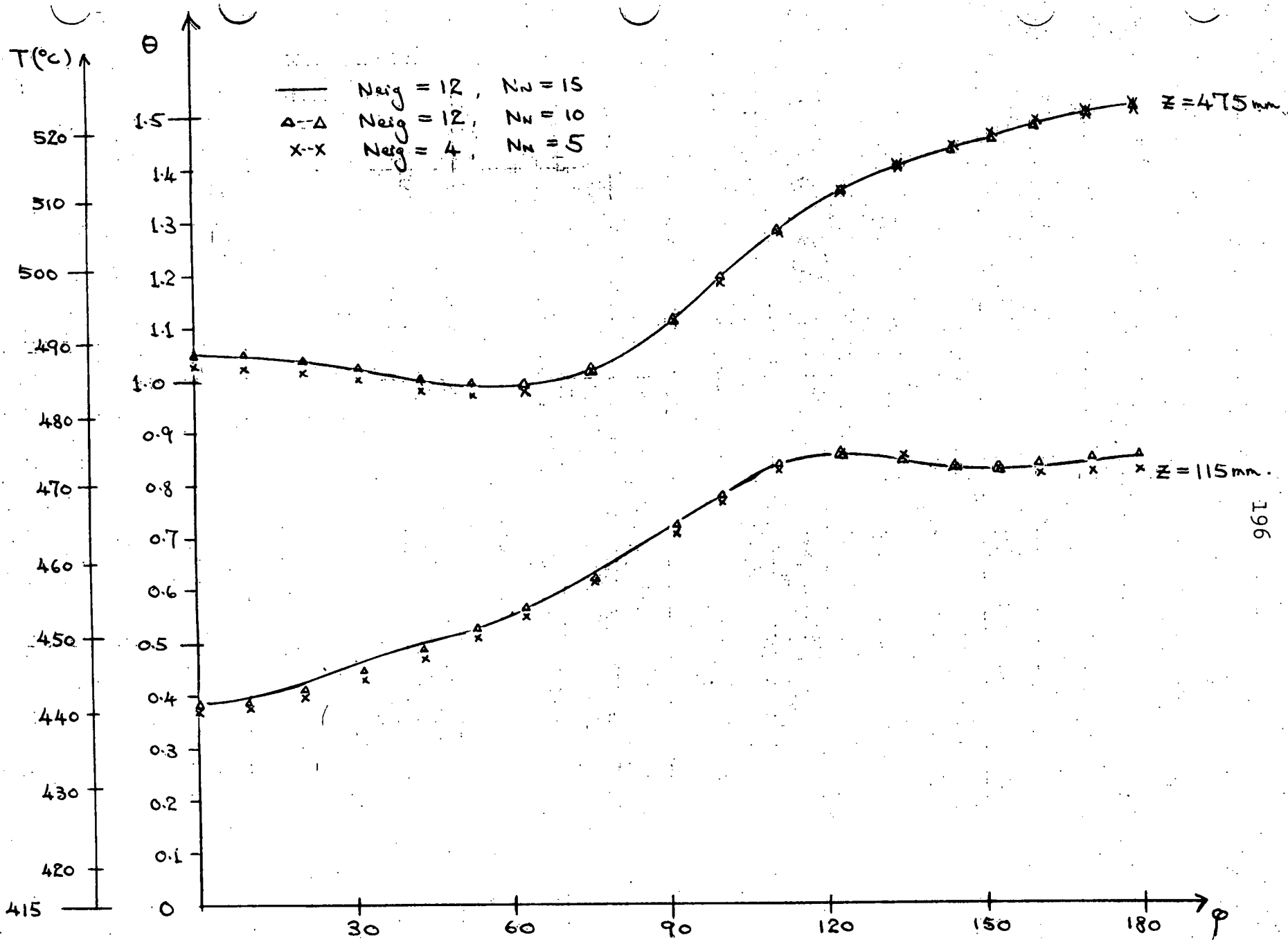


Fig. 13: Effect of Upper Limit in the Harmonics Upon the Corner Pin Clad Temperature Distribution



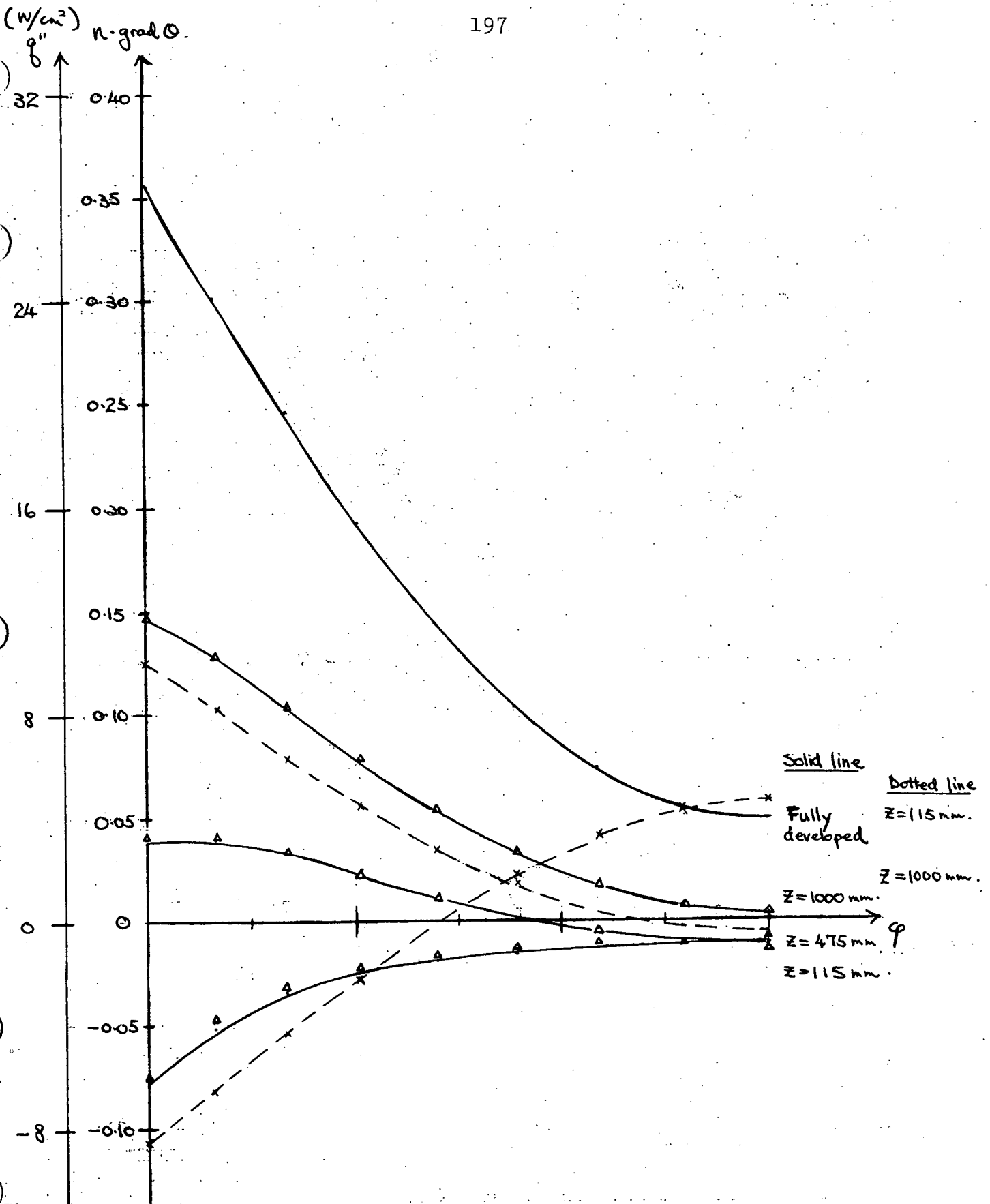


Fig. 14: Effects of Upper Limits in the Eigenvalues and Harmonics upon the Axial Development of the Heat Flux Distribution

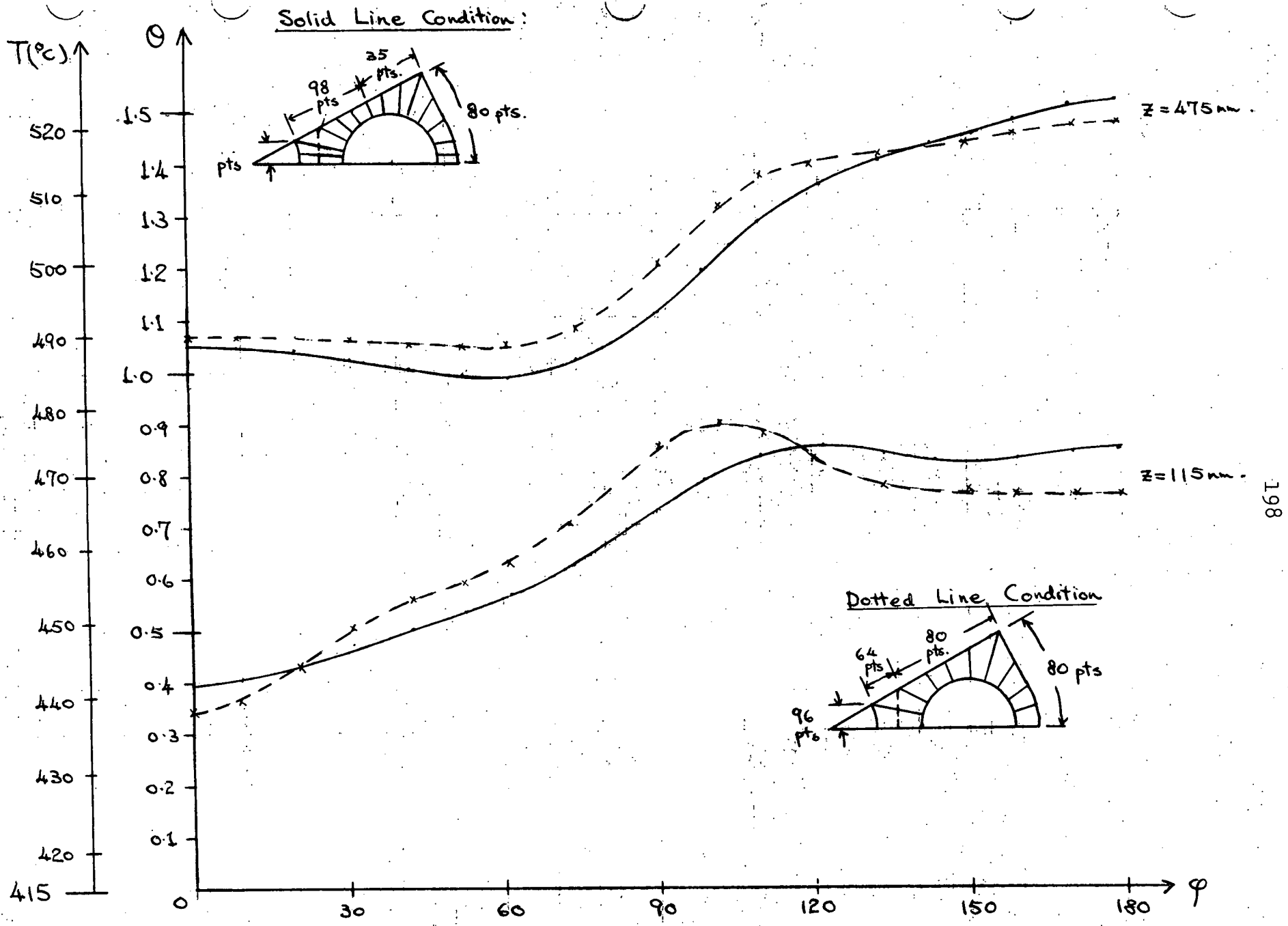


Fig. 15: Effect of Different Sets of Points at the Inlet Cross-Section Upon the Corner Pin Clad Temperature Distribution

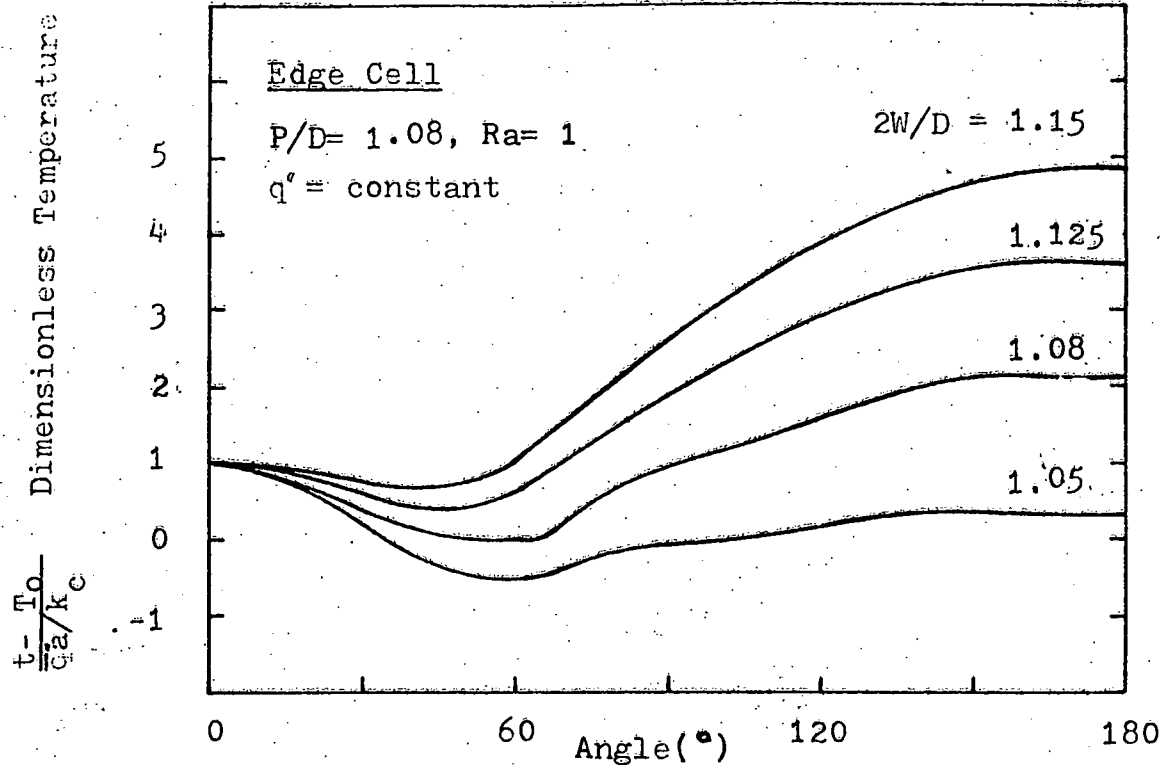
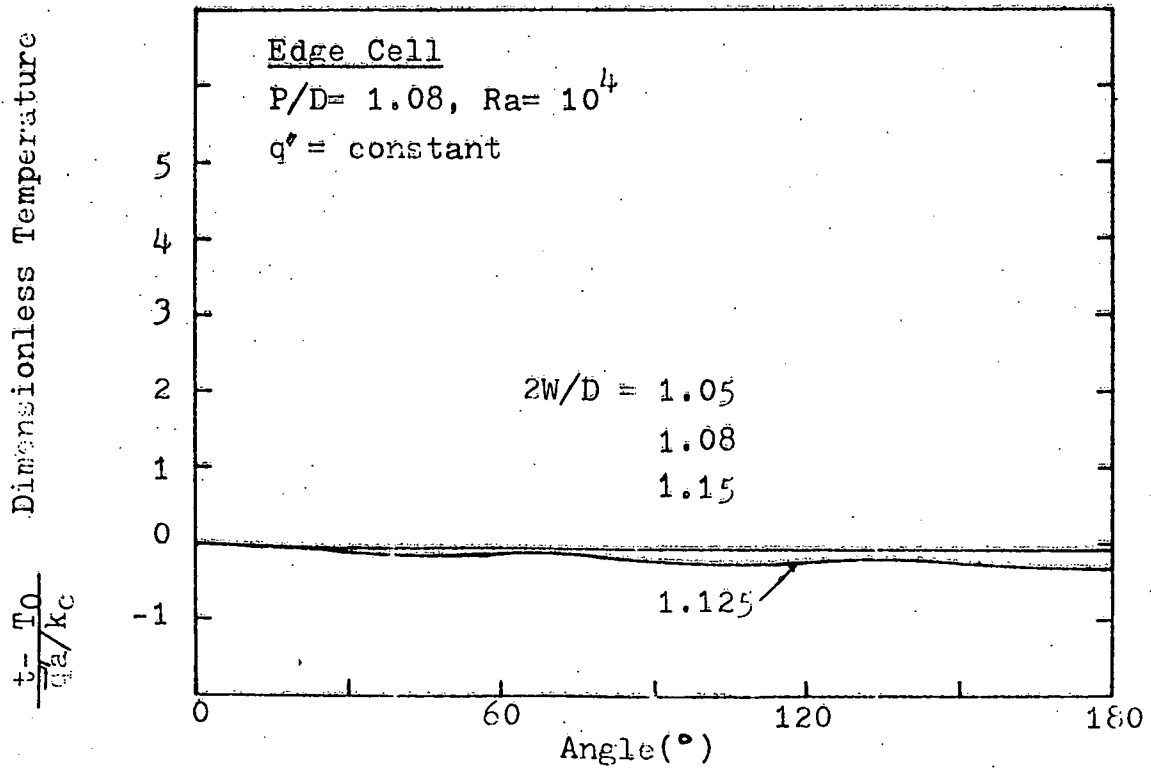


Fig. 16 Peripheral Temperature Variation along outside Clad Surface (a) for  $P/D=1.08$  and  $Ra=1$ , and (b) for  $P/D=1.08$  and  $Ra=10^4$  in Edge Cell.



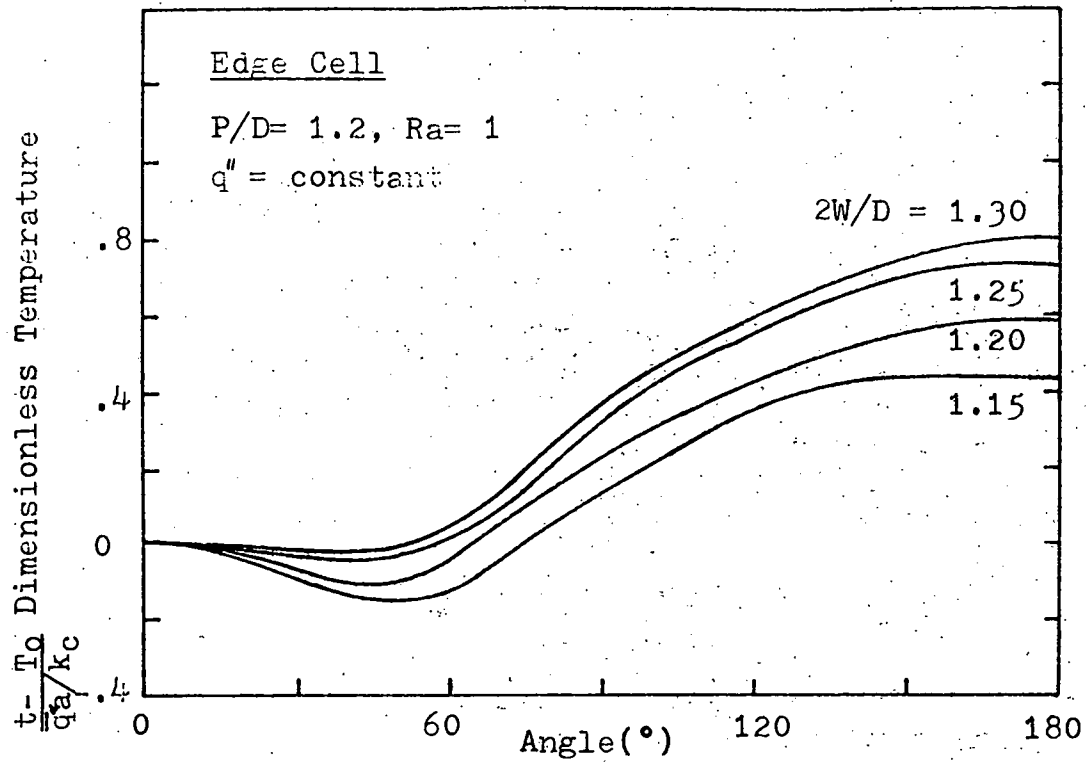
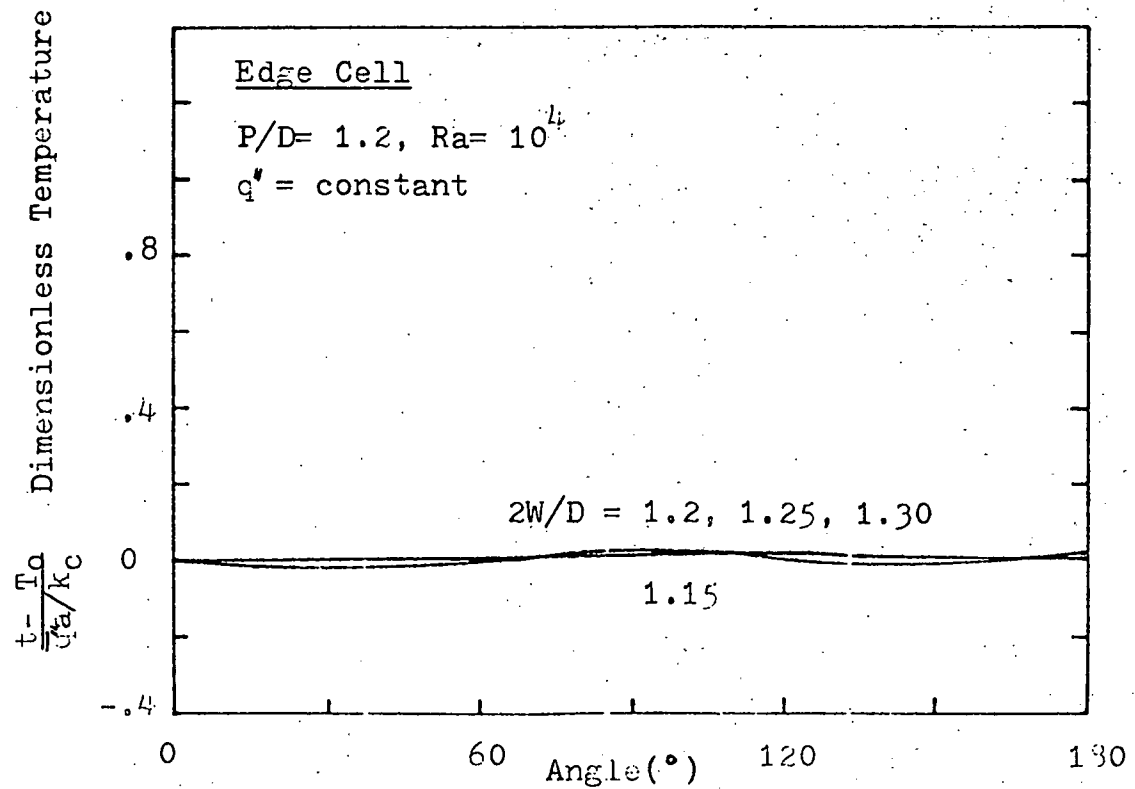


Fig. 17 Peripheral Temperature Variation along outside Clad Surface for  $P/D = 1.20$

(a)  $Ra = 1$   
 (b)  $Ra = 10^4$



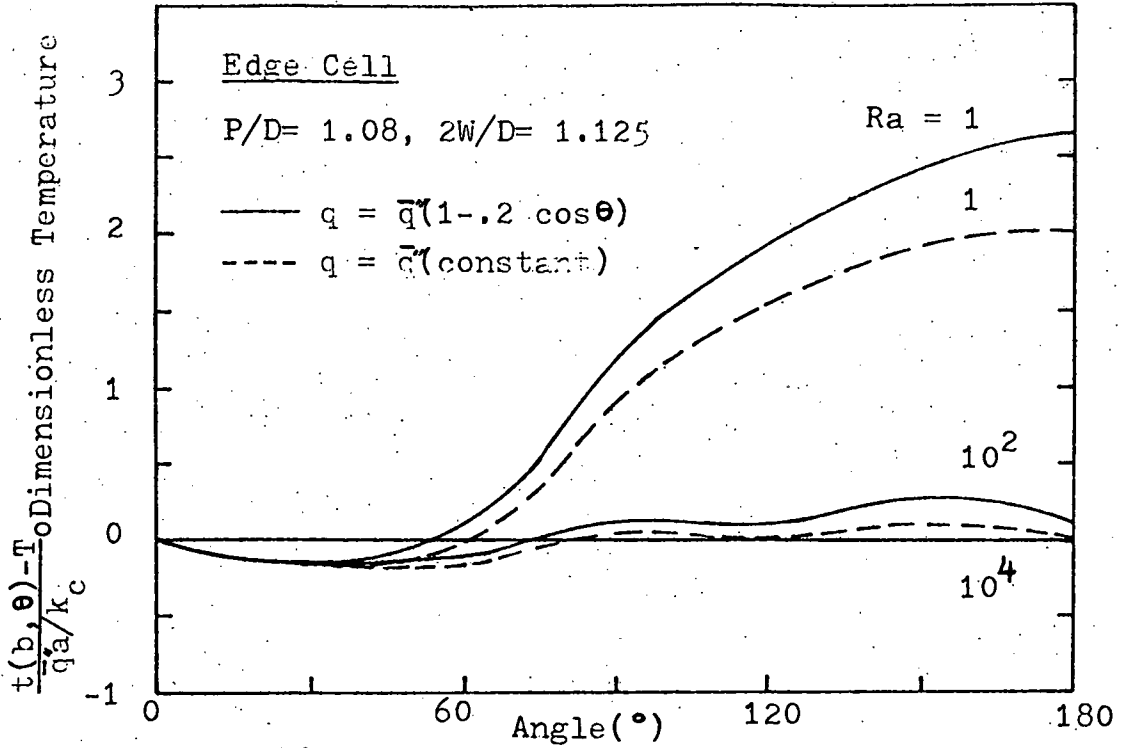
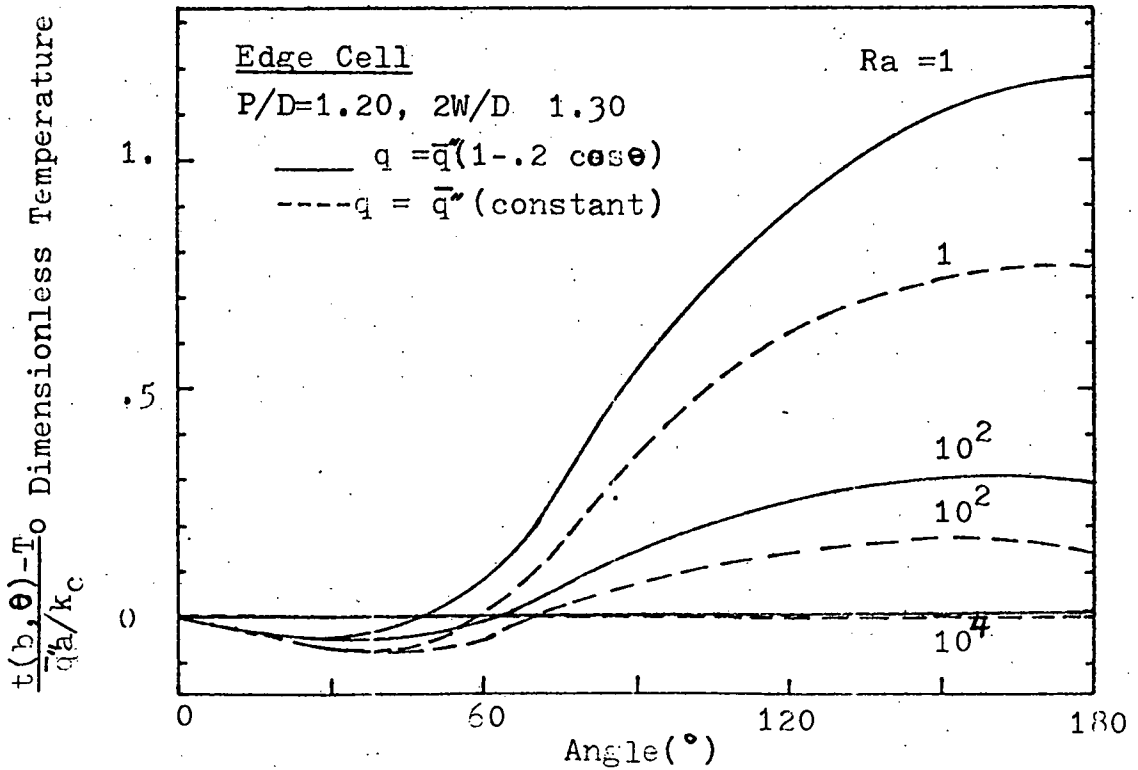


Fig. 18. Peripheral outside Clad Surface Temperature Variation for both constant and varying heat flux at (a)  $P/D=1.08$  and  $2W/D= 1.125$   
 (b)  $P/D=1.20$  and  $2W/D= 1.30$



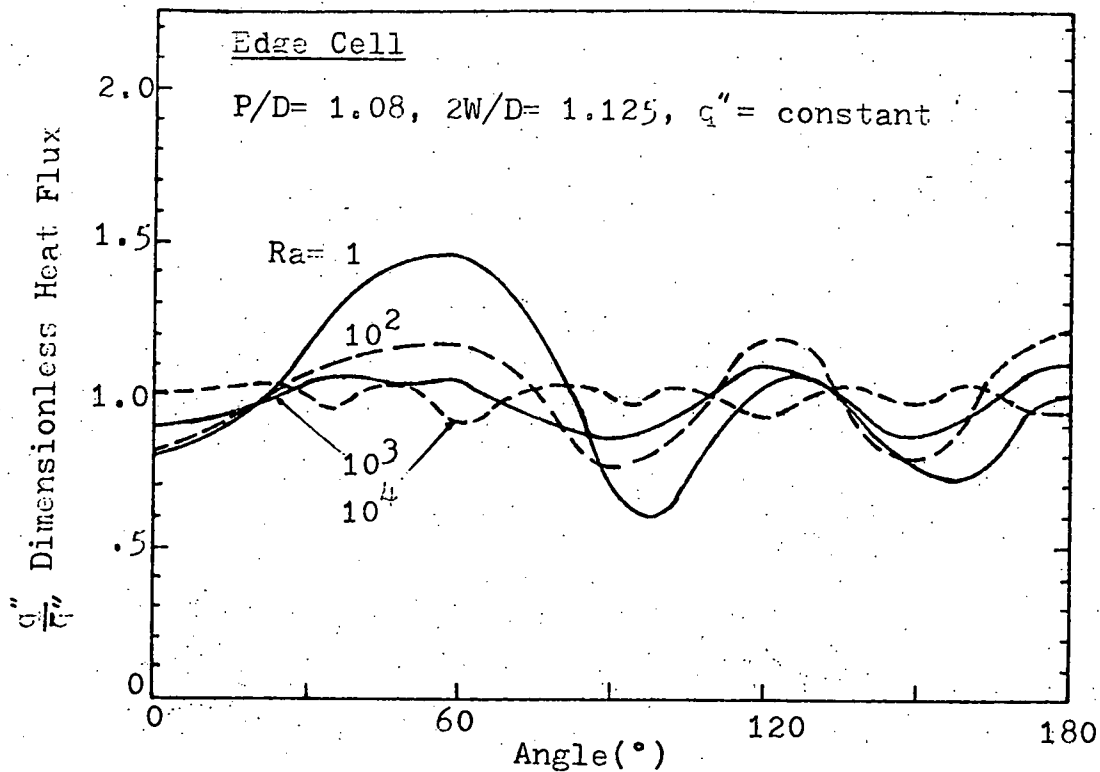
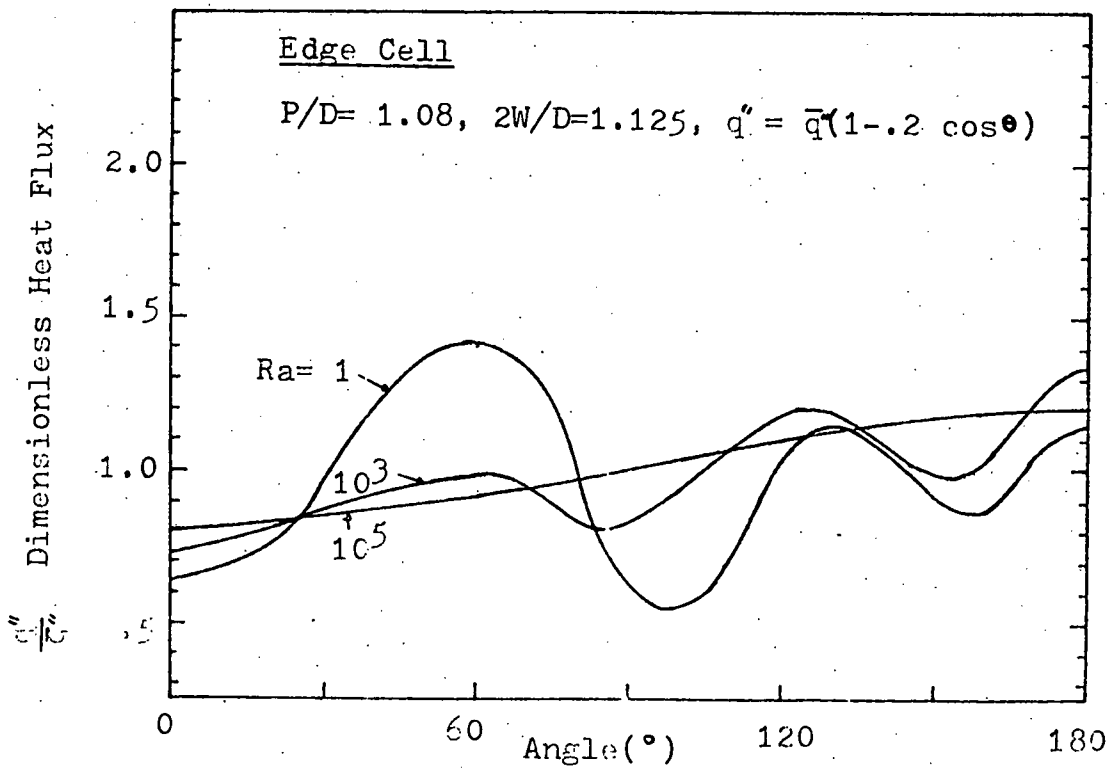


Fig. 19 Peripheral Heat Flux Variation for  $P/D = 1.08$  and  $2W/D = 1.125$  at  
 (a)  $q'' = \text{constant}$   
 (b)  $q'' = \bar{q}''(1 - 0.2 \cos \theta)$



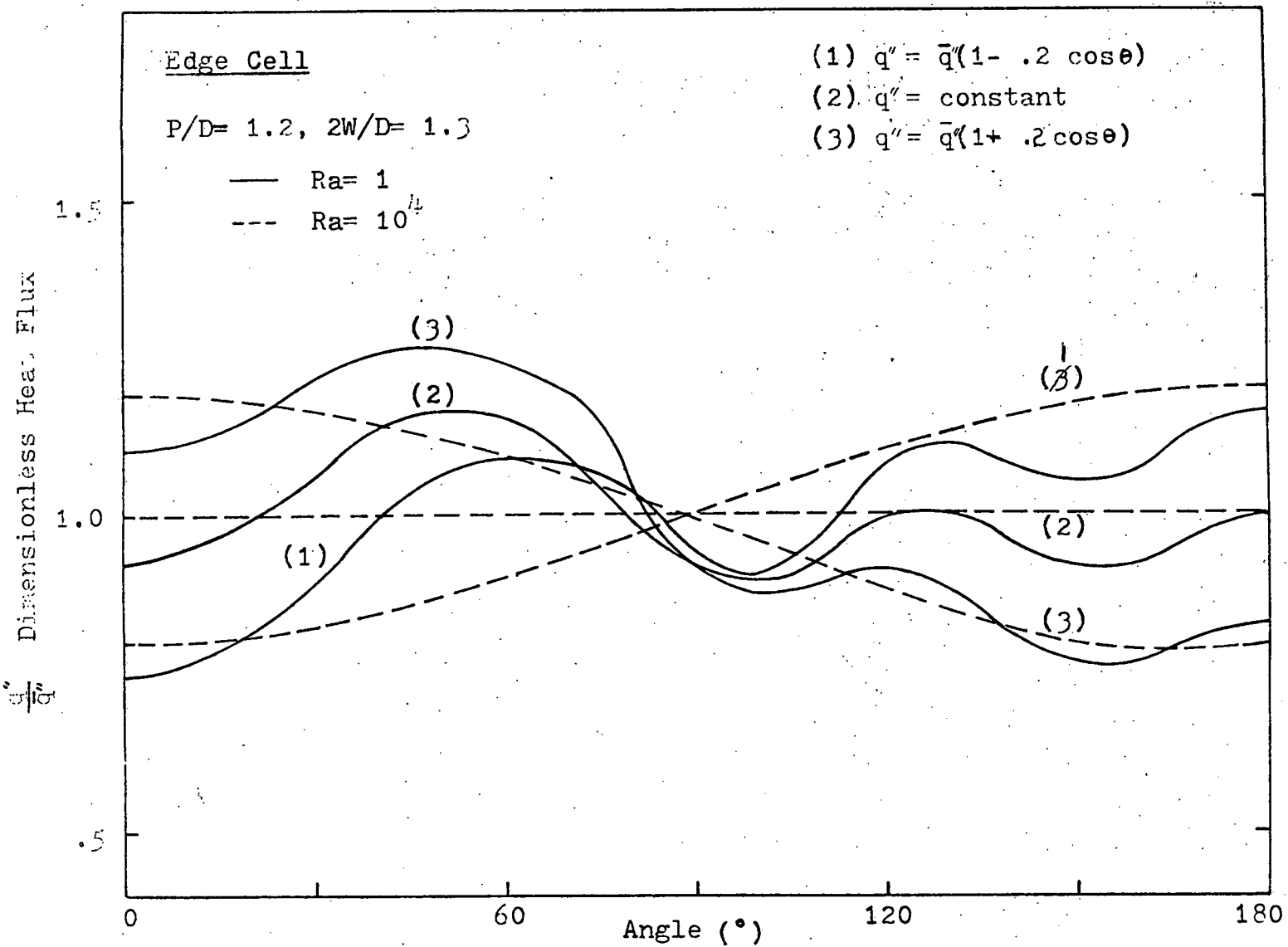


Fig. 20 Peripheral Heat flux Variation for  $P/D= 1.2$  and  $2W/D=1.3$  at three different Heat Fluxes around inside surface.

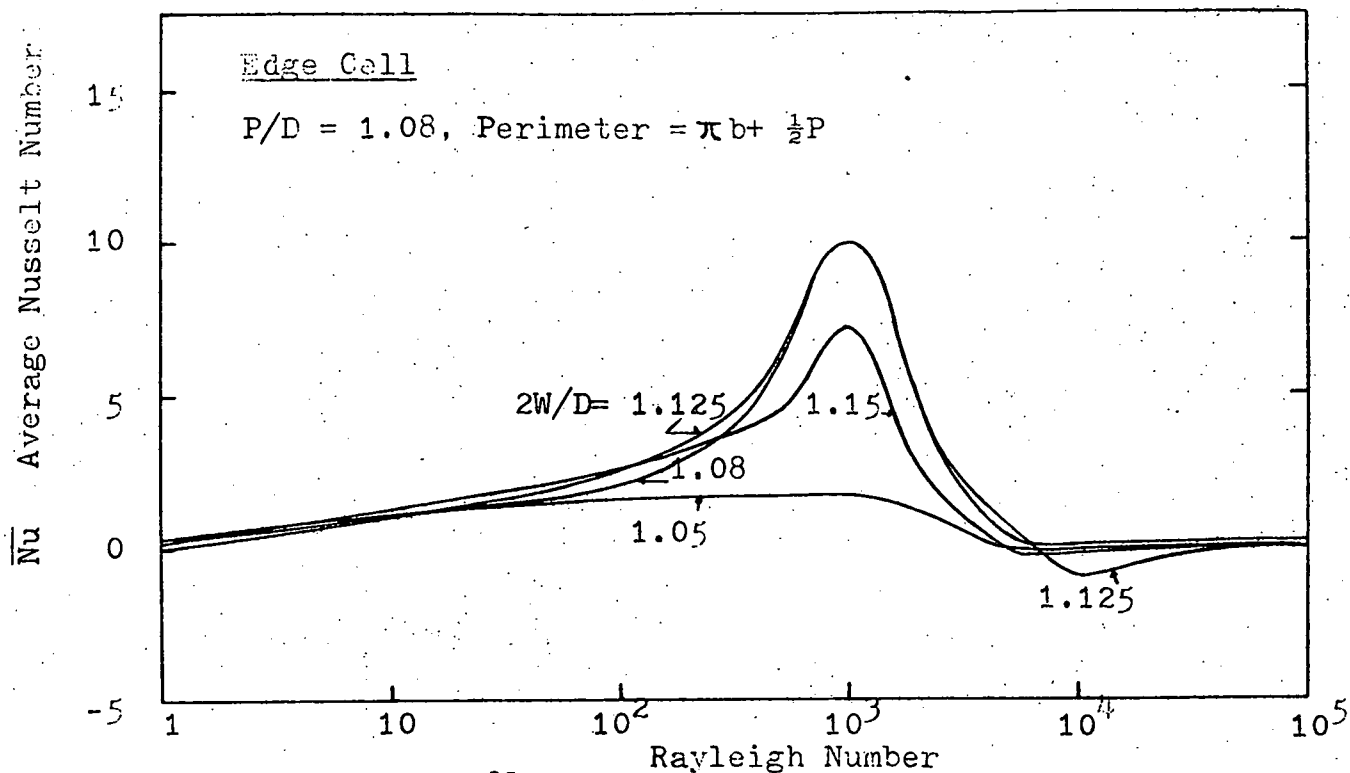


Fig. 21 Average Nusselt Number vs Rayleigh Number for  $P/D = 1.08$  based on Perimeter  $b + \frac{1}{2}P$ .

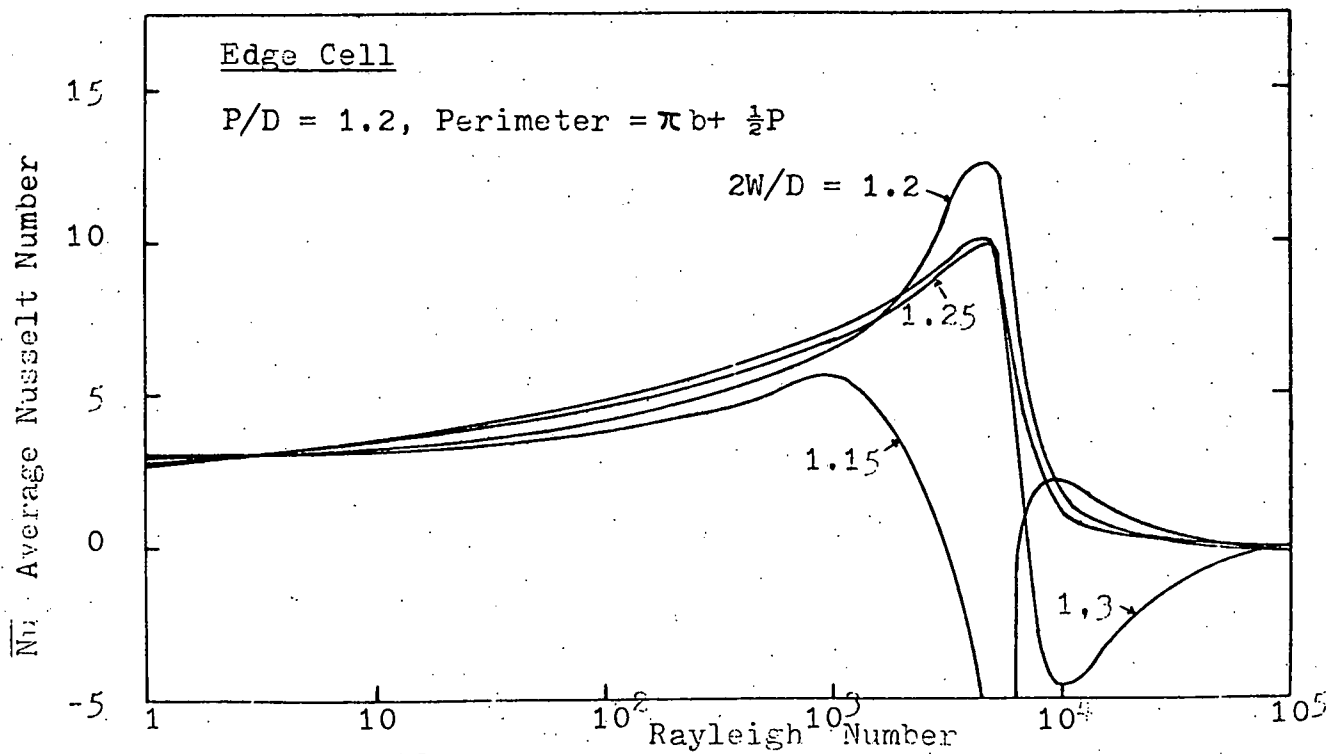


Fig. 22 Average Nusselt Number vs Rayleigh Number for  $P/D = 1.2$  and Perimeter =  $b + \frac{1}{2}P$ .



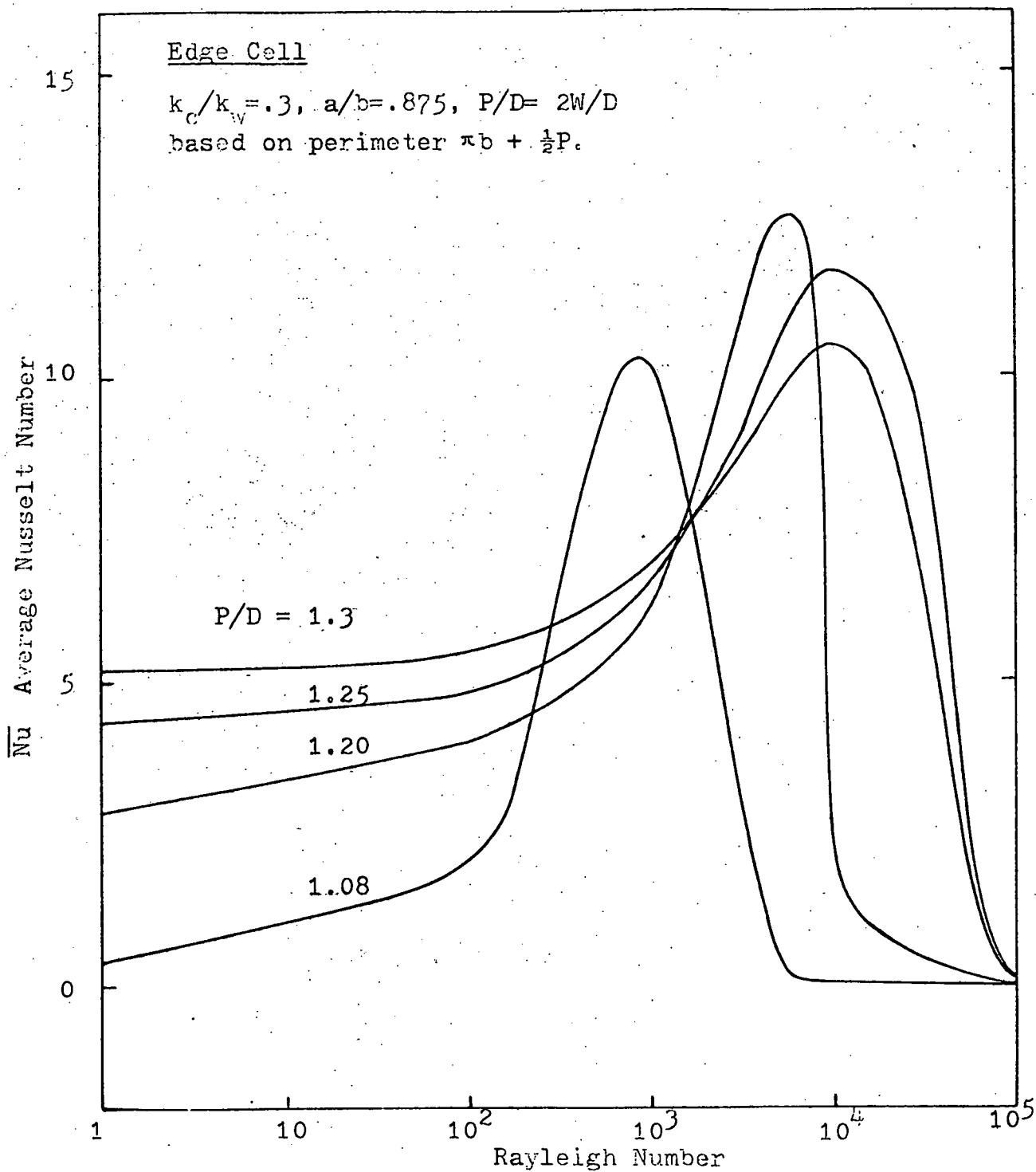


Fig. 23. Average Nusselt Number vs Rayleigh Number  
 For  $P/D = 2W/D$  based on Perimeter  $\pi b + \frac{1}{2}P$ .

Edge Cell

— P/D= 1.08, 2W/D= 1.125

--- P/D= 1.2, 2W/D= 1.3

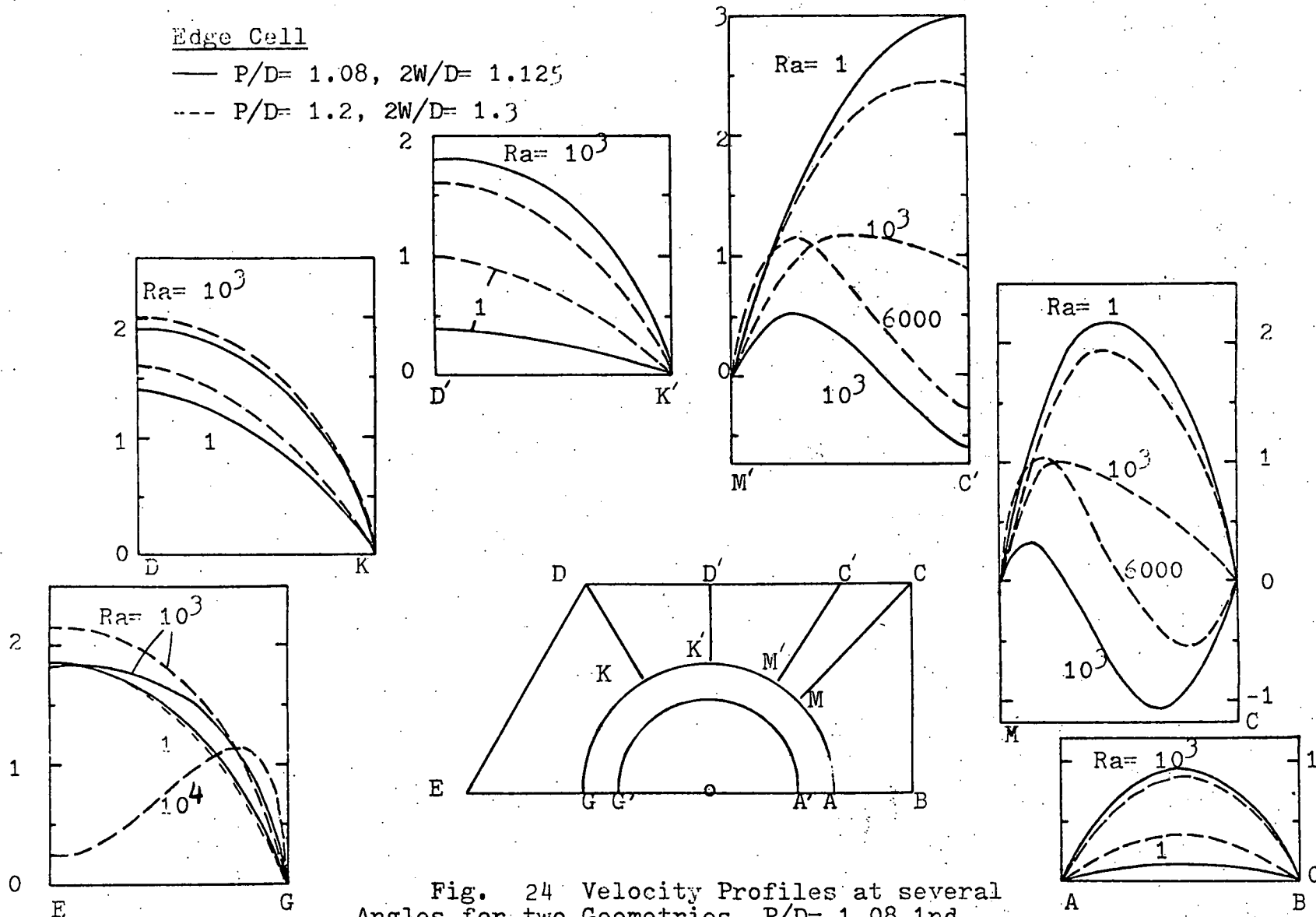


Fig. 24 Velocity Profiles at several Angles for two Geometries, P/D= 1.08 and 2W/D= 1.125, P/D= 1.20 and 2W/D= 1.30.

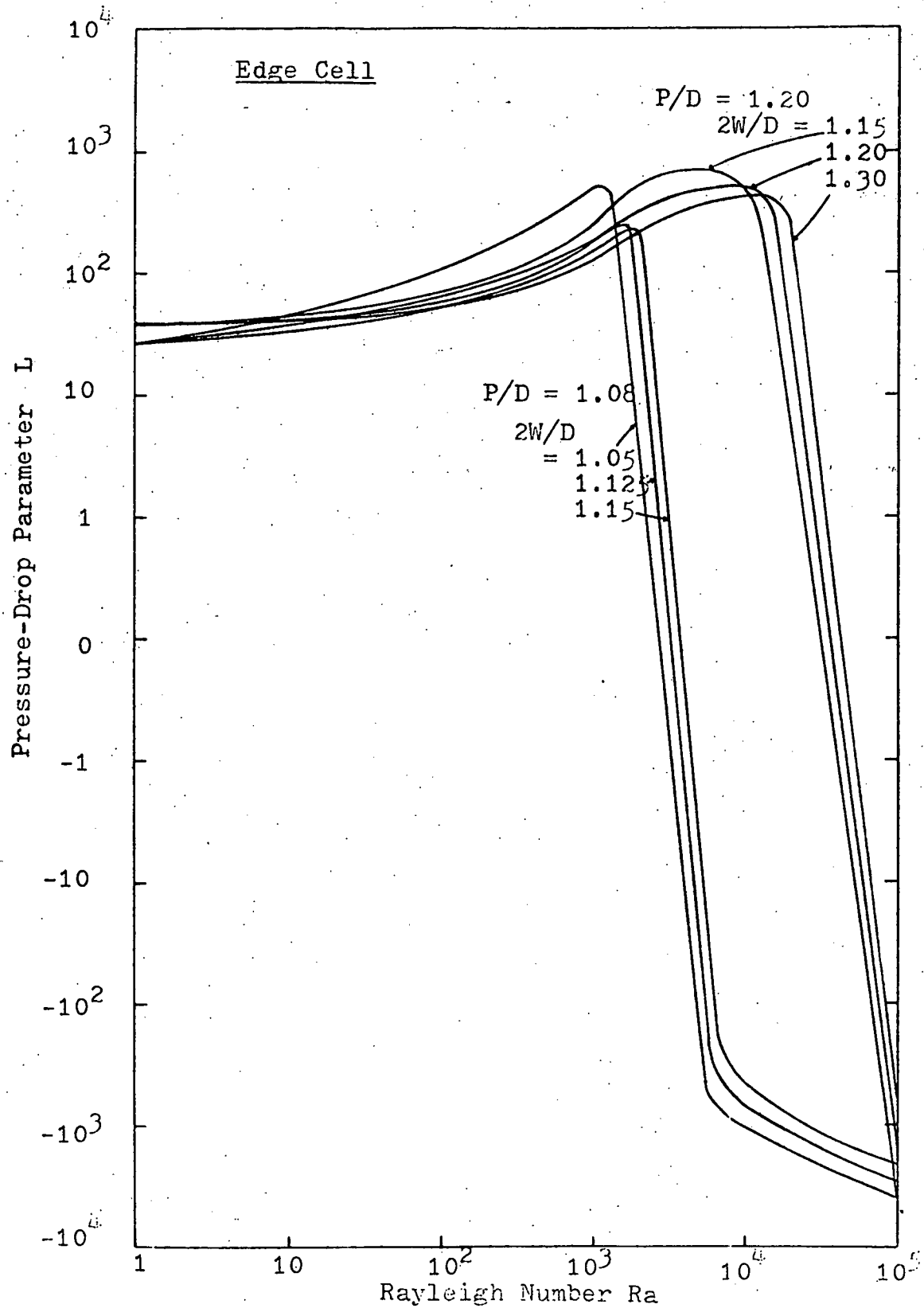
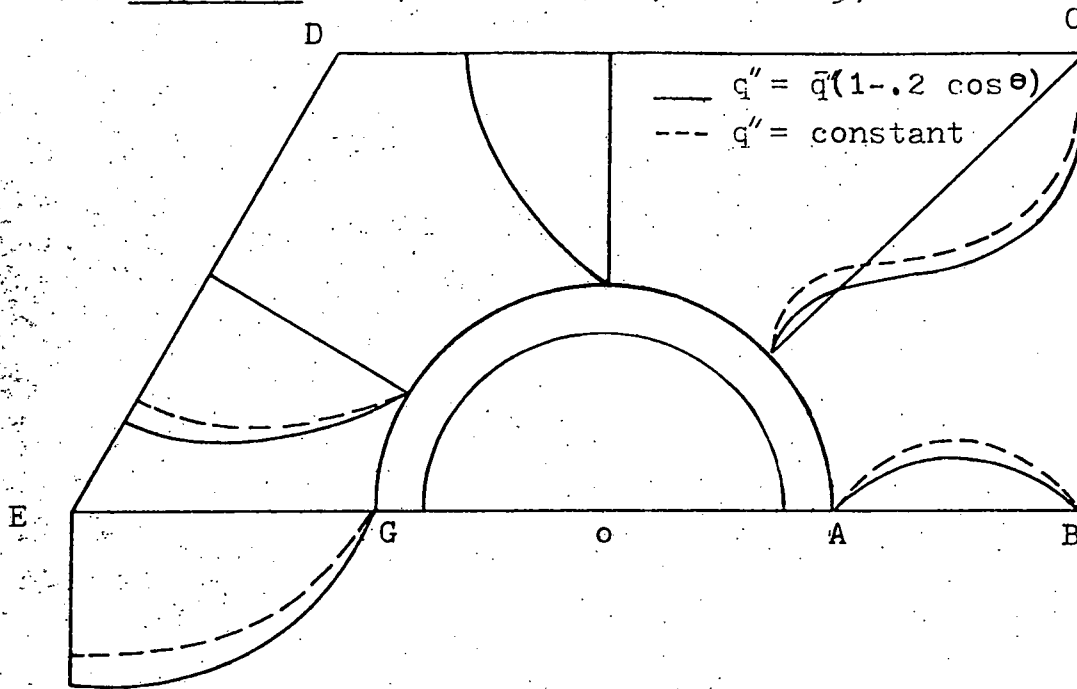


Fig. 25. Pressure-drop Parameter vs Rayleigh Number for  $P/D = 1.2$  and  $1.08$ .

(a) Edge Cell  $P/D = 1.08$ ,  $2W/D = 1.125$ ,  $Ra = 10^3$



(b) Edge Cell  $P/D = 1.20$ ,  $2W/D = 1.30$ ,  $Ra = 10^3$

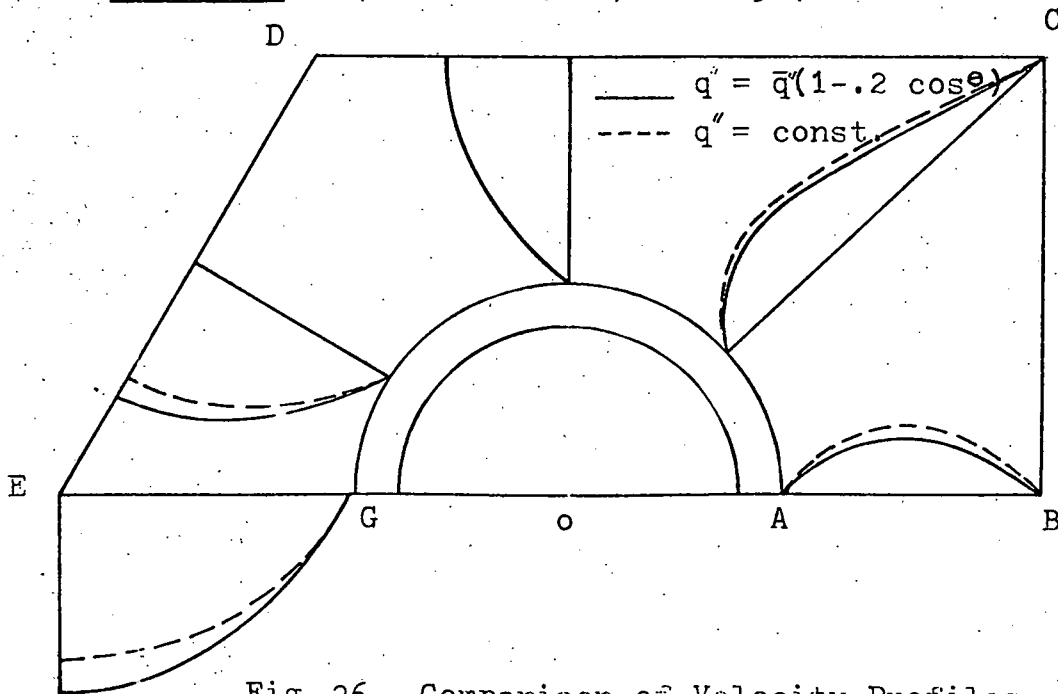


Fig. 26 Comparison of Velocity Profiles in Coolant between  $q'' = \bar{q}(1 - 0.2 \cos \theta)$  and  $q'' = \text{constant}$ .